Application of 2D-IR Spectroscopy to metalcarbonyls: photochemistry and isomerisation dynamics in solution.

by

Dr. Rafal Kania

Department of Physics
University of Strathclyde

Kania R. J.

A thesis presented in fulfilment of the requirements for the degree of Doctor of Philosophy.

August 2012

‘This thesis is the result of the author’s original research. It has been composed by the author and has not been previously submitted for examination which has led to the award of a degree.’

Signed:
Date:

Parts of this thesis are based on:

(1) Kania, R.; Stewart, A. I.; Clark, I. P.; Greetham, G. M.; Parker, A. W.; Towrie, M.; Hunt, N. T. *Physical Chemistry Chemical Physics : PCCP* **2010**, *12*, 1051-63.

(2) Kania, R.; Frederix, P. W. J. M.; Wright, J. A.; Ulijn, R. V.; Pickett, C. J.; Hunt, N. T. *The Journal of Chemical Physics* **2012**, *136*, 044521-9.

(3) R. Kania, S. Kaziannis and N. T. Hunt, ”Measuring molecular dynamics in solution with ultrafast 2D-IR spectroscopy” *Annual meeting of Spectroscopy and Dynamics Group of RSC* **2011** poster.

(4) R. Kania and N. T. Hunt, ”Ultrafast 2D-IR Studies of the Structural and Vibrational Dynamics of the (Propylcyclopentadienyl)Tungsten Tricarbonyl Dimer” *Annual meeting of Spectroscopy and Dynamics Group of RSC* **2010** oral presentation.

Table of Contents

Thesis abstract

The thesis presents work conducted by the author on the development of an ultrafast multidimensional infrared spectrometer, followed by studies of metalcarbonyl photochemical and isomerisation dynamics in solutions.

The first chapter discusses fundamental concepts in chemical reactivity and dynamics, followed by the principles of steady state and time-resolved infrared spectroscopic methods as applied to studies of ultrafast chemical reactivity.

The second chapter gives an account of the design and operation principles of the existing 2D-IR spectrometer followed by details of the development of UV-VIS frequency pump-probe experiment expanding the capacities of the in-house spectrometer toward ultrafast photochemistry via time-resolved infrared spectroscopy (TRIR).

The third chapter reports the findings of TRIR studies of the photochemistry and ultrafast conformational isomerisation of a metallocarbonyl compound designed to mimic the active centre of the hydrogenase family of enzymes.

The fourth chapter deals with ground state and UV-triggered ultrafast dynamic processes of triiron dodecacarbonyl (Fe_3CO_{12}) in n-heptane solution, with particular interest in the detection of fluxional behaviour related to CO bridge permutation.

The fifth chapter demonstrates exhaustive structural and dynamical studies of a substituted metalcarbonyl catalyst using both 2D-IR and Transient 2D-IR spectroscopies both as tools for separation of multicomponent contributions to a complex infrared spectrum and analysis of relaxation dynamics.

The sixth and final chapter presents work on the development of a vibrational echo 2D-IR spectrometer and associated software for spectrometer control and data processing.

1. Introduction

Chemical reactions are of major interest to the chemical and pharmaceutical industries and play a large part in the worldwide economy. Hence, understanding of such processes lies within the scope of both chemistry and physics and is of crucial importance the progress of civilization. In general, chemical reactions can be viewed as a collision of two reactants e.g. atoms, molecules or a mixture of both leading to a crossing of the energy barrier separating reactants from products, which differ by the structural arrangement of atoms.[1] The magnitude and probability of crossing energy barrier permits the division of chemical reactions into reversible and non-reversible processes. Reversible reactions are those where collision induced interconversion lead to a dynamic balance while non-reversible reactions lead to permanent conversion to the product state with negligible concentration of reactants. The crucial aspect of a reaction is the acquisition of the required activation energy by the reactants in conjunction with the reactive collision. From this perspective, an important reaction step involves the acquisition of sufficient energy by the reactants to clear the activation barrier. Such a process can be realised by a gradual build up of reactant excitation to a point sufficient to clear the activation barrier in a reactive collision or by absorption of a single photon, which induces electronic excitation that weakens bonding of the molecule. The acquired activation energy facilitates the rearrangement of reactants into products followed by the dissipation of excess energy by the products.[2] This energy-based description of chemical reaction conforms to the observed vast range of timescales ranging from femtoseconds to geological periods reflecting the cumulative probability of acquiring the activation energy and transition from reactant to product state in reactive collision event.[1,3,4] From a practical perspective, the interest of science and industry is focused on very fast reactions that frequently include ultrafast timescale steps. The latter feature can be conveniently studied for photochemically induced reactions where instantaneous acquisition of activation energy is followed by ultrafast reaction steps. Studies of fast chemical processes largely concentrate on reactions in the liquid phase since these exhibits the highest collision rate of the principle states of matter. The solutions of reactants provide optimal control over reaction progress, while the solvent frequently facilitates reaction by stabilising reactants and products leading to reduction of

activation barrier, and accelerates post reaction energy dissipation. This interest in chemical mechanisms and the role of ultrafast processes stimulates constant development of spectroscopic methods for studies of liquid phase and chemical reactions in solutions.

Chemical reactions that are viewed as atomic rearrangements involving formation or breaking of chemical bonds leading to changes in molecular structure and bonding do not cover the full extent of processes relevant to chemical dynamics.[4-26] The vast majority of polyatomic molecules exist in more than one geometrical form, called an isomer, often exhibiting similar but distinct chemical properties and reactivity. The transition from one geometrical arrangement to another faces an activation energy barrier similar to that of a chemical reaction, but the whole process does not involve breaking or formation of a chemical bond. These chemically relevant processes are named isomerisations because they proceed through the stages similar to a chemical reaction but the final result is simply an altered molecular geometry. The most frequent mechanism of isomerisation is rotation of a portion of a molecule around a single σ-type bond leading to a new spatial configuration or conformation.[3,27-36] Within the latter category, we can separate the biologically relevant processes of conformational isomerisation that occur in macromolecules like proteins. In such processes, geometrical changes are correlated with reorganisation of the hydrogen bond network, forming a synthetic process that can be viewed as hydrogen bond permutation leading to new molecular geometry.[37-57] It is important to note that hydrogen bond reorganisation is not accompanied by cleavage of bonds between the hydrogen and the donor atom, hence we can apply the term isomerisation to such processes. Another feature of isomerisation processes is a generally lower activation barrier in comparison to chemical reactions requiring bond rearrangements.[1,3,7,29,32,58-60] The low activation barrier for isomerisation causes many of these processes to fall within the ultrafast time domain making it more difficult to recognise and characterise. Similarly, the central role of the bond in chemical transformations makes spectroscopic methods capable of studying its nature a principal tool for characterisation of mechanism and dynamics of chemical processes.

1.1. Chemical bond - dynamic description

A chemical bond is an attraction existing between atoms permitting the formation of complex structures such as molecules. The proximity of atoms in molecule causes overlap of atomic valence orbitals creating lower energy molecular orbitals whose population by electrons results in binding together two or more atoms. To analyse a bond's dynamical behaviour it is often convenient to separate the orbital-bound motion of light electrons from the heavy nuclei by applying the Born-Oppenheimer approximation; a postulate that permits separation of electronic and nuclear motion. The changes of inter-nuclei distance resulting from nuclear motion are bounded by the well-shaped potential surface determined by the electron distribution arising from the shape of molecular orbitals. The combination of ceaseless thermal motion of nuclei and this molecular orbital-originated potential forcing the nuclei back to an equilibrium position causes bond oscillations at a characteristic frequency expressed in the following classical physics formula (1)

$$\omega_{Bond} = \sqrt{\frac{k}{\mu}} \tag{1}$$

where ω_{Bond}, k, μ are a bond oscillation frequency, force constant and reduced mass, respectively. A more appropriate description of the chemical bond is provided by the Quantum Harmonic Oscillator (QHO) model that includes quantization of energy of elemental particles. In the QHO picture, oscillatory motion is split into discrete vibrational levels starting from non-zero for the lowest energy oscillations. The equidistant energy ladder of the QHO model represents an infinite stepwise increase of oscillation amplitude expressed in following formula (2)

$$E_\nu = \hbar\omega\left(\nu + \frac{1}{2}\right),\ \nu = 0,1,2,\ldots N \tag{2}$$

where ω, and ν denote angular frequency and vibrational quantum number, respectively. From the perspective of a chemical reaction, such a simplified description of the vibration of a chemical bond is insufficient since it does not permit bond breaking. A more realistic picture is provided by the Quantum Anharmonic Oscillator model that introduces the concept of a limitation of oscillatory excitation and interactions of oscillatory modes, called vibrational coupling. Anharmonicity is introduced by the expansion of QHO energy formulae into a power series in relation

to vibrational quantum number ν. To express the bond excitation limit, it is sufficient to cut-off power series expansion at quadratic terms as shown in the equation (3)

$$E_{anh} = \hbar\omega\left[\left(\nu+\tfrac{1}{2}\right)-\left(\nu+\tfrac{1}{2}\right)^2 x_e^o - \left(\nu+\tfrac{1}{2}\right)\left(\nu'+\tfrac{1}{2}\right)x_e^c + higher\ order\ terms\right] \quad (3)$$

where $x_e^{o,c}$ denotes the first anharmonic constants – an energy corrections due to anharmonicity of molecular vibrator x_e^o and couplings to other vibrators x_e^c while ν and ν' denote the vibrational quantum number of the principal and coupled oscillator. The anharmonic oscillator energy level separation decreases with rising quantum number leading to a dissociation threshold when $(\nu+½) < (\nu+½)^2 x_e^o$. Mixed quadratic terms $(\nu+½)(\nu'+½)x_e^c$ introduce vibrational coupling between two different frequency oscillatory modes. The major factor contributing to vibrational coupling are dipole-dipole interactions, arising from the fact that displacement of nuclei during vibrational motion generates a transient dipole moment that can interact with transient dipole moments associated with other vibrations. The second, purely mechanical, vibrational coupling factor contributes when two or more oscillators share a common atom or group of atoms. In such a situation, two or more vibrations involve displacing a common atom or group of atoms in different way, hence those vibrations are correlated or the introduced deformation of geometry does not preserve the position of the molecular centre of gravity; a necessary condition for the motion to be classified as a vibrational mode.

The quantum mechanical description of the bond reveals a link between molecular vibrations and reactivity. Since most chemical reactions involve bond breaking or formation, such a process is equivalent to disappearance or appearance of new vibrational modes in the system, respectively. This observation has several implications for chemical reactions. Firstly, the height of activation energy barrier is connected with the anharmonicity of the molecular bond x_e^o to be cleaved or formed. Secondly, the product state must shed excess activation energy and vibrational excitation in order to stabilise the molecular system in the new configuration. Since the anharmonic oscillator picture of the chemical bond implies vibrational coupling, the chemical reaction description must include not only product state vibrational relaxation but also vibrational energy redistribution over coupled states accompanying population relaxation. The close relation of the chemical bond with

the vibrational structure of molecules makes understanding it important for studies of chemical reactivity. This relation puts infrared absorption spectroscopy techniques that discern the vibrational structure of molecules at the frontier of chemical reactions studies.[1,4,5,7,11,17,18,58,61-65] Furthermore, time-resolved infrared spectroscopy permits studies of vibrational coupling and population relaxation of product or reactant states independently, aiding evaluation of the chemical reaction mechanism.[21,24-26,34-36,52,60,64-67]

1.2. Chemical reaction dynamics and dynamic equilibrium

The established relationship between the chemical reaction and anharmonic molecular vibrations permit us to portray a chemical reaction as the process of clearing an activation barrier by the collapse of a near-dissociation threshold excited vibrator. The Transition State Theory (TST)[68] utilises this picture to plot chemical reaction energetics as the three level diagram shown in Figure 1.

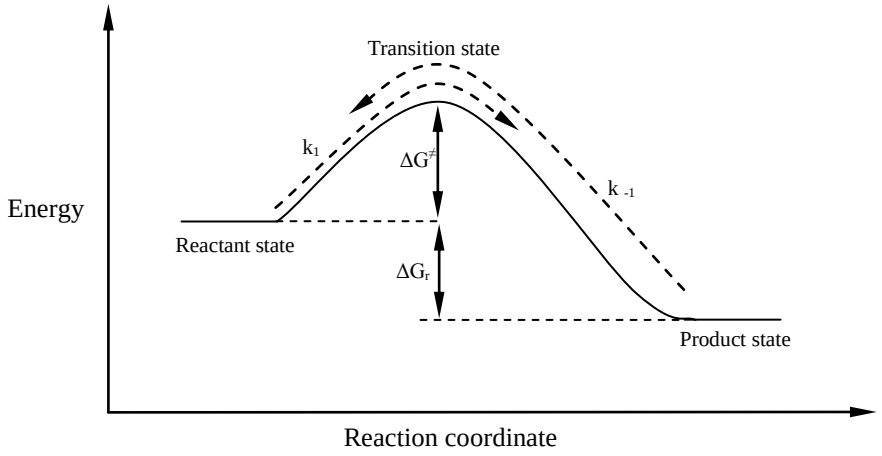

Figure 1. Schematic depiction of reversible chemical reaction energetics.

The diagram involves three levels: the reactant state, a common transition state lying at the top of the activation energy barrier and the product state. The chemical reaction rate in the TST picture depends on two factors: the height of energy barrier and the transition state collapse rate. The height of the energy barrier is a function of the molecular orbital binding energy that has to be overcome to rearrange reactant into the product and the differences in formation energies of both states. The second

factor to be considered in this model is the collapse of the transition state, portrayed as a cross-over of the dissociation barrier by a near-threshold-excited molecular vibrator. Such a process is thought to be stochastic in nature, showing that not all reactants that acquired sufficient energy will successfully transfer into products. The latter feature makes TST applicable to reversible and non-reversible chemical processes alike.

Transition State Theory (TST) expresses Eq. 4 the forward reaction rate (k_1) as a function of the energy barrier which in depends upon the activation free energy $\Delta G^{\neq}$ required to reach the transition state and the transmission coefficient κ, which represents the probability of formation of the product state from the transition state.

$$k_1 = \kappa \frac{k_B T}{h} e^{\frac{-\Delta G^{\neq}}{RT}} \tag{4}$$

The pre-exponential factor k_BT/h is proportional to the frequency of the vibrational mode responsible for the collapse of the transition state, which limits the maximum reaction rate to ~160 fs^{-1}. The rate of reverse process (k_{-1}) can be expressed in terms of the forward reaction parameters as follows Eq. 5

$$k_{-1} = \kappa \frac{k_B T}{h} e^{\frac{-\left(\Delta G^{\neq} + \Delta G_r\right)}{RT}} \tag{5}$$

where the energy barrier faced by the reverse reaction equals the sum of the activation free enthalpy $\Delta G^{\neq}$ of forward reaction and free enthalpy of reaction ΔG_r expressing the difference in free formation energy of reactant and product states. The existence of both forward and reverse reactions leads to a dynamical equilibrium state, where the number of molecules transferred from reactant to product states equals the number of molecules transferred in the opposite direction. In such a situation the concentrations of both reactant and product are time independent, hence the concentration ratio can be represented by the dimensionless equilibrium constant K (Eq. 6).

$$K = \frac{k_1}{k_{-1}} = \frac{[Products]}{[Substrates]} \tag{6}$$

In thermodynamics, the equilibrium constant K is linked with the reaction free enthalpy ΔG_r for any mass conserving system by following equation (7)

$$\Delta G_r = -RT \ln K \tag{7}$$

The latter relations provide measurement of asymmetry of energy barrier for forward and reverse reaction allowing estimation of the complementary reaction rate on the basis of one reaction rate and thermodynamical data.

1.3. Electronic transitions and photochemistry

Prior to the introduction of infrared absorption spectroscopy, a brief description of photochemical reactions is presented in this section. Photochemical reactions rely on electronic excitation by photons carrying an energy exceeding the amount needed to dissociate a chemical bond in a molecule. Electronic motion, as with vibrational motion in molecule, is quantized, leading to discrete energy levels with up to a pair of electrons occupying a given orbital. The outermost electronic energy levels are occupied by atomic valence electrons in molecular orbitals which contribute to chemical bond.[1] Therefore, excitation of electrons in these orbitals, requiring UV-Vis frequency radiation, directly affects molecular bonding. Any outer shell electronic excitation that promotes electrons from a bonding molecular orbital to non- or anti-bonding molecular orbital thus weakens the forces holding molecule together. A weakened chemical bond is prone to dissociation, a process named photolysis, which lead to a sequence of photochemical and photophysical processes.[1,11,23,24,69,70] In the following chapters we demonstrate the application of this chemical reaction triggering method for various metalcarbonyl compounds. The metalcarbonyls are a group of molecules a simplest organometallics containing metal ion bonded with CO molecule via carbon atom. Since all metalcarbonyls represent a consistent photochemical behaviour, it is beneficial to discuss a generalised picture of a photochemical reaction sequence for these compounds. A typical photochemical reaction sequence for a generic metalcarbonyl molecule in solution is illustrated in Figure 2. The UV-Vis frequency irradiation of $M(CO)_x$ generates an excited state metastable $M(CO)_x^*$ molecule (1), which undergoes fast vibrational cooling (2) to the lowest vibrational level of the electronically excited state. This vibrationally cooled excited state molecule may undergo further radiative or non-radiative relaxation to the ground electronic state (3) followed by subsequent vibrational cooling (4). An alternative way of shedding excitation energy is through photoinduced dissociation of a CO ligand (5) forming an unstable ligand-deficient transient species $M(CO)_{x-1}$.

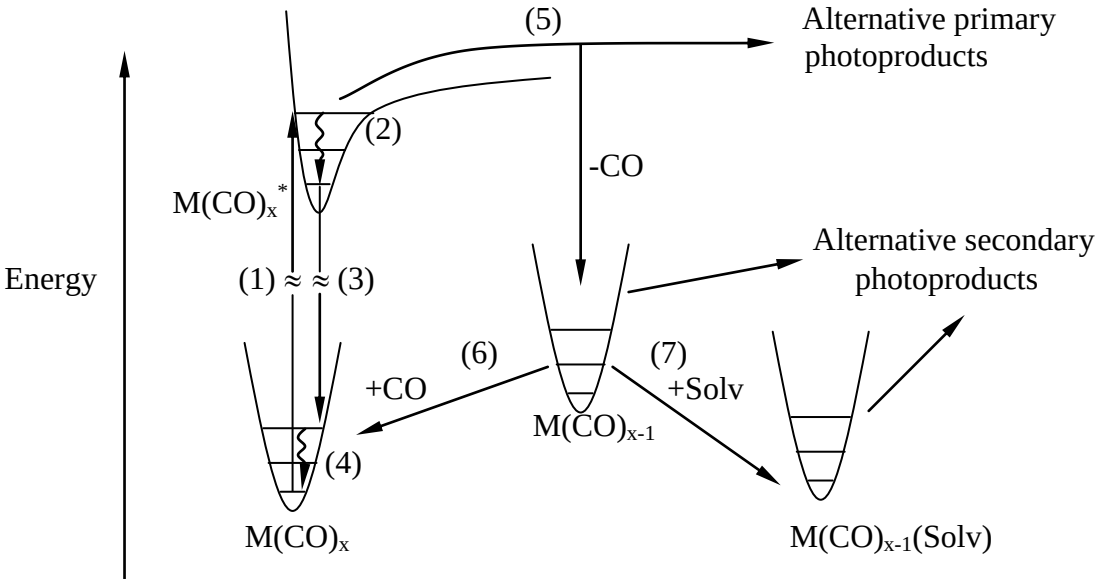

Figure 2. Photophysics and photochemistry of generic metalcarbonyl derivative in solution.

The unstable primary photoproduct, $M(CO)_{x-1}$, can stabilise by reforming the parent molecule via the of process of geminate recombination (6) or fill the vacant coordination site with a solvent molecule (7), forming an adduct $M(CO)_{x-1}(Solv)$. Depending on the molecular structure, alternative photoreaction sequences[22,24,63] may occur although the slow diffusion constants of most common liquids leads to capture of photogenerated fragments in the solvent cage for sufficiently long to favour geminate recombination and solvent adduct formation over other transient stabilisation pathways involving reactions with other solutes, which typically form on nanosecond and longer timescales.

1.4. Principles of steady-state infrared spectroscopy

As the great majority of molecules consist of more than two atoms, it is important to develop a proper way of representing oscillatory motion of polyatomic molecules. A molecule built from *N* atoms has *3N* degrees of motional freedom where *3* of them represent translation of the entire molecule and a further *3* (*2* in case of linear molecules) represent rotation around the molecular centre of gravity. The remaining 3N-6 (3N-5) degrees of freedom represent the characteristic oscillatory motions of the molecule named vibrational modes. One way to separate different

molecular vibrations is divide them according symmetry properties of the nuclear motions involved in a particular mode. The set of 3N-6 (3N-5) linearly independent symmetry-resolved vibrations form a basis of normal modes which can represent any complex molecular vibration.[1] Such symmetry-based division of molecular vibrations plays an important role in infrared spectroscopy since the absorption of mid-infrared radiation is linked with changes of the molecular dipole moment during vibrations. Absorption spectroscopy introduces the transition moment integral as a way to express the theoretical probability of a transition between two quantum levels expressed as (Eq. 8)

$$\mu_{fi} = \int \Psi_f \hat{\mu} \Psi_i d\tau \qquad (8)$$

where $\Psi_{i,f}$ are the initial and final molecular wavefunctions and $\hat{\mu}$ is transition moment operator. The absorption intensity is proportional to square of transition moment integral μ_{fi}, which is non-zero only if it contains contributions invariant in all molecule symmetry elements. For the absorption of infrared radiation, the transition moment operator principle leads to the selection rule that the vibrational quantum number ν can change by +1 for absorption or –1 for emission:

$$\Delta\nu = \pm 1$$

The mid-infrared absorption spectrum is dominated by fundamental vibrational transitions $\nu_{0\rightarrow 1}$ from ground to first excited state. This is because the typical energy spacing of molecular vibrational levels lies in the range 400-4000 cm^{-1}, way above the average thermal excitation energy at room temperature (~200cm^{-1}). However, closer examination of a typical infrared spectrum reveals the presence of weak additional transitions at frequencies close to the values of linear combinations of the fundamental frequencies. These transitions are named overtones when the frequency is approximately double that of a single fundamental mode or a combination mode when it nears the sum of two different fundamental frequencies. The presence of additional absorption bands are the effect of inherent anharmonicity in molecular vibrations, facilitating the process of "intensity borrowing" from fundamental modes via vibrational coupling.[1,62,67,71]

The absorption lineshapes registered by steady-state infrared spectroscopy are determined by vibrational relaxation processes. The absorption lineshape is a result

of two processes, population relaxation, characterised by the vibrational lifetime (T_1), and the coherence dephasing process, characterised by the coherence lifetime (T_2). Population relaxation arises from the limited lifetime of excited states and determines the minimal natural linewidth of the transition peak. Coherence dephasing is the result of interactions of molecules in excited vibrational states with other molecules that causes loss of the phase information acquired in an excitation by an optical field.[67,72,73] When coherence dephasing dynamics are faster than population relaxation, absorption lineshape experiences inhomogeneous line broadening. Unlike in the gas phase where coherence dephasing is caused by phase shifts introduced by collisions and small frequency shifts due to Doppler effect, such processes in solutions have a more complex form. Interactions of solvent molecules with the solute cause continued changes in the phase and frequency of a relaxing vibration. The latter process is conventionally described for relaxation in solution by the Frequency-Frequency Correlation Function (FFCF) which is used to describe the temporal evolution of vibrational mode frequency subjected to stochastic solute-solvent interactions. The discussion of the form of FFCF function is beyond the scope of thesis however the final chapter discusses absorption lineshape characteristics that are related to the FFCF function.

Information of vibrational dynamics can be followed by measuring linewidth changes in steady state infrared spectra. In this approach a full linewidth at half maximum (FWHM) is reciprocally proportional to observed coherence dephasing lifetime (T_2^*). The observed coherence-dephasing lifetime (T_2^*) has two contributions from populational relaxation lifetime (T_1) and pure coherence dephasing lifetime (T_2) as shown in following equations (9)

$$FWHM \propto \frac{1}{T_2^*}, \quad \frac{1}{T_2^*} = \frac{1}{2T_1} + \frac{1}{T_2} \tag{9}$$

Unfortunately the steady-state infrared spectroscopy does not offer any straightforward way of separating contributions to the (T_2^*) lifetime, which seriously limits studies of vibrational relaxation by this technique.

As discussed before, infrared spectroscopy is a convenient tool for monitoring chemical reactions owing to the ability to detect changes of a fundamental vibrational signature and monitor the dynamics of chemical processes including

measurement of vibrational relaxation dynamics.[6,25] This feature permits the study of chemical reactions involving breakdown or formation of new bonds. Moreover, the isomerisation processes important for chemical transformations that do not involve bond rearrangement are still within the scope of infrared absorption spectroscopy owing to the impact of geometrical rearrangements on molecular symmetry that in turn affects the molecular vibrational signature. The latter feature is an asset of infrared absorption spectroscopy in comparison to NMR spectroscopy, another technique extensively applied to study chemical reaction dynamics.[6,27-30,32,33,65,74-76]
The major disadvantages of steady-state infrared spectroscopy as a tool for studying chemical reactions arise from temporal and spectral limitations. The infrared absorption spectrometer utilising a continuous wave incoherent source of mid-infrared radiation has a limited temporal resolution entirely dependent on the acquisition rate of infrared detectors, at best a few nanoseconds.[75] Secondly the method-specific lineshapes provide crude estimation of vibrational relaxation, in particular solute-solvent interaction dynamics limiting chemical process characterisation.[67] Finally, the low dimensionality of infrared spectra prohibits the observation of vibrational coupling and vibrational energy redistribution dynamics which are important contributors to chemical reaction studies.

1.5. Time-Resolved Infrared (TR-IR) spectroscopy

The development of pulsed laser radiation sources gave rise to pump-probe spectroscopy, a new technique offering far greater temporal resolution than its steady-state counterparts. Significant breakthroughs were achieved with the introduction of the Ti:Sapphire laser gain medium in 1986[77] followed by development of Kerr Lens Modelocking technique[78] displaced dye lasers in producing stable femtosecond pulse trains, which combined with efficient non-linear optical materials for light frequency conversion triggered development of sub-nanosecond timescale spectroscopies in the UV-VIS and IR frequency ranges. This temporal resolution leap was essential for studies of vibrational relaxation occurring on femto-to-picosecond timescales and ultrafast chemical processes. The first pump-probe spectrometers recording time-resolved infrared spectra perturbed the measured system with an intense pump pulse and followed spectral changes over picosecond

timescales with broadband probe pulses. Depending on the pump frequency, pump-probe techniques can be subdivided into UV_{pump}-UV_{probe},[62,70] IR_{pump}-IR_{probe}[67] and UV_{pump}-IR_{probe} spectroscopy[5-7,21,22,24,58,62,63,65,75,79] (TR-IR) for pump frequency inside or outside probe pulse spectrum, respectively.[67] A common application of ultrafast UV_{pump}-UV_{probe}[62,70] and UV_{pump}-IR_{probe} spectroscopy[5-7,21,22,24,58,62,63,65,70,75,79] are to trigger photolysis events in solution and follow excitation, relaxation and photochemical reaction sequences by observing changes in UV-Vis or Infrared spectrum, respectively. Since electronic excitation of molecules leads to variety of photophysical and photochemical processes, UV_{pump}-UV_{probe} and TR-IR spectroscopy have become a basic techniques for the detection and characterisation of short-lived transients and excited states.[79] In contrast, the application of transient pump-probe infrared spectroscopy has concentrated on detailed studies of vibrational relaxation of solutes in thermodynamical equilibrium.

A major disadvantage of both 1D pump-probe spectroscopies is the inherent congestion of the recorded spectrum due to the one-dimensional representation of the spectra, which contain contributions from many species.[4,63,67,72,80] For UV_{pump}-IR_{probe} spectroscopy, the overlap of multiple absorption bands belonging to both parent molecule and photoproducts limits the resolvable structural and dynamical information. Moreover, studies of vibrational relaxation processes on the basis of lineshapes are complicated by vibrational cooling process affecting the shape of spectral lines immediately after UV-Vis frequency excitation. Transient pump-probe infrared spectroscopy overcomes the latter problem by replacing high energy UV-Vis excitation with mid-infrared excitation, which is more suited to registering vibrational relaxation dynamics but provide no information about transient species of essence to chemistry. Pump-probe techniques were the first to exploit the non-linearity of molecular vibrators to record the 3rd order molecular response which carries, among other things, information about the higher vibrational energy levels that expose anharmonicity and vibrational couplings. Yet again, overlapping peaks on 1D spectrum prohibit the separation and extraction of all components of the non-linear molecular response, limiting the available spectral and dynamical information. To take full advantage of the 3rd order molecular response signal in the mid-infrared, a family of higher dimensionality infrared techniques were developed.

1.6. Principles of two-dimensional infrared spectroscopy

The 2D-IR spectroscopy differs from the previously described transient pump-probe infrared spectroscopy by the application of a pump pulse with a shaped frequency spectrum in order to separate contributions from excitations of individual vibrational modes. This frequency spectrum shaping permits the construction of a two-dimensional picture of the infrared spectrum of a molecule, exposing all components of the 3rd order molecular response in a clearer manner than 1D techniques. The advantage of 2D-IR spectroscopy over transient pump-probe infrared techniques is that the former technique isolates components of 3rd order molecular response within the frequency window covered by broadband infrared pulses so it is therefore imperative to discuss the origins of the non-linear signals present in a 2D spectrum. The principles behind this spectroscopy can be deduced using Maxwell's equations (Eq. 10.1-4) for dielectric, but nonmagnetic (B=H), media[81,82]

$$\vec{\nabla} \bullet \vec{D} = \rho \qquad 10.1$$

$$\vec{\nabla} \times \vec{E} = \frac{\partial \vec{B}}{\partial t} \qquad 10.2$$

$$\vec{\nabla} \bullet \vec{B} = 0 \qquad 10.3$$

$$\vec{\nabla} \times \vec{B} = \mu_0 \frac{\partial \vec{D}}{\partial t} + \mu_0 \vec{J} \qquad 10.4$$

Assuming that the measured system lacks free charge carriers ρ, J = 0 and one can rewrite Maxwell's equations into an inhomogeneous wave equation (11.1) with a polarisation driving term.

$$-\Delta \vec{E} + \frac{1}{c^2}\frac{\partial^2 \vec{E}}{\partial t^2} = -\frac{4\pi}{c^2}\frac{\partial^2 \vec{P}}{\partial t^2} \qquad 11.1$$

$$\vec{D} = \varepsilon_0\left(\vec{E} + 4\pi\vec{P}\right) \qquad 11.2$$

$$\vec{P} = \chi^{(1)}\vec{E} + \chi^{(2)}\vec{E}^2 + \chi^{(3)}\vec{E}^3 + \ldots \qquad 11.3$$

$$\chi^{(n)}(t) = \int_0^\infty dt_1 \ldots dt_n R^{(n)}(t_1 \ldots t_n) \qquad 11.4$$

In non-linear limit, the polarisation term is expanded into a series according to powers of the electric field with growing rank susceptibilities as a proportionality

coefficient. The susceptibilities are semi-finite integrals of the molecular response function that represents molecular relaxation processes for a consecutive set of electric field interactions. The solution of the inhomogeneous wave equation with the linear polarisation term yields the complex-valued frequency-dependent refractive index n(ω) (Eqs 12.1-3).

$$\vec{E}(\vec{r},t) = A_0 e^{-i(\omega t - \vec{k}\cdot\vec{r} + \varphi)} \tag{12.1}$$

$$\vec{P}^{(1)}(\omega) = \int_{-\infty}^{\infty} d\omega\, \chi^{(1)}(\omega) A_0 e^{i\omega t + i\vec{k}\cdot\vec{r} + i\varphi} \tag{12.2}$$

$$n(\omega) = n'(\omega) + in''(\omega) = \sqrt{1 + \chi^{(1)}(\omega)} \tag{12.3}$$

The real part of the complex refractive index represents dispersion while the imaginary part represents linear absorption was already discussed for steady-state infrared absorption spectroscopy. Considering a centrosymmetric systems like solutions, non-zero susceptibilities are those involving the odd electric field powers (Eq. 13.1), making third order susceptibility the primary non-linear polarisation term as a source of the signal for non-linear spectroscopy (Eq. 13.2). The third order polarisation involves the combination of three independent electric field interactions leading to new frequency outputs in the process of four-wave mixing.

$$\chi^{(2)} = 0 \tag{13.1}$$

$$\vec{P}^{(3)}(\omega_1,\omega_2,\omega_3) = \int_{-\infty}^{\infty} d\omega_1 \int_{-\infty}^{\infty} d\omega_2 \int_{-\infty}^{\infty} d\omega_3\, \chi_n^{(3)}(\vec{k}_3,\vec{k}_2,\vec{k}_1,\omega_3,\omega_2,\omega_1)\vec{E}_3(\vec{k}_3,\omega_3)\vec{E}_2(\vec{k}_2,\omega_2)\vec{E}_1(\vec{k}_1,\omega_3) \tag{13.2}$$

From the 2D-IR spectroscopy standpoint, constraints imposed by the spectro-temporal profile of the pulsed laser radiation and the input beam geometry used in the experiments limits the detectable components of the 3rd order response to the following four-wave mixing patterns Eq. 14.1 and 14.2

$$\omega_{Sig}^{(3)} = \mp\omega_1 \pm \omega_2 + \omega_3 \tag{14.1}$$

$$k_{Sig}^{(3)} = \mp k_1 \pm k_2 + k_3 \tag{14.2}$$

where $\omega_{1,2,3}$, $k_{1,2,3}$ are the frequencies and wave vectors of the interacting waves while ω_{sig}, k_{sig} denote resulting new output frequencies with corresponding wave vectors.[83] The 3rd order molecular response in the mid-infrared spectral region of interest is dominated by the frequencies of vibrational excitations of the solute. This

effect can be assigned to the resonant enhancement of the non-linear signal arising from wave-matter interactions at frequencies $\omega_{1,2,3}$ coinciding with vibrational excitation involving at least one populated level. These specific frequencies of the non-linear response are best discussed for a system with a vibrational mode structure consisting of a pair of coupled anharmonic vibrators. The schematic representation of these vibrational energy levels is shown in Figure 3.

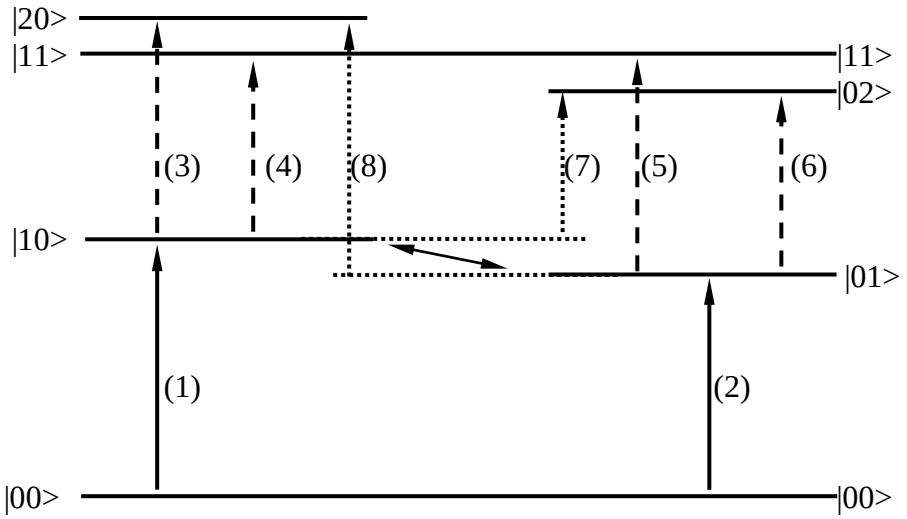

Figure 3. The energy level schematic for pair of coupled anharmonic vibrators where solid arrows represent first and second interactions while dashed and dotted arrows represent third interaction.

The anharmonicity causes a decreasing spacing of vibrational levels with v, resulting in a systematic decrease in the energy required for vibration excitation between successive levels. The presence of vibrational coupling facilitates the exchange of population between vibrational levels leading to a common vibrational ground state while higher levels are capable of exchanging population (double-head arrow in Fig. 3). In addition, coupling results in the appearance of combination mode levels |11> which represent collective excitations of two vibrational modes. The simplest case of the 3rd order response is the degenerate four-wave mixing experiment where the first two interactions are of the same frequency $\omega_1=\omega_2$. The conclusions drawn for such a case are universal to all variants of 2D-IR spectroscopy. The first two interactions in the degenerate case are of common frequency, hence the resonant signal

enhancement is gained only for frequencies coinciding with the fundamental vibrational transitions (*1*) to |10> or (*2*) to |01> levels (solid arrows Fig. 3). The strong wave–matter interaction of the femtosecond laser pulses leads to population of the first excited state |10> or |01>. Population of the excited vibrational levels induced by the first interactions give rise to new frequency components of the 3rd order response apart from those of fundamental frequencies. These new frequency components coincide with the energies of the first to second excited state transitions and first excited states to the combination state transitions (dashed arrows in Fig. 3) (*3*), (*4*) for |10> manifold and (*5*), (*6*) for |01> manifold, respectively. Following the initial excitation, the exchange of population by the coupled |10> and |01> levels is possible which further results in additional cross-level transitions (dotted arrows in Fig. 3) (*7*) for |10> and (*8*) for |01>.[64,84] For energy conservation, such processes require interaction with a third vibrational or rovibrational mode in order to bridge the gap between the excitation photon and the energy of the final state to which population is transferred. In this process the energy difference between the involved fundamental modes results in the creation or annihilation of a low frequency >200cm^{-1} vibrational or rovibrational quantum coupled with the vibrational modes of interest.

1.6.1. Double-resonance 2D-IR spectroscopy

The double-resonance 2D-IR spectroscopy technique implements the principles of degenerate four-wave mixing to generate and isolate the discussed specific 3rd order response signal for molecules in solution. This quasi-frequency domain technique utilises two mid-IR pulse trains: an intense, narrowband pump and weaker, broadband probe.[67,84,85] The pump pulse acts as the first two interactions of the discussed degenerate four-wave mixing scheme owing to the limited frequency range covered by pump pulse spectrum. The broadband probe pulse then acts as the third interaction, triggering the non-linear response in the direction of probe pulse, as stipulated by degenerate four-wave mixing pattern. The spatial overlap of the linear and non-linear molecular responses require isolation of the 3rd order signal from the linear background by subtraction of the spectrum recorded with the pump pulse present from those without the pump pulse. This procedure means that all the

fundamental frequencies present in both linear and the non-linear signal appear as negative features due to pump pulse transition bleaching while all additional frequencies absent in the linear spectrum appear as positive spectral features. Sweeping the pump pulse frequency window across probe pulse spectrum permits spreading the 3rd order molecular response signal components over two axes for the pump frequency, ω_1, and probe frequency, ω_3 respectively. The example 2D-IR spectrum for the previously discussed case of the coupled anharmonic vibrators is shown in Figure 4.

On the diagonal of the 2D spectrum are located the fundamental transitions, while in the off-diagonal region appear additional peaks (frequency components). When the pump frequency coincides with either of the fundamental transitions ((1) or (2) in Fig. 3) the probe pulse triggers a 3rd order response at frequencies coinciding with this fundamental $\nu(0\rightarrow1)$ transition (solid circles in Fig. 4) along with those of higher excitations to the second vibrational level $\nu(1\rightarrow2)$ and the combination mode $\nu(10\rightarrow11)$, $\nu(01\rightarrow11)$ (dashed circles in Fig. 4). Scanning the pump-probe delay time permits the measurement of ultrafast dynamical processes involving the signals present in the 2D spectrum for example vibrational relaxation. In the case of solutes which display an efficient exchange of population between fundamental |10> and |01> levels, additional frequencies are present in the non-linear signal representing cross-level transitions $\nu(10\rightarrow02)$ and $\nu(01\rightarrow20)$ (dotted circles in Fig. 4) though these are typically observed only at non-zero pump-probe delay times.

The double-resonance 2D-IR spectroscopy allows not only characterisation of ultrafast chemical reaction dynamics but also vibrational relaxation and coupling dynamics for the reactant and product separately, providing a complete picture of a chemical process. Moreover, typically the pump pulse duration will be in the region of 1.5 to 2 ps, which distorts spectra obtained at short delay times due to the temporal overlap of the pump and probe pulses, prohibiting measurement of sub-picosecond dynamics. The practical simplicity of the double-resonance technique does however make it a robust tool for studying picosecond timescale vibrational relaxation and chemical dynamics in solution.[3,4,34,67,71,84,86-88] The temporal and spectral resolution limitations of double resonance 2D-IR did however stimulate development of the time-domain vibrational echo 2D-IR spectroscopy method which exhibits improved

spectral resolution and provides access to sub-picosecond dynamics allowing 2D-IR spectroscopy to tackle congested spectra and provide more accurate studies of solute-solvent interaction dynamics.[64,67,86]

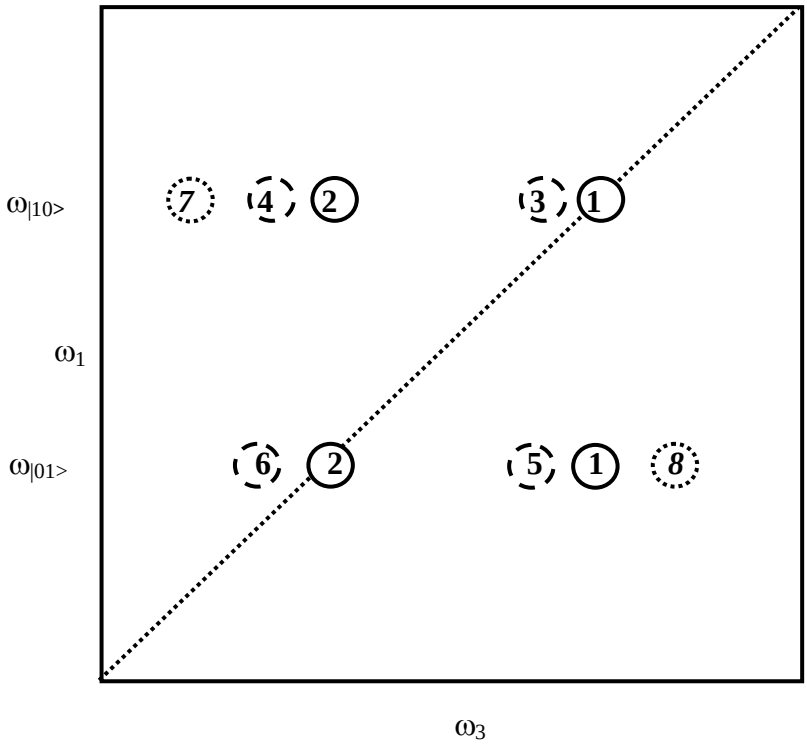

Figure 4. The 2D spectrum for pair of coupled anharmonic vibrators depicted in (Fig. 3) where solid circles represent fundamental transition $\nu_{0\rightarrow1}$ and $\nu_{1\rightarrow2}$ overtone transitions, dashed circle combinational modes $\nu_{01\rightarrow11}$ and $\nu_{10\rightarrow11}$, while dotted circles represent cross-level transition $\nu_{10\rightarrow02}$, and $\nu_{01\rightarrow20}$.

1.6.2. Vibrational echo 2D-IR spectroscopy

The time-domain 2D-IR spectroscopy technique relies on the interference of three broadband femtosecond infrared pump pulses at the sample, introducing a collective excitation of solute vibrational levels and leading to the emission of a coherent vibrational echo signal. The phase-resolved detection system allows isolation of the coherent signal components containing the 3rd order response from incoherent contributions, improving the 2D spectrum quality by eliminating non-coherent noise components.[9,14,37,38,43-45,47,51,53,60,62,72,86,89-91]

Since the time-domain technique relies on the introduction of coherences into the molecular system vibrations, the analysis of the 3rd order echo signal requires a full quantum treatment of the wave-matter interactions. The simplest theoretical approach to the system coherence propagation involving multiple wave-matter interactions utilises the density matrix propagation approach.[67] The density matrix depiction of this process provides a series of expressions for different vibrational echo contributions representing pathways for the coherent interaction of three consecutive laser pulses with the solute molecules. Each of these pathways represents an allowed permutation of coherent wave-matter interactions constrained by the four-wave mixing pattern observable in 2D-IR spectroscopy. A convenient way of expressing these pathways is Feynman diagrams, representing the evolution of the density matrix for a particular interaction scheme. The convenience of such notation is that each Feynman diagram can be translated into the appropriate molecular response functions $R_n(t_1, t_2, t_3)$ that are responsible for the appearance of particular spectral features present in a 2D-IR spectrum. The discussion of Feynman diagrams will be limited to two diagrams while the full account for a single and coupled pair of vibrators is presented in Ref. 63. The Feynman diagrams and resulting molecular response signal contributions R_1 and R_5 for fundamental frequency diagonal features are presented below

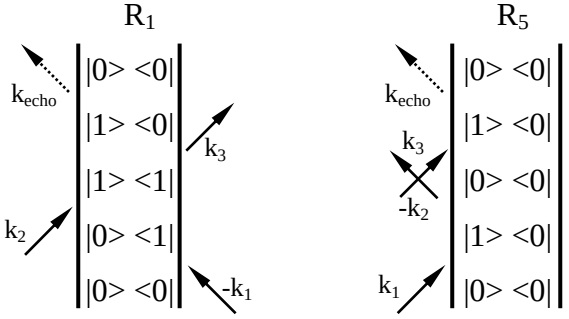

1 2 3 4

$$R_1(t_3,t_2,t_1) \propto \left(\mu_{10}\, e^{+i\omega_1 t_1} e^{-t_1/T_2^*}\right)\left(\mu_{10} e^{-t_2/T_1}\right)\left(\mu_{01} e^{-i\omega_3 t_3} e^{-t_3/T_2^*}\right)\left(\mu_{01}\right) \qquad \omega_1 = \omega_3 = \omega_{01}$$

$$R_5(t_3,t_2,t_1) \propto \left(\mu_{10}\, e^{-i\omega_1 t_1} e^{-t_1/T_2^*}\right)\left(\mu_{01} e^{-t_2/T_1}\right)\left(\mu_{10} e^{-i\omega_3 t_3} e^{-t_3/T_2^*}\right)\left(\mu_{01}\right) \qquad \omega_1 = \omega_3 = \omega_{01}$$

where $\mu_{01,10}$, $\omega_{1,\ 3}$, T_1, and T_2^* are transition dipole moments and frequencies, populational and observed coherence dephasing lifetimes, respectively. The arrows

indicate coherent interaction between the quantum field and the solute vibrations leading to a particular state of the molecular system represented by the density operator. The inward arrows represent transitions of excitation from a field to the molecular system while outward ones depict the reverse process.

The first interaction stimulates transfer of coherence from the field to the molecular system on the right hand side of the diagram R_1 and left hand side of diagram R_5. In the period that follows, called first coherence period τ_1 ($\tau_1=t_2-t_1$), the molecular system exhibits an oscillatory coherence decay at the solute fundamental vibrational frequency (ω_{01}) with exponential damping characterised by the T_2^* lifetime. This process gives rise to the first term of the non-linear molecular response function governing the particular relaxation pathway that is equivalent to the ($-\omega_1$) and (ω_1) frequency contributions in the four-wave mixing scheme, respectively. It is to be noted that in the case of the diagram R_1, coherence oscillations considered are with opposite phase to the field, while for the diagram R_5, coherence oscillations are in-phase with the field. The second interaction occurs on the left hand side of the diagram R_1 and indicates a subsequent wave–molecular system coherence transfer for the diagram while in the case of the R_5 diagram, the molecular system loses the previously acquired coherence by stimulated coherence transfer from the molecular system to the field. This process gives rise to the second term of the non-linear molecular response function governing the particular relaxation pathway that is equivalent to the (ω_2) and ($-\omega_2$) frequency contributions in the four-wave mixing scheme, respectively. In the second coherence period τ_2 ($\tau_2=t_3-t_2$) that follows, the coherence oscillations are quelled[73], exposing a pure population relaxation, characterised by the T_1 lifetime, as accounted for in the second term of the molecular response function. The selected cases represent two different mechanisms of quenching coherent oscillations. In the case of the R_1 diagram, the oscillatory coherence decay is quenched owing to superposition of previous two coherences which propagate with opposite phases while for the R_5 diagram the second interaction stimulates transfer of the previously acquired coherence from the molecular system into field exposing non-oscillatory population decay.

The third interaction is on the right hand side of the R_1 diagram and indicates a stimulated transfer of coherence from the molecular system to the field while in the

case of the R_5 diagram, the molecular system is re-excited into a coherence state. This process gives rise to the third term of the non-linear molecular response function that is equivalent to the (ω_3) frequency contribution in the four-wave mixing scheme, respectively. In the third coherence period τ_3 (t_{echo}-t_3=τ_3) that follows the molecular system exhibits an oscillatory coherence decay at the solute fundamental vibrational frequency (ω_{01}) with exponential damping characterised by the T_2^* lifetime. In the case of the R_1 diagram the oscillatory coherence decay is in-phase with the field owing to annihilation of the out-of-phase coherence oscillations by the third interaction while for the R_5 diagram the third interaction reintroduced coherence oscillations to the molecular system. The third coherence period τ_3 is terminated when constructive superposition of all the coherence dephasing processes involved trigger emission of a photon echo signal occurring within the time up to the first coherence period duration ($\tau_3 \leq \tau_1$). This process is denoted as a fourth term of the non-linear molecular response function and gives rise to the output of a frequency term (ω_{Sig}) in the four-wave mixing scheme.

The 3rd order molecular response functions arising from the specific interaction schemes relevant to 2D-IR spectroscopy contain two oscillatory terms. Since the solute molecules are initially in the vibrational ground state, the first oscillatory term involves only the fundamental $\nu(0\rightarrow1)$ frequencies while the second oscillatory term can involve the fundamental $\nu(0\rightarrow1)$ or higher level $\nu(1\rightarrow2)$ transition frequencies. This gives 6 different Feynman diagrams representing pathways contributing to echo signals for an individual anharmonic vibrator. The existence of vibrational coupling is manifest by combination mode energy levels which expand the second oscillatory term spectrum to cover $\nu(10\rightarrow11)$, and $\nu(01\rightarrow11)$ transition frequencies. This gives 20 Feynman diagrams for the previously discussed coupled anharmonic vibrators, involving six principal and two forbidden "cross-level" frequencies present in the photon echo spectrum. Another important feature of the photo echo signal is complementarities of the contributions. Every signal contribution expressed by a Feynman diagram has a complementary signal in the form of a complex conjugate term differing by the phase of the first oscillatory term. The existence of pairs of conjugate components is displayed in the non-linear geometry where each interacting wave has a unique (k_1, k_2, k_3) wave vector. In this

configuration, the signal is emitted in two directions corresponding to rephasing (k_R) Eq. 15.1 and non-rephasing (k_{NR}) Eq. 15.2 pathways

$$k_R = -k_1 + k_2 + k_3 \tag{15.1}$$

$$k_{NR} = k_1 - k_2 + k_3 \tag{15.2}$$

each containing part of the signal of the specified order following the first two interactions. As previously discussed, Feynman diagrams represent the common frequency 3rd order response signal components that propagate into the rephasing (R_1) and non-rephasing (R_5) directions. To obtain complex conjugate pathways to those presented in R_1 and R_5 functions it is sufficient to form new elements by a mirror reflection of first two interactions with the corresponding changes in the resulting coherence states expressed by the density operators. Such a spatial distribution of the 3rd order response signals present an impediment to measurements: In general there are two ways of redirecting the components of the specific 3rd order molecular response in one direction. The first way relies on the approach demonstrated for the degenerate four-wave mixing case where the propagation direction of the first two interacting waves is collinear (k_1=k_2). The second approach applies permutations of the temporal order of the first two interactions. For first interaction, with the k_1 direction pulse arriving before the second interaction (k_2) the echo signal is produced as was presented above Eqs. 15.1-2 but if the temporal order of the first two interactions is reversed, the photon echo signal emission direction is altered as shown Eq 16.1-2 allowing acquisition of non-rephasing signal

$$k_R^{'} = -k_2 + k_1 + k_3 = k_1 - k_2 + k_3 = k_{NR} \tag{16.1}$$

$$k_{NR}^{'} = k_2 - k_1 + k_3 = -k_1 + k_2 + k_3 = k_R \tag{16.2}$$

The former approach allows direct measurement of an absorptive photon echo signal because the non-rephasing terms are automatically cancelled, while the latter requires combining of two signal components with the time ordering of the first two pulses reversed to produce a purely absorptive 2D-IR spectrum by summing the two components.

The presented expressions for the 3rd molecular response functions indicate that the whole echo signal is made up of multiple pathways that are proportional to the fourth power of the transition dipole moment, which amounts to an extremely

weak non-linear signal. The detection of such weak signals is made more accessible by heterodyne amplification. In principle, heterodyne amplification of the optical signal can be performed by spatially overlapping the weak system response signal with a high intensity optical field which acts as a local oscillator (LO) followed by detection of the resulting interference. In the case of a collinear beam arrangement, the photon echo signal is emitted in the direction of the third interaction, permitting a self-heterodyning process with the transmitted part of the 3rd laser pulse. For the non-collinear arrangement the photon echo signal is emitted in a separate direction, requiring an additional laser beam to serve as the Local Oscillator (LO) for heterodyne amplification and phase sensitive detection.

The fundamental difference between vibrational echo and double-resonance-derived 2D-IR spectra is that the former are obtained in the time-domain and generate relaxation of coherences and the spectrum is recorded by scanning coherence periods τ_1, and τ_3 for a given value of the waiting time (T_w). To translate such a signal into the frequency domain representation as demonstrated in Fig. 3, it is necessary to perform a Fourier transformation of the 2D interferogram which contains multiple frequency components originating from the oscillatory decay observed in the first and third coherence periods as shown in Eq. 17. The second non-oscillatory coherence period named waiting time (T_w) remains unaltered to serve the same purpose as the pump-probe delay time in the double-resonance technique.

$$S(t_3,t_2,t_1)\xrightarrow{2D\ FT}S(\omega_3,T_w,\omega_1) \qquad (17)$$

In practice it is beneficial to directly record the spectrum of the photon echo signal using array detectors thus reducing the Fourier transformation process to one interferogram relating to the delay time corresponding to the first coherence period rather than a double transformation along τ_1, and τ_3 times.

Time-domain 2D-IR spectroscopy provides superior temporal and spectral resolution in comparison to the double-resonance technique at the expense of a longer spectrum acquisition time and a smaller tolerance for errors in pulse timing. Additional sources of error come from the more complicated processing of time-domain data requiring Fourier transformation using FFT algorithms. Progress in instrumentation and data processing techniques for vibrational echo 2D-IR constantly reduces the influence of the above factors to increase the range of applications of

photon echo spectroscopy in comparison to the double-resonance technique. The final chapter discusses current progress in vibrational echo 2D-IR technique development and presents further simplifications of existing designs aimed at combating factors limiting its use.

1.7. Non-equilibrium 2D-IR spectroscopy

The concept of non-equilibrium 2D-IR spectroscopy was developed to extend applications of 2D-IR techniques toward studies of excited state molecules and transients. This technique is similar to TR-IR spectroscopy and relies on perturbation of an electronic state of the solute by a UV-Vis frequency pulse and following the subsequent electronic relaxation pathways by 2D-IR spectroscopy. Unlike TR-IR spectroscopy, the 2D-IR technique requires at least two mid-infrared frequency pulses, hence non-equilibrium 2D-IR spectroscopy can be separated into two related and complementary techniques which differ only in the time order of the IR and UV pulse interactions. In Transient 2D-IR spectroscopy[17,40,41,49,50,62,80,86,91-97] the UV-Vis interaction precedes the normal sequence of mid-infrared interactions required for 2D-IR spectroscopy, permitting investigation of transients and photoproducts. In the complementary T2D-IR exchange spectroscopy (T2D-IR-EXSY) method [61,80] the UV-Vis frequency interaction is placed during the waiting time period T_w of the 2D-IR pulse sequence, permitting investigation of the vibrational relaxation of the electronically excited solute and uncovering correlation of ground state and excited state vibrational levels. By virtue of the extra pulse interaction, both T-2D-IR techniques are technically 5^{th} order experiments but in the case of Transient 2D-IR spectroscopy, which is perhaps of more mainstream interest to chemical dynamics research, the experiments can be designed to study a pseudo-3^{rd} order response from the non-equilibrium molecules present in solution as is described in Chapter 5. Such a situation is achievable because the coherence induced by the preceding UV-Vis pump pulse has dephased before the mid-infrared 2D-IR interaction sequence begins. On the contrary, in the case of the T2D-IR EXSY technique, the 5^{th} order response is the primary interest because it represents the propagation of vibrational relaxation over electronic excitation, allowing 'vibrational labelling'.[61,80] The pseudo 3^{rd} order Transient 2D-IR spectroscopy confers the benefits of 2D-IR spectroscopy into

research on non-equilibrium species by permitting investigations of the structure and vibrational relaxation of transient species in solution as well as following ultrafast chemical reaction sequences, exposing chemical relaxation pathways of parent molecule.

1.8. Applications of 2D-IR spectroscopic techniques

The principal applications of 2D-IR spectroscopies exploit the ability to measure vibrational relaxation dynamics and resolve contributions from multiple processes and vibrational modes. Additionally, the relatively low excitation energy of mid-infrared radiation permits the characterisation of equilibrium and near-equilibrium chemical reactions which occurring on sub-nanosecond timescales that are inaccessible for classical (UV pumped) pump-probe optical techniques.

The principal function of 2D-IR spectroscopy is to resolve mode-specific contributions to vibrational relaxation processes. In general, there are two contributions to the overall vibrational relaxation of a molecule; population relaxation (T_1) and pure coherence dephasing (T_2). The volumetric decay of a 2D-IR peak is caused by population relaxation while temporal shape evolution is caused by spectral diffusion. Population relaxation in molecules featuring vibrational coupling (Fig. 3) is more complex since excitation energy is distributed and transferred over several vibrational modes. In such systems, population relaxation processes are accompanied by intramolecular vibrational relaxation (IVR).[98] The 2D-IR spectroscopy visualises vibrational coupling as off-diagonal cross-peaks at zero waiting times and these peaks also permit studies of IVR processes dynamics in parallel to regular population relaxation by relative changes in the amplitude of cross-peaks and diagonal peaks as the waiting time proceeds. The benefit of a 2D-IR spectrum for spectral diffusion studies arises from the two-dimensional representation of the lineshape. As stressed before inhomogeneous processes in liquids are more complicated than in the gas phase and involve solute-solvent interactions which induce phase and frequency changes. Limiting our consideration to the fundamental frequency features located on the diagonal of the 2DIR spectrum, spectral diffusion dynamics cause lineshape evolution. For short waiting times, spectral features are diagonally elongated, exhibiting a far narrower antidiagonal

cross-section than diagonal one. As the pump-probe or waiting time window increases the lineshape evolves to become circular with a uniform cross-section in all directions. The diagonal cross-section of fundamental frequency features at short waiting times represents the inhomogeneous frequency width of the ensemble of molecules characterised by a particular vibrational frequency at zero waiting time, which is observed as inhomogeneous broadening in the steady-state (FTIR) picture. The antidiagonal cross-section of these peaks represents the distribution of vibrational frequencies determined by fast, so-called homogeneous processes which contribute to coherence dephasing (T_2^*). The lineshape evolution in the antidiagonal direction depends on the dynamics of solute-solvent interactions on the vibrational frequency that are responsible for spectral diffusion in liquids.[67,99] The dynamics of this vibrational frequency evolution is commonly expressed by the frequency-frequency correlation function (FFCF) that defines the frequency-domain lineshape of a vibrational transition. It is to be noted that only vibrational echo 2D-IR spectroscopy provides an accurate representation of spectral lineshapes while in the case of the double-resonance technique, pump axis line broadening tends to mask the natural peak shape.

The additional dynamical characteristics occurring in solution can be gained from analysing the polarisation dependence of double-resonance 2D-IR spectroscopy signals. Due to rotation of absorbing molecules, the polarisation acquired in the pumping process is randomised with the rate of absorber revolution. The Magic Angle (MA theor. value 54.7^o) orientation of the pump-probe polarisation automatically removes the rotational contribution from the dynamics of spectral features. However, performing separate measurements for parallel and perpendicular pump-probe polarisation under the same conditions will permit calculation of the rotation-free Eq. 18 and anisotropy[72] (An) Eq. 19 according to the following expressions

$$MA = I_{||} + 2I_{\perp} \tag{18}$$

$$An = \frac{I_{\parallel} - I_{\perp}}{I_{\parallel} + 2I_{\perp}} \tag{19}$$

where $I_{||}$, $I_{\perp}$ represent parallel and perpendicular polarisation spectral data respectively. Since the anisotropy decay depicts polarisation loss due to absorber

revolution, the calculated anisotropy decay rate is proportional to the rotation rate of solute molecules. The same principle is applicable for fundamental frequency bleaches obtained in 1D TR-IR spectra. In the case of vibrational echo 2D-IR spectroscopy there are four polarisations to be considered for three wave-molecular system coherence transfers and the photon echo signal. In the latter case the ability to manipulate the individual components of the four wave mixing scheme permits not only measuring the polarisation anisotropy decay *An* but also establishing other specific polarisation combinations that can be used to suppress diagonal peaks and improve clarity of off-diagonal features.[90,92,100]

The 2D-IR techniques supply great deal of information about molecular structure and ultrafast chemical reactions. The non-linear 2D-IR spectrum relates the structure of higher-lying vibrational levels, exposing anharmonicity and vibrational couplings. Such molecule specific vibrational information supports molecular structure determination including the differentiation of geometrical isomers. Additionally, the 2D representation of the vibrational spectrum provides a significant advancement in the ability to separate overlapping spectra of different species present in solution. Measuring the anharmonicity of vibrational modes assists in the direct estimation of bond dissociation energies which are an important factor in chemical reaction studies. From a structure identification perspective, 2D-IR spectroscopy is frequently compared to the 2D-NMR technique which provides comparable information derived from nuclear spin interactions.[74] Still, the 2D-IR technique is a superior dynamic structural tool since it allows access to sub-nanosecond timescales, freezing all but ultrafast molecular motions which affect structural resolution. Infrared methods also possess an inherent sensitivity to changes in molecular symmetry. The latter feature permits detailed studies of ultrafast geometrical rearrangements of molecules, such as conformational isomerisation of proteins[51,53,55,66,101] and geometrical isomerisation of polymetallic complexes.[3,4,17,59,60,102-104]

As indicated above, one of the most important applications of 2D-IR spectroscopy is the evaluation of ultrafast chemical reaction dynamics. In general, there are fewer spectroscopic methods accessing sub-nanosecond timescales with sensitivity to chemical and geometrical transformations. Even further advancement is

achieved in studies of ultrafast equilibrium reactions where 2D spectra provide independent measures of forward and backward reaction rates.[10,12,14,59,105-107] The spectroscopic evaluation of chemical reaction dynamics relies on the kinetics of spectral changes arising from the appearance and disappearance of features specific to product and reactant states, respectively. In a 2D-IR spectrum, each chemical state is represented by a specific set of diagonal and off-diagonal spectral features due to the fundamental vibrational modes and coupling patterns of the molecule. The occurrence of chemical process transforming the reactant into products is then represented by the growth of cross-peaks linking the two separate sets of spectral features specific to each chemical state. An example of such a cross-peak pattern for the reversible chemical transformation of a reactant (R) into a product (P) is shown in Figure 5, where each chemical state is characterised by single anharmonic vibrator peak set. In an ultrafast, reversible chemical process, a molecule in the reactant state (R) undergoes ultrafast inter-conversion into the product state (P) within the waiting time window (T_w) producing a cross-peak (F), while a molecule in the product state (P) undergoes the reverse reaction toward the reactant state (R), producing the corresponding cross-peak (B). This chemical transformation process gives rise to a reaction-rate controlled growth of cross-peaks linking the product and substrate states. There is thus a fundamental difference between cross-peaks arising from a chemical process and those arising from vibrational coupling because the latter appear instantaneously and decay due to population relaxation. It is important to note that since chemical reaction interconverts one molecular vibrational system into another the cross-peak pattern is those of the final state, either of reactant or product, depending on the reaction direction. This is different from vibrational coupling where the cross-peaks pattern is determined by the existence of common combination mode level. A common combination mode level causes that the spacing of vibrational coupling cross-peaks to be uniform for peak sets above and below the diagonal, imposing certain symmetry relation not necessarily true for chemical processes. Moreover, the growth rate of cross-peaks corresponding to the forward reaction (F) reflects the forward reaction rate (k_1) Eq. 4 while the growth rate of the backward reaction cross-peaks represents the backward reaction rate (k_{-1}) Eq. 5. In the case of a strictly symmetric activation barrier corresponding to a lack of free

enthalpy of reaction ($\Delta G_r = 0$) those two growth rates are equal. In other cases, the growth rates of cross-peaks below and above diagonal may be different. Such a rate difference for chemical process-derived cross-peaks in extreme cases may lead to asymmetric 2D spectrum where only the faster forward process (k_1) reaction features (F) are present.

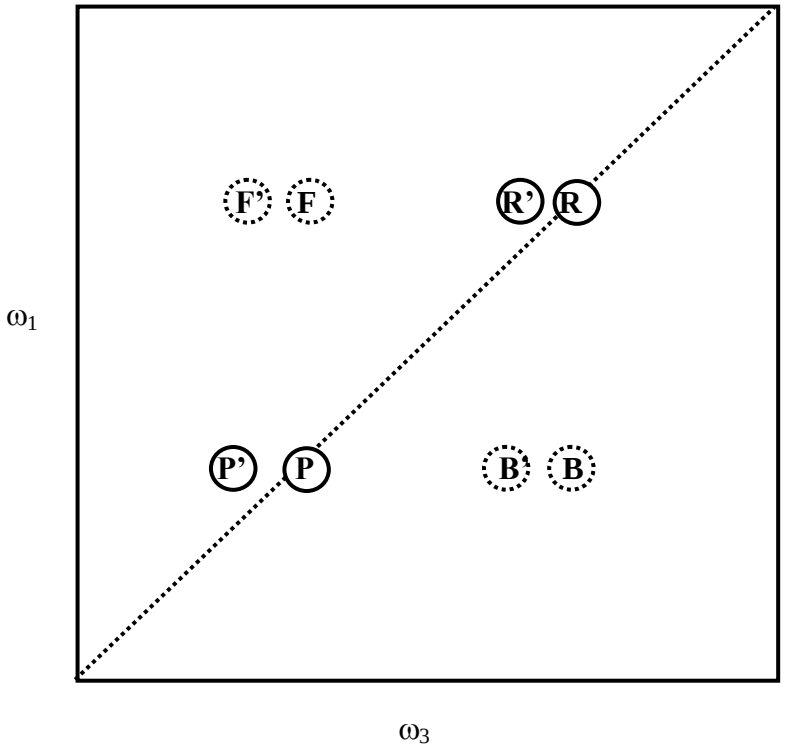

Figure 5. The 2D spectrum of chemical system made of Reactant (R) and product (P) states undergoing reversible ultrafast inter-conversion reaction. The solid circles represent $\nu_{0\rightarrow1}$ and $\nu_{1\rightarrow2}$ vibrational transitions of molecules (S) and (P) while dotted circle represent cross-peaks due to inter-conversion process in forward (F) and backward (B) direction.

The presence of off-diagonal cross-peaks for chemical processes permits establishing reaction rates for chemical reaction sequences common for photochemical processes[8,11,16,22,24,63,69] even when spectral features are strongly overlapping. Finally, the ability to separate measurements of forward and backward reaction rates is unique to 2D-IR spectroscopy, opening up new frontiers in studies of the kinetics and thermodynamics of ultrafast chemical reactions at equilibrium. This unique feature was adopted in studies of hydrogen bond dynamics in proteins and proton exchange

reactions.[9,14,99,105,106] The power of novel 2D-IR techniques has been shown in the latter case where the exchange dynamics of a particular type of hydrogen bond was measured[9,14,105,107,108] that is not possible for other ultrafast optical methods.[109-116]

References:

(1) Atkins, P. W. *In Physical Chemistry*; Freeman: New York, **2006**.

(2) Glowacki, D. R.; Rose, R. A.; Greaves, S. J.; Orr-Ewing, A. J.; Harvey, J. N. *Nature Chemistry* **2011**, *3*, 850.

(3) Cahoon, J. F.; Sawyer, K. R.; Schlegel, J. P.; Harris, C. B. *Science (New York, N.Y.)* **2008**, *319*, 1820.

(4) Kania, R.; Stewart, A. I.; Clark, I. P.; Greetham, G. M.; Parker, A. W.; Towrie, M.; Hunt, N. T. *Physical Chemistry Chemical Physics: PCCP* **2010**, *12*, 1051.

(5) Glyn, P.; Johnson, F. P. A.; George, M. W.; Lees, A. J.; Turner, J. J. *Inorganic Chemistry* **1991**, *30*, 3543.

(6) Zhao, X.; Georgakaki, I. P.; Miller, M. L.; Yarbrough, J. C.; Darensbourg, M. Y. *Journal of the American Chemical Society* **2001**, *123*, 9710.

(7) Portius, P.; Yang, J.; Sun, X.-Z.; Grills, D. C.; Matousek, P.; Parker, A. W.; Towrie, M.; George, M. W. *Journal of the American Chemical Society* **2004**, *126*, 10713.

(8) Cahoon, J. F.; Kling, M. F.; Schmatz, S.; Harris, C. B. *Journal of the American Chemical Society* **2005**, *127*, 12555.

(9) Kim, Y. S.; Hochstrasser, R. M. *Proceedings of the National Academy of Sciences of the United States of America* **2005**, *102*, 11185.

(10) Zheng, J.; Kwak, K.; Asbury, J.; Chen, X.; Piletic, I. R.; Fayer, M. D. *Science (New York, N.Y.)* **2005**, *309*, 1338.

(11) Cahoon, J. F.; Kling, M. F.; Sawyer, K. R.; Frei, H.; Harris, C. B. *Journal of the American Chemical Society* **2006**, *128*, 3152.

(12) Kwak, K.; Zheng, J.; Cang, H.; Fayer, M. D. *The Journal of Physical Chemistry B* **2006**, *110*, 19998.

(14) Zheng, J.; Kwak, K.; Chen, X.; Asbury, J. B.; Fayer, M. D. *Journal of the American Chemical Society* **2006**, *128*, 2977.

(15) Artero, V.; Fontecave, M. *C. R. Chimie* **2008**, *11*, 926.

(16) Ridley, A. R.; Stewart, A. I.; Adamczyk, K.; Ghosh, H. N.; Kerkeni, B. n.; Guo, Z. X.; Nibbering, E. T. J.; Pickett, C. J.; Hunt, N. T. *Inorganic Chemistry* **2008**, *47*, 7453.

(17) Anna, J. M. B., C. R.; McCanne, R.; Nee, M. J.; Kubarych, K. J. *In Central Regional Meeting of the American Chemical Society* Cleveland, OH, United States, **2009**; Vol. CRM-493.

(18) Capon, J.-F.; Gloaguen, F.; Petillon, F. Y.; Schollhammer, P.; Talarmin, J. *Coordination Chemistry Reviews* **2009**, *253*, 1476.

(19) Park, S.; Odelius, M.; Gaffney, K. J. *The Journal of Physical Chemistry B* **2009**, *113*, 7825.

(20) Greco, C.; Fantucci, P.; De Gioia, L.; Suarez-Bertoa, R.; Bruschi, M.; Talarmin, J.; Schollhammer, P. *Dalton Transactions* **2010**, *39*, 7320.

(21) Kaziannis, S.; Santabarbara, S.; Wright, J. A.; Greetham, G. M.; Towrie, M.; Parker, A. W.; Pickett, C. J.; Hunt, N. T. *The Journal of Physical Chemistry B* **2010**, *114*, 15370.

(22) Sawyer, K. R.; Cahoon, J. F.; Shanoski, J. E.; Glascoe, E. a.; Kling, M. F.; Schlegel, J. P.; Zoerb, M. C.; Hapke, M.; Hartwig, J. F.; Webster, C. E.; Harris, C. B. *Journal of the American Chemical Society* **2010**, *132*, 1848.

(23) Stewart, A. I.; Wright, J. A.; Greetham, G. M.; Kaziannis, S.; Santabarbara, S.; Towrie, M.; Parker, A. W.; Pickett, C. J.; Hunt, N. T. *Inorganic Chemistry* **2010**, *49*, 9563.

(24) Clark, I. P.; George, M. W.; Greetham, G. M.; Harvey, E. C.; Long, C.; Manton, J. C.; Pryce, M. T. *The Journal of Physical Chemistry A* **2011**, *115*, 2985.

(25) Yu, L.; Greco, C.; Bruschi, M.; Ryde, U.; De Gioia, L.; Reiher, M. *Inorganic Chemistry* **2011**, *50*, 3888.

(26) Kania, R.; Frederix, P. W. J. M.; Wright, J. A.; Ulijn, R. V.; Pickett, C. J.; Hunt, N. T. *The Journal of Chemical Physics* **2012**, *136*, 044521.

(27) Adams, R. D. C., F. A. *Inorganica Chimica Acta* **1972**, *7*, 153.

(28) Adams, R. D. C., D. E.; Cotton, F. A. *Journal of the American Chemical Society* **1974**, *96*, 749.

(29) Ewing, P.; Farrugia, L. J.; Rycroft, D. S. *Organometallics* **1988**, *7*, 859.

(30) Wey, H. G.; Betz, P.; Topalovic, I.; Butenschoen, H. *Journal of Organometallic Chemistry* **1991**, *411*, 369.

(31) Virrels, I. G.; George, M. W.; Johnson, F. P. A.; Turner, J. J.; Westwell, J. R. *Organometallics* **1995**, *14*, 5203.

(32) Gelling, A.; Olsen, M. D.; Orrell, K. G.; Osborne, A. G.; Sik, V. *Inorganica Chimica Acta* **1997**, *264*, 257.

(33) Creber, M. L.; Orrell, K. G.; Osborne, A. G.; Sik, V.; Hursthouse, M. B.; Abdul Malik, K. M. *Journal of the Chemical Society, Dalton Transactions* **2000**, 4218.

(34) Baiz, C. R.; McRobbie, P. L.; Anna, J. M.; Geva, E.; Kubarych, K. J. *Accounts of Chemical Research* **2009**, *42*, 1395.

(35) Baiz, C. R.; McRobbie, P. L.; Preketes, N. K.; Kubarych, K. J.; Geva, E. *The Journal of Physical Chemistry A* **2009**, *113*, 9617.

(36) Donten, M. L.; Hamm, P.; VandeVondele, J. *The Journal of Physical Chemistry B* **2011**, *115*, 1075.

(37) Zanni, M. T.; Gnanakaran, S.; Stenger, J.; Hochstrasser, R. M. *The Journal of Physical Chemistry B* **2001**, *105*, 6520.

(38) Woutersen, S.; Hamm, P. *Journal of Physics: Condensed Matter* **2002**, *14*, R1035.

(39) Woutersen, S.; Pfister, R.; Hamm, P.; Mu, Y.; Kosov, D. S.; Stock, G. *The Journal of Chemical Physics* **2002**, *117*, 6833.

(40) Bredenbeck, J.; Hamm, P. *The Journal of Chemical Physics* **2003**, *119*, 1569.

(41) Bredenbeck, J.; Helbing, J.; Behrendt, R.; Renner, C.; Moroder, L.; Wachtveitl, J.; Hamm, P. *The Journal of Physical Chemistry B* **2003**, *107*, 8654.

(42) Khalil, M.; Demirdöven, N.; Tokmakoff, A. *Physical Review Letters* **2003**, *90*, 2.

(43) Cheatum, C. M.; Tokmakoff, A.; Knoester, J. *The Journal of Chemical Physics* **2004**, *120*, 8201.

(44) Chung, H. S.; Khalil, M.; Tokmakoff, A. *Biophysics Journal* **2004**, *86*, 526A.

(45) Demirdoven, N.; Cheatum, C. M.; Chung, H. S.; Khalil, M.; Knoester, J.; Tokmakoff, A. *Journal of the American Chemical Society* **2004**, *126*, 7981.

(46) Smith, A. W.; Cheatum, C. M.; Chung, H. S.; Demirdoven, N.; Khalil, M.; Knoester, J.; Tokmakoff, A. *Biophysics Journal* **2004**, *86*, 619A.

(47) Kim, Y. S.; Wang, J.; Hochstrasser, R. M. *The Journal of Physical Chemistry B* **2005**, *109*, 7511.

(48) Fang, C.; Senes, A.; Cristian, L.; De Grado, W. F.; Hochstrasser, R. M. *Proceedings of the National Academy of Sciences of the United States of America* **2006**, *103*, 16740.

(49) Kolano, C.; Helbing, J.; Kozinski, M.; Sander, W.; Hamm, P. *Nature* **2006**, *444*, 469.

(50) Chung, H. S.; Ganim, Z.; Jones, K. C.; Tokmakoff, A. *Proceedings of the National Academy of Sciences of the United States of America* **2007**, *104*, 14237.

(51) Ishikawa, H.; Kim, S.; Kwak, K.; Wakasugi, K.; Fayer, M. D. *Proceedings of the National Academy of Sciences of the United States of America* **2007**, *104*, 19309.

(52) Cervetto, V.; Hamm, P.; Helbing, J. *The Journal of Physical Chemistry B* **2008**, *112*, 8398.

(53) Ganim, Z.; Chung, H. S.; Smith, A. W.; Deflores, L. P.; Jones, K. C.; Tokmakoff, A. *Accounts of Chemical Research* **2008**, *41*, 432.

(54) Bodis, P.; Panman, M. R.; Bakker, B. H.; Mateo-Alonso, A.; Prato, M.; Buma, W. J.; Brouwer, A. M.; Kay, E. R.; Leigh, D. a.; Woutersen, S. *Accounts of Chemical Research* **2009**, *42*, 1462.

(55) Backus, E. H. G.; Bloem, R.; Donaldson, P. M.; Ihalainen, J. A.; Pfister, R.; Paoli, B.; Caflisch, A.; Hamm, P. *The Journal of Physical Chemistry B* **2010**, *114*, 3735.

(56) Smith, A. W.; Lessing, J.; Ganim, Z.; Peng, C. S.; Tokmakoff, A.; Roy, S.; Jansen, T. L. C.; Knoester, J. *The Journal of Physical Chemistry B* **2010**, *114*, 10913.

(57) Woys, A. M.; Lin, Y.-S.; Reddy, A. S.; Xiong, W.; de Pablo, J. J.; Skinner, J. L.; Zanni, M. T. *Journal of the American Chemical Society* **2010**, *132*, 2832.

(58) Cervetto, V.; Bregy, H.; Hamm, P.; Helbing, J. *The Journal of Physical Chemistry A* **2006**, *110*, 11473.

(59) Zheng, J.; Kwak, K.; Xie, J.; Fayer, M. D. *Science (New York, N.Y.)* **2006**, *313*, 1951.

(60) Anna, J. M.; Ross, M. R.; Kubarych, K. J. *The Journal of Physical Chemistry A* **2009**, *113*, 6544.

(61) Bredenbeck, J.; Helbing, J.; Hamm, P. *Journal of the American Chemical Society* **2004**, *126*, 990.

(62) Helbing, J.; Bonacina, L.; Pietri, R.; Bredenbeck, J.; Hamm, P.; van Mourik, F.; Chaussard, F.; Gonzalez-Gonzalez, A.; Chergui, M.; Ramos-Alvarez, C.; Ruiz, C.; López-Garriga, J. *Biophysics Journal* **2004**, *87*, 1881.

(63) Cahoon, J.; Kling, M.; Sawyer, K.; Andersen, L.; Harris, C. *Journal of Molecular Structure* **2008**, *890*, 328.

(64) Hunt, N. T. *Chemical Society Reviews* **2009**, *38*, 1837.

(65) Wright, J. A.; Pickett, C. J. *Chemical Communications* **2009**, 5719.

(66) Ishikawa, H.; Kwak, K.; Chung, J. K.; Kim, S.; Fayer, M. D. *Proceedings of the National Academy of Sciences of the United States of America* **2008**, *105*, 8619.

(67) Hamm, P.; Zanni, M. *Concepts and Methods of 2D Infrared Spectroscopy*; Cambridge University Press: Cambridge, **2011**.

(68) Laidler, K. J.; King, M. C. *The Journal of Physical Chemistry* **1983**, *87*, 2657.

(69) Probst, B.; Rodenberg, A.; Guttentag, M.; Hamm, P.; Alberto, R. *Inorganic Chemistry* **2010**, *49*, 6453.

(70) Klán, P.; Wirz, J. *In Photochemistry of Organic Compounds: From Concepts to Practice*; Wiley-Blackwell: **2009**.

(71) Kaziannis, S.; Wright, J. A.; Candelaresi, M.; Kania, R.; Greetham, G. M.; Parker, A. W.; Pickett, C. J.; Hunt, N. T. *Physical Chemistry Chemical Physics: PCCP* **2011**, *13*, 10295.

(72) Fayer, M. D.; Marcel Dekker, Inc.: New York, Basel, **2001**.

(73) Rector, K. D.; Kwok, A. S.; Ferrante, C.; Tokmakoff, A.; Rella, C. W.; Fayer, M. D. *The Journal of Chemical Physics* **1997**, *106*, 10027.

(74) Ernst, R. R.; Bodenhausen, G.; Wokaun, A. *Principles of Nuclear Magnetic Resonance in One and Two Dimensions.*, Clarendon, Oxford, **1987**.

(75) Jablonskyte, A.; Wright, J. A.; Pickett, C. J. *Dalton Transactions* **2010**, *39*, 3026.

(76) Gleeson, J. W.; Vaughan, R. W. *The Journal of Chemical Physics* **1983**, *78*, 5384.

(77) Moulton, P. F. *Journal of the Optical Society of America B* **1986**, *3*, 125.

(78) Spence, D. E.; Kean, P. N.; Sibbett, W. *Optics Letters* **1991**, *16*, 42.

(79) Towrie, M.; Grills, D. C.; Dyer, J.; Weinstein, J. A.; Matousek, P.; Barton, R.; Bailey, P. D.; Subramaniam, N.; Kwok, W. M.; Ma, C.; Phillips, D.; Parker, A. W.; George, M. W. *Applied Spectroscopy* **2003**, *57*, 367.

(80) Bredenbeck, J.; Helbing, J.; Kolano, C.; Hamm, P. *ChemPhysChem* **2007**, *8*, 1747.

(81) Shen, Y. R. *The principles of nonlinear optics*; Wiley, **1984**.

(82) Boyd, R. W. *Nonlinear Optics*; 2nd ed.; Academic Press: New York, **2003**.

(83) Gelin, M. F.; Egorova, D.; Domcke, W. *Accounts of Chemical Research* **2009**, *42*, 1290.

(84) Banno, M.; Ohta, K.; Yamaguchi, S.; Hirai, S.; Tominaga, K. *Accounts of Chemical Research* **2009**, *42*, 1259.

(85) Hamm, P.; Lim, M.; Hochstrasser, R. M. *The Journal of Physical Chemistry B* **1998**, *102*, 6123.

(86) Cervetto, V.; Helbing, J.; Bredenbeck, J.; Hamm, P. *The Journal of Chemical Physics* **2004**, *121*, 5935.

(87) Stewart, A. I.; Clark, I. P.; Towrie, M.; Ibrahim, S. K.; Parker, A. W.; Pickett, C. J.; Hunt, N. T. *The Journal of Physical Chemistry B* **2008**, *112*, 10023.

(88) Bonner, G. M.; Ridley, A. R.; Ibrahim, S. K.; Pickett, C. J.; Hunt, N. T. *Faraday Discussions* **2010**, *145*, 429.

(89) Asplund, M. C.; Lim, M.; Hochstrasser, R. M. *Chemical Physics Letters* **2000**, *323*, 269.

(90) Hochstrasser, R. *Chemical Physics* **2001**, *266*, 273.

(91) Baiz, C. R.; Nee, M. J.; McCanne, R.; Kubarych, K. J. *Optics Letters* **2008**, *33*, 2533.

(92) Bredenbeck, J.; Helbing, J.; Hamm, P. *The Journal of Chemical Physics* **2004**, *121*, 5943.

(93) Bredenbeck, J. H., J.; Hamm, P. *Journal of the American Chemical Society* **2004**, *126*, 990.

(94) Bredenbeck, J.; Helbing, J.; Kolano, C.; Hamm, P. *ChemPhysChem* **2007**, *8*, 1747.

(95) Bredenbeck, J.; Helbing, J.; Nienhaus, K.; Nienhaus, G. U.; Hamm, P. *Proceedings of the National Academy of Sciences of the United States of America* **2007**, *104*, 14243.

(96) Strasfeld, D. B.; Ling, Y. L.; Shim, S. H.; Zanni, M. T. *Journal of the American Chemical Society* **2008**, *130*, 6698.

(97) Baiz, C. R.; McCanne, R.; Nee, M. J.; Kubarych, K. J. *The Journal of Physical Chemistry A* **2009**, *113*, 8907.

(98) Jansen, T. L. C.; Knoester, J. *Accounts of Chemical Research* **2009**, *42*, 1405.

(99) Elsaesser, T. *Accounts of Chemical Research* **2009**, *42*, 1220.

(100) Middleton, C. T.; Strasfeld, D. B.; Zanni, M. T. *Optics Express* **2009**, *17*, 14526.

(101) Bagchi, S.; Falvo, C.; Mukamel, S.; Hochstrasser, R. M. *The Journal of Physical Chemistry B* **2009**, *113*, 11260.

(102) Baiz, C. R.; McCanne, R.; Kubarych, K. J. *Journal of the American Chemical Society* **2009**, *131*, 13590.

(103) Milota, F.; Sperling, J.; Nemeth, A.; Mancal, T.; Kauffmann, H. F. *Accounts of Chemical Research* **2009**, *42*, 1364.

(104) Anna, J. M.; Kubarych, K. J. *The Journal of Chemical Physics* **2010**, *133*, 174506.

(105) Kwak, K.; Rosenfeld, D. E.; Chung, J. K.; Fayer, M. D. *The Journal of Physical Chemistry B* **2008**, *112*, 13906.

(106) Zheng, J.; Fayer, M. D. *The Journal of Physical Chemistry B* **2008**, *112*, 10221.

(107) Rosenfeld, D. E.; Kwak, K.; Gengeliczki, Z.; Fayer, M. D. *The Journal of Physical Chemistry B* **2010**, *114*, 2383.

(108) Moilanen, D. E.; Wong, D.; Rosenfeld, D. E.; Fenn, E. E.; Fayer, M. D. *Proceedings of the National Academy of Sciences of the United States of America* **2009**, *106*, 375.

(109) Santa, I.; Foggi, P.; Righini, R.; Williams, J. H. *The Journal of Physical Chemistry* **1994**, *98*, 7692.

(110) Hunt, N. T.; Kattner, L.; Shanks, R. P.; Wynne, K. *Journal of the American Chemical Society* **2007**, *129*, 3168.

(111) Ratajska-Gadomska, B.; Bialkowski, B.; Gadomski, W.; Radzewicz, C. *The Journal of Chemical Physics* **2007**, *126*, 184708.

(112) Turton, D. A.; Wynne, K. *The Journal of Chemical Physics* **2008**, *128*, 154516.

(113) Heisler, I. A.; Mazur, K.; Meech, S. R. *The Journal of Physical Chemistry B* **2011**, *115*, 1863.

(114) Mazur, K.; Heisler, I. A.; Meech, S. R. *The Journal of Physical Chemistry A* **2011**.

(115) Yamaguchi, S.; Mazur, K.; Heisler, I. A.; Shirota, H.; Tominaga, K.; Meech, S. R. *The Journal of Chemical Physics* **2011**, *135*, 134504.

(116) Turton, D. A.; Sonnleitner, T.; Ortner, A.; Walther, M.; Hefter, G.; Seddon, K. R.; Stana, S.; Plechkova, N. V.; Buchner, R.; Wynne, K. *Faraday Discussions* **2012**, *154*, 145.

2. Experimental

This experimental section will present the development of an existing ultrafast 2D-IR spectrometer to facilitate new types of experiment. This will be followed by discussion of improvements to spectrometer control software and the design of dedicated automated signal pre-processing software used to support data handling for all types of measurements. For completeness, discussion of the 2D-IR spectrometer development is preceded by a short introduction to the steady-state infrared spectrometer used in preliminary experiments for time-resolved infrared studies.

The design of the time-resolved infrared spectrometer encompasses four functional units: a radiation source, functional optical table, sample area and detection system. The ultrafast time-resolved spectrometers utilize a femtosecond pulsed laser light source that operates in the near infrared region and as such the application of devices based on the optical parametric amplification process and frequency mixing are used to access 3-11 μm range wavelengths. Such a versatile solution has additional benefits in allowing the generation of pulsed radiation in higher frequency regions that are required for UV_{pump}-IR_{probe} and Transient 2D-IR experiments. The most common light source for modern ultrafast spectrometers is a Ti:Sapphire based ultrafast laser system operating at λ=800nm with optical parametric amplifiers powering up- or down-conversion modules to produce ultrashort pulses at desired frequency within broad range of spectrum covering UV-Vis to mid-infrared.[1-3]

The laser radiation is directed to the experimental area of the optical table in order to redistribute the radiation into the desired number of beams and into units for any required pulse shaping in the individual experiments. Examples of the latter include pulse spectrum-shaping techniques for double resonance 2D-IR and interferometers for vibrational echo measurements.[4] The former approach utilizes pulse shaping by a dispersive grating element combined with a slit to produce a narrow bandwidth pulse. A similar effect can be obtained via a Fabry-Pérot filter (etalon).[3,5-9] The latter method utilizes an interferometer assembly. The techniques utilizing a grating based or an etalon filter for pulse shaping are simpler to realize and more robust but they suffer from limitations with respect to the pulse duration

while interferometer assembly based spectrometers overcome this effect but require high precision interferometry that significantly lengthens measurement process.[10-22] The current state-of-the-art in the construction of multidimensional infrared spectrometers concentrates on optimization of a pulse shaping solution for robust and fully automatic acquisition of good quality time domain 2D-IR spectrum without the need for interferometers.

The sample area is incorporated into the optical table where the incoming light beams are focused into the liquid sample housed in a cell between transparent windows allowing output signal to be directed toward the detection assembly. The detection of mid-infrared radiation is realised by a fast response photoconductive detector most commonly based on mercury cadmium telluride (MCT).[6] Additional benefits of using photoconductive materials are possibility to construct multielement arrays which permit construction of spectrographs for simultaneous detection over a spectral window. The major challenge in the detection of commonly used mid-infrared laser pulses is their ultrashort duration much faster than the MCT detector response time. Alternative detection systems rely on frequency up-conversion toward the near-infrared-to-visible spectral range, for which higher sensitivity ultrafast detectors are available.[10,11] In parallel to the spectrometer optical assembly design process, development of instrumental methods and control software progressed enabling automation of experimental processes as well as crude data pre-processing to improve quality of the acquired spectra using numerical methods.

2.1. Steady-state FT-IR spectrometer

Steady-state infrared (FTIR) spectroscopy measurements are an important preliminary step used in preparation for time-resolved infrared spectroscopy experiments. The FT-IR spectrum reveals the location of the fundamental vibrational transitions of the solute allowing calibration of the frequency range of time-resolved spectra and testing of solute stability over the times required for data collection. In addition, studying temperature induced changes of the infrared spectrum of the solute permits detection and characterisation of isomerisation equilibrium while studies of the effects of UV-Vis frequency irradiation on FT-IR spectra supports analysis and detection of the secondary products of photochemical processes. Infrared absorption

spectra were recorded on a single beam Fourier Transform spectrometer (Vertex70) provided by Bruker. The spectrometer comprises an incandescent mid-infrared light source combined with a KBr beam splitter based Michelson interferometer. The reference system was based on a CW HeNe laser and interferometry provides accurate interferometer arm length measurements leading to a maximum spectral resolution of 0.5 cm^{-1}. The interferometer output is passed through the sample which is placed in a cell (Harrick) made of a pair of CaF_2 windows separated by an exchangeable Teflon® spacer used to regulate optical path length. The transmitted radiation is detected by a broadband pyroelectric detector based on a doped triglycine sulphate (DTGS) crystal.

The spectrometer performed steady-state infrared spectral acquisitions at ambient or varying temperature. The ambient temperature experiments used a regular airtight cell holder while the variable temperature experiments utilised a thermocell featuring an electrical heater and a coolant flow conduit. Depending on the temperature range used, measurements were performed using either the electrical heater for high boiling point solutions, such as n-heptane or circulated coolant from a thermostatic bath for temperature control of low boiling point solvents such as dichloromethane.

2.2. Two-dimensional infrared spectrometer

The existing Strathclyde laser infrared spectrometer was designed for the acquisition of 2D-IR spectrum utilizing the double resonance approach. In the following section, the existing design is discussed along with the development and testing of a UV-VIS pump optical path which expanded the spectrometer measurement capacity to include UV_{pump}-IR_{probe} method.

2.2.1. Spectrometer radiation source - laser system

The basis of the laser system is a mode-locked Ti:Sapphire oscillator (Micra 5, Coherent) combined with a regenerative amplifier (Legend, Coherent). The Micra oscillator is made of Ti:Sapphire crystal bearing main optical resonator powered by a 5W continuous-wave λ=532 nm Diode Pumped Solid State (DPSS) laser system (Verdi, Coherent). The Verdi laser consists of a ring cavity with

Nd:YVO_4 crystal gain media, optical isolator and LBO crystal and high power laser diodes operating at λ=808 nm. The diode light pumped laser gain medium produces laser action at wavelength λ=1064 nm propagating in one direction owing to optical isolator. The intracavity non-critical phase matched LBO crystal acts as output coupler by doubling laser operation frequency. The doubled frequency radiation λ=532 nm escapes cavity through a dichroic mirror. The Verdi laser head radiation is focused on the Ti:Sapphire crystal located in the oscillator cavity. The oscillator optical resonator is arranged into a linear cavity containing a Ti:Sapphire crystal, a prism compressor unit and mobile mirror mounted on a solenoid actuator. The purpose of mobile mirror is to initiate pulsed operation regime by introducing high magnitude power fluctuations via cavity losses modulation. The formation of ultrashort pulses is achieved by soft aperture Kerr-lens modelocking (KLM) mechanism where focusing of pump radiation on active media crystal provides higher gain for Kerr-lens focused ultrashort pulses than in continuous wave mode operation. Stabilisation of the ultrashort pulse operation regime is supported by a chirp compensating prism compressor unit made of a pair of counter oriented prisms and the terminal window of the oscillator cavity, additionally permitting limited range tuning of the pulse duration. The main cavity produces an 80 MHz repetition rate pulse train of approximately 35 fs duration pulses. The chirped ultrashort pulse frequency spectrum is characterised by a distorted Gaussian-like frequency distribution with bandwidth of ~80 nm (FWHM).

The oscillator seeds a Ti:Sapphire based regenerative amplifier (Legend, Coherent) pumped by a 25W λ=532nm Q-switched nanosecond laser system (Evolution, Coherent). The amplifier system is made of three main sections, a seeding pulse stretching module, an amplifier optical cavity and an output pulse compression module. The first section stretches the oscillator seeding pulse with the aid of a grating based pulse shaping module that truncates the seed frequency bandwidth slightly below 80nm. The processed seed pulses are injected into the main linear optical resonator housing a Ti:Sapphire crystal and two intracavity electro-optic modulators (Pockels cells) for control of the amplification process. The first Pockels cell controls the gain medium seeding process by matching the polarisations of the pump laser with the oscillator seed that initiates amplification of

the seed pulse. The second Pockels cell controls cavity dumping by aligning polarisation of the amplified pulses with the intracavity birefringent filter (Wollaston prism) facilitating pulse ejection. The pulse amplification and ejection process is controlled by a synchronisation and delay generator (SDG, Coherent). The SDG generator synchronises the amplification time window with the trailing edge of nanosecond pump laser pulse. The first Pockels cell is synchronised to select single seed pulse from 80Mhz/~13ns pulse train of Micra-5 output to be amplified. The seed pulse undergoes amplification over 3 to 4 repetitions of ~10 ns roundtrip of amplifier optical resonator. The amplified pulse is ejected from amplifier cavity by SDG generator trigger pulse activating second Pockels cell. The amplification process is repeated every 1ms resulting in ultrashort pulse train repetition rate of 1 kHz where second Pockels cell activation signals permits synchronisation of the other modules of the spectrometer. The amplified pulse that acquired chirp during amplification process is directed onto a grating based pulse compressor unit that removes chirp while providing fine tuning of the pulse duration. The autocorrelator measured amplifier output pulse durations raging from 60 to 100 fs that translates into 39 to 65 fs actual pulse duration assuming manufacturer suggested hyperbolic secant temporal lineshape function (established for Micra-5).

The amplifier output is a λ = 800nm centred pulse train with a 1 kHz repetition rate and an average power of 3 W and is split between two identical white-light-seeded optical parametric amplifiers (OPA, Topas-C). The schematic of a two stage optical parametric amplifier with a white-light continuum is shown in Figure 6. The OPA input beam of a λ=800nm centred pulse train from the amplifier is split into two pumping beams on BS 1 (Fig. 6). The transmitted pumping beam is directed onto a second beam splitter (BS 2 on Fig. 6) which transmits ~5% of the pump beam for white light seed generation while the rest is used for pumping of the first beta barium borate (BBO 1 on Fig. 6) crystal. The residual pump beam radiation is directed onto a Sapphire plate (Sapph on Fig. 6) that, owing to self-phase modulation, stretches the frequency bandwidth of the pulse toward a white light continuum. The Sapphire plate output is focused and crossed under an acute angle with the first pumping beam within the first BBO 1 crystal.

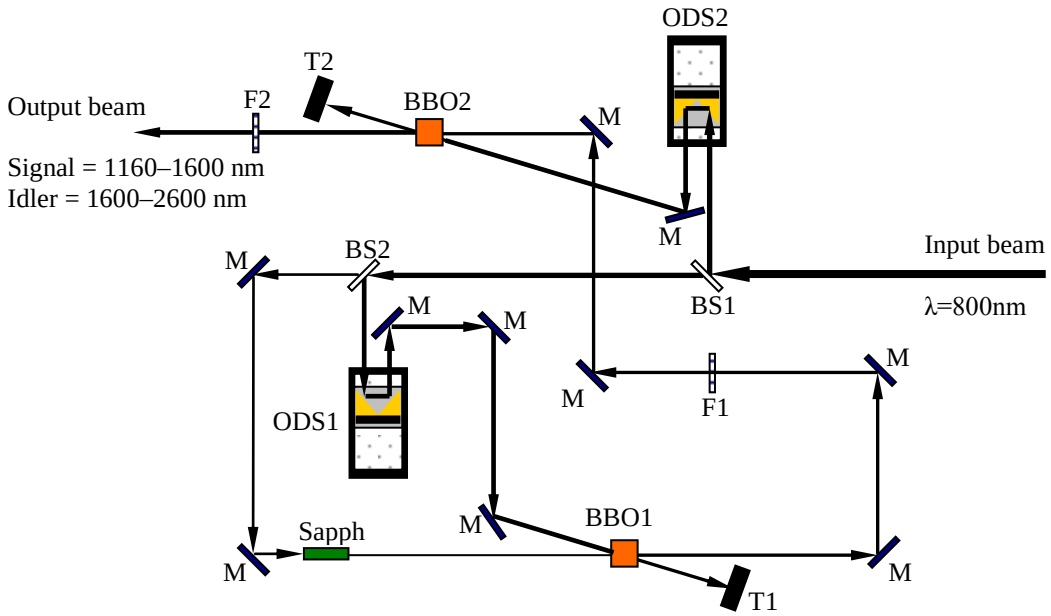

Figure 6. Schematic of two step white-light-seeded optical parametric amplifier (TOPAS-C). The labels BBO 1 and 2 denote beta barium borate crystals while Saph denote Sapphire plate. Remaining labels denote beam splitters (BS 1, 2), optical delay stages (ODS1, 2), low pass filters (F1, 2), beam stops (T1, 2) and mirrors (M).

The white light seed promotes a parametric process, splitting the amplifier output photons into two lower frequency photons denoted as the signal and idler. Correct phase matching of the white light seed with the pump beam promotes the amplification of the parametric process frequencies at the expense of pump radiation intensity. The BBO1 crystal output is passed through a low pass filter >800 nm (F1 on Fig. 6) to eliminate the residual white light seed and scattered pump radiation. The isolated signal and idler radiation is crossed with the second pump beam within the second BBO 2 (Fig. 6) crystal that performs the subsequent process of signal and idler amplification. A second low pass filter (F2 on Fig. 6) eliminates scattered pump radiation from the OPA output. The critical phase matching of pulsed radiation in a non-linear material requires control of the beam incidence angles aided by rotational holders of the BBO crystals and pulse delay time, which is facilitated by two optical delay stages (ODS 1&2 on Fig. 6). The OPA output radiation covers a spectral range of 1160-2600 nm in two sub ranges 1160-1600 and 1600-2600 nm for the signal and idler beams, respectively. The signal and idler exhibit perpendicular mutual

polarisation that may be used for separation of both frequency components of the OPA output. The output of one OPA is coupled with a non-collinear difference frequency generator (DFG, Topas) to produce mid-infrared radiation in the desired frequency range. The DFG module uses a polarising beam splitter to separate the signal and idler frequencies of the OPA output into separate pathways. The signal and idler beam are then crossed at a small angle within a $AgGeS_2$ crystal to generate difference frequency radiation emitted into a unique direction. Tuning of the OPA output frequency is followed by phase matching adjustment of the optical axis orientation of the $AgGeS_2$ crystal to allow generation of mid-infrared radiation covering wavelengths from 3 to 11μm.

The output of the second OPA was equipped with a second harmonic generator (SHG, Topas) module. The SHG module contains non-linear materials that are efficient in higher harmonic generation to convert the OPA output radiation into a selection of frequencies covering the UV–Vis spectral range. Selection of the SHG module output frequency is achieved by rotation of the harmonic-generating crystal to alter the phase matching conditions for the sum frequency generation process.

2.2.2. Optical table assembly

The optical table experimental layout incorporates existing optical paths designed for double-resonance 2D-IR spectroscopy experiments and the newly constructed UV-Vis pump experiment. The schematic layout of the spectrometer optical assembly is shown in Figure 7 where a green background indicates the newly constructed part. The optical table is fitted with gold-coated dispersive and reflective optics to minimise radiation losses and CaF_2 based refractive optics that are effective at mid-infrared frequencies.

2.2.2.1. Existing 2D-IR spectrometer optical table

The DFG output beam is collimated with a telescope made of two bicovex lenses L1 f= 100mm and L2 f= 50mm (Fig. 7) and passed through a pair of 2 mm aperture irises (Ir 1, 2 on Fig. 7). The initial DFG output beam is asymmetrically split (WBS 2 on Fig. 7) into pump and probe beams, ~90% of the radiation energy is transmitted into the pump path while ~10% energy is reflected into the probe path.

The broadband pump pulse is diffracted on a blazed gold-coated grating (G on Fig. 7) with 300 groves/mm towards a concave mirror (CM 7 on Fig. 7), which creates a horizontal distribution of frequencies. The spatially distributed broadband pulse is then directed toward a motorised adjustable slit (SL on Fig. 7) which is placed in front of a reflecting mirror (M8 on Fig. 7). The motorised slit (SL) constrains the broadband pulse into a narrowband pump pulse with a frequency window determined by the slit width. Translation of the slit across the mirror (M8) diameter facilitates scanning of the narrowband pump pulse frequency window over the initial pulse frequency spectrum. The narrowband pump pulse is then returned to the grating (G), descending ca. 1 cm with reference to the incoming beam. The narrowband pump pulse is refocused onto a parallel beam path by the grating (G) and is directed through the 3 mm aperture irises (Ir3, 4) towards the sample area consisting of the sample cell (S on Fig. 7) and a pair of off-axis parabolic mirrors (PBM 1, 2 on Fig. 7).

The probe pulse is directed through a set of mirrors (M12, 13 on Fig. 7) onto a gold-coated retro-reflector mounted on optical delay stage (ODS 1) to facilitate pump-probe time delay control. The ODS 1 output is then guided through 3mm aperture irises (Ir 5, 6 on Fig. 7) into the sample area where the first off-axis parabolic mirror (PBM 1) focuses the incoming beams into a single focal spot inside the sample cell (S). The transmitted probe pulse radiation is then recollimated by the second off-axis parabolic mirror (PBM 2) while the transmitted pump pulse radiation is blocked by a beam stop (T2 on Fig. 7). The probe radiation exiting the sample is subsequently focused by a biconvex lens L3 (Fig. 7) f= 50mm into the entrance slit of a monochromator which forms part of the detection system. The mutual polarisation of the pump and probe radiation is controlled by a combination of a polariser (Pol on Fig. 7) and a half-wave plate (λ½ on Fig. 7) which is used to rotate the pump beam polarisation plane. Isolation of the non-linear response signal requires the acquisition and subsequent subtraction of pump-on and pump-off spectra, which is facilitated by a synchronised chopper (OM1 on Fig. 7) operating at half the laser repetition rate (500Hz).

The alignment of the double resonance 2D-IR experiment is realised with the aid of a visible reference from a CW HeNe laser (λ=632.8 nm)

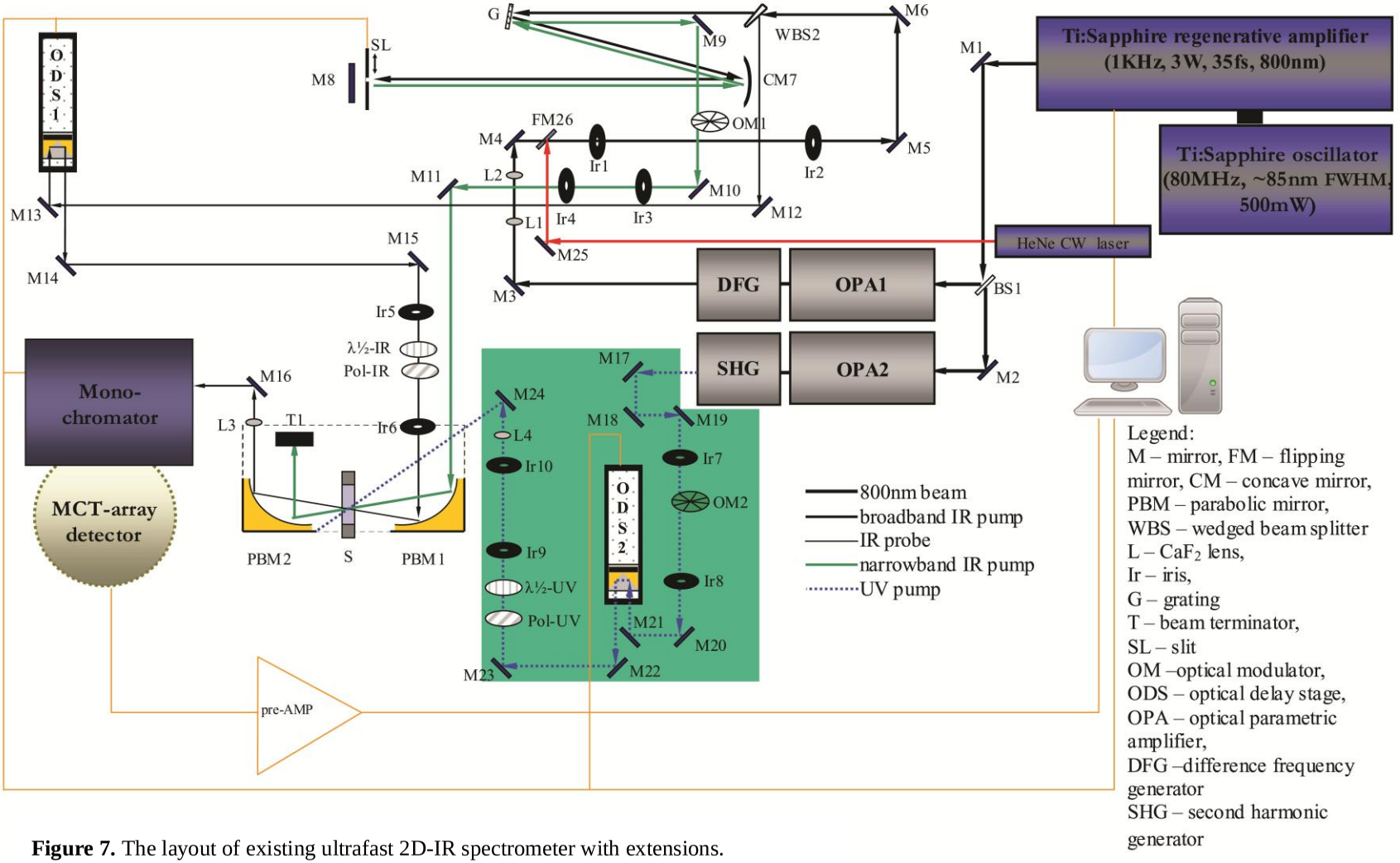

Figure 7. The layout of existing ultrafast 2D-IR spectrometer with extensions.
Green area encloses UV-VIS pump path constructed by author.

which is overlapped with the mid-infrared optical beam path (FM 26 on Fig. 7) by passage through a pair of common reference irises (Ir1, 2) where the 3-4 mm aperture was used to avoid strong scattering of mid-infrared radiation on iris edges. Routine alignment involves adjustment of the pump radiation pulse shaping unit and spatial overlap of the pump and probe beams inside the sample cell. Alignment of the pump radiation pulse shaper starts from a crude grating (G) angle positioning using the 1st diffraction order of the HeNe laser beam. The pump pulse shaper module transmits part of the reference HeNe laser radiation, which is sufficient for initial alignment of pump and probe overlap within the sample area by passing both the visible references through a pinhole (75 μm) placed in the sample holder (S). Further correction of the grating tilt angle is performed with mid-infrared radiation transmitted through the pulse shaper and visualised by the frequency-resolved detection system (MCT array based spectrograph) by measuring pinhole scattered pump path radiation. In the first step the correction of grating tilt facilitate matching mid-infrared pulse frequency distribution with selected MCT spectrograph frequency window additionally providing control of infrared generation unit adjustment (OPA1 and DFG). On completion of grating tilt correction the slit assembly (SL) is mounted to limit pulse frequency distribution to narrow frequency window adjustable by changing slit width. The optimal setting of narrowband pump frequency window should match sample absorption linewidth.[6] In final step the pulse shaper frequency coverage can be established by scanning slit position across the boundaries of M8 window.

Final optimisation of the mid-infrared beam overlap is performed using a reference sample solution of known spectral signature and slow vibrational relaxation. In the first stage, the sample position is scanned in parallel to the incoming beam direction with a broadband pump-probe configuration (as in transient TR-IR spectroscopy) and pump-probe delay time within a tenth of a picosecond from the expected time zero position. When the signal is detected, further optimisation proceeds toward maximisation of output signal strength by scanning the sample position with concomitant correction of the pump beam angle to counteract sample walk-off until the beams overlap at their focal points producing strongest response.

2.2.2.2. Development of UV-VIS pump optical assembly

The newly developed UV-VIS pump beam path is shown in Fig. 7 on a green background. The new optical table development was a collaborative effort of the author with a co-working postgraduate. The author was responsible for designing, assembling and testing the new experimental set-up by finding time zero between the UV_{pump} and IR_{probe} pulses, while the co-worker was responsible for installing polarisation optics and replacing Aluminium mirrors with 45^{o} incidence angle optimised UV dielectric optimised for near 100% reflectance at 355nm light with except of (M24 on Fig. 7) mirror optimized for 30^{o} incidence angle.

The UV-VIS output beam from the SHG module of the OPA was passed through a pair of 1mm aperture irises (Ir7, 8 on Fig. 7), facilitating alignment of the input beam by adjusting the entrance mirror pair (M18, 19 on Fig. 7). Subsequently, the beam is fed into a gold-coated retro-reflector mounted on an optical delay stage (ODS 2 on Fig. 7) which produces a parallel output beam directed into a second pair of 1mm aperture irises (Ir9, 10 on Fig. 7) throughout (M22-23 on Fig. 7) mirrors. The overlap of the UV_{pump} and IR_{probe} beams was realised by the (M24 on Fig. 7) mirror while the UV beam waist was tuned by a biconvex lens L4 f= 200mm placed on a translation stage. The polarisation of the UV pump beam was controlled by a combination of a Wollaston prism polariser (Pol-UV on Fig. 7) and a half-wave plate (λ½-UV on Fig. 7). The acquisition of pump-on/pump-off spectra for UV_{pump}-IR_{probe} and in future for Transient 2D-IR experiments was facilitated by a chopper (OM 2 on Fig. 7) synchronised to the laser trigger signal, operating at half the laser repetition rate (500Hz) for TRIR measurements.

Since intense UV radiation is destructive for both the window material (CaF_2) and the sample, sample holder modifications were required to address this. To slow down deterioration of the sample windows, a rastering system was built to support motion of the sample cell in two directions perpendicular to the incoming laser beams. This was facilitated by Strathclyde workshop and was designed around an assembly of two electric motors. Additionally, an airtight sample circulation system was constructed using Teflon® micro tubing to refresh the sample cell content from a bulk sample tank. The circulation in this system was driven by a commercial low-pressure peristaltic pump (Cole-Palmer Masterflex® variable-speed pump).

The new optical assembly required both temporal and spatial overlap of the UV beam with the existing infrared beams of the double-resonance 2D-IR experiment. In the first stage, spatial overlap of the infrared probe beam was achieved by passing the UV pump and visible reference of the probe beam through a pinhole mounted in the sample holder as described previously for IR pump beam alignment. Subsequently, the pinhole was replaced by a germanium plate and the time delay of the UV beam was scanned to detect mid-infrared radiation absorption induced by pump pulse excitation of germanium. The absorption signal was maximised by scanning the position of the germanium plate within the sample area along with concomitant UV beam angle adjustment to follow Ge plate walk off. Finally, the position of the biconvex lens (L4) was scanned to find the optimum focusing of the UV and IR beams. Afterwards, a minimum step scan of the UV_{pump}-IR_{probe} time delay (ODS 2) was performed to determine estimated time zero position. The representative plot of Ge plate infrared radiation absorption observed at 1950 cm^{-1} for $UV_{pump} - IR_{probe}$ delay times is shown in Figure 8 along with a semi-Gaussian curve was fitting to the absorption edge. The Gaussian curve apex indicates the estimated time zero position in reference to a default zero stage position. As pulse initiated Ge absorption does not appear instantaneously an additional unaccounted error is expected for presented calculations.

2.1.1. Two-dimensional infrared spectrometer detection system

The TR-IR spectrometer detection system uses a grating-based monochromator combined with a 64-element MCT photoconductive array detector. The monochromator (Triax 190, Horiba) features one adjustable slit-controlled entrance port and two perpendicular exit ports for narrow and wide angle detection. Diffraction is realised by a turret mounted set of three reflective blazed gratings with 150, 300 and 1200 lines/mm to cover the UV-Vis-mid IR frequency range. The monochromator-dispersed radiation is detected by a nitrogen cooled 64-element MCT photoconductive IR array detector (MCT-6-64, Infrared Associates Inc.) powered by multi-channel pre-amplifier (IR-6416, Infrared System Development Corp.) and equipped with 16 additional external inputs,

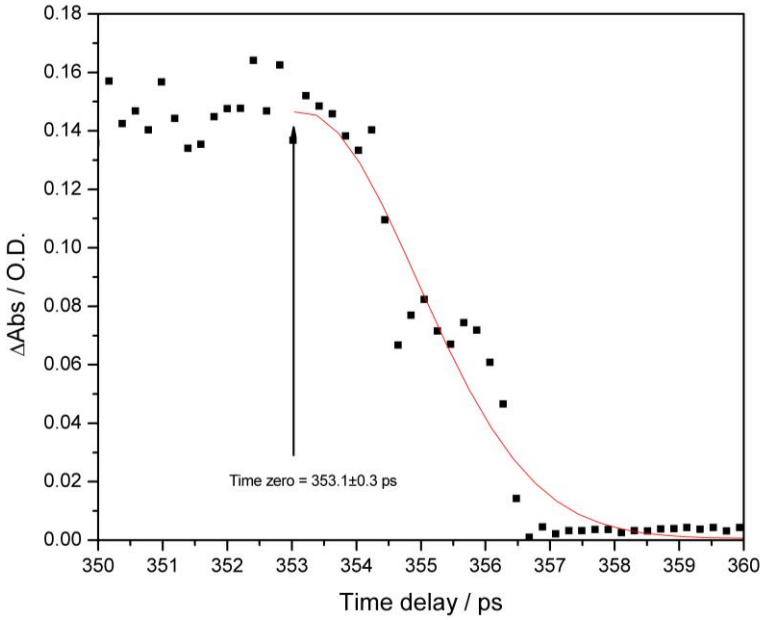

Figure 8. The representative plot of Ge plate mid-infrared absorption observed at 1950 cm^{-1} as a function of UV_{pump}-IR_{probe} time delay. The red trace represents semi-Gaussian fitting of absorption edge.

real-time multiplexer and 16-bit A/D converter. Detection of the ultrashort laser bursts by the picosecond response time MCT detector requires pre-triggering of the data acquisition system facilitated by an external triggering signal provided by the SDG generator. The Integrated signal intensity is collected over a 2.3 ns temporal window set between 300 ps to 2.6 ns after the arrival of the triggering signal. The recorded intensity for each channel is digitized by the A/D converter and multiplexed with signals from the 16 external inputs. The resulting cumulative digital signal is transferred to an I/O card in the computer responsible for controlling the spectrometer. Calculation of the pump on-pump off difference spectrum referred requires the synchronised signal from the chopper delivered through one of the external pre-amplifier inputs.

The presented detection system records the frequency-resolved self-heterodyned signal that arises from the interference of the transmitted probe pulse and the sample specific response signal. Since the infrared detector operates in the square-law regime, recording the intensity of the electric field rather than its amplitude, the total measured signal $S(\omega)$ can be expressed in Eq. 20

$$S(\omega) = \left|E(\omega) + E_{sig}(\omega)\right|^2 = I(\omega) + 2\left(E(\omega)\cdot E_{sig}(\omega)\right) + I_{sig}(\omega) \propto I(\omega) + 2\,\mathrm{Re}\left[E(\omega)\cdot E_{sig}(\omega)\right] \qquad (20)$$

where E, I and E_{sig}, I_{sig} are the electric field amplitudes and intensities for transmitted probe pulse and sample-specific response signal, respectively. The intensity of the sample-specific response signal, $I_{sig,}$ is so small that it gives a negligible contribution to the total intensity S. The major term incorporating the sample-specific response signal is the complex valued interference term of the signal and transmitted radiation electric fields. The detection system registers only the real part of the interference signal, hence the total measured intensity S can be approximated by the sum of the intensity of the transmitted probe pulse and the sample-specific response carrying the real part of the interference term. The simplest way of recovering the interference term is applying an optical modulation of the pump pulse train, which is realised by choppers (OM 1, 2). The chopping of the pump pulse train provides a pure transmitted probe pulse spectrum ($I_{pump\ off}$ = I), which subtracted from the un-chopped signal ($I_{pump\ on}$) and so isolates the intensity of interference term ΔI (real part) from the overall signal Eq. 21

$$\Delta I = I_{pump\ on} - I_{pump\ off} \propto 2\,\mathrm{Re}\left[E(\omega)\cdot E_{Sig}(\omega)\right] \qquad (21)$$

The differential intensity ΔI is a somewhat inconvenient way of presenting the sample-specific molecular response. In optical spectroscopy, absorbance is the preferred unit used to represent a molecular response via the Beer–Lambert law that connects material absorption with absorber concentration. The acquisition mode selection can be expanded to include absorbance as a way of presenting the molecular response signal. The exact method of recording absorbance requires the recording of pump-on and pump-off spectra in an absorbance representation followed by calculation of the differential absorbance.[1] The approximate method of absorbance calculation employed by author uses pump-on and pump-off intensity ratio relative to absorption as shown in Eq. 22

$$Abs = \log\left(\frac{I_{pump\ off}}{I_{pump\ on}}\right) \propto -\log\left(1 + \frac{2\,\mathrm{Re}\left[E(\omega)\cdot E_{sig}(\omega)\right]}{I(\omega)}\right) \qquad (22)$$

where the logarithm of the pump off/on intensity ratio is proportional to the logarithm of background-corrected ratio of the transmitted probe radiation to the interference term. Such simplification of the absorbance calculation is permitted

under the assumption that the incoming probe pulse intensity varies negligibly over the two consecutive laser shots used to calculate this function. The laser pulse spectrum fluctuations are a major source of distortion in the measured differential intensity ΔI and absorption *Abs* and cannot be corrected due to the lack of a probe pulse reference detector. To minimize the distortion introduced by laser source fluctuations the $\Delta I/Abs$ spectra can be calculated on a shot-to-shot basis and averaged over a selected number of shot pairs. The indiscriminate averaging procedure removes stochastic laser pulse spectrum fluctuations but is limited by experimental time constrains. The indiscriminate averaging over a larger sampling population gives better results but in the same time it extends the experimental time and increases the risk of sample quality deterioration and laser power drift. Arriving at this limitation of indiscriminate averaging, the author proposed further improvements of the averaging procedure. The major downside of the limited sample population used in averaging is that larger pulse spectrum fluctuations occur statistically less frequently than minor ones, hence the final spectrum is more affected by the former than the latter contribution. The elimination of larger fluctuations can be achieved by introducing weighting factors calculated for each shot pair. The weighting factors are calculated on the basis of pulse power and spectrum fluctuations probed by selected elements of the main MCT detector array that are free from sample-specific signal. The new procedure relies on the observation that signal peaks occupy only part of the detection array, while the remaining elements record a low intensity solvent background that exposes the fluctuations of the laser source. By default, a new normalisation system can use near edge pixels due to the fact that the Gaussian–like laser pulse frequency spectrum results in a significant power drop at the edges of the detector array. Low intensity areas of the spectrum suffer from low Signal-to-Noise (S/N) ratio that is disadvantageous for data collection. Still those channels when free from sample spectral features can be used for pulse fluctuation probing. The internal power normalisation system was designed using five channels according to the following eq. 23

$$Norm = \frac{\left(\frac{\left| I_3^{pump\ on} - I_3^{pump\ off} \right|}{2 \times 100\%} \times Power\ deviation\ threshold\ [\%] \right) - \frac{\sum_i^5 \left| I_i^{pump\ on} - I_i^{pump\ off} \right|}{5}}{\frac{\left| I_3^{pump\ on} - I_3^{pump\ off} \right|}{2 \times 100\%} \times Power\ deviation\ threshold\ [\%]} \tag{23}$$

where the normalisation factor is calculated as a scaled difference between the expected intensity drift window calculated on the basis of the difference of pump-on/pump-off intensity for the middle (third) channel multiplied by the desired power deviation threshold and mean of the five channel pump-on/pump-off intensity deviation. All pairs of spectra giving a normalisation factor outside the range 0 to 1 can be discriminated from the average while those within range could be multiplied by a corresponding normalisation factor acting as a weighting factor. A complementary jitter/skew discrimination system was created to eliminate excessive shot-to-shot spectrum shape deviations that were not detected by power based normalisation. The jitter/skew discrimination system could implement power independent first-to-fifth channel tilt calculated according following equation 24

$$Disc = \left(\left| I_5^{pump\ on} - I_5^{pump\ off} \right| \times \frac{Jitter\ threshold[\%]}{100\%} \right) - \left| \left| I_1^{pump\ on} - I_1^{pump\ off} \right| - \left| I_5^{pump\ on} - I_5^{pump\ off} \right| \right| \quad (24)$$

The discrimination factor could be calculated as the difference of an absolute value of the power drift-corrected tilt of the spectrum for the most distant channels and the jitter threshold scaled power deviation for fifth channel. All pairs of spectra returning a negative jitter value could be eliminated from the average. The normalisation and jitter control panel is shown in Figure 9.

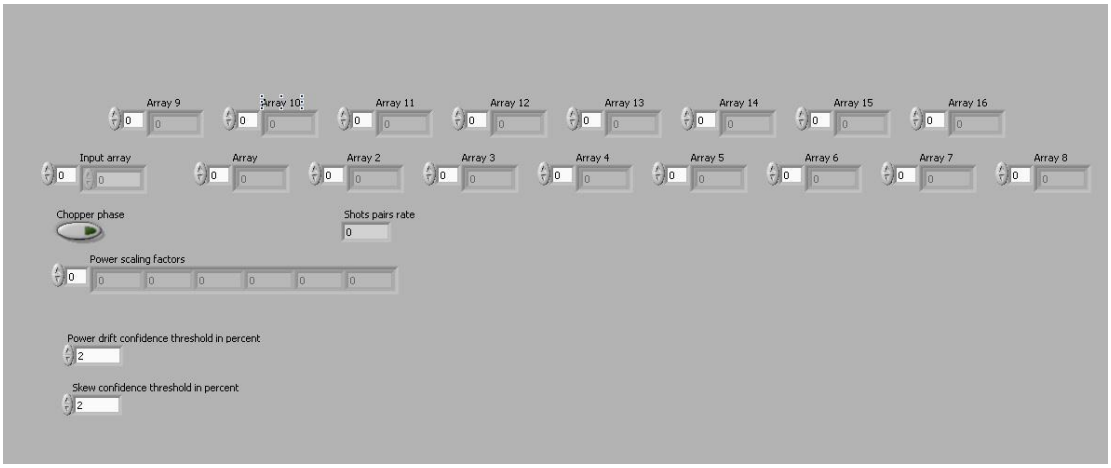

Figure 9. Normalisation and jitter/skew control panel with confidence level inputs and scaling factor streaming display with shot pair rate counter for assessing discrimination depth.

The modular design of the Labview® software allows a free redistribution of calibration channels over the entire array depending on experimental constraints. The depth of discrimination needs to be established individually on the basis of current laser system power instability and sample properties such as the presence of spectral features at the edge of the detection frequency range. The additional modules presented in this section were created and tested on the Strathclyde 2D-IR spectrometer, although they were not used in the acquisition of the experimental data presented in Chapters 3-5. During the tests of the normalisation system the current cumulative laser power fluctuation level was estimated to be ~3% since for that value, 50% of laser shot pairs were discriminated.

2.1.2. Existing 2R-IR spectrometer control software

The existing TR-IR spectrometer has dedicated Labview® software initially developed for the control of double-resonance 2D-IR experiments, which was adopted without change to UV_{pump}-IR_{probe} experiments. The main panel of the spectrometer control suite is shown in Figure 10. The program suite consists of three major modules: a detection system control, manual stage and slit positioning control and experiment parameter control. The detection system module sets the signal integration window by defining a start point and scan duration while the reference background spectrum collection records ambient radiation and detector noise level for referencing the signal spectrum.

The manual stage and slit positioning modules are designed to provide direct access to the computer controlled delay stages (ODS1, 2). The manual control module is equipped with a graphical MCT detector output display to aid delay time adjustment and facilitate signal optimisation. The experiment control module is split into three subunits each designed for a different type of experiment. The kinetic scan module records fixed frequency pump-probe kinetic traces used for TR-IR and 2D-IR experiments while modules specific to the double-resonance 2D-IR technique perform a pump frequency scan of the motorised slit (SL) for a fixed or variable pump-probe time delay configuration. All experimental types require the specification of the data acquisition type, number of laser shots for averaging, number of experiment repetitions or scans and a filename for the spectral data. The

kinetic scan experiment requires a defined slit position for the fixed pump frequency and a time delay scan range and step resolution divided into three separate sub-ranges. The double-resonance 2D-IR experiment modules require specification of both slit and optical time delay scan ranges and step resolution. The existing spectrometer software control suite was expanded over additional modules in order to facilitate vibrational echo 2D-IR experiments discussed in Chapter 6.

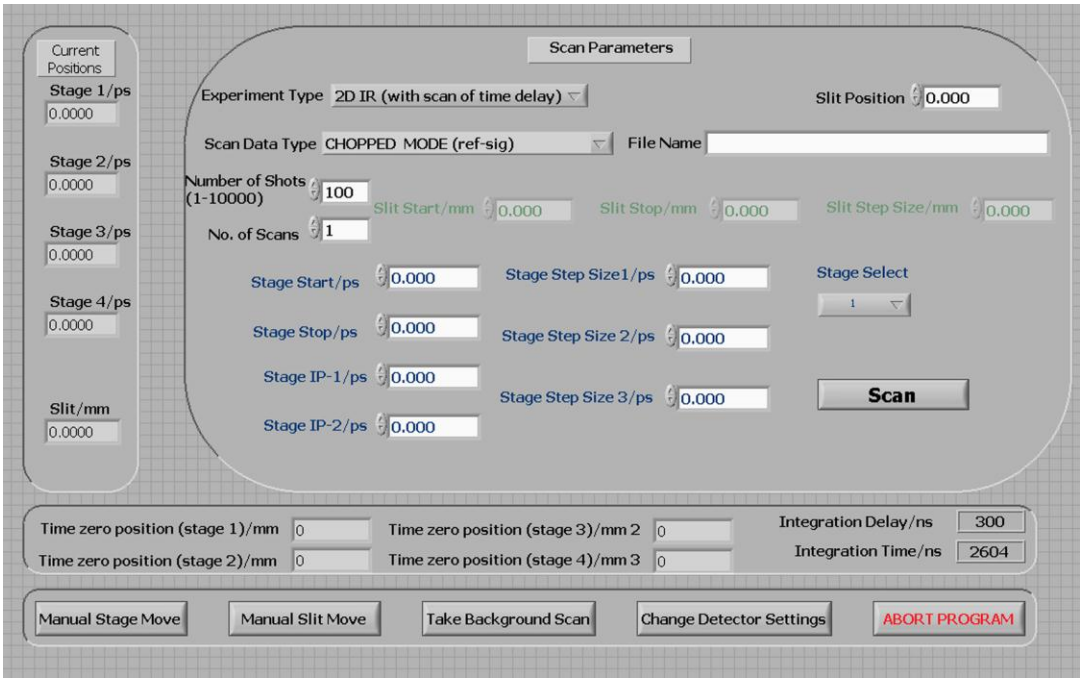

Figure 10. Main panel of 2D-IR spectrometer control software suite.

2.2. Data processing software

The raw spectrometer data needs to be corrected on account of distortions introduced by the single detector configuration and the method specific post-processing approach. The averaging procedure discussed for spectrum distortions related to power fluctuations introduces a skew to the mean spectrum baseline. Additionally, the mean sample spectrum is affected by pump radiation scattering noise, an effect magnified by the 2.3 ns detection time integration window. To remove distortion and noise contributions from the raw spectral data, a baselining program was designed. To handle the baseline skew, a subtraction of a cubic polynomial fit to the peak free background was applied, while removal of the pump scatter contribution was accomplished by subtracting a negative pump-probe time

delay spectrum. The negative pump-probe time delay spectra do not feature sample-specific molecular response signals but do contain effects due to pump light scattering and detector noise contributions. The main panel of the 2D data baselining program written in Labview® is shown in Figure 11. The input 2D data matrix is split into column vectors containing a multi-shot averaged spectrum for a particular pump-probe delay time or slit position for a double-resonance 2D-IR experiment.

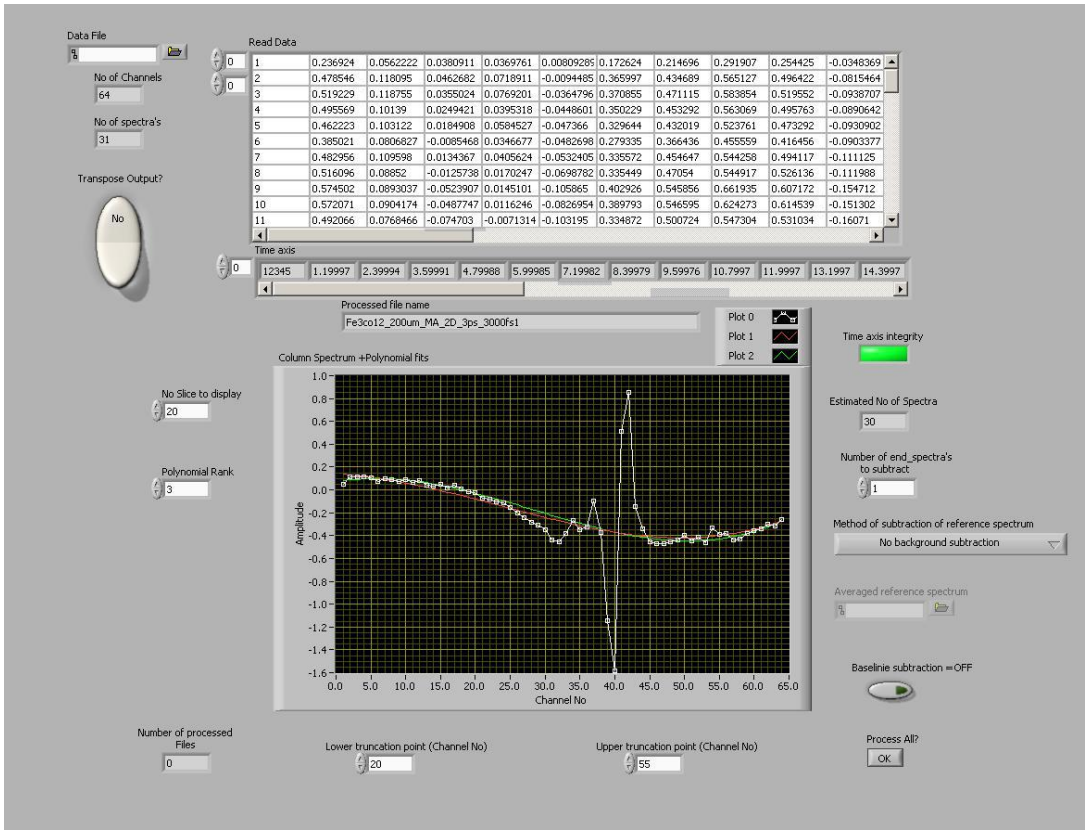

Figure 11. The main panel of pre-processing program for 2D spectra background and cubic baseline subtraction.

The spectral slices are presented on a graphical panel with two additional traces: a red one which represents the selectable-rank polynomial baseline fit to the entire spectrum while the green one represents the cubic polynomial fit to regions of the spectrum determined by two selectable cut-off channel numbers. The rank of polynomial to be subtracted from the spectra was fixed at cubic as a compromise between the ability to approximate the typical curvature of the baseline and retaining the proper shape of actual peaks. Failure to select the cut-off channels results in a full spectrum cubic baseline fit subtraction. The pump scatter reference spectrum

removal is realised by subtraction of an averaged spectrum created from selected number of spectra at the front or end of the data matrix or alternatively from an external file containing a single column reference spectrum recorded with a negative pump-probe delay time. To streamline data processing the program operates in a batch mode, automatically processing and renaming consecutively the numbered files produced by the spectrometer control program using a common set of registering parameters.

A comparison of the global and selected-range cubic baseline subtraction approaches are demonstrated on a 2D spectrum slice for the (n-propyl-cyclopentadienyl)tungsten tricarbonyl [(*pr*-Cp)W(CO)$_3$]$_2$ dimer in n-heptane shown in Figure 12.

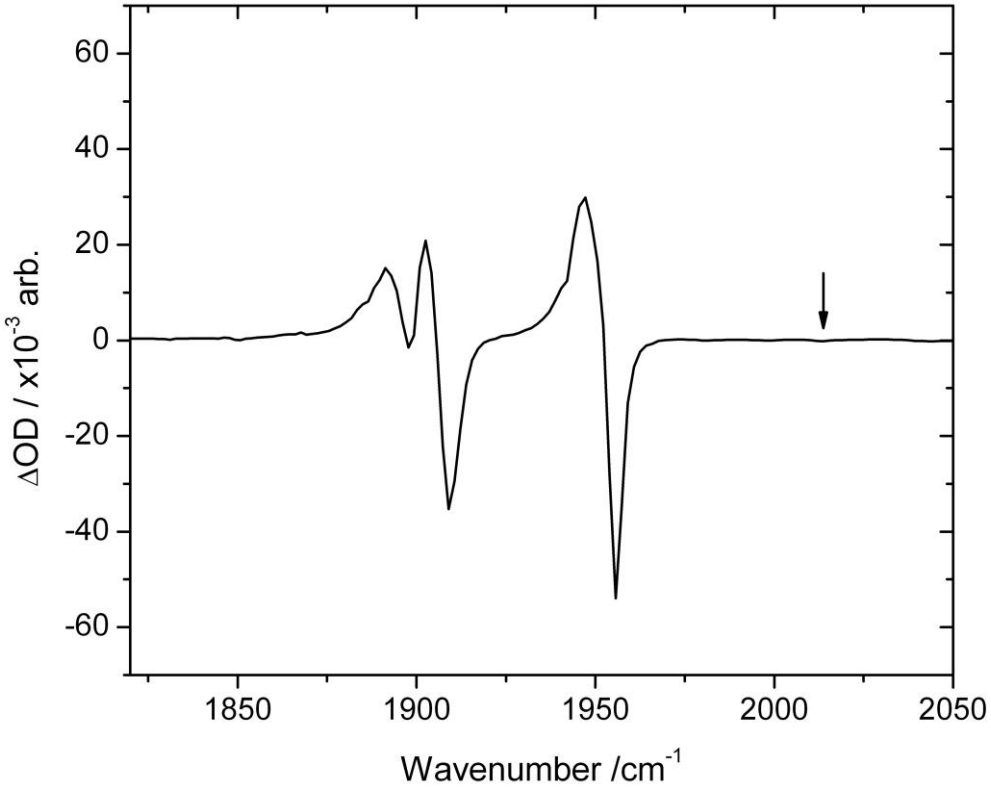

Figure 12. The horizontal slice through 2D-IR spectrum of [(*pr*-Cp)W(CO)$_3$]$_2$ in n-heptane for pumped main absorption peak at 1951 cm^{-1} and 3 ps pump-probe delay time. Arrow indicates very weak absorption peak at 2013 cm^{-1}.

The spectrum slice registered for a 3 ps pump-probe delay time for a pump frequency coincidental with the main absorption peak at 1951 cm^{-1} features a weak peak at 2013 cm^{-1}.

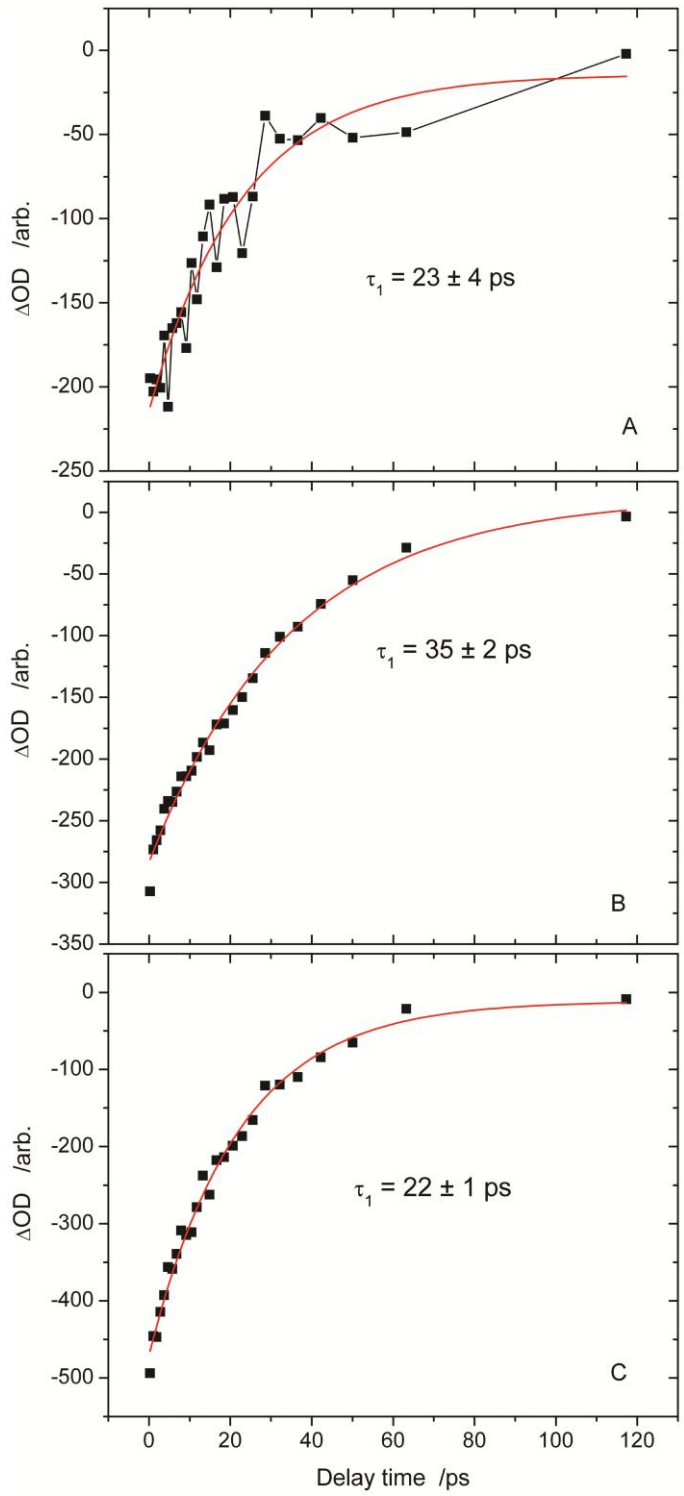

Figure 13. The 2013cm^{-1} feature amplitude based kinetic traces for raw spectrum (A), globally fitted baseline subtraction (B) and selected sub-ranges fitted baseline subtraction (C). Red traces are single-exponential fits of kinetic data with indicated signal decay time τ_1.

The 2013cm^{-1} feature amplitude represents ~0.5% of the main absorption peak and is strongly affected by baseline fluctuations. Kinetic traces of the amplitude of this peak for raw, global and selected range baseline corrected spectra are shown in Figure 13. The red traces represent the best single-exponential decay fits for each data set. The raw kinetic trace (fig. 13A) plot is strongly affected by shot-to-shot baseline fluctuations producing a poor quality fit of the decay rate with a correlation factor of 0.91. In the global baseline corrected kinetic trace (fig. 13B) the frequency fluctuation effects are entirely suppressed yielding a good quality (R=0.99) fit but with a significantly different decay rate constant τ_1 than those of the raw spectrum. This undesired effect can be assigned to slice spectrum (Fig. 12) asymmetry, which contributes to the baseline polynomial fit that becomes dependant on the decay rate of the main spectral features. An alternative way of performing the baseline polynomial fit is to use the peak free regions of the spectrum to determine the actual baseline shape. The corrected kinetic trace using this method is shown in Fig. 13C. This baselining approach removes the baseline fluctuation contribution from the kinetic trace providing a good fit (R=0.99) of the decay rate while maintaining curvature fidelity as demonstrated by a comparable decay rate constant τ_1 to that of the raw data.

Pre-processed raw spectra require axis frequency calibration which is performed by referencing fundamental transition peak positions on the time-resolved spectrum against fundamental transition frequencies measured by FT-IR spectroscopy. The calibration is realised by linear regression of the identifiable fundamental transition peaks against method-specific frequency parameters. The main panel of the axis calibration program is shown in Figure 14. The uploaded 2D spectrum is visualised in the form of a data table while the graphical panels display both vertical and horizontal slices throughout the most intense peak on the 2D spectrum. The slice-shifting facilitates identification of the positions of fundamental transitions while two column tables match the numerical values of peak positions with the corresponding FT-IR-derived frequencies. These two columns are used by linear regression modules to build a calibrated frequency axis for the current spectral data. The axis view toggle switch changes the spectrum graphical panel between input and calibrated axis views to control the calibration process.

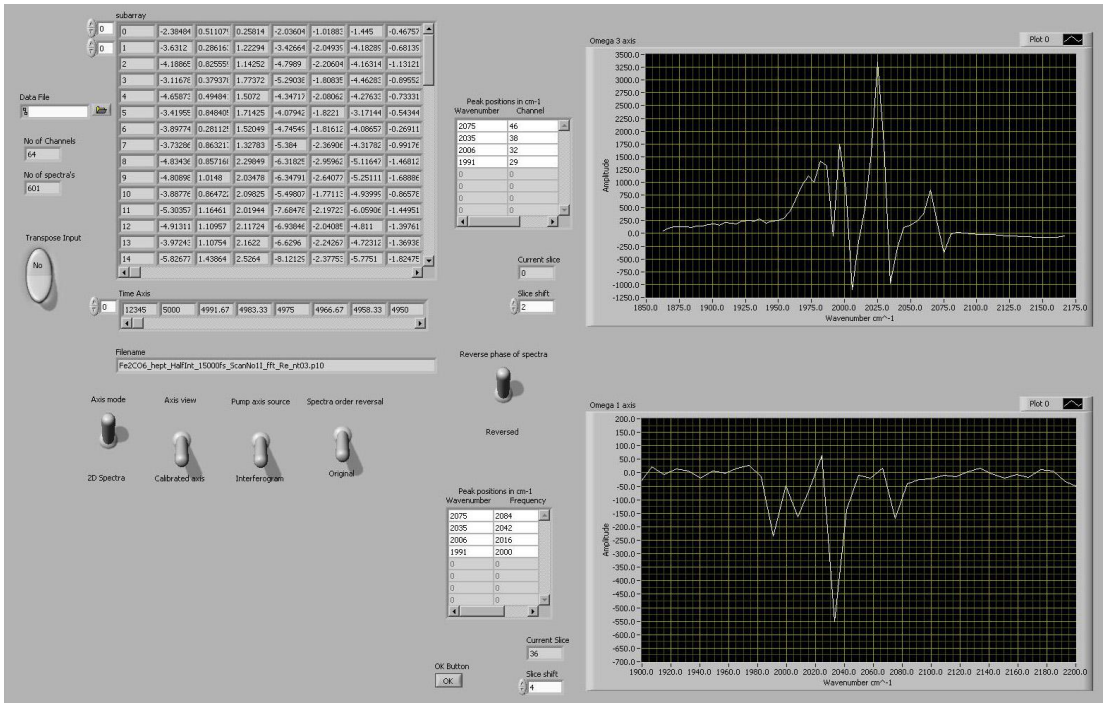

Figure 14. Main panel of visually aided 2D spectra axis calibration program

The axis mode switch disables pump axis calibration for the processing of kinetic trace data matrices. The pump axis switch selects the specific calibration method for the pump vector data containing either slit position or FFT derived frequencies for double-resonance or photon echo 2D-IR techniques, respectively. On termination, the program duplicates the input file replacing the original frequency axis with the calibrated ones.

2.3. Acknowledgements

The author would like to acknowledge the contributions of Ian A. Stewart a co-working postgraduate and Dr. Spyros Kaziannis in the expansion of the 2D-IR spectrometer to include UV-Vis pump experiments.

References:

(1) Towrie, M.; Grills, D. C.; Dyer, J.; Weinstein, J. A.; Matousek, P.; Barton, R.; Bailey, P. D.; Subramaniam, N.; Kwok, W. M.; Ma, C.; Phillips, D.; Parker, A. W.; George, M. W. *Applied Spectroscopy* **2003**, *57*, 367.

(2) Helbing, J.; Nienhaus, K.; Nienhaus, G. U.; Hamm, P. *The Journal of Chemical Physics* **2005**, *122*, 124505.

(3) Andresen, E. R.; Gremaud, R.; Borgschulte, A.; Ramirez-Cuesta, A. J.; Züttel, A.; Hamm, P. *The Journal of Physical Chemistry. A* **2009**, *113*, 12838.

(4) Cervetto, V.; Helbing, J.; Bredenbeck, J.; Hamm, P. *The Journal of Chemical Physics* **2004**, *121*, 5935.

(5) Pensack, R. D.; Banyas, K. M.; Barbour, L. W.; Hegadorn, M.; Asbury, J. B. *Physical Chemistry Chemical Physics:PCCP* **2009**, *11*, 2575.

(6) Hamm, P.; Zanni, M. *Concepts and Methods of 2D Infrared Spectroscopy*; Cambridge University Press: Cambridge, **2011**.

(7) Zhang, Z.; Piatkowski, L.; Bakker, H. J.; Bonn, M. *Nature Chemistry* **2011**, *3*, 888.

(8) Andresen, E. R.; Hamm, P. *The Journal of Physical Chemistry B* **2009**, *113*, 6520.

(9) Shim, S.-H.; Zanni, M. T. *Physical Chemistry Chemical Physics: PCCP* **2009**, *11*, 748.

(10) Anna, J. M.; Nee, M. J.; Baiz, C. R.; McCanne, R.; Kubarych, K. J. *Journal of the Optical Society of America B* **2010**, *27*, 382.

(11) Nee, M. J.; McCanne, R.; Kubarych, K. J.; Joffre, M. *Optics Letters* **2007**, *32*, 713.

(12) Bloem, R.; Garrett-Roe, S.; Strzalka, H.; Hamm, P.; Donaldson, P. *Optics Express* **2010**, *18*, 1747.

(13) Deflores, L. P.; Nicodemus, R. A.; Tokmakoff, A. *Optics Letters* **2007**, *32*, 2966.

(14) Helbing, J.; Hamm, P. *Journal of the Optical Society of America* **2011**, *28*, 171.

(15) Kwak, K.; Rosenfeld, D. E.; Fayer, M. D. *The Journal of Chemical Physics* **2008**, *128*, 204505.

(16) Middleton, C. T.; Strasfeld, D. B.; Zanni, M. T. *Optics Express* **2009**, *17*, 14526.

(17) Roberts, S. T.; Loparo, J. J.; Ramasesha, K.; Tokmakoff, A. *Optics Communications* **2011**, *284*, 1062.

(18) Shim, S. H.; Strasfeld, D. B.; Ling, Y. L.; Zanni, M. T. *Proceedings of the National Academy of Sciences of the United States of America* **2007**, *104*, 14197.

(19) Shim, S. H.; Zanni, M. T. *Physical Chemistry Chemical Physics: PCCP* **2009**, *11*, 748.

(20) Volkov, V.; Schanz, R.; Hamm, P. *Optics Letters* **2005**, *30*, 2010.

(21) Xiong, W.; Strasfeld, D. B.; Shim, S.-H.; Zanni, M. T. *Vibrational Spectroscopy* **2009**, *50*, 136.

(22) Xiong, W.; Zanni, M. T. *Optics Letters* **2008**, *33*, 1371.

3. Photochemistry of a [FeFe]hydrogenase active centre model – an evidence of photoinduced isomerisation of parent molecule.

The dwindling supply and heavy environmental costs of fossil fuels has accelerated research into alternative sources of energy such as hydrogen fuel.[1-8] However, the generation of high energy hydrogen fuel from its most abundant resource, water, suffers from many limitations. For example, water electrolysis using conventional metallic electrodes faces a large overpotential significantly reducing the efficiency of the process. One way to combat this problem is finding efficient catalysts that eliminate, or reduce, the additional activation barrier faced by proton reduction on metallic surfaces. One direction of such scientific pursuits started with the elucidation of the structure of several metaloenzymes called hydrogenases which are known to carry out efficient catalysis of the reversible conversion of protons to dihydrogen in biological systems. Hydrogenase metaloenzymes consist of three functional parts, a protein scaffold responsible for hosting the metallic cofactor and transporting reactants and products, a bimetallic catalytic centre that facilitates the red-ox process of dihydrogen formation, and a chain of electron-rich cubane-like Fe_4S_4 clusters which provide electrons for the reduction process.[8-10] The hydrogenases are divided into several subfamilies of which the most promising are the nickel iron [NiFe]hydrogenases and iron only [FeFe]hydrogenases which differ in terms of the nature of the bimetallic active site structure.[10-12] Particular interest was directed toward the homometallic [FeFe]hydrogenases, which are easier to structurally duplicate and modify via chemical synthesis. The iron only hydrogenase active site consists of a diiron dithiolate cluster supported by a bridging CO ligand. The remaining basal ligand positions are filled with monodentate CO and CN ligands while one axial position is occupied by sulphur ligand bridging to the first Fe_4S_4 cluster.[13-22] The homometallic [FeFe]hydrogenase active centre structure is shown in Figure 14. The double bridging dithiolate ligand enforces a particular active centre configuration while the cysteinyl bridge facilitates coupling with the chain of electron rich Fe_4S_4 clusters. The remaining CO and CN ligands (Fig. 15) tune the red-ox properties of the iron centres to a support highly reducing Fe^+ oxidation state

capable of reducing protons to dihydrogen. The development of a successful catalyst suitable for large-scale industrial applications requires a concerted effort in developing new structural candidates[11,12,14,23-31] and understanding of the underlying chemical reaction mechanism[5,10,13,15,17-22,32-34] of dihydrogen formation in the natural enzyme as well as its synthetic counterparts. An integral part of these reaction mechanism studies are time-resolved infrared spectroscopy investigations which permit observation of the initial stages of a chemical reaction in the ultrafast domain.

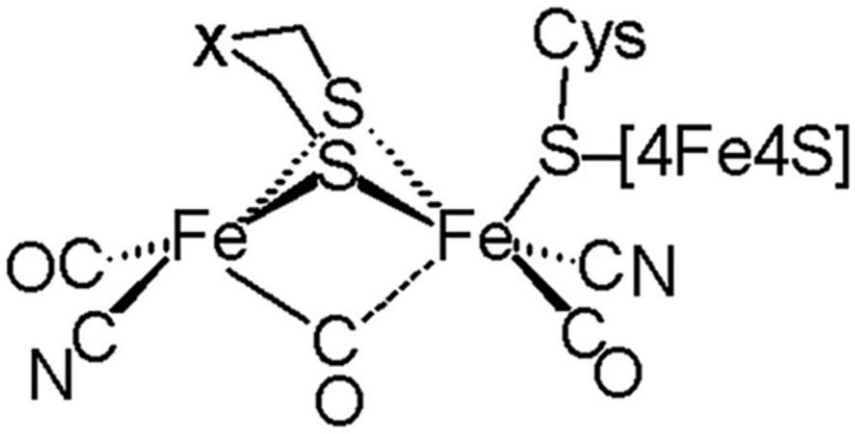

Figure 15. Structure of [FeFe]hydrogenase active centre.

Such studies are of fundamental interest due to the fact that, in the naturally occurring enzymes, the catalytic centre is preserved in a very reactive coordinatively unsaturated form (Fig. 15) that supports reactant binding and internal redox processes. Artificial hydrogenase-like catalysts aim to duplicate the reactivity of the natural enzyme in order to achieve the high turnover rate required for industrial applications. Unfortunately, such a structural configuration is not easily replicated by straightforward chemical synthesis of active centre mimics alone but it may be created by the photoinduced dissociation of a monodentate ligand such as CO from a coordinatively saturated hydrogenase mimic.

Numerous model compounds mimicking the natural [FeFe]hydrogenase active centre[11,12,14,23-31] have been synthesized and tested to determine both their proton affinity and catalytic activity with respect to the production of molecular hydrogen. Among them a family compounds with the general formulae $(\mu\text{-}S(CH_2)_3S)Fe_2(CO)_4(L)_2$ (L = CO,CN,PMe_3) have been shown to be promising

candidates for further development.[8,17,22,34] Preliminary studies of the chemistry of these model systems have shown catalytic activity toward hydrogen production with successful preliminary applications for sunlight powered water photolysis. Previously reported time-resolved infrared spectroscopic studies of the dynamics and photochemistry of (μ-$S(CH_2)_3S)Fe_2(CO)_4(L)_2$ (L=CO,CN) systems[13,15,19-21,35] in a range of solvents and solvent mixtures, with particular interest in the hexacarbonyl (L=CO) system, have shown that, in all cases, UV excitation of the metal to ligand charge transfer transition (MLCT) triggered formation of an asymmetrical CO ligand deficient transient species followed by the process of geminate recombination and solvent substitution. In most cases, a stable solvent adduct of general formula (μ-$S(CH_2)_3S)Fe_2(CO)_3(L)_2$(Solv) (L=CO,CN) was detected. Additionally, ground state investigations of these systems by 2D-IR spectroscopy have revealed weak vibrational coupling between CO and CN^- ligands alongside evidence for CN ligand induced acceleration of the vibrational relaxation rate in comparison to the pure carbonyl derivative, further showing that the nature of heterogeneous ligand L plays important role in vibrational energy redistribution in both natural enzyme and synthetic models.

In this chapter the effect upon reactivity and solvatation dynamics of replacing two carbon coordinated CO ligands with trimethylphosphine groups is investigated. The compound (μ-$S(CH_2)_3S)Fe_2(CO)_4(PMe_3)_2$ (**1**) has been shown to form a bridged protonation product (μ-$H)Fe_2(pdt)(CO)_4(PMe_3)_2$ under acidic conditions and the associated mechanism and kinetics have been studied with millisecond time resolution by stopped-flow UV-VIS and FT-IR methods.[9,18,32,34] Such behaviour is not observed for the hexacarbonyl or dicyano synthetic derivatives. Additionally, the neutral trimethylphosphine derivative exists in two isomeric forms with a concentration ratio that depends upon the nature of the solvent. Thus far, no ultrafast time-resolved studies of the photochemistry of this system have been carried out. By using a combination of TRIR spectroscopy and DFT simulations, the effect of geometrical isomerisation and changing the ligand (L) upon the ultrafast photochemistry of the compound can be studied, providing further insight into the influence of ligand modifications upon catalytic performance.

3.1. Experimental

The model compound (μ-$S(CH_2)_3S)Fe_2(CO)_4(PMe_3)_2$ (**1**) used in this work was produced by established synthetic routes[9] while the solvents were obtained from Sigma-Aldrich and used without further purification. The oxygen- and moisture-sensitivity of **1** required that samples were handled in a nitrogen protective atmosphere environment and that all solvents were dried over CaH_2 and purged with N_2 prior to use. For FTIR measurements, the samples were held in airtight cells (Harrick Scientific) consisting of a pair of CaF_2 windows separated by a 200μm thickness PTFE spacer while in TRIR studies the cell content was continuously refreshed by a closed-loop circulation of bulk solution stored in a nitrogen flushed reservoir. Additionally the sample cell was rastered in two dimensions with aid of a two-motor assembly to prevent window damage by UV radiation. The concentration of the solutions was adjusted to yield the desired sample optical density of around 0.5 in the carbonyl ligand (ν_{CO}) stretching mode region. For an n-heptane solution this equated to a concentration of 1.3 mM and it was established that the OD at UV_{pump} frequency of 355 nm was around 0.35 under these conditions. In the case of other solvents the concentration of **1** was higher to achieve required mid-IR absorption due to line broadening.

Steady state FTIR spectra were recorded on a Bruker Vertex 70 spectrometer in a standard cell while temperature dependent FTIR measurements were performed in a thermostatically controlled cell (Harrick Scientific model TFC-525-3) accurate to ±1 K.

3.1.1. TR-IR Spectrometer

The TR-IR measurements were performed on the Strathclyde spectrometer with the aid of the newly developed UV-VIS pump path described in a previous chapter. Briefly, a regeneratively amplified Ti:Sapphire laser system (Coherent) producing 35 fs duration pulses centred at 800 nm with a repetition rate of 1kHz was used to pump two white light seeded optical parametric amplifiers (OPA). One OPA produced UV_{pump} pulses with a wavelength of λ = 355 nm via higher harmonic (4^{th}) generation, which were used as while the second OPA generated IR_{probe} pulses via difference frequency generation (DFG) of the signal and idler radiation from the

OPA. The spectral profile of the latter pulses was centred near 1950 cm^{-1} with a bandwidth of >200 cm^{-1}. The pump-probe time delay was controlled by an optical delay line and the relative polarization of the pump and probe pulses were set to the magic angle to remove the effects of molecular rotation from the signal. To facilitate collection of pump on-pump off difference spectra, a chopper operating at half the laser repetition rate (500 Hz) was used to modulate the pump pulse train. The transmitted probe radiation was dispersed via a grating spectrometer and recorded using liquid nitrogen cooled 64-element HgCdTe array. The spectral and temporal resolution obtained from this apparatus was ~ 4 cm^{-1} and 150 fs respectively.

3.1.2. Data Analysis

The data analysis was performed via a global analysis method. The spectro-temporal experimental data matrix f(ν,t) was represented as a sum of Gaussian spectral lines $G_i(\nu)$ each with an associated temporal decay function $T_i(t)$ Eq. 25.

$$f(\nu,t)=\sum_{i}^{n} G_i(\nu)\cdot T_i(t) \tag{25}$$

The experimental data fitting was performed iteratively by the successive fitting of subsequent Gaussian peaks each with a fixed position and width across the time axis while the amplitude was left free to vary. When the required number of Gaussian lines was established the global analysis routine performed a final all-parameter fitting. The results of fitting 9 fixed-width Gaussians to a whole spectrum data matrix are shown in Figs 16 (a)-(c) for **1** in heptane solution for selected time delay slices. The stability of the solution was tested by cyclic variation of a subset of initial parameters. To recover the temporal function $T_i(t)$ for each spectral feature the Gaussian peak amplitude variation across the time axis was fitted to single- or bi-exponential function. The resulting temporal decays of spectral features were comparable to those obtained from direct fitting of peaks amplitude against pump-probe delay times for well-separated spectral features to test the validity of the Gaussian peak approximation approach. The global analysis routine relies on a Levenberg-Marquardt algorithm performing χ^2 Chi-square minimization to find optimal parameters.

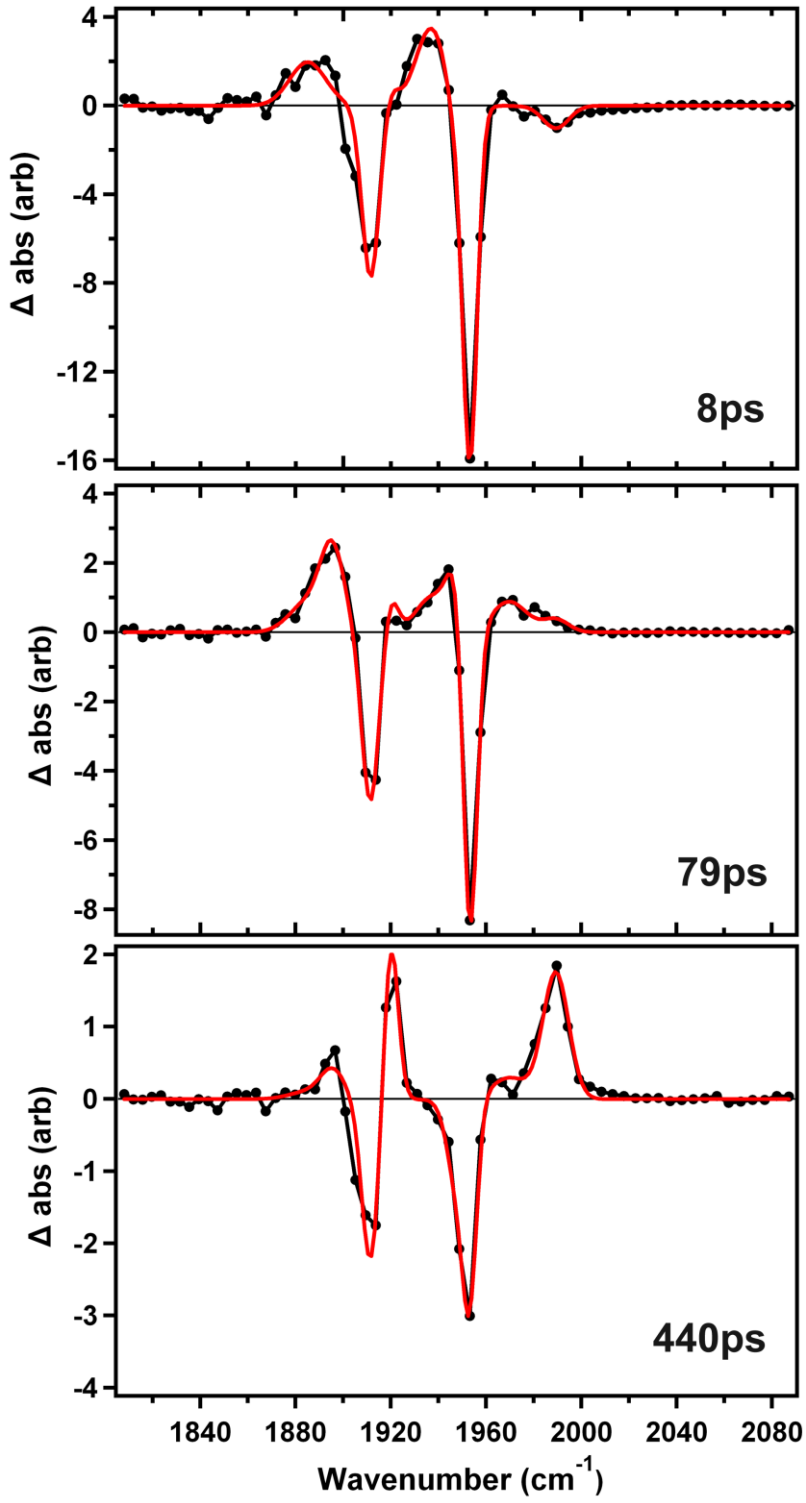

Figure 16. The representative TRIR spectrum (black) of **1** in n-heptane solution at pump-probe delay times 8, 79 and 440 ps fitted with amalgam of 9 Gaussian line shapes (red) whose peak positions and line widths was found experimentally and hold constant across all available pump-probe delay time slices by multi-dataset fitting routine of Igor® 6.

3.1.3. Density Functional Theory calculations

All DFT calculations were carried out using the Gaussian 03 package.[36] The calculations were performed on molecules *in vacuo* using the hybrid B3LYP functional[37-39] and LanL2DZ basis set. The latter employs the Dunning/Huzinaga valence double-ζ D95 V basis set[40] for first-row atoms and Los Alamos Effective Core Potential plus DZ on atoms from Na-Bi.[41-43] The choice of the functional and basis set combination was dictated by a compromise between the accuracy of the energy estimation and the infrared spectrum prediction.[44,45] Due to weak interaction of the solvent with the transient molecule in the solvent adduct, establishing accurate total energy required correction for Basis Set Superposition Error.[46] No other scaling and correction factors were applied. Harmonic frequency calculations were performed on the optimised geometry structures while transition state searches were performed using the Synchronous Transit-Guided Quasi-Newton (STQN) method.[47,48]

3.2. Results

3.2.1. Steady state FT-IR spectroscopy

The infrared absorption spectrum of **1** is shown in Figure 17(a) for solutions in n-heptane, MeOH and MeCN. When dissolved in n-heptane, **1** displays three intense bands at 1895, 1909 and 1954 cm^{-1} alongside a fourth, much weaker, transition at 1990 cm^{-1}. In MeOH and MeCN solutions the absorption lines display a red-shifted and broadened profile, while the highest frequency mode, which is extremely weak in heptane, has an intensity comparable to other transitions leading to three visible bands at 1904 (1899), 1946 (1943) and 1984 (1880) cm^{-1} for MeOH (MeCN). The lowest frequency band displays a red-side shoulder consistent with the coalescence of two transitions which were observed as separate features in heptane solutions. The linewidths of the peaks originating from a single transition was 5, 8 and 10 cm^{-1} in heptane, MeOH and MeCN respectively. The increased linewidths in the polar solvents are attributable to inhomogeneous broadening, indicating a rise in the strength of solute-solvent interactions in polar solvents in comparison to heptane,

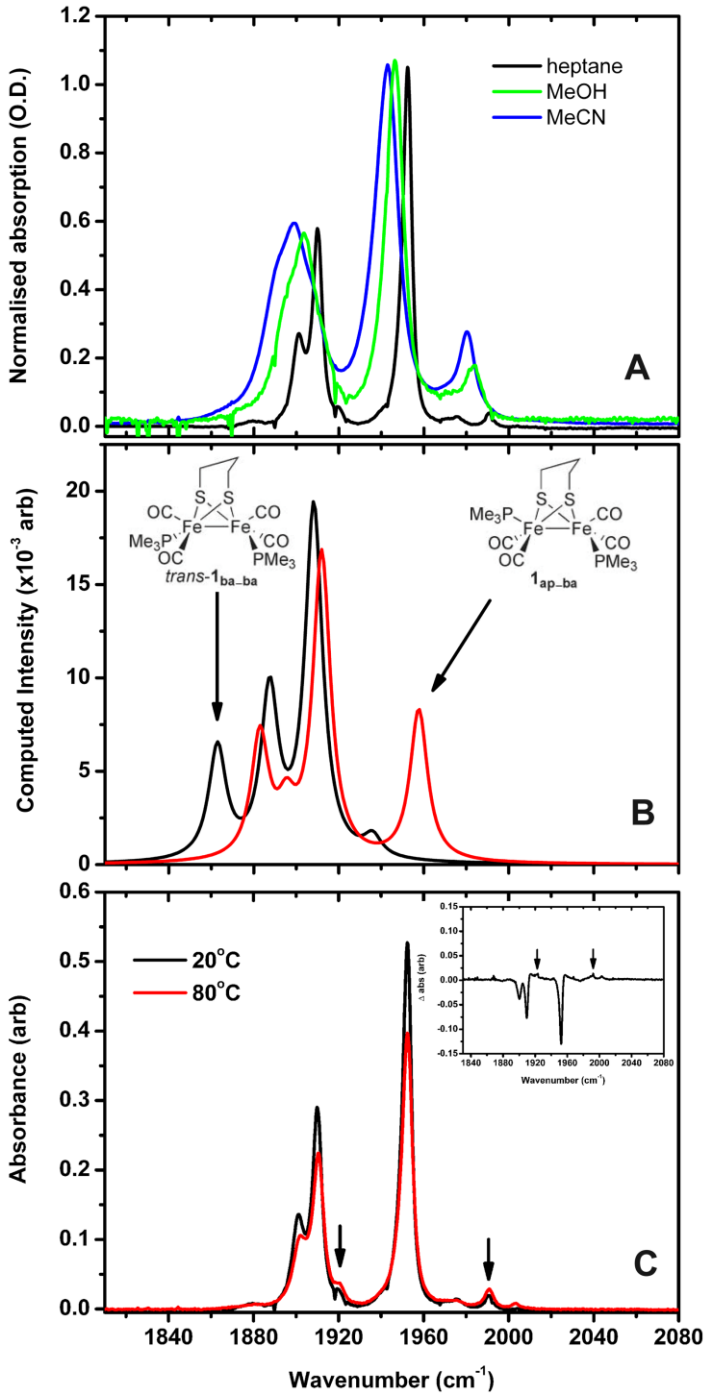

Figure 17. (A) A solvent absorption corrected normalised ν_{CO} region of FT-IR spectrum of **1** dissolved in n-heptane (black), MeOH (green) and MeCN (blue), (B) DFT calculated infrared spectra of ***trans*-1$_{BA-BA}$** (black) and **1$_{AP-BA}$** (red) isomeric forms and their structures, (C) ν_{CO} region of FT-IR spectrum of **1** dissolved in n-heptane at 20°C, 80°C and their difference spectrum (inset). The arrows indicate absorption growth due to isomeric equilibrium.

though 2D-IR studies of similar species have indicated that the associated mechanisms and dynamics of inhomogeneous broadening differ between MeOH and MeCN solutions[49]: The former solvent interacts strongly with the solute via hydrogen-bonds formed between the terminal oxygen of the CO ligand and the hydroxyl group of the alcohol whereas the latter exhibits a large dipole moment (3.92 D) that affects vibrational relaxation particularly of polar solutes.[35] The intensity change of the high frequency peak is correlated to increasing solvent polarity and can be attributed to the presence of different geometrical isomers of **1**. Out of the four possible structural arrangements of the carbonyl and trimethylphosphine ligands in **1** only two have been observed experimentally. The structures and infrared spectra of these two isomeric forms, denoted ***trans*-1$_{\mathbf{BA\text{-}BA}}$** and **1$_{\mathbf{AP\text{-}BA}}$** (where BA and AP indicate basal and apical ligand positions respectively) are displayed in Fig.17(b). The ***trans*-1$_{\mathbf{BA\text{-}BA}}$** isomer was found to be prevalent in the solid state while the **1$_{\mathbf{AP\text{-}BA}}$** form was detected in polar solvent solutions by ^{31}P NMR spectroscopy.[18,32] The DFT structural optimisations and energy calculations have been carried out for both isomeric forms. These indicate that a 4.3 kJ/mol energy difference exists between the ***trans*-1$_{\mathbf{BA\text{-}BA}}$** and **1$_{\mathbf{AP\text{-}BA}}$** structures with the latter lying higher in energy. The calculations also indicate a significant difference in the overall dipole moment for the two forms with that of ***trans*-1$_{\mathbf{BA\text{-}BA}}$** predicted to be 1.9 D while the **1$_{\mathbf{AP\text{-}BA}}$** structure leads to a value of 5.5 D. This is consistent with experimental indications that the ***trans*-1$_{\mathbf{BA\text{-}BA}}$** isomer is the dominant form in non-polar heptane while in polar solvents the ratio of isomers should be shifted in favour of the **1$_{\mathbf{AP\text{-}BA}}$** form. The DFT predicted infrared spectra of both isomers (Fig.17(b)) reinforce this assignment of the FT-IR spectra**.** In both cases there are four fundamental transitions due to absorption in the ν_{CO} region but for ***trans*-1$_{\mathbf{BA\text{-}BA}}$** form the highest frequency mode has very low intensity compared to the main peaks, which is not the case for the **1$_{\mathbf{AP\text{-}BA}}$** isomer. This is consistent with the rising intensity of the high frequency peak in the experimental FTIR spectrum observed when switching from heptane to MeOH or MeCN suggesting that this is suitable indicator of the **1$_{\mathbf{AP\text{-}BA}}$** isomer concentration in solution.

Further support for this isomeric equilibrium can be obtained from the thermal dependence of the FTIR spectrum of **1** in heptane. Example spectra are

displayed in Figure 17(c) which shows that increasing the temperature leads to a decrease in the intensity of the three main ν_{CO} peaks and a concomitant gain in the intensity of the 1990 cm^{-1} peak, as expected for a thermal redistribution of the isomeric equilibrium position. In addition, the higher temperature spectrum reveals the presence of another transition assignable to the $\mathbf{1_{AP\text{-}BA}}$ isomer located at 1922 cm^{-1}. It is apparent from Fig. 17(b) that all predicted $\mathbf{1_{AP\text{-}BA}}$ isomer transitions are blue shifted in relation to ***trans*-$\mathbf{1_{BA\text{-}BA}}$**, which explains the appearance of a band at 1922 cm^{-1} in the thermal FT-IR experiment. Although vibrational frequencies predicted by DFT are expected to show errors in relation to the absolute experimental frequencies, the overall patterns and relative line positions have generally been found to be in good agreement with experiment when using this combination of functional and basis set.[22,44,45,50]

3.2.2. Time-resolved IR spectroscopy

Time-resolved difference spectra in the ν_{CO} region showing the effects of UV irradiation at λ=355 nm of **1** in heptane, MeOH and MeCN are presented in Figs 18(a)-(c). The data are shown for three time delays that are representative of the observed dynamics: 3 ps, immediately following excitation, an interim state near 80 ps and 425 ps when most of the primary photochemical processes are complete.

In the spectra obtained for **1** dissolved in heptane (Fig.18(a), black) with a pump-probe delay of 3 ps, three negative features are observed that are coincident with the main peaks observed in the FTIR spectrum of this sample. These features were present at the earliest pump-probe delay times and are assignable to bleaches arising from depletion of the concentration of **1** by the UV pulse. Small bleach is also observed at 1990 cm^{-1} consistent with a reduction in the concentration of the $\mathbf{1_{AP\text{-}BA}}$ isomer which is present in small quantities in heptane solutions. These bleaches are accompanied at short delay times by the instantaneous appearance of broad, positive features shifted to lower wavenumber. These are consistent with earlier studies of hydrogenase model systems using TR-IR and are assignable to a combination of the short-lived MLCT excited state, vibrationally hot species formed by irradiation and tricarbonyl photoproducts created by the loss of a CO ligand, which has been shown to occur on sub-picosecond timescales.[13,19]

At intermediate pump-probe time delays (80 ps, Fig.18(a), red) the bleaches show some recovery while the transient absorptions decay via narrowing and blue shifting, a process consistent with vibrational cooling and relaxation of MLCT excited state and hot ground state features. This evolution reveals narrower photoproduct lines that originate from CO loss, these are red shifted in relation to the parent tetracarbonyl as would be expected on account of the increased electron back donation into carbonyl π^* orbitals that weakens the C=O bond strength reducing the force constant k and leading to a decrease of the CO oscillator frequency.

The traces at 425 ps (Fig.18(a), green) show further decrease in the amplitude of the bleaches assignable to geminate recombination and recovery of the parent molecule. The bleach recovery is greater than 75% of the initial amplitude at this time delay suggesting a dominant geminate recombination process in heptane. The photoproduct peaks present in the 3 ps and 80 ps traces have virtually disappeared by 425 ps and have been replaced by two new peaks at 1922 and 1990 cm^{-1}. These features are assignable by comparison with the FTIR spectra and DFT calculations discussed above to formation of the $\mathbf{1}_{\mathbf{AP\text{-}BA}}$ isomer suggesting that the isomerisation equilibrium position is shifted somewhat by irradiation and CO photolysis. The positive peaks due to the $\mathbf{1}_{\mathbf{AP\text{-}BA}}$ isomeric form and the residual parent bleaches showed evidence of a subsequent nanosecond timescale recovery process with similar kinetics suggesting a slow recovery towards the thermal equilibrium position. In heptane solution no further positive peaks assignable to solvent coordination of the vacant site left by the CO ligand were observed, in contrast to the hexacarbonyl derivative of **1**, which showed a significant fraction of solvent adduct formation.

The data obtained in MeOH (Fig.18(b)) and MeCN (Fig.18(c)) solutions are broadly similar to those in heptane and can be assigned to similar processes and species. In contrast to heptane however, both MeOH and MeCN solutions gave rise to further non-vanishing positive peaks in the 1840-1880 cm^{-1} region, suggestive of a competition between geminate recombination and solvent substitution leading to tricarbonyl derivatives of general formula $(\mu\text{-}S(CH_2)_3S)Fe_2(CO)_3(PMe_3)_2(Solv)$ (Solv= MeCN, MeOH). The position of these bands to the red of the parent molecule and peaks due to the tricarbonyl intermediate are entirely consistent with previous studies.[13,19]

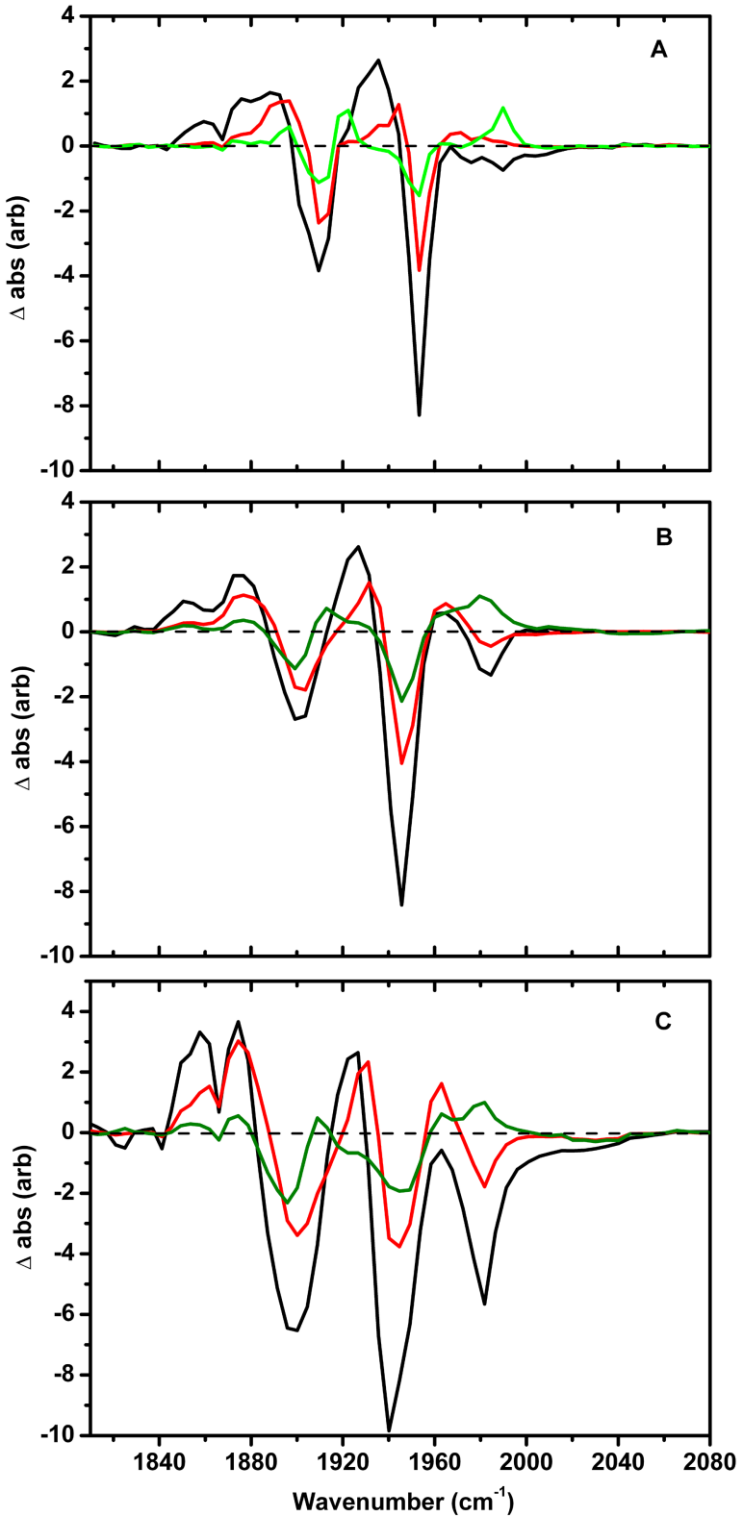

Figure 18. Normalized magic angle TR-IR spectra of **1** in n-heptane (A), MeOH (B) and MeCN (C) at 3 ps (black), 80 ps (red) and 428 ps (green) pump-probe delay times.

3.2.3. DFT simulations

DFT calculations were performed to confirm the assignment of TRIR spectral features to intermediates and solvent substituted photoproducts. Separate calculations were devoted to the evaluation of energy barriers for isomerisation of transient tricarbonyl species allowing ore complete assignment of the reaction mechanism. The results of infrared spectral simulations are shown in Figure 19. The simulations predict a general down-shift of the ν_{CO} bands of all CO ligand deficient species either with a vacancy, like in the transient $Fe_2(pdt)(CO)_3(PMe_3)_2$, or in the solvent adduct $Fe_2(pdt)(CO)_3(Solv)(PMe_3)_2$ Solv = MeOH or MeCN, in relation to those of the parent molecule. It is also noted, though not shown, that loss of a trimethylphosphine ligand was simulated via DFT calculations and was predicted to cause a large blue shift of the photoproduct bands in comparison to the parent. The latter clearly indicates that the results of 355 nm excitation are only assignable to species arising from CO loss. In the case of heptane solutions, the formation of a coordinatively bonded solvent product could not be achieved. To estimate the solvent adduct stabilisation energy one of the stable transient configurations was selected which originated from the ***trans*-1$_{\mathbf{BA\text{-}BA}}$** isomer with one of apical CO ligands removed. The energies for the transient and solvent alone and the BSSE corrected energy for the solvent adduct of these two molecules were calculated.[46] The stabilisation energy was expressed according following equation

$$\Delta E_{stab} = E_{adduct} - \left(E_{transient} + E_{solvent}\right) \quad (26)$$

The calculations were performed with propane as a solvent molecule instead of heptane to improve geometry optimisation performance and reduce computational cost. The calculated stabilisation energy is negligible with value around 0.5 kJ/mol suggesting a minimal energy gain in the formation of a solvent adduct. The DFT simulated infrared spectrum of a solvent adduct with a propane molecule, is characterised by three transitions broadly matching those for the other solvent products but with no corresponding lines on TR-IR spectrum at 440ps (Fig.18a) and longer timescales.

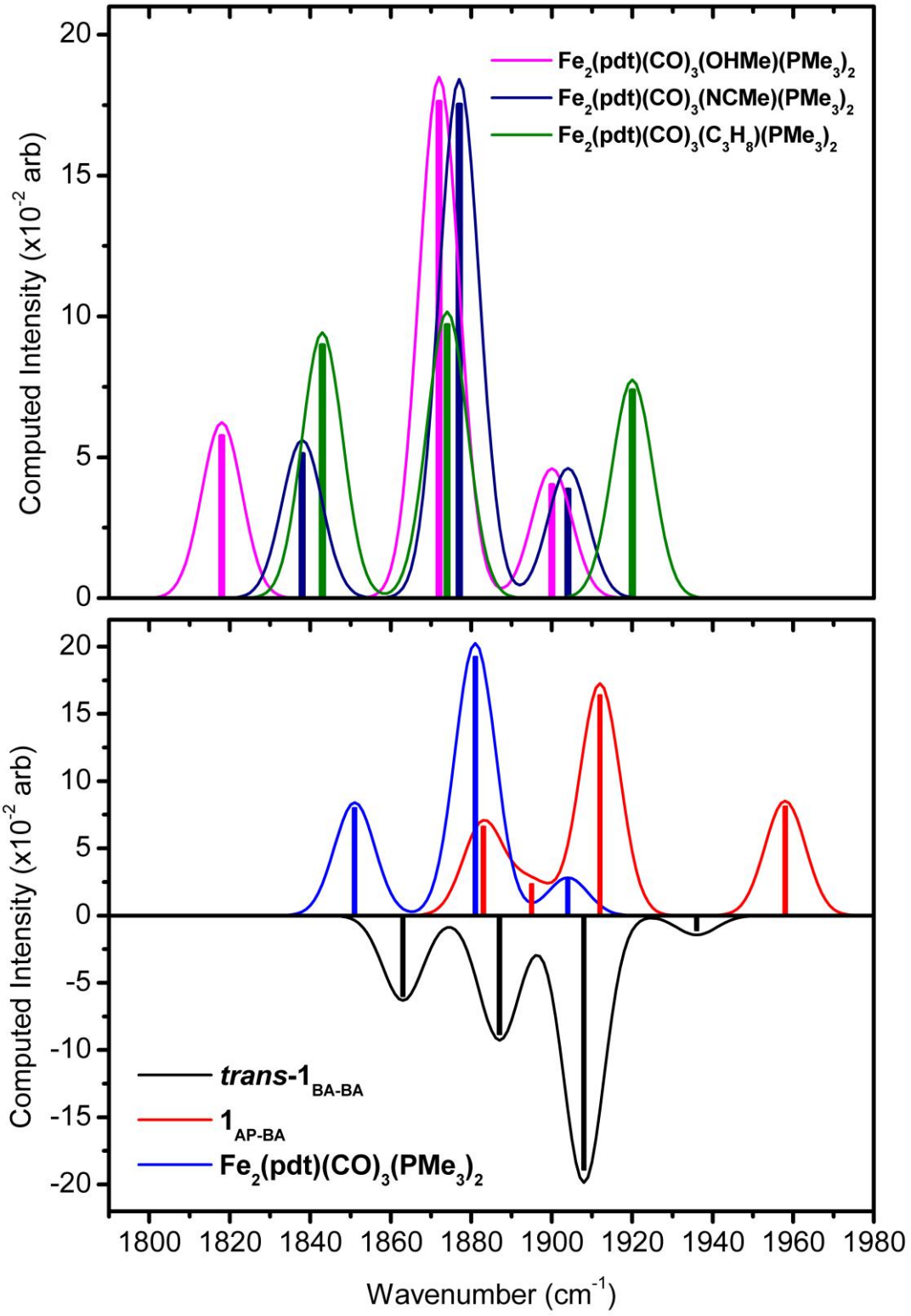

Figure 19. The DFT calculated infrared spectra of **trans-1$_{BA-BA}$**, **1$_{AP-BA}$**, transient $Fe_2(pdt)(CO)_3(PMe_3)_2$ and $Fe_2(pdt)(CO)_3(HOMe)(PMe_3)_2$, $Fe_2(pdt)(CO)_3(NCMe)(PMe_3)_2$, $Fe_2(pdt)(CO)_3(C_3H_8)(PMe_3)_2$ photoproducts.

The absence of evidence for solvent adduct formation for **1** in heptane stands in opposition to the results for the hexacarbonyl derivative where a solvent adduct is formed in detectable amounts, further underlining the differences in model compound reactivity induced by iron centre ligand environment modifications.[13,19,20,35]

In order to explore the possible mechanism of photolysis-induced isomerisation, a series of DFT simulations were performed concerning transient species reorganisation. The results of these simulations are summarised in Figure 20. UV-irradiation of **1** results in loss of CO ligand leading to an asymmetrical tricarbonyl species (Fig. 20(A)) maintaining the geometry of the parent molecule. Any attempt to move the bulky PMe_3 ligand toward the apical–basal configuration as in $\mathbf{1}_{\mathbf{AP\text{-}BA}}$, led to the formation of a coordinatively saturated bridged species (Fig. 20(C)) via a 45^o rotation of the FeL_3 unit, rotating one of CO ligand into an equatorial position. DFT calculations estimate the transition state (Fig. 20(B)) energy for this process to be about 32 kJ/mol above the energy of the asymmetrical transient (Fig. 20(A)) while the bridged species (Fig. 20(C)) has a formation energy that is about 35.7 kJ/mol lower than any asymmetrical transient configuration. Continued rotation of FeL_3 unit over the subsequent energy barrier leads to the desired apical–basal configuration (Fig. 20(D)) however due to the high initial activation energy required to attain the bridged form it is very unlikely that the overall process will be fast enough to fall within the time window limited by geminate recombination. An alternative isomerisation route is through the relocation of a PMe_3 ligand of the FeL_2 unit into an apical position forming an asymmetrical transient (Fig. 20(E)). This was explored in DFT simulations however the generally small energy changes associated with the angular motion of ligands prevented geometry optimisation convergence. In summary, the calculations of the energy barriers for the rearrangement of the unsaturated tricarbonyl species indicate a large activation barrier for the discussed pathways except for the one invoking permutation of the PMe_3 ligand within the FeL_2 unit. Such rearrangement faces the smallest sterical strain owing to a diminished coordination number of the FeL_2 unit and produces no additional predicted spectral lines that would be expected if the reaction went through a bridged transient (Fig. 20(E)) intermediate.

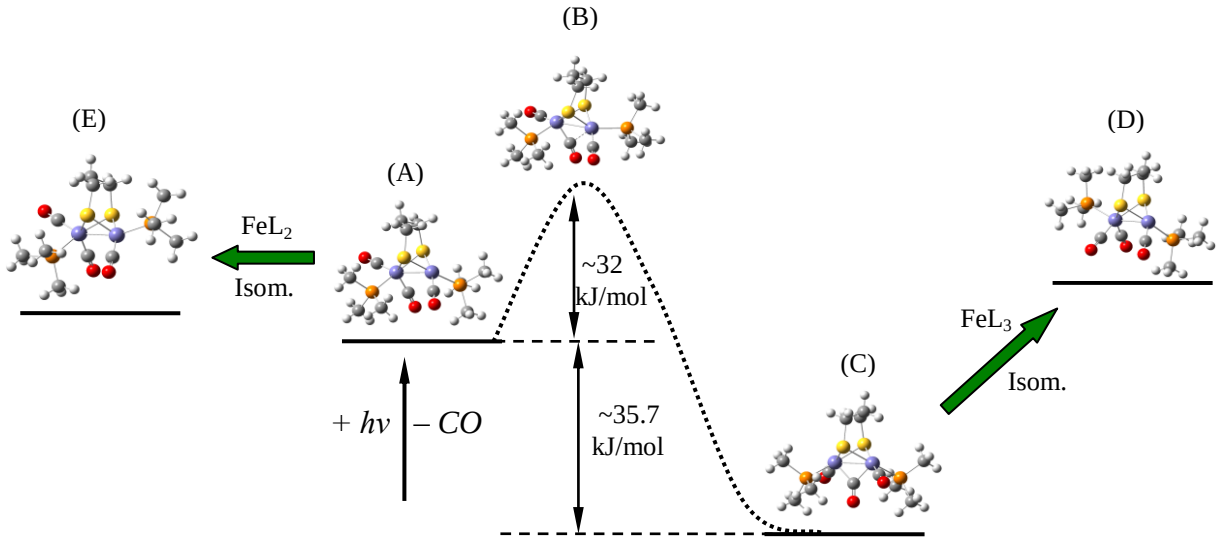

Figure 20. The DFT calculated energies of **trans-1$_{BA-BA}$** derived transient $Fe_2(pdt)(CO)_3(PMe_3)_2$ isomerisation.

3.2.4. Kinetics of Time-Resolved IR spectra

In order to quantify the timescales of the observed processes, the TRIR difference spectra were fit to a series of Gaussian lineshape functions over all the available time slices simultaneously using the global analysis approach described above. The time dependence of selected TRIR features obtained from the amplitudes of the Gaussian functions used in the global fitting for each of the solvents are presented in Figure 21 (a)-(c). The dynamics were obtained by fitting Gaussian peak amplitudes to a series of single or bi-exponential decay functions. The results are collated in Table 1. The overlap of the various broad positive and negative features often led to difficulties in isolating individual peak dynamics but general patterns clearly emerge.

In the case of the parent bleaches, these displayed a biexponential recovery (black traces in Fig. 21 and Table 1) with the faster decay timescale in the 15-40 ps region and the longer timescale in the 100-200 ps range depending on the solvent. By contrast the broad low frequency features observed at early times decayed with single exponential dynamics in the 15-40 ps range (red traces in Fig. 21).

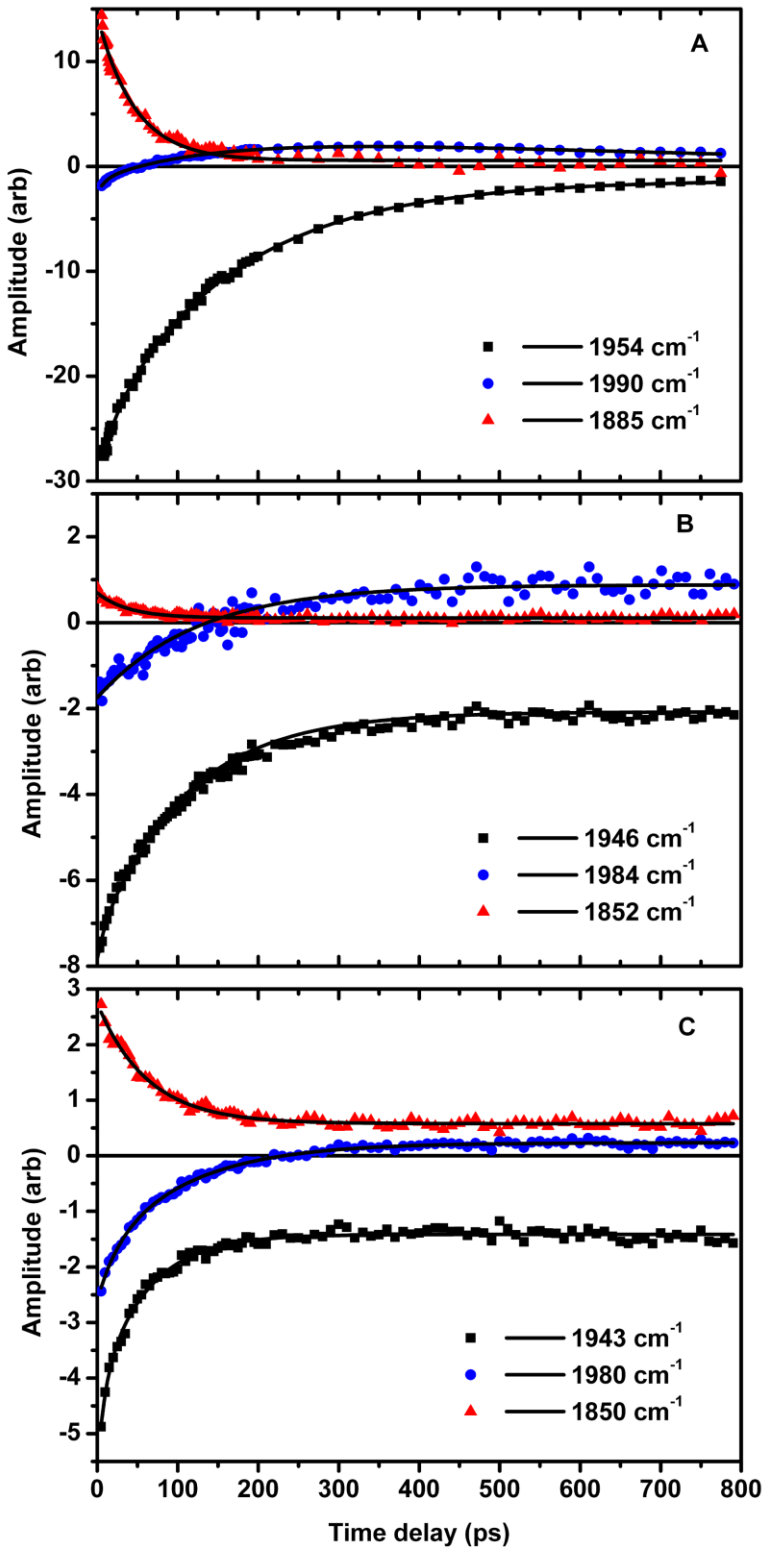

Figure 21. Time dependencies of Gaussian peak lineshapes from fitting results for **1** in n-heptane (A), MeOH (B), MeCN (C). Black indicates a main parent bleach recovery kinetics, blue shows dynamics of high frequency $\mathbf{1}_{\mathbf{AP\text{-}BA}}$ isomer peak, red shows the dynamics of a lowest frequency positive peak.

Table 1. Results of fitting temporal dependencies of Gaussian peak amplitudes of **1** solution in n-heptane, MeOH and MeCN solutions derived from fitting of TR-IR spectra. Life times τ_1 and τ_2 represent exponential decays while τ_R represent exponential rise.

Solvent	Peak position [cm^{-1}]	Peak width [cm^{-1}]	τ_R [ps]	τ_1 [ps]	τ_2 [ps]	Line Assignment
heptane	1857	10.5		20		MLCT decay and vibrational cooling
	1885	19		38		MLCT decay and vibrational cooling
	1897	15	23	197		Tricarbonyl cooling and geminate recombination
	1909	8		51*	400*	parent bleach
	1919	9	171	>1ns		Isomerisation
	1936	17		38		MLCT decay and vibrational cooling
	1948	11	23	150		Tricarbonyl cooling and geminate recombination
	1954	7		26	166	parent bleach
	1990	9	170	>1ns		Isomerisation
MeOH	1852	15		38		MLCT decay and vibrational cooling
	1882	16	16	133		Tricarbonyl cooling and geminate recombination
	1904	12		32*	265*	parent bleach
	1910	14	152			Isomerisation
	1930	14		45		MLCT decay and vibrational cooling
	1938	14	28	139		Tricarbonyl cooling and geminate recombination
	1946	10		12	114	parent bleach
	1984	13	138			Isomerisation
MeCN	1850	13.5		65		MLCT decay and vibrational cooling
	1872	13.5	21	115		Tricarbonyl cooling and geminate recombination
	1899	22		22	195*	parent bleach
	1908	26	112			Isomerisation
	1919	15		60		MLCT decay and vibrational cooling
	1930	10	22	105		Tricarbonyl cooling and geminate recombination
	1943	14		28	95	parent bleach
	1980	12	93			Isomerisation

* dynamics of lowest frequency bleach is corrupted by overlap of ***trans*-1$_{BA\text{-}BA}$** and **1$_{AP\text{-}BA}$** isomer transitions.

This is consistent with assignment of this timescale to the relaxation of the MLCT excited state and vibrational cooling (Table 1) and coincides with the narrowing and blue shifting of those features towards intermediate pump-probe time delays. The latter effect is seen in the fit by the 15-40 ps rise of narrower Gaussian peaks immediately to the red of the parent bleaches. Identified as cooling and geminate recombination in Table 1, these peaks are assignable to tricarbonyl species that become visible as cooling proceeds and which then decay with the 100-200 ps timescale as recombination proceeds. Finally, the photoproduct peaks (blue traces) due to the higher energy isomer were observed to show a rise time in the 100-200 ps time range followed by a nanosecond decay profile. It is noted that these peaks start from a negative value owing to the bleaching of the initial population of the $\mathbf{1}_{\mathbf{AP\text{-}BA}}$ isomer, which then recovers and crosses zero value changing from bleach to transient absorption as the experiment proceeds. The kinetics indicates a complex mechanism schematically presented in Figure 22.

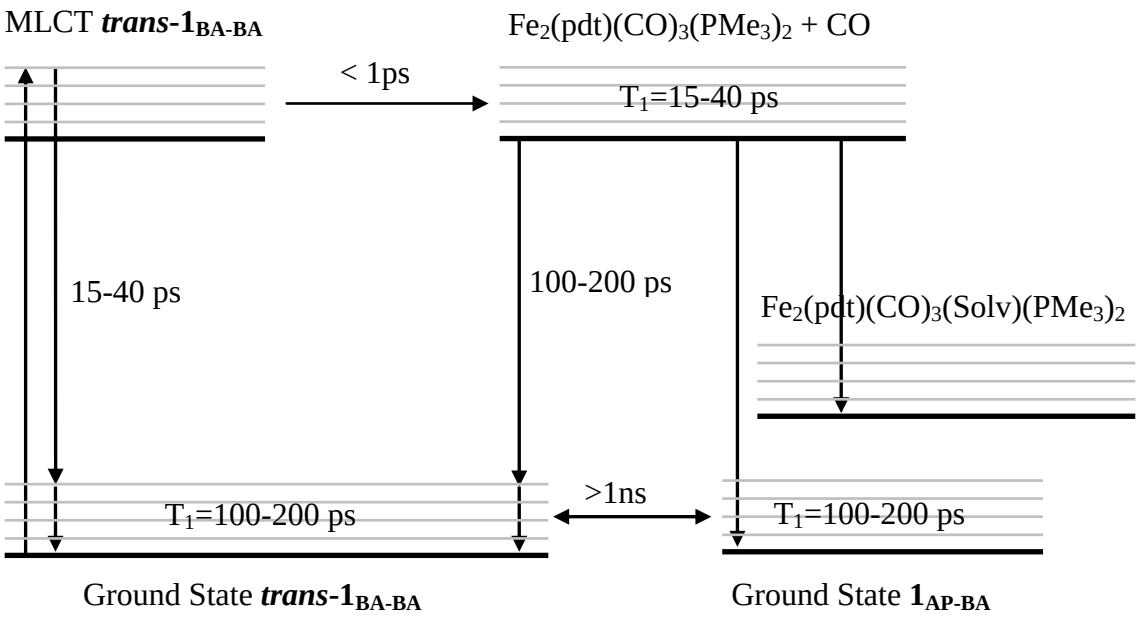

Figure 22. Diagram summarising processes and timescales following excitations of **1** at 350nm. The T_1 indicates vibrational relaxation timescales span for three different solvents used.

The MLCT excited-state relaxation and vibrational cooling of the transient species formed following photolysis proceeds rapidly within similar 15-40 ps timescale.

Subsequently the longer 100-200 ps timescale are associated with geminate recombination. The geminate recombination dynamics are observed in bleach recovery and in the growth of positive peaks due to the $\mathbf{1}_{\mathbf{AP\text{-}BA}}$ isomer. Such processes are indicative of parent molecule isomerisation on geminate recombination rather than the rearrangement of vibrationally hot species prior t recombination. The slight but significant decay of the $\mathbf{1}_{\mathbf{AP\text{-}BA}}$ isomer observed in heptane solution (Fig. 21(a)) suggests beyond picosecond timescale that re-equilibration of the isomer ratio to that observed before UV excitation occurs. The incomplete recovery of the bleaches in case of MeOH and MeCN solutions suggests the presence of long-lived species consistent with the formation of stable secondary solvent adduct photoproducts. The timescales for formation of these adducts are indistinguishable from those of vibrational cooling and this suggests that the solvent adducts form in a fashion that is competitive with geminate recombination. The three solvents show some differences in the observed timescales with the values obtained for cooling and recombination being somewhat shorter in MeOH and MeCN than in heptane.

3.3. Discussion

The results indicate that the photochemistry of **1** in solution shows several similarities with previous studies of the hexacarbonyl derivative. Indeed the observed timescales for cooling and relaxation on tens of ps alongside geminate recombination within 200 ps are in excellent agreement with prior work and suggest relatively little influence of the trimethylphosphine ligands on the dynamics following irradiation.[13,19,20] This is perhaps to be expected due to the fact that the relaxation and cooling are largely controlled by intramolecular processes determined by solute structure that is similar in the compared compounds. Similarly, geminate recombination as a function of the immediate solvent cage environment is expected to give consistent dynamics for related solute-solvent systems. Certain differences are observed however, perhaps most notably in relation to the formation of solvent adducts of **1** in MeOH and MeCN but not in heptane. In the case of the hexacarbonyl species, solvent adduct formation was observed in heptane indicating a change in the ligand chemistry arising from the substitution of CO for trimethylphosphine at two coordination sites. This is consistent with studies of protonation of **1** and the

hexacarbonyl that showed that former compound protonates readily in low pH conditions while the latter does not.[7,18,34] These observations suggest that the presence of the PMe_3 groups lead to a greater electron density localized on the bimetal centre that encourages protonation. The lower vibrational frequencies of the CO stretching transitions of **1** in comparison to the hexacarbonyl variant support this and it is also noticeable that the fraction of solvent adducts formed in MeCN and MeOH solutions was rather smaller than observed for the hexacarbonyl.[13,19] An alternative possibility is that steric factors at the metal centres prevent ligand association at the vacant coordination site. The PMe_3 species will be significantly larger than CO though this alone does not explain the relative propensities for solvent coordination. A third possibility in the involvement of an agostic interaction between the phosphine and the vacant site on the metal schematically depicted below.[52]

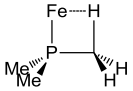

The observation of isomerisation at the Fe centres in **1** following CO photolysis is extremely interesting as it opens up the possibility to study the effects of interchange between the terminal groups at the Fe centre on the catalytic activity of hydrogenase models. It is not known whether geometrical isomerisation affects the natural hydrogenases but it is relevant for the majority of synthesized biomimetic compounds with heterogeneous Fe centre coordination shells. The implications of this data are that CO loss followed by geminate recombination changes the isomer ratio in favour of the $\mathbf{1_{AP\text{-}BA}}$ form in relation to the thermodynamic equilibrium at ambient temperature. The ultrafast nature of the isomerisation process excludes vibrationally hot parent molecule isomerisation since DFT calculations suggest that the barrier to this interconversion process is about 38 kJ/mol, consistent with much longer time scales. Another indicator that thermal re-equilibration is not occurring is the slow nanosecond recovery of the equilibrium concentration ratio suggesting that the thermal processes are by no means ultrafast. Initially, the indications appear to be that the less sterically crowded FeL_2 unit is flexible enough to drive intrinsic ultrafast interconversion of the ligand positions, even when one is a bulky PMe_3 ligand. DFT calculations of the transient $(\mu\text{-}S(CH_2)_3S)Fe_2(CO)_3(PMe_3)_2$ species have been performed in order to further understand the mechanism for ligand interconversion.

These show that the tricarbonyl species forms stable asymmetric structures with ligand geometries close to those observed in the parent molecule. Attempts to determine the energy barrier for ligand permutation consistently led to a CO bridged species $(\mu\text{-CO})Fe_2(pdt)(CO)_2(PMe_3)_2$ possessing a geometry similar to the hydrogenase active centre (Fig. 13). The CO bridged structures were on average 35.7 kJ/mol lower in energy than the most stable asymmetric forms but were separated from the asymmetrical configurations by an energy barrier of similar magnitude. While by no means conclusive, the large energy barrier to interconversion of the tricarbonyl transient alongside the lack of experimental evidence for a formation of bridged intermediate make it seem unlikely that the transient species undergo isomerisation prior to geminate recombination. The DFT simulations of angular motion of PMe_3 ligand within FeL_2 unit were inconclusive, leaving open the question of the activation barrier for the ligand permutation process. The high rate of recombination suggest that such isomerisation should be viewed as a bimolecular process where a CO molecule substitutes vacant site in transient forcing motion of other ligands into final positions. The similar timescales for geminate recombination and isomerisation product formation also suggest that the recombination event participates in the reorganisation. In such a process, the outcome is controlled by the mutual orientation of both the incoming CO and remaining monodentate ligands near the vacant site as neither of two molecules are static in solution. In fact the high anisotropy decay rates of 15-25 ps observed for the parent species indicate fast solute rotation leading to a randomisation of the CO ligand approach trajectory to the transient species. Since there is no evidence of spontaneous isomerisation of the transient isomerisation must be decided by the attack trajectory of the CO molecule on the less sterically hindered FeL_2 unit. In this mechanism the resulting ratio of isomers is determined by the probabilities of the attack configuration leading to $\mathbf{1}_{\mathbf{AP\text{-}BA}}$ and ***trans*-$\mathbf{1}_{\mathbf{BA\text{-}BA}}$** forms rather than the thermodynamic equilibrium isomer ratio. Parallel studies of **1** in gel matrix environment support the above hypothesis that rotational randomisation of the reaction geometry in the geminate recombination process is responsible for photo-triggered isomerisation of the parent molecule. In gel matrix experiments, the **1** solution in $MeOH/D_2O$ was mixed with Low Molecular Weight Hydrogelator (Fmoc-Leu-Leu).[53] The investigation of such

hydrogels shows strong evidence that **1** is encapsulated within the gel matrix in mostly hydrophobic pockets. The encapsulation has a pronounced effect on the compound stability and photochemistry. The major change though is that **1** in the gel showed no evidence of the isomerisation that was apparent in solution experiments. The absence of isomerisation simplifies the post-excitation relaxation process to one of straightforward geminate recombination and a competitive pathway of solvent substitution. The geminate recombination in a gel matrix system was found to be significantly faster than in solutions based on a similar solvent mixture. Those two effects can be rationalized by the existence of hydrophobic pockets hosting the metalcarbonyl solute. This environment hinders rotation of the tricarbonyl transient, blocking isomerisation according to the previously discussed bimolecular mechanism. By comparison, the intrinsic isomerisation via a bridged transient would be far less affected by this high 'viscosity' environment though this was not observed. The 'viscous' gel environment also promotes geminate recombination by slowing down escape of photogenerated fragments of parent molecule.

3.4. Conclusions

In summary we have employed time-resolved infrared spectroscopy to observe the primary and secondary photochemical processes of a hydrogenase enzyme-inspired model compound in polar and non-polar solvents. It has been determined that UV light induced excitation of MLCT bands leads to photodissociation of a CO ligand with relaxation and vibrational cooling processes occurring on tens of picoseconds timescales alongside geminate recombination on 100 ps timescales. Recombination is observed to cause isomerisation of the parent molecule resulting in a transient perturbation of the equilibrium position towards an energetically less-stable isomeric form of **1** in all solvents studied. Comparison of photodissociation experiments in different solvents further shows that in apolar heptane solution the tricarbonyl intermediate species undergoes almost complete geminate recombination within the experimental time window while in MeCN and MeOH coordination of a solvent molecule competes with recombination leading to semi-stable solvent adducts.

3.5. Further research perspectives

The ongoing gel matrix experiments support the hypothesis that the rotational randomisation of the reaction geometry affects the isomeric ratio in geminate recombination. Comparison of photodissociation experiments in different solvents indicates that in apolar n-heptane solution only a metastable intermediate is formed which undergoes almost complete geminate recombination within the experimental time window while in MeCN and MeOH coordination of solvent molecule competes with geminate recombination leading to tricarbonyl photoproducts.

Presented study constitutes a basis for further investigations of this compound that lie outside scope of this thesis. Experiments using the more advanced Transient-2D IR technique that expose vibrational couplings of photoproducts would allow better separation and identification of the infrared signatures of transient species and photoproducts. Similar Transient-2D IR spectroscopy measurements of gel matrix samples would improve understanding of reactivity changes imposed by the environment, supporting or excluding the proposed mechanism of isomerisation. Finally, the evidence of post recombination thermal equilibrium process requires extending our TR-IR study to nanosecond to microsecond timescales in order to probe the influence of the solute-solvent interaction on the rate of isomer ratio re-equilibration. The longer timescale TR-IR studies are of relevance to the practical aspects of hydrogenase mimics synthesis. The compound **1** exhibits significant affinity toward binding protons.[7,18,34] The proton binding to the Fe centre of hydrogenase and their mimics is speculated to be a crucial step in the dihydrogen formation reaction. Thus, longer timescale TR-IR studies of **1** solution with photoacid are a suitable tool to access dynamics and support establishing mechanisms of the proton binding reaction.

3.6. Acknowledgements

The author would like to acknowledge contributions of Pim W. J. M. Frederix in TR-IR measurements of **1** in solution and gel phase and of Dr. Spyros Kaziannis in expansion of in-house 2D-IR spectrometer capacity toward UV_{pump}-IR_{probe} experiments.

References:

(1) Wang, H.-Y.; Wang, W.-G.; Si, G.; Wang, F.; Tung, C.-H.; Wu, L.-Z. *Langmuir* **2011**, *26*, 9766.

(2) Brown, K. A.; Dayal, S.; Ai, X.; Rumbles, G.; King, P. W. *Journal of the American Chemical Society* **2011**, *132*, 9672.

(3) Streich, D.; Astuti, Y.; Orlandi, M.; Schwartz, L.; Lomoth, R.; Hammarström, L.; Ott, S. *Chemistry - A European Journal.* **2010**, *16*, 60.

(4) Probst, B.; Rodenberg, A.; Guttentag, M.; Hamm, P.; Alberto, R. *Inorganic Chemistry* **2010**, *49*, 6453.

(5) Greco, C.; Fantucci, P.; De Gioia, L.; Suarez-Bertoa, R.; Bruschi, M.; Talarmin, J.; Schollhammer, P. *Dalton Transactions* **2010**, *39*, 7320.

(6) Probst, B.; Kolano, C.; Hamm, P.; Alberto, R. *Inorganic Chemistry* **2009**, *48*, 1836.

(7) Artero, V.; Fontecave, M. *C. R. Chimie* **2008**, *11*, 926.

(8) Chong, D.; Georgakaki, I. P.; Mejia-Rodriguez, R.; Sanabria-Chinchilla, J.; Soriaga, M. P.; Darensbourg, M. Y. *Dalton Transactions* **2003**, 4158.

(9) Zhao, X.; Georgakaki, I. P.; Miller, M. L.; Yarbrough, J. C.; Darensbourg, M. Y. *Journal of the American Chemical Society* **2001**, *123*, 9710.

(10) Capon, J.-F.; Gloaguen, F.; Petillon, F. Y.; Schollhammer, P.; Talarmin, J. *Coordination Chemistry Review* **2009**, *253*, 1476.

(11) Tard, C.; Pickett, C. J. *Chemistry Review* **2009**, *109*, 2245.

(12) Gloaguen, F.; Lawrence, J. D.; Rauchfuss, T. B.; Benard, M.; Rohmer, M. M. *Inorganic Chemistry* **2002**, *41*, 6573.

(13) Ridley, A. R.; Stewart, A. I.; Adamczyk, K.; Ghosh, H. N.; Kerkeni, B. N.; Guo, Z. X.; Nibbering, E. T. J.; Pickett, C. J.; Hunt, N. T. *Inorganic Chemistry* **2008**, *47*, 7453.

(14) Song, L.-C.; Wang, L.-X.; Yin, B.-S.; Li, Y.-L.; Zhang, X.-G.; Zhang, Y.-W.; Luo, X.; Hu, Q.-M. *European Journal of Inorganic Chemistry* **2008**, 291.

(15) Stewart, A. I.; Clark, I. P.; Towrie, M.; Ibrahim, S. K.; Parker, A. W.; Pickett, C. J.; Hunt, N. T. *The Journal of Physical Chemistry. B* **2008**, *112*, 10023.

(16) Thomas, C. M.; Liu, T.; Hall, M. B.; Darensbourg, M. Y. *Inorganic Chemistry* **2008**, *47*, 7009.

(17) Galinato, M. G. I.; Whaley, C. M.; Lehnert, N. *Inorganic Chemistry* **2010**, *49*, 3201.

(18) Jablonskyte, A.; Wright, J. A.; Pickett, C. J. *Dalton Transactions* **2010**, *39*, 3026.

(19) Kaziannis, S.; Santabarbara, S.; Wright, J. A.; Greetham, G. M.; Towrie, M.; Parker, A. W.; Pickett, C. J.; Hunt, N. T. *Journal of Physical Chemistry B* **2010**, *114*, 15370.

(20) Stewart, A. I.; Wright, J. A.; Greetham, G. M.; Kaziannis, S.; Santabarbara, S.; Towrie, M.; Parker, A. W.; Pickett, C. J.; Hunt, N. T. *Inorganic Chemistry* **2010**, *49*, 9563.

(21) Kaziannis, S.; Wright, J. A.; Candelaresi, M.; Kania, R.; Greetham, G. M.; Parker, A. W.; Pickett, C. J.; Hunt, N. T. *Physical Chemistry Chemical Physics: PCCP* **2011**, *13*, 10295.

(22) Yu, L.; Greco, C.; Bruschi, M.; Ryde, U.; De Gioia, L.; Reiher, M. *Inorganic Chemistry* **2011**, *50*, 3888.

(23) Song, L.-C.; Gai, B.; Wang, H.-T.; Hu, Q.-M. *Journal of Inorganic Biochemistry* **2009**, *103*, 805.

(24) Song, L.-C.; Luo, X.; Wang, Y.-Z.; Gai, B.; Hu, Q.-M. *Journal of Organometallic Chemistry* **2009**, *694*, 103.

(25) Apfel, U.-P.; Halpin, Y.; Görls, H.; Vos, J. G.; Weigand, W. *European Journal of Inorganic Chemistry* **2011**, 581.

(26) Apfel, U.-P.; Kowol, C. R.; Kloss, F.; Gourls, H.; Keppler, B. K.; Weigand, W. *Journal of Organometallic Chemistry* **2011**, *696*, 1084.

(27) Durgaprasad, G.; Bolligarla, R.; Das, S. K. *Journal of Organometallic Chemistry* **2011**, *696*, 3097.

(28) Harb, M. K.; Apfel, U.-P.; Sakamoto, T.; El-Khateeb, M.; Weigand, W. *European Journal of Inorganic Chemistry* **2011**, 986.

(29) Lounissi, S.; Capon, J.-F.; Gloaguen, F.; Matoussi, F.; Petillon, F. Y.; Schollhammer, P.; Talarmin, J. *Chemical Communnications* **2011**, *47*, 878.

(30) Singleton, M. L.; Crouthers, D. J.; Duttweiler, R. P.; Reibenspies, J. H.; Darensbourg, M. Y. *Inorganic Chemistry* **2011**, *50*, 5015.

(31) Tang, Y.; Wei, Z.; Zhong, W.; Liu, X. *European Journal of Inorganic Chemistry* **2011**, 1112.

(32) Wright, J. A.; Pickett, C. J. *Chemical Communnications* **2009**, 5719.

(33) Erdem, Ö. F.; Schwartz, L.; Stein, M.; Silakov, A.; Kaur-Ghumaan, S.; Huang, P.; Ott, S.; Reijerse, E. J.; Lubitz, W. *Angewandte Chemie Int. Ed.* **2011**, *50*, 1439.

(34) Jablonskytė, A.; Wright, J. A.; Pickett, C. J. *European Journal of Inorganic Chemistry* **2011**, 1033.

(35) Bonner, G. M.; Ridley, A. R.; Ibrahim, S. K.; Pickett, C. J.; Hunt, N. T. *Faraday Discussions* **2010**, *145*, 429.

(36) Gaussian 03 Revision B.03, M. J. F., G. W. Trucks, H. B. Schlegel, G. E. Scuseria, M. A. Robb, J. R. Cheeseman, J. A. Montgomery, Jr., T. Vreven, K. N. Kudin, J. C. Burant, J. M. Millam, S. S. Iyengar, J. Tomasi, V. Barone, B. Mennucci, M. Cossi, G. Scalmani, N. Rega, G. A. Petersson, H. Nakatsuji, M. Hada, M. Ehara, K. Toyota, R. Fukuda, J. Hasegawa, M. Ishida, T. Nakajima, Y. Honda, O. Kitao, H. Nakai, M. Klene, X. Li, J. E. Knox, H. P. Hratchian, J. B. Cross, C. Adamo, J. Jaramillo, R. Gomperts, R. E. Stratmann, O. Yazyev, A. J. Austin, R. Cammi, C. Pomelli, J. W. Ochterski, P. Y. Ayala, K. Morokuma, G. A. Voth, P. Salvador, J. J. Dannenberg, V. G. Zakrzewski, S. Dapprich, A. D. Daniels, M. C. Strain, O. Farkas, D. K. Malick, A. D. Rabuck, K. Raghavachari, J. B. Foresman, J. V. Ortiz, Q. Cui, A. G. Baboul, S. Clifford, J. Cioslowski, B. B. Stefanov, G. Liu, A. Liashenko, P. Piskorz, I. Komaromi, R. L. Martin, D. J. Fox, T. Keith, M. A. Al-Laham, C. Y. Peng, A. Nanayakkara, M. Challacombe, P. M. W. Gill, B. Johnson, W. Chen, M. W. Wong, C. Gonzalez, and J. A. Pople, **2003**.

(37) Lee, C.; Yang, W.; Parr, R. G. *Physical Review B* **1988**, *37*, 785.

(38) Miehlich, B.; Savin, A.; Stoll, H.; Preuss, H. *Chemical Physics Letters* **1989**, *157*, 200.

(39) Becke, A. *Journal of Chemical Physics* **1993**, *98*, 5648.

(40) Dunning Jr., T. H.; Hay, P. J. In *Modern Theoretical Chemistry*; III, H. F. S., Ed.; Plenum: New York, **1976**; Vol. 3, p 1.

(41) Hay, P. J.; Wadt, W. R. *Ab initio effective core potentials for molecular calculations. Potentials for the transition metal atoms Sc to Hg*; AIP, **1985**; Vol. 82.

(42) Hay, P. J.; Wadt, W. R. *Ab initio effective core potentials for molecular calculations. Potentials for K to Au including the outermost core orbitals*; AIP, **1985**; Vol. 82.

(43) Wadt, W. R.; Hay, P. J. *Ab initio effective core potentials for molecular calculations. Potentials for main group elements Na to Bi*; AIP, **1985**; Vol. 82.

(44) Feng, X.; Gu, J.; Xie, Y.; King, R. B.; Schaefer, H. F. *Journal of Chemical Theory and Computations* **2007**, *3*, 1580.

(45) Tye, J. W.; Darensbourg, M. Y.; Hall, M. B. *Journal of Computation Chemistry* **2006**, *27*, 1454.

(46) Persson, B. J.; Taylor, P. R. *Theoretical Chemistry Accounts: Theory, Computation, and Modeling (Theoretica Chimica Acta)* **2003**, *110*, 211.

(47) Peng, C.; Schlegel, H. B. *Israel Journal of Chemistry* **1994**, *33*, 449.

(48) Peng, C.; Ayala, P. Y.; Schlegel, H. B.; Frisch, M. J. *Journal of Computation Chemistry* **1996**, *17*, 49.

(49) Hunt, N. T.; Turner, A. R.; Wynne, K. *The Journal of Physical Chemistry B* **2005**, *109*, 19008.

(50) Kania, R.; Stewart, A. I.; Clark, I. P.; Greetham, G. M.; Parker, A. W.; Towrie, M.; Hunt, N. T. *Physical Chemistry Chemical Physics: PCCP* **2010**, *12*, 1051.

(51) Zheng, J.; Kwak, K.; Fayer, M. D. *Accounts of Chemical Research* **2007**, *40*, 75.

(52) Sassmannshausen, J. *Dalton Transactions* **2012**, 1477.

(53) Frederix, P. W. J. M.; Kania, R.; Wright, J. A.; Lamprou, D. A.; Ulijn, R.; Pickett, C. J.; Hunt, N. T. *Dalton Transactions* **2012**, 13112.

4. The time-resolved infrared spectroscopy studies of photochemistry and ultrafast fluxionality of Fe_3CO_{12} in solution.

The development of 2D-IR has opened up new frontiers in the area of molecular dynamics in solution. The existing techniques for studying dynamics in solution were either limited to the nanosecond timescale like NMR techniques[1-9] or as ultrafast UV_{pump}-IR_{probe} spectroscopy designed for studying up to sub-picosecond timescale photochemistry and excited state dynamics.[10-21] The new 2D-IR spectroscopy method bridged this gap enabling the study of ultrafast molecular dynamics of solutions at equilibrium. Since birth the of 2D-IR spectroscopy it has been proven to be an excellent tool to study hydrogen bond dynamics in non-polar[22-26] and polar solutions,[27-34] the conformational dynamics of biologically important macromolecules like proteins,[35-38] and the geometrical interconversion dynamics of coordination compounds including fluxional dynamics.[1-5,39,40] Unlike intermolecular and protein conformational dynamics which may be studied with other ultrafast spectroscopic techniques like time-resolved Optical Kerr Effect,[33,41-48] picosecond timescale chemical isomerisation dynamics are molecular geometry altering processes with no associated bond rearrangement. Such processes require ultrafast and molecular symmetry sensitive spectroscopic methods like 2D-IR spectroscopy. Although the 2D-IR technique is perfectly suited for investigating geometrical isomerisation and fluxional dynamics in metalcarbonyls and related systems the subject as such received much less attention than hydrogen bond dynamics.

Metalcarbonyls have proven to be effective catalysts for a variety of organic reactions[49-58] and have been extensively researched over the last few decades. Most efforts were devoted to the development of better homo- and hetero-geneous catalysts linked with the characterisation of structure and the origins of catalytic activity. The elucidation of the hydrogenase enzyme structure mentioned in the previous chapter brought renewed interest in metalcarbonyl catalysts and particularly hydrogenase mimics as a key part of future sustainable systems for hydrogen fuel production.[20,55,56,59-67] Studies of metalcarbonyl molecules frequently encountered

geometrical isomerisation dynamics in solution which were commonly investigated by NMR techniques.[7-9] More recently, the measurement of ultrafast fluxional behaviour was demonstrated for the first time for $Fe(CO)_5$ solutions in heptane using double-resonance 2D-IR spectroscopy.[68] The results indicated that this simple carbonyl complex swaps CO ligands between coordination sites on timescales of 8 ps, a value equivalent to the average time spent by a CO ligand in a particular coordination site. This phenomenon is of crucial importance to the chemistry of coordination compounds in general and catalysis in particular as it shows the dynamic nature of coordination compounds and exposes the mechanism of ligand exchange. This work has inspired the author to further exploration of ultrafast geometrical isomerisation dynamics in complex metalcarbonyl systems in pursuit of fluxional dynamics and other isomerisation mechanisms.

Preliminary DFT simulations of $Fe_3(CO)_{12}$ (**2**) indicated the presence of two isomeric forms with one facing an activation barrier of only ~11 kJ/mol which compares well with estimated ~10 kJ/mol for ligand exchange in $Fe(CO)_5$. If the reaction energetics picture implied by DFT calculations is correct then the 2D-IR spectrum should reveal time-resolved off-diagonal peaks related to the isomerisation process. Major difference between $Fe(CO)_5$ and $Fe_3(CO)_{12}$ is that, in the latter case, isomerisation is related to bridging carbonyl ligand configurations. Still, the process of bridging carbonyl rearrangement is driven by the ultrafast exchange of CO ligands between coordination sites, the process which determines the ultrafast fluxional behaviour of the $Fe(CO)_5$ system.

Since many metalcarbonyls are used as photocatalysts in chemical reactions it would be informative to study the ultrafast photochemistry and excited state dynamics using TR-IR spectroscopy to augment this isomerisation dynamics research. It is particularly important since there is general lack of systematic TR-IR spectroscopy studies of photochemistry of **2** in solution. By comparison, the thorough TR-IR studies of $Fe(CO)_5$ solutions in heptane showed rich photochemistry particularly on nanosecond and longer timescales.[16] This work revealed an unusual mechanism where UV radiation excitation may result in a double photodissociation $Fe(CO)_3$ transient apart from the expected single CO ligand photodissociation process. The latter tetracarbonyl transient undergoes regular geminate recombination

or stable solvent adduct formation. The photoproduct $Fe(CO)_4$(hept) exists in a single geometrical configuration and shows no geometrical isomerisation process. Additionally evidence of photoinduced ultrafast isomerisation of a hydrogenase mimic presented in a previous chapter clearly showed usefulness of UV_{pump}-IR_{probe} techniques for detecting and investigating isomerisation dynamics. In the hydrogenase mimic TR-IR measurements, UV light induced CO ligand photodissociation shifted the ratio of isomeric forms enhancing weaker spectral features of higher energy isomer and exposing slower re-equilibration dynamics.

4.1. Experimental

Compound $Fe_3(CO)_{12}$ (**2**) and n-heptane were obtained from Sigma-Aldrich and used without further purification. Since **2** exhibits moderate moisture-sensitivity, the solvent was dried over CaH_2 and purged with N_2. The working solutions were freshly prepared in a protective atmosphere (Glovebox) and additionally purged with N_2 prior to use. For FT-IR and 2D-IR measurements, the samples were held in airtight cells (Harrick Scientific) consisting of a pair of CaF_2 windows separated by a 200μm thickness PTFE spacer while for TRIR studies the cell content was continuously refreshed by closed-loop circulation with bulk solution held in a nitrogen-filled reservoir. Additionally the sample cell was rastered in two dimensions to prevent window damage. The concentration of the solutions was adjusted to yield the desired main peak optical density around 0.35 in the carbonyl ligand stretching mode (ν_{CO}) region, which corresponded to an optical density at the UV pump frequency (355 nm) saturating the UV-Vis spectrometer detection system.

Steady state FTIR spectra were recorded on a Bruker Vertex 70 spectrometer in standard cell while temperature dependent measurements were performed in a thermostatically controlled cell (Harrick Scientific model TFC-525-3) accurate to ±1 K. The FT-IR spectroscopy measurements of the isomerisation kinetics of **2** were performed on freshly prepared samples by a constant-interval repeated spectrum scan facilitated by the Opus® software suite. Sample preparation accounts for an average "dead" time of 8 minutes between adding solvent and starting the registration of infrared spectra.

4.1.1. Time-resolved infrared spectrometer

The time-resolved infrared spectroscopy measurements were performed with the Strathclyde spectrometer using the double-resonance 2D-IR setup and the newly developed UV-Vis pump path for TR-IR measurements. Both types of time-resolved infrared spectroscopy experiments use a pump-probe configuration with a probe path and one of two available pump beam paths. The TRIR experiments utilize an UV-Vis pump while double-resonance 2D-IR experiments use a narrow bandwidth mid-infrared pump.

The spectrometer is powered by a regeneratively amplified Ti:Sapphire laser system (Coherent) producing 35 fs duration pulses centred at 800 nm with a repetition rate of 1kHz. The laser system radiation was downconverted by a combination of optical parametric amplifier with difference frequency generator to produce a mid-infrared frequency pulsetrain centred near 2047 cm^{-1} with a bandwidth of >200 cm^{-1}. Part of the laser system output was upconverted by a combination of an optical parametric amplifier with second harmonic generating crystals to produce UV frequency radiation with a centre wavelength of λ = 355 nm obtained through 4^{th} harmonic generation.

The double-resonance 2D-IR spectrometer optical assembly splits the mid-infrared frequency radiation into two beams: a probe and pump bearing 10% and 90% of overall energy respectively. For the 2D-IR experiments the pump beam bandwidth profile was shaped by the grating-based pulseshaping module discussed earlier producing ca. 10 cm^{-1} bandwidth pump pulses with a frequency scan range of 1940-2080 cm^{-1}. The pump pulse width roughly matched the linewidth of the FT-IR spectral features of **2**, providing the optimum pump axis resolution for the 2D-IR measurements.[69] The pump-probe time delay was controlled by an optical delay line located in the probe beam path. The polarization of the pump pulse train was controlled by a half-wave plate and polariser combination. To facilitate collection of pump on-pump off difference spectra, a chopper operating at half the laser repetition rate (500 Hz) was used to modulate pump pulse train. For detection, the transmitted probe radiation was dispersed on a monochromator grating and recorded using liquid nitrogen cooled 64-element HgCdTe array. The probe radiation spectral and temporal resolution obtained from this apparatus was ~ 4 cm^{-1} and 150 fs respectively.

The TR-IR experiments used the shared mid-infrared probe path described above and the newly constructed UV-Vis optical patch containing an optical modulator, additional optical delay line and a half-wave plate/polariser pair for controlling the pump radiation polarisation. The UV-Vis pump-probe delay times could be measured up to 2ns. In all experiments the pump -probe polarisation was set to the magic angle to remove the effects of molecular rotation from the signals.

4.1.2. Data Analysis

The data analysis of TR-IR and 2D-IR kinetic traces was performed using the global analysis fit of multiple spectra datasets to Eq. 25 (p. 69) as demonstrated in the previous chapter.

4.1.3. Density Functional Theory calculations

All DFT calculations were carried out using the Gaussian 03 package using the functionals, basis sets and optimization algorithms previously discussed.[70-81] Due to the weak interaction of the solvent with the transient molecule in the adduct, estimating adduct formation energy required correction for Basis Set Superposition Error.[82] No other scaling and correction factors were applied.

4.2. Results

4.2.1. Steady state FT-IR spectroscopy

The infrared absorption spectrum of **2** in n-heptane solution is shown in Figure 23a. When dissolved, **2** displays two intense bands at 2024 and 2047 cm^{-1} alongside a third, much weaker, transition at 2002 cm^{-1}. The absorption lines protrude from a very broad dome shaped feature extending over 50 cm^{-1} around the central line (2024 cm^{-1}). The FWHM of the peaks of the narrow transitions was about 4-5 cm^{-1} while the dome shaped feature was estimated to be 27 cm^{-1}. The structural data indicated that, in solid state, **2** exists in an asymmetric form with a double CO bridge linking one edge of the Fe3 triangle.[83] However DFT simulated infrared spectra show (Fig. 23b) two major lines of comparable intensity associated with this form along with several (~100 times) weaker features forming a red-side elevated

background. The presence of a third, weaker but distinctive line suggests the presence of a second geometrical form of **2** in solution.

To work out plausible stable geometrical configurations of **2**, DFT simulations were employed. Calculations have shown that 33.5 kJ/mol above the most stable double bridged $\mathbf{2_{BB}}$ isomer exists a triple bridged $\mathbf{2_{BBB}}$ form. The $\mathbf{2_{BBB}}$ isomer exhibits a highly symmetric structure (D_{3h}) and a similar infrared spectrum with two major lines as shown in Figure 23b. The DFT predicted infrared spectrum of both isomers (Fig. 23(b)) reinforces previous assignment of the FT-IR spectra**.** The presence of three distinctive infrared spectral features implies a coincidence of $\mathbf{2_{BB}}$ and $\mathbf{2_{BBB}}$ isomer spectral lines, consistent with the blue shift of $\mathbf{2_{BB}}$ transitions. It is widely accepted that the vibrational frequencies predicted by DFT methods are expected to show errors in relation to the absolute experimental frequencies, though the overall patterns and relative line positions have generally been found to be in good agreement with experiment when using this combination of functional and basis set.[17,80,81,84-85]

Further support for this isomeric equilibrium was obtained from the thermal dependence of the FT-IR spectra of **2** in heptane presented in Figure 23c. Series of spectra show that increasing temperature leads to a decrease in the intensity of the two main ν_{CO} peaks and a concomitant gain in the intensity of the 2002 cm^{-1} peak as expected for a thermal redistribution of isomeric form concentrations. The central feature at 2024 cm^{-1} exhibits slight frequency drift ~1 cm^{-1} correlated with the temperature rise suggesting the coincidence of spectral lines of both isomers.

The significant (33.5 kJ/mol) estimated energy barrier for isomerisation of $\mathbf{2_{BB}}$ into $\mathbf{2_{BBB}}$ form may be expected to give rise to slow re-equilibration kinetics following the dissolution of the pure $\mathbf{2_{BB}}$ isomer found in the solid state. A series of ν_{CO} region FT-IR spectra obtained for a freshly prepared solution of **2** recorded with a constant time interval is shown in Figure 24. In the initial spectrum only two features characteristic of the $\mathbf{2_{BB}}$ form are present with the $\mathbf{2_{BBB}}$ feature at 2002 cm^{-1} almost non-existent. In time, the main $\mathbf{2_{BB}}$ isomer transition at 2047 cm^{-1} significantly decreases in intensity in a fashion correlated with the growth of the $\mathbf{2_{BBB}}$ isomer feature at 2002 cm^{-1}.

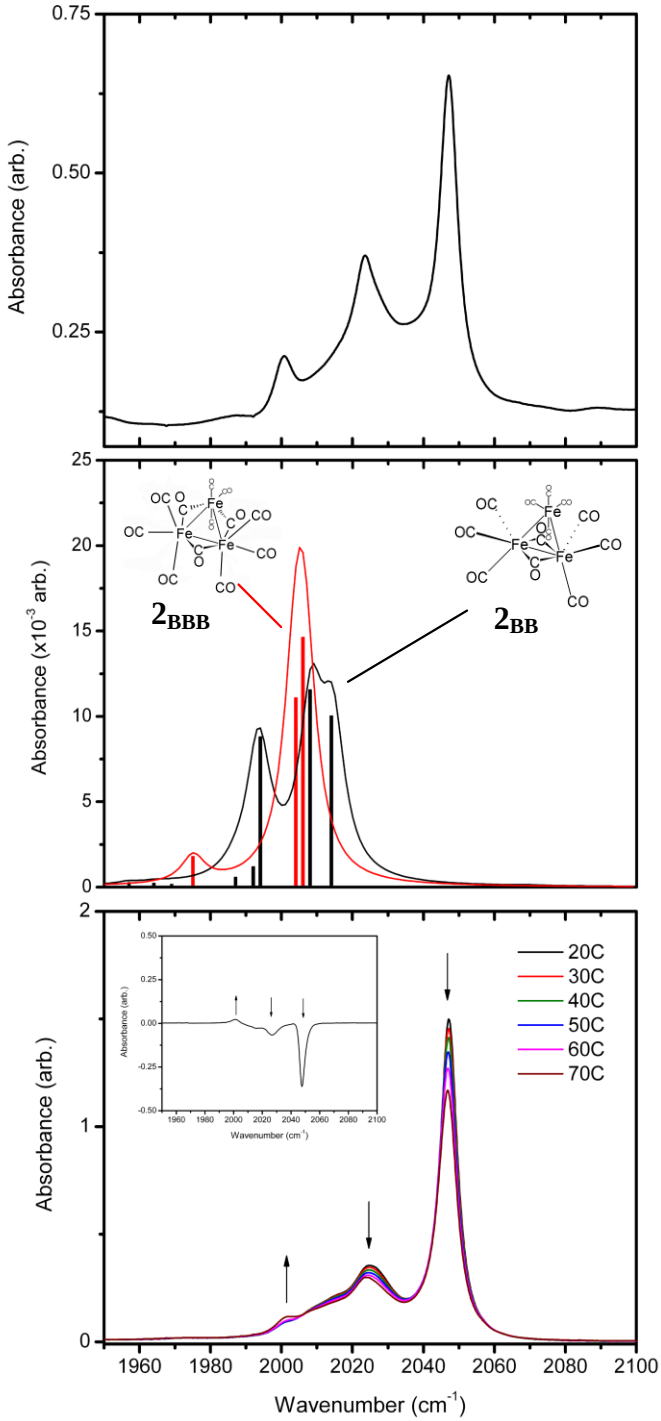

Figure 23. (A) The solvent corrected ν_{CO} region of infrared spectrum of **2** in n-heptane, (B) DFT calculated infrared spectra isomers $\mathbf{2_{BB}}$ (black) and $\mathbf{2_{BBB}}$ (red) with marked vibrational frequencies, (C) the temperature induced infrared spectrum changes for **2** in n-heptane for 20°C to 70°C range with arrows indicating temperature correlated changes. Inset shows difference spectrum for 20°C and 70°C traces.

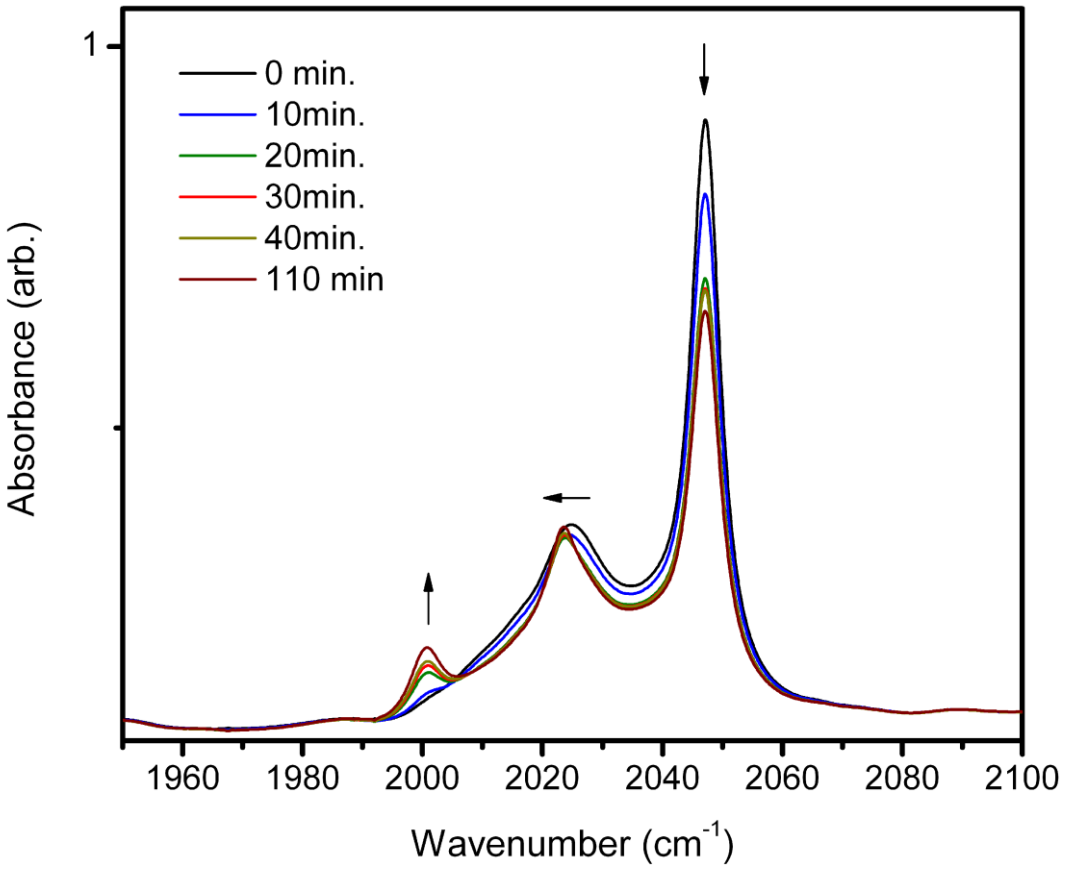

Figure 24. The time evolution of ν_{CO} region of FT-IR spectrum for freshly prepared solution of **2** in n-heptane measured at constant temperature of 20^{o}C. The time zero spectrum corresponds to time delay of 8 min. after adding **2** into solvent. The arrows indicate spectral changes direction.

The central feature at 2024 cm^{-1} exhibits more complex behaviour with an initial decrease in amplitude followed by a red shift and regain of its former amplitude at long times. Such behaviour suggests that both isomers contribute to this spectral feature in a manner that is consistent with DFT simulation findings.

In order to quantify the kinetics of this process, each consecutive infrared spectrum was fit to four Gaussian functions with widths and positions fixed for the three observed narrow transitions and one broad peak accounting for the dome-like background feature attributable to the multiple weak transitions of **2** isomers and the solvent. The resulting kinetic traces were fitted to single exponential functions leading to an average timescale of 1800 s, with similar results from both Gaussian lineshapes and a direct fit of the peak amplitudes. According to TST-derived rate

constant equations the energy barrier separating the $\mathbf{2_{BB}}$ and $\mathbf{2_{BBB}}$ isomer corresponding to the measured kinetic rates is ~44.5 kJ/mol. The obtained value of the energy barrier can, in theory be further split into the predicted 33.5 kJ/mol arising from the difference in stability of the isomers and ~11 kJ/mol representing the activation energy of the reverse process.

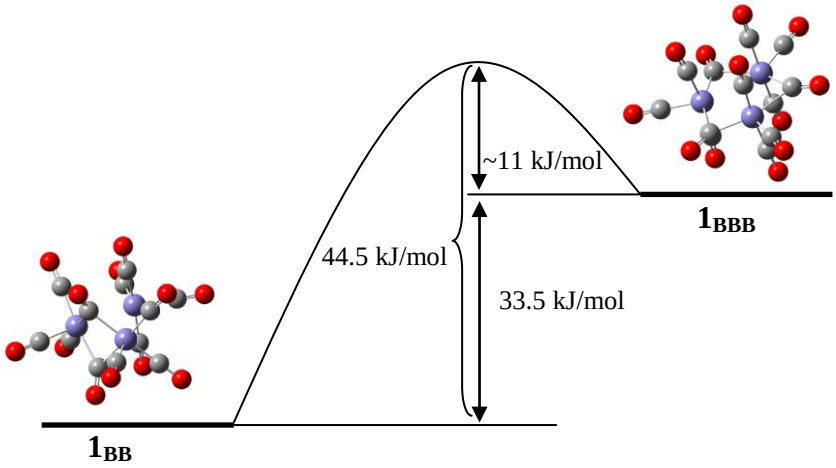

The estimated value of this activation energy compares well with the value of 11.7 kJ/mol obtained from DFT calculations of the transition state energy for isomerisation. By comparison with work of $Fe(CO)_5$, such an activation barrier for the reverse process of converting $\mathbf{2_{BBB}}$ into $\mathbf{2_{BB}}$ isomer would be expected to result in a picosecond timescale chemical interconversion dynamics that can be detected by 2D-IR spectroscopic technique.

4.2.2. 2D IR spectroscopy

The double resonance 2D-IR spectrum of **2** in heptane solution with a 20 ps pump-probe delay is shown in Figure 25. The 2D-IR spectrum consists of three diagonal features (*1* in Fig. 25) located at coordinates (2002, 2002), (2024, 2024) and (2047, 2047) where (ω_3, ω_1) notation corresponds to the probe and pump axis frequencies, respectively. The diagonal features are consistent with the three fundamental transitions observed in the FT-IR spectrum.

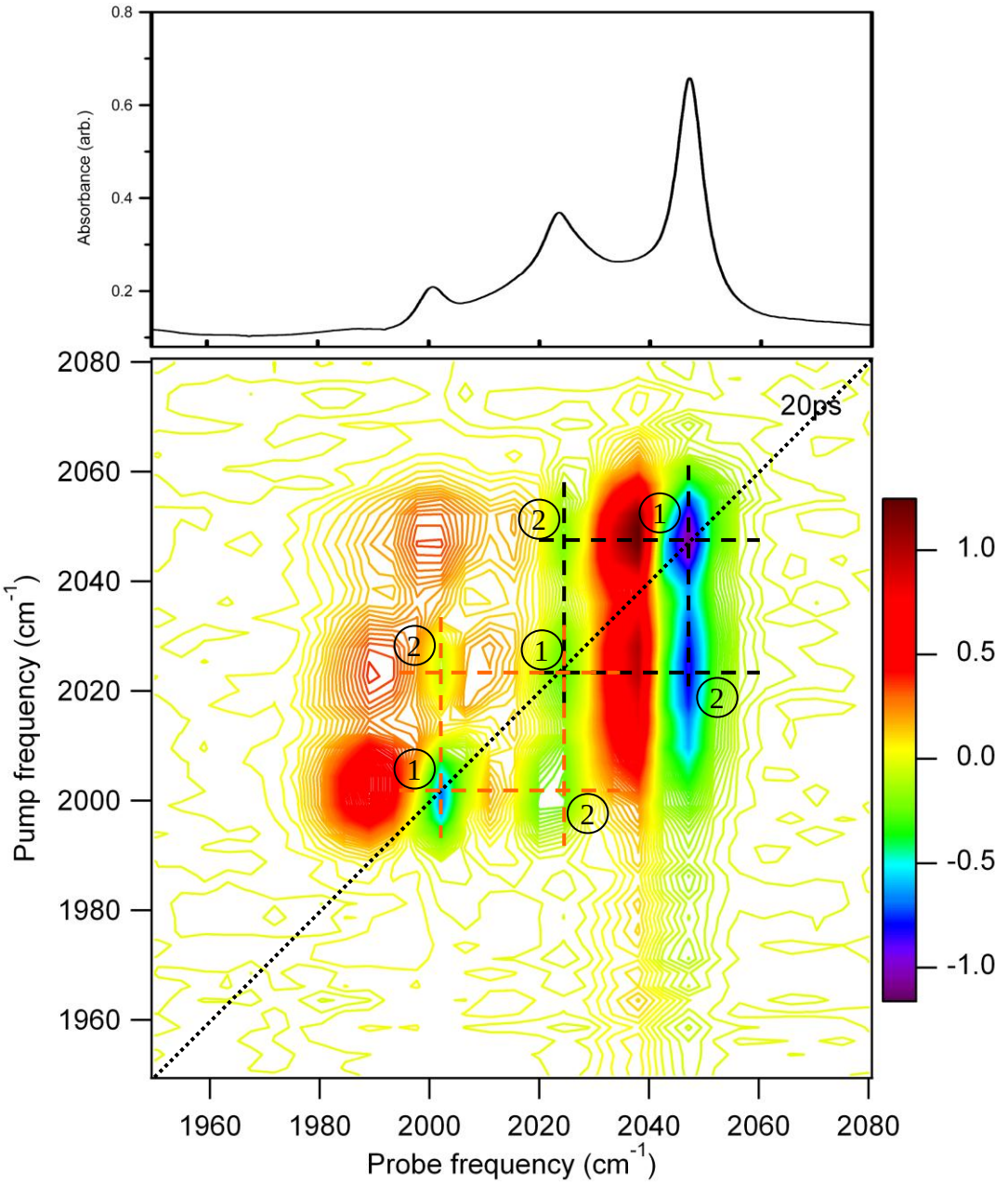

Figure 25. (top) The FT-IR spectrum of **2** in n-heptane at 293K. (Bottom) The 2D-IR spectrum of **2** in solution for 20ps pump-probe delay time. The dotted line display diagonal directions while dashed lines denote coupling patterns for $\mathbf{2_{BB}}$ (black) and $\mathbf{2_{BBB}}$ (orange) isomer.

The off-diagonal peak pairs (*2* in Fig. 25) appear at coordinates (2002, 2024), (2024, 2002) and (2047, 2024), (2024, 2047) as two separate vibrational coupling patterns

linking the diagonal peak at 2002 with that at 2024 and 2047 with 2024 respectively. There is no clear evidence for the coupling of the 2002 with 2047 cm^{-1} peak above the diagonal of the 2D map while the corresponding area below the diagonal is strongly affected by pump axis broadening. The identified coupling pattern is consistent with the existence of two isomers, the dominant $\mathbf{2_{BB}}$ and less stable $\mathbf{2_{BBB}}$ forms, each characterized by two spectral lines. It is to be noted that, as postulated from the steady-state FT-IR kinetics, the central broad feature has contributions from both isomers and hence shows 2D-IR cross-peaks to both lateral diagonal features.

Steady-state FT-IR kinetics experiments indicate that only interconversion from the $\mathbf{2_{BBB}}$ to the $\mathbf{2_{BB}}$ isomer faces an activation barrier small enough to result in the picosecond timescale dynamics observable in a 2D spectrum. Such dynamical asymmetry could theoretically affect a 2D-spectrum such that only exchange cross-peaks arising from the reverse reaction are visible. In the event that such ultrafast interconversion would occur an additional cross-peak linking the diagonal features due to separate isomers should arise below diagonal of the spectrum.

To explore the existence of ultrafast interconversion of the $\mathbf{2_{BBB}}$ to the $\mathbf{2_{BB}}$ isomer kinetic traces were recorded for a pump frequency fixed at the 2047 and 2002 cm^{-1} transitions. The horizontal 2D spectral slices at selected pump frequencies are shown in Figure 26. The horizontal slices through the 2D spectrum (Fig. 26a) at pump frequencies which coincides with the main $\mathbf{2_{BB}}$ transition displays two negative and two positive features. The strongest pair of features originates from the bleaching of the fundamental $\nu_{0\rightarrow1}$ frequency of the $\mathbf{2_{BB}}$ transition at the pump frequency with an absorption due to the $\nu_{1\rightarrow2}$ transition red shifted from this by 7 cm^{-1} due to local mode anharmonicity. The second peak pair originates from bleaching of the coupled fundamental $\nu_{0\rightarrow1}$ $\mathbf{2_{BB}}$ frequency at 2024 cm^{-1} while the corresponding absorption due to the combination band $\nu_{01\rightarrow11}$ transition is enveloped by a broad positive artefact centred at 1998 cm^{-1}.

The horizontal slice of the 2D spectrum (Fig. 26b) for a pump frequency coincidental with $\mathbf{2_{BBB}}$ isomer transition at 2002 cm^{-1} displays three pairs of negative and positive features.

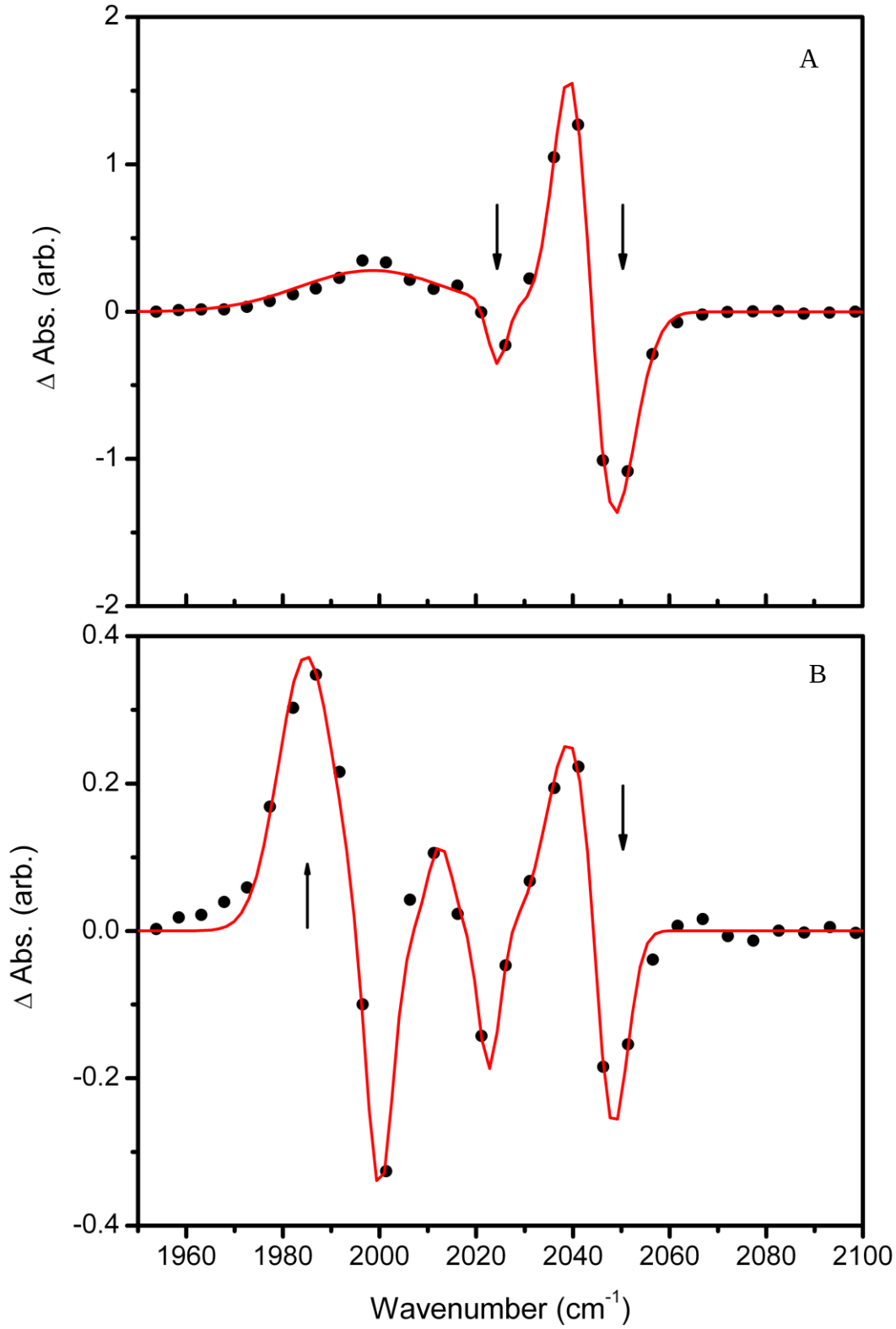

Figure 26. The horizontal slices through representative 2D-IR spectrum of **2** in n-heptane solution throughout diagonal features at 2047 cm^{-1} (A) and 2002 cm^{-1} (B) for 20ps pump-probe delay time. Red line represents global analysis fit while arrows indicate diagnostic features.

The strongest pair of features originates from bleaching of the fundamental $\nu_{0\rightarrow1}$ frequency of the $\mathbf{2_{BBB}}$ transition at the pump frequency with an absorption due to the $\nu_{1\rightarrow2}$ transition red shifted by about 15 cm^{-1} due to local mode anharmonicity. The middle peak pair originates from the bleaching of the coupled fundamental $\nu_{0\rightarrow1}$ $\mathbf{2_{BBB}}$ frequency at 2024 cm^{-1} and the corresponding absorption due to the combination band $\nu_{01\rightarrow11}$ transition. High frequency peak pair present at all pump-probe delay times originates from the simultaneous excitation of the $\mathbf{2_{BB}}$ isomer transition at 2047 cm^{-1} that is visible as pump axis broadening on the 2D-IR spectrum (Fig. 25).

A superposition of Gaussian lineshapes was used to fit the horizontal 2D spectral slices and recover vibrational dynamics for the observed transitions. The time dependences of the selected spectral features obtained from the amplitudes of Gaussian functions are shown in Figure 27. Vibrational dynamics were recovered by fitting a single or bi-exponential decay function to the Gaussian peak amplitudes. The fitting results are collated in Table 2.

For a pump frequency of 2047 cm^{-1} the observed diagonal peak pair of the $\mathbf{2_{BB}}$ isomer vibrational transition displays a bi-exponential decay with a fast decay time of ~2 ps followed by a slow decay with a timescale of 120-150 ps (Table 2). The off diagonal cross peak to the second $\mathbf{2_{BB}}$ isomer transition displays a single exponential decay with a timescale similar to the diagonal features.

Table 2. Results of fitting temporal dependencies of diagonal and off-diagonal peak amplitudes of **2** in heptane solution derived from 2D-IR spectra slices. Lifetimes τ_1, τ_2 represent exponential decay rates.

Pump frequency [cm^{-1}]	Peak position [cm^{-1}]	Peak width [cm^{-1}]	τ_1 [ps]	τ_2 [ps]	Line Assignment
2047	2047	5	2	135	Diagonal bleach $\nu(0\rightarrow1)$
	2040	4	2	125	Diagonal absorption $\nu(1\rightarrow2)$
	2024	2	147		Off-diagonal bleach $\nu(0\rightarrow1)$
2002	2002	3	8	153	Diagonal bleach $\nu(0\rightarrow1)$
	1984	6	2	97	Diagonal absorption $\nu(1\rightarrow2)$
	2047	3	122		Off-diagonal bleach $\nu(0\rightarrow1)$
	2040	5	174		Off-diagonal absorption $\nu(1\rightarrow2)$

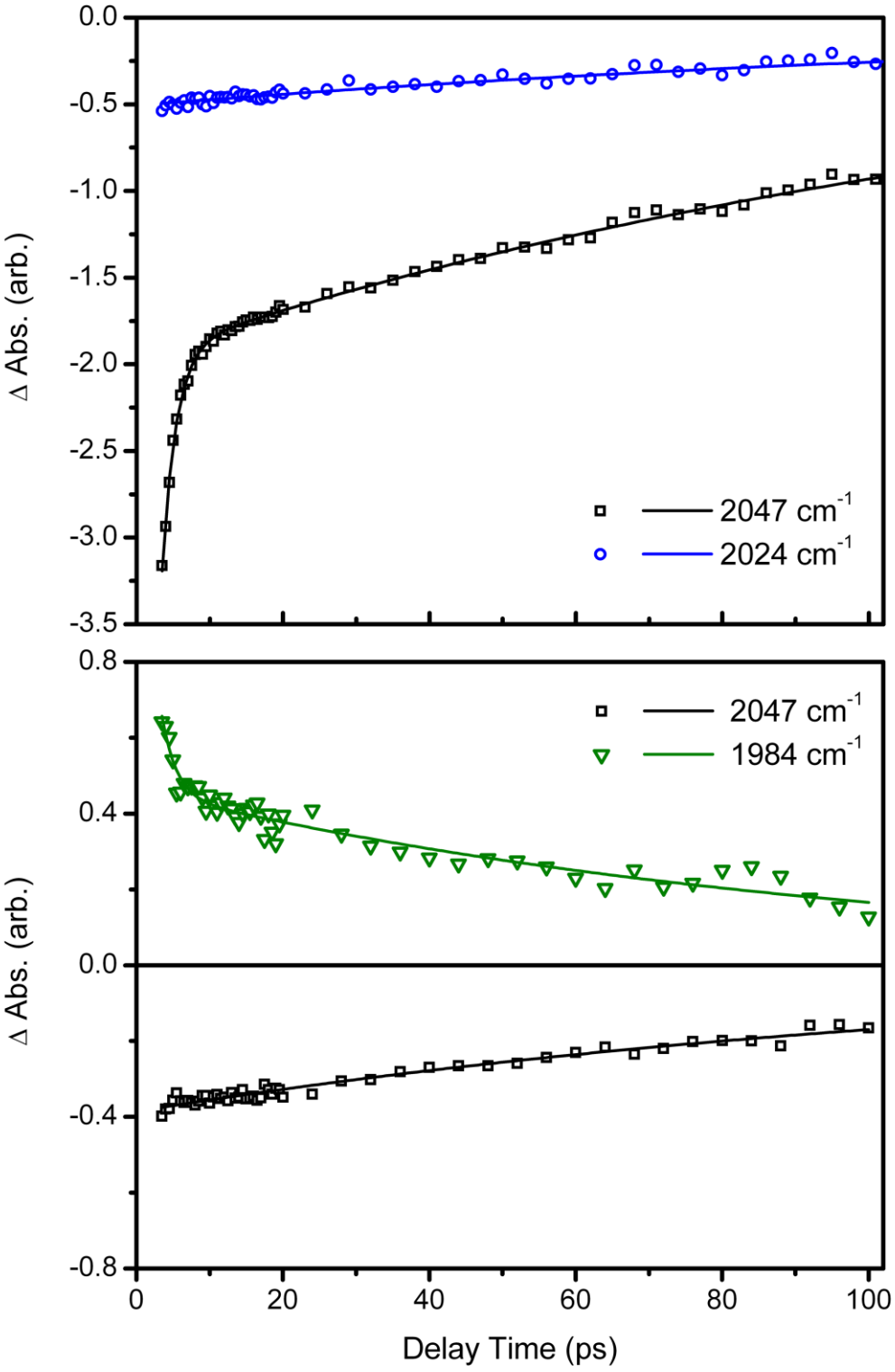

Figure 27. The vibrational dynamics of selected peaks in horizontal slices 2D spectrum of **2** solution recorded for pump frequency fixed at 2047 cm^{-1} (top) and 2002 cm^{-1} (bottom). Solid lines represent single exponential fits of cross peaks decays (traces 2024 cm^{-1} and 2047 cm^{-1} (bottom)) and bi-exponential fits of pumped peaks decays (traces 1984 cm^{-1} and 2047 cm^{-1} (bottom)).

For a pump frequency of 2002 cm^{-1} the observed diagonal peak pair of the $\mathbf{2_{BBB}}$ isomer vibrational transition displays a bi-exponential decay with a fast decay time of ~2 ps followed by a slow decay with a timescale of ~100 ps. The off-diagonal peak pair attributable to the high frequency fundamental feature of the $\mathbf{2_{BB}}$ isomer displays a single exponential decay with a timescale of ~120 ps. Both isomers in heptane solution exhibit similar rapid picosecond timescale Internal Vibrational Relaxation followed by slower population relaxation with a timescale of 100-150ps. For a pump frequency of 2047 cm^{-1} the observed diagonal peak pair of the $\mathbf{2_{BB}}$ isomer vibrational transition displays a bi-exponential decay with a fast decay time of ~2 ps followed by a slow decay with a timescale of 120-150 ps (Table 2). The off diagonal cross peak to the second $\mathbf{2_{BB}}$ isomer transition displays a single exponential decay with a timescale similar to the diagonal features. For a pump frequency of 2002 cm^{-1} the observed diagonal peak pair of the $\mathbf{2_{BBB}}$ isomer vibrational transition displays a bi-exponential decay with a fast decay time of ~2 ps followed by a slow decay with a timescale of ~100 ps. The off-diagonal peak pair attributable to the high frequency fundamental feature of the $\mathbf{2_{BB}}$ isomer displays a single exponential decay with a timescale of ~120 ps. Both isomers in heptane solution exhibit similar rapid picosecond timescale Internal Vibrational Relaxation followed by slower population relaxation with a timescale of 100-150ps. The vibrational dynamic characteristics of both isomers of **2** are in agreement with other metalcarbonyl systems in heptane solution.[14,16,26,86,87]

The presence of cross-peaks between the vibrational levels of separate isomeric forms of **2** may arise either from a chemical exchange process or from simultaneous vibrational excitation, which is frequently observed when vibrational transitions of different compounds overlap with sufficient intensities. However in the case of chemical exchange the cross-peaks are expected to grow in time with the rate characterising the underlying chemical process while in collective excitation the spectral features of both compounds appear instantaneously. The cross-peak behaviour in the horizontal slice coincident with the separate $\mathbf{2_{BBB}}$ isomer line matches those expected for collectively excited transitions with no apparent evidence of an isomeric exchange process as estimated by (TST) to display lifetime of about 18 ps.

4.2.3. Time-resolved IR spectroscopy

The time-resolved infrared difference spectra of **2** in heptane subjected to femtosecond UV irradiation at λ=355 nm are shown in Figure 28. The TR-IR spectra with a corresponding fit to four Gaussian functions are shown for two indicative time delays of 8 ps and 440 ps.

In the spectra obtained for a pump-probe delay of 8 ps, (Fig 28a) one negative feature is observed that is coincident with the main peak observed in the infrared spectrum of **2**. This feature was present at the earliest pump-probe delay times and is assignable to a bleach of the parent molecule absorption arising from depletion of the prevalent $\mathbf{2_{BB}}$ isomer concentration by the UV pump pulse. This bleach is accompanied at short delay times by the instantaneous appearance of broad, positive features at lower frequency (2036 cm^{-1}). A positive absorption peak appears on the red side of the bleach while a second broad positive absorption peak covers the frequency range where two remaining bleaches of **2** are expected. These are consistent with earlier studies of metalcarbonyl compounds and are assignable to a superposition of the short-lived MLCT excited state, vibrationally hot species formed by irradiation, and the undecacarbonyl photoproduct created by the loss of a CO ligand, which has been shown to occur on sub ps timescales.[12,14,16,20,21] The photoproduct lines that originate from CO loss are red shifted in relation to the parent molecule transitions as would be expected on account of the increased electron back donation into carbonyl π* orbitals. The trace at 440 ps (Fig 28b) shows main bleach amplitude and linewidth decay assignable to vibrational cooling followed by geminate recombination leading to recovery of the parent molecule. The bleach recovery is greater than 75% of the initial amplitude at this time delay but incomplete within experiment time window suggesting a competition of geminate recombination process with solvent adduct formation. The adduct formation is further confirmed with presence of non-vanishing absorption peaks at 2036 cm^{-1} and bleach at 2024 cm^{-1} visible at longer delay times and persists for the rest of time window.

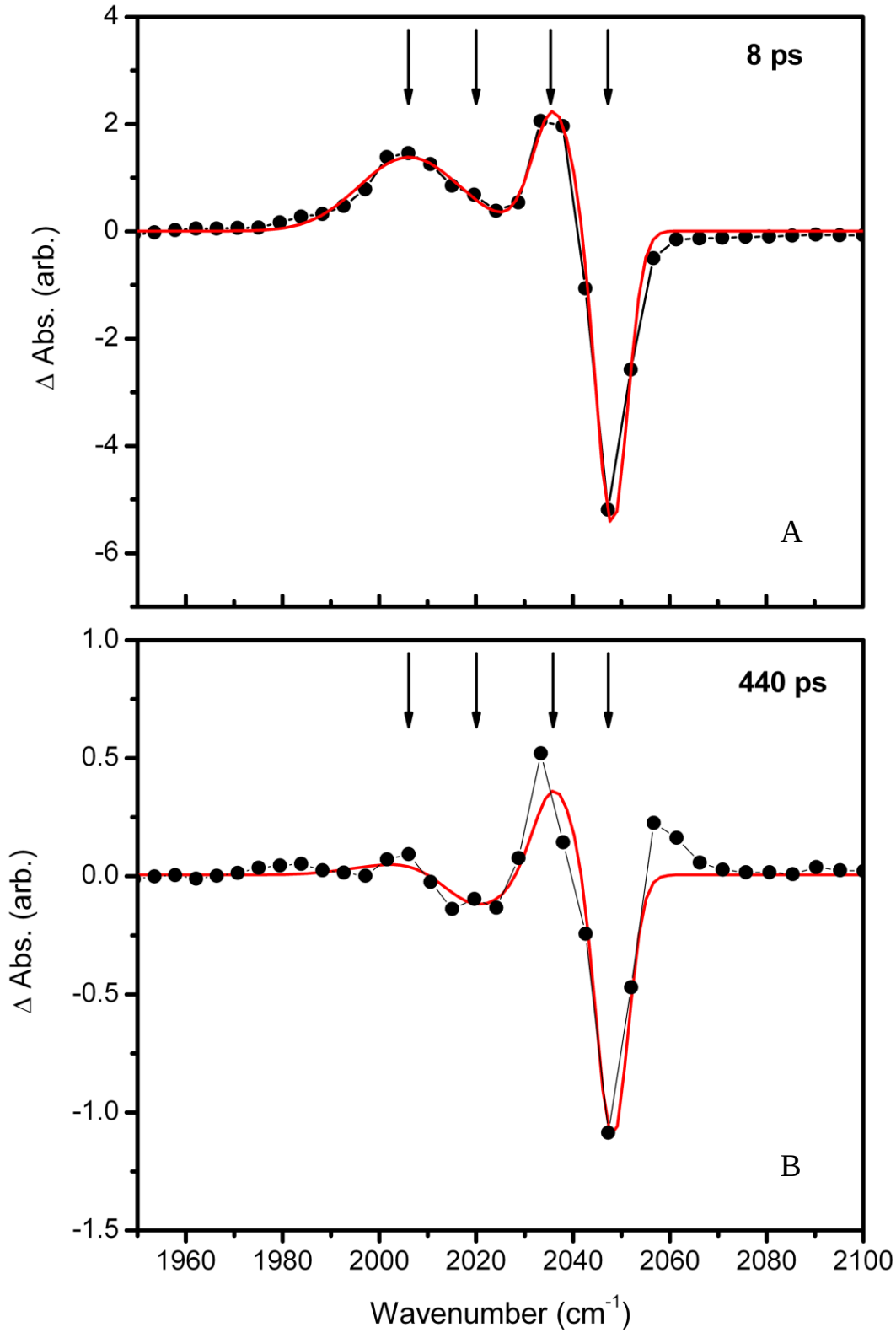

Figure 28. Magic angle TR-IR spectra of **2** in n-heptane at 8 ps (A) and 440 ps (B) pump-probe delay times. Red line represents global analysis fit of 4 Gaussian peaks superposition with arbitrary fixed positions (see Table 3) marked by arrows.

The broad positive feature at lower frequency apparent at early times significantly decays leaving narrow photoproduct peak positioned at 2006 cm^{-1}.

The overall process is consistent with those observed in the case of other metalcarbonyl systems where the initial vibrational cooling and formation of transient species due to CO ligand loss is followed by competition of geminate recombination with solvent adduct formation. The congestion of the spectrum prevents isolation of the MLCT excited state peaks from the transient species features while the overlap of peaks due to transient species with solvent adduct peaks can be assigned to a weak interaction of the solvent with the transient species leading to a strong similarity of vibrational spectrum.

DFT calculations were performed to simulate the infrared spectra and compare the stability of an intermediate species and solvent adduct. Results of infrared spectral simulations are shown in Figure 29. The simulations of solvent adduct spectra were performed with propane instead of heptane to improve geometry optimisation performance and to reduce computational cost. It has been shown elsewhere that the length of alkane chain in solvent adducts has little effect on the simulated infrared spectra.[12,17,19,20] The simulations predict a general downshift of the ν_{CO} bands for all photoproducts though the shifts are relatively small and hence indistinct. The spectral congestion caused by the proximity of the vibrational frequencies of transient and solvent adduct becomes even more aggravated when considering presence of the typically red shifted MLCT excited state vibrational transitions[14,16,19-21] which cannot be calculated in a ground state DFT approach. In heptane solution, formation of a coordinatively bonded solvent product could not be achieved, raising questions about the stability of the transient-solvent aggregate. The simulation of possible solvent adducts with propane instead heptane showed evidence for sufficient stabilization energy. The stabilization energy calculated as a formation energy difference between the solvent adduct and the sum of the molecular formation energies of the constituents (Eq. 26) returned a value of 21 kJ/mol, sufficient for stabilisation of such an aggregate. The evidence for stable solvent adduct formation for **2** in heptane is comparable to the results for several other metalcarbonyl systems where solvent adducts are observed in detectable amounts.[14-16,19-21]

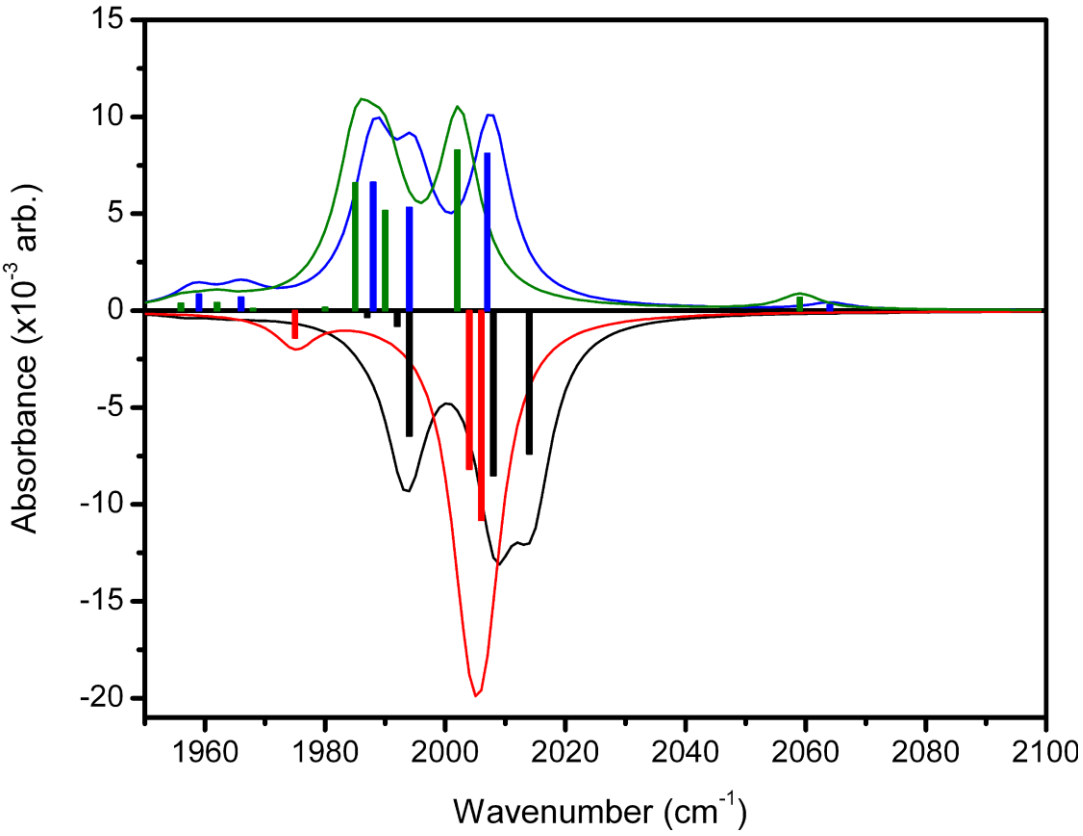

Figure 29. The DFT calculated infrared spectra of $\mathbf{2_{BB}}$ (black), $\mathbf{2_{BBB}}$ (red), transient $Fe_3(CO)_{12}$ (blue) and solvent adduct $Fe_3(CO)_{11}(C_3H_8)$ (green).

In order to quantify the timescales of photochemical processes, the TR-IR difference spectra were fit to a superposition of Gaussian lineshapes over all available time slices simultaneously using aglobal analysis approach. The time dependence of selected TR-IR features obtained from the amplitudes of the Gaussian functions are presented in Figure 30. The dynamics were obtained by fitting Gaussian peak amplitudes to single or bi-exponential decay functions. The results are collated in Table 3. The congestion of the spectrum in the lower frequency range was handled by limiting the number of Gaussian peaks to two, placed initially at the FT-IR frequencies of the parent molecule. The additional feature on the blue side of the main parent bleach (Fig. 28b) is the result of an overlap of a broader photoproduct band with the main bleach band exposed by vibrational cooling at longer time delays and as such it cannot be reproduced by fixed width Gaussian lineshape fitting.

Table 3. Results of fitting temporal dependencies of Gaussian peak amplitudes of **2** in heptane solution derived from fitting of TR-IR spectra. Life times τ_1 and τ_2 represent exponential decays while τ_R represent exponential rise.

Peak position [cm^{-1}]	Peak width [cm^{-1}]	τ_R [ps]	τ_1 [ps]	τ_2 [ps]	Line Assignment
2047	3.5		17	184	Parent bleach
2036	4.5	5	175		Undecacarbonyl cooling and geminate recombination
2020	7	10	138		Undecacarbonyl cooling and geminate recombination
2006	9		20	182	MLCT decay, undecacarbonyl cooling and geminate recombination

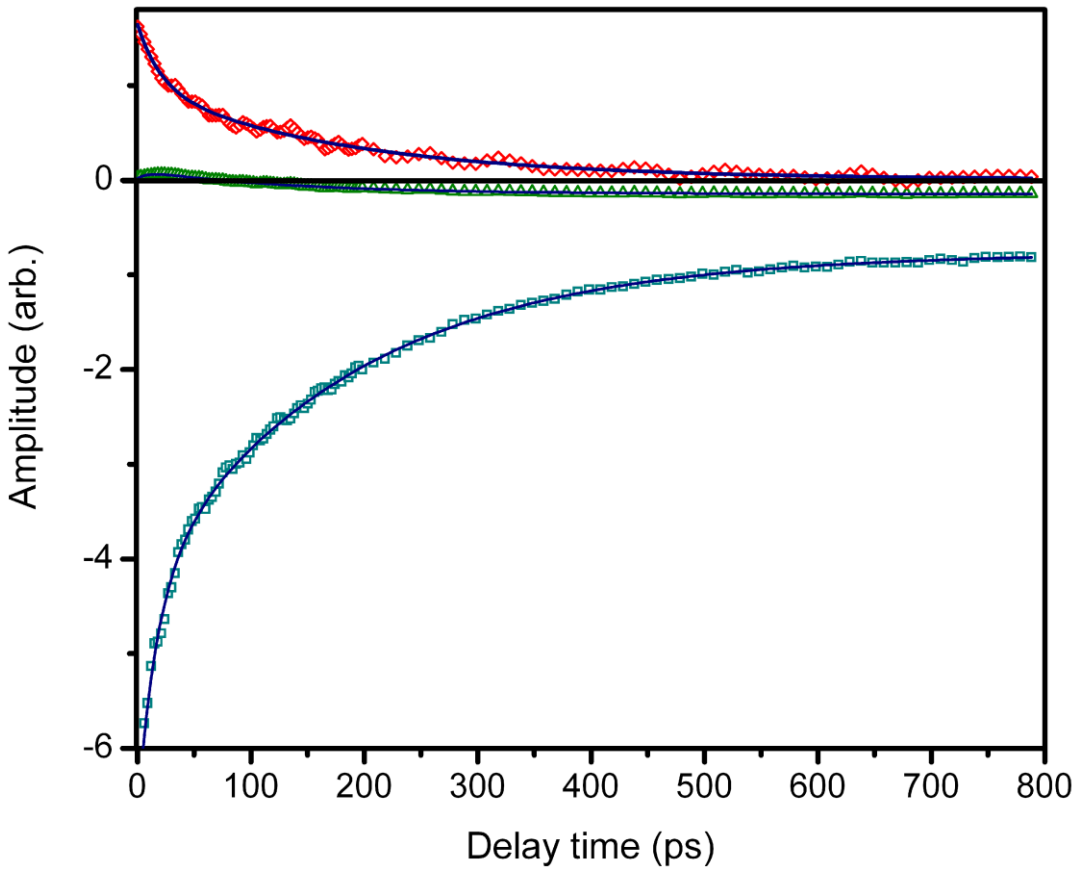

Figure 30. Time dependencies of amplitudes Gaussian peak components of GA fitted TR-IR spectra of **2** where solid lines represent single- or bi-exponential decay fits. Blue indicates main parent bleach recovery kinetics, red shows decay of a low frequency absorption peak and olive shows recovery kinetics of peak located at central line of parent molecule.

The main parent molecule bleach at 2047 cm^{-1} displayed a bi-exponential recovery (blue in Fig 30 and Table 3) with the faster decay timescale in the 15-20 ps region and the longer timescale in the 170-180 ps range. This is consistent with the assignment of these timescale to vibrational cooling followed by geminate recombination. Analogous behaviour was observed for the broad low frequency positive feature at 2020 cm^{-1} which decayed in a bi-exponential fashion with similar timescales (red in Fig 30 and Table 3). Narrowing of this positive feature reveals a second parent molecule bleach at 2024 cm^{-1} (olive in Fig 28 and Table 3), which, when fitted separately displays bi-exponential behaviour with an initial rise followed by a longer timescale decay with a timescale broadly similar to the main negative feature. The second positive feature located at 2036 cm^{-1} shows similar bi-exponential behaviour with a sharp initial rise followed by longer timescale decay in the 170-180 ps range.

The kinetics indicate a relatively simple mechanism in which vibrational cooling of the transient species formed following photolysis occurs rapidly within in tens of picoseconds while the 170-180 ps decay time can be associated with geminate recombination. Incomplete recovery of both negative features at longer timescales suggests a solvent adduct formation though the inseparable overlap of spectral features prevents isolation of spectral contributions from other transient species signatures. The non-vanishing absorption bands at 2036 and 2006 cm^{-1} are expected to contain contributions from solvent adduct transitions while the transition at 2020 cm^{-1} decays with geminate recombination completely, as would be expected for purely transient spectral line. Congestion and overlap of the positive and negative features make it impossible to properly assign the MLCT excited state transition contributions to particular absorption bands. However the low frequency absorption (2006 cm^{-1}) shows instantaneous rapid vibrational cooling with no frequency drift (Fig. 30). Such behaviour has been observed for MLCT excited state lines for metalcarbonyls in solution[14,19-21] suggesting a possible contribution from this process.

4.3. Discussion

The results of the steady-state FT-IR spectroscopic studies of the ν_{CO} region of **2** in heptane solution indicate the existence of a geometrical isomerisation equilibrium that is also consistent with ground state DFT simulations and temperature difference FT-IR spectroscopy. The simulated transition state energy suggests the existence of an asymmetrical energy barrier between isomers. Such asymmetry creates a disparity in the forward and backward reaction rates of which the latter could have been expected to be ultrafast. This situation separates the $Fe_3(CO)_{12}$ isomerisation process from that of $Fe(CO)_5$ [68] which is known to display ultrafast interconversion dynamics and is unlike the majority of other metalcarbonyl systems[2,7-9,39,40] where no ultrafast interconversion dynamics are observed. In the case of $Fe(CO)_5$ isomerisation, the ultrafast reaction rate is caused by a very low reaction activation barrier with a formally zero reaction enthalpy for CO ligand permutation (the complexes interconvert into themselves via lower symmetry transition state). On the opposite side are metalcarbonyls systems displaying such large activation energy for interconversion that no ultrafast interconversion dynamics occur regardless of the reaction enthalpy.

To further investigate this geometrical isomerisation, a double-resonance 2D-IR spectrum was recorded. The 2D-IR spectrum confirms the presence of two isomeric forms of **2**. Since fundamental transitions of both isomers are overlapping for the central peak frequency the only diagnostic peaks for chemical interconversion would be cross-peaks between diagonal transitions belonging solely to one isomer. The cross peaks arising from this chemical exchange process were expected to appear as below diagonal cross-peaks which originate from the transformation of $\mathbf{2_{BBB}}$ to $\mathbf{2_{BB}}$ isomer. The observed off-diagonal features at this position were however identified as a collective excitation, excluding the existence of ultrafast geometrical interconversion with the expected, estimated, lifetime of 18 ps. However, the limited time window of the acquired double-resonance 2D-IR spectrum and intense artefacts in the crucial spectral area exclude the detection of any slower dynamical processes occurring at timescales beyond 100 ps. The available time window for a 2D-IR spectrum measurement is permanently limited by the vibrational relaxation rate. The only way to enhance the sensitivity of this spectroscopic method is to avoid spectral

artefacts by recording the 2D-IR spectrum again using the vibrational echo acquisition method but this will not circumvent the vibrational relaxation time scale issue. The increased spectral resolution of vibrational echo 2D-IR spectroscopy measurements could remove these artefacts and enable detection of peaks due to chemical exchange processes at time scales up to the vibrational lifetime of compound **2**, providing a definitive answer to the existence of ultrafast geometrical interconversion process.

The 2D-IR spectrum derived vibrational relaxation dynamics display no significant differences between isomers of **2**. The few picosecond timescale IVR process dynamics indicates very fast vibrational energy redistribution among coupled modes while similar timescales of population relaxation dynamics indicate no marked changes in solute-solvent interaction strength between isomeric forms. The latter was expected owing to the negligible difference of dipole moments between the isomeric forms, predicted to be 0.8 D (DFT). The IVR and populational relaxation timescales are similar to those found for other metalcarbonyls in non-polar solutions.[14,16,17,19,21,39,40,88]

The TR-IR investigation of the photochemistry of **2** in heptane solution shows a relatively simple photoinduced chemical reaction process similar to one recorded for $Fe(CO)_5$ and several other polymetallic metalcarbonyls such as (μ-$S(CH_2)_3S)Fe_2(CO)_6$.[12,16,19-21] UV excitation leads to sub-picosecond dissociation of a CO ligand followed by ultrafast geminate recombination. Incomplete recovery of the parent molecule features combined with non-vanishing transient absorptions suggests that the geminate recombination process is competing with transient stabilisation in the form of a solvent adduct. DFT calculations were employed to estimate the solvent adduct stabilisation energy and the significant stabilisation energy (21 kJ/mol) obtained for the transient solvent aggregate supports the initial assignment of non-vanishing absorptions due to this species. The region where photoproduct bands are expected however was crowded allowing only a speculative assignment of the expected contributions on the basis of observed dynamics and the level of bleach recovery. Unfortunately, the DFT simulations of photoproduct infrared spectra revealed a close similarity of the transient and solvent adduct vibrational fingerprint, providing no further clues to disentangle the spectral

congestion. The observed post-UV excitation relaxation dynamics reveal two distinctive timescales of about 20 ps and 140-190 ps assigned to two principal processes of vibrational cooling and geminate recombination which are in excellent agreement with prior work on the photochemistry of various metalcarbonyls in non-polar solutions.[12,14,16,19-21] No distinct MLCT excited state lines were observed for the system. The TR-IR spectrum showed no indication of UV -triggered geometrical isomerisation similar to that seen in dynamic studies of $(\mu\text{-}S(CH_2)_3S)Fe_2(CO)_6(PMe_2)_3$ discussed in a previous chapter.

4.4. Conclusions

In summary we have employed steady state and two-dimensional infrared spectroscopy to explore the geometrical interconversion process in a polymetallic metalcarbonyl in heptane solution augmented by ultrafast photochemistry studies using TR-IR spectroscopy. It has been determined that **2** in heptane solution exists in two stable isomers $\mathbf{2_{BB}}$ and $\mathbf{2_{BBB}}$ involved in a dynamic equilibrium. Both steady state FT-IR spectroscopy and DFT simulations indicated an asymmetric energy barrier that shifts **the** equilibrium toward the more stable $\mathbf{2_{BB}}$ isomer while a small predicted activation barrier for the reverse transformation of $\mathbf{2_{BBB}}$ to $\mathbf{2_{BB}}$ suggested the presence of an ultrafast dynamical rate. The forward reaction $\mathbf{2_{BB}}$ to $\mathbf{2_{BBB}}$ rate measurements indicated a lifetime of tens of minutes while the ultrafast 2D-IR spectroscopy has not provided an indication for an ultrafast rate of the reverse reaction $\mathbf{2_{BBB}}$ to $\mathbf{2_{BB}}$. Still, the limited available time window and poor quality of the double resonance spectra may have contributed to the lack of dynamical processes detection and it would have been insensitive to processes with lifetimes beyond >100ps important in case that DFT estimated interconversion energy barrier was slightly underestimated. Vibrational echo 2D-IR spectroscopy could offer better spectra quality and it may be capable detecting interconversion within hundreds picosecond time scales.

The TR-IR spectroscopy was employed to observe the primary and secondary photochemical processes of a **2** in heptane solution. It has been determined that UV light induced excitation of MLCT bands leads to photodissociation of a CO ligand with relaxation and vibrational cooling processes occurring on about 20 ps timescales

followed by geminate recombination on 140-190 ps timescales. Detailed analysis of the photoproduct spectrum and dynamics was impeded by spectral congestion that permitted only speculative assignment of features due to transient species. The apparent incomplete recovery of parent molecule bands and non-vanishing transient absorption bands indicated the formation of stable solvent adducts further confirmed by DFT calculations.

4.5. Further research perspectives

The presented data clearly indicate the existence of ground state chemical reactions with differences in the reaction rates for forward and reverse processes that may be ultrafast in nature. Although the applied double-resonance 2D-IR spectroscopy has not indicated ultrafast rates of the reverse reaction kinetics here further investigations with higher resolution vibrational echo 2D-IR technique may provide definitive answer.

The TR-IR studies of ultrafast photochemistry in solution revealed relatively simple primary and secondary photochemical reaction processes. Still, the extensive overlap of spectral lines prevents separation and detailed dynamical analysis of closely related photoproducts, exposing basic weakness of this approach. More detailed analysis of this photochemistry would be possible through application of the Transient 2D-IR technique. The cross-peak pattern on the Transient 2D map should enable at least partial separation of individual spectral contributions to the overall process by additionally probing the vibrational dynamics of transient species. Additionally the Transient 2D-IR spectrum is capable of detecting and measuring the process of UV-induced geometrical isomerisation that could augment ground state 2D-IR investigations.

4.6. Acknowledgements

The author would like to acknowledge contributions of Dr. Spyros Kaziannis in expansion of 2D-IR spectrometer to host TR-IR measurements.

References:

(1) Roquette, P.; Maronna, A.; Reinmuth, M.; Kaifer, E.; Enders, M.; Himmel, H.-J. R. *Inorganic Chemistry* **2011**, *50*, 1942.

(2) Ewing, P.; Farrugia, L. J.; Rycroft, D. S. *Organometallics* **1988**, *7*, 859.

(3) Creber, M. L.; Orrell, K. G.; Osborne, A. G.; Sik, V.; Hursthouse, M. B.; Abdul Malik, K. M. *Journal of the Chemical Society, Dalton Transactions* **2000**, 4218.

(4) Gelling, A.; D. Olsen, M.; G. Orrell, K.; G. Osborne, A.; Sik, V. *Journal of the Chemical Society, Dalton Transactions* **1998**, 3479.

(5) Gelling, A.; Olsen, M. D.; Orrell, K. G.; Osborne, A. G.; Sik, V. *Inorganica Chimica Acta* **1997**, *264*, 257.

(6) Adams, R. D. C., D. E.; Cotton, F. A. *Journal of the American Chemical Society* **1974**, *96*, 749.

(7) Downton, P. A.; Mailvaganam, B.; Frampton, C. S.; Sayer, B. G.; McGlinchey, M. J. *Journal of the American Chemical Society* **1990**, *112*, 27.

(8) Wey, H. G.; Betz, P.; Topalovic, I.; Butenschoen, H. *Journal of Organometallic Chemistry* **1991**, *411*, 369.

(9) Chudek, J. A.; Hunter, G.; Paton, J. D.; Walmsley, B. A. *Polyhedron* **1995**, *14*, 2691.

(10) Cervetto, V.; Bregy, H.; Hamm, P.; Helbing, J. *The Journal of Physical Chemistry A* **2006**, *110*, 11473.

(11) Cahoon, J.; Kling, M.; Sawyer, K.; Andersen, L.; Harris, C. *Journal of Molecular Structure* **2008**, *890*, 328.

(12) Kaziannis, S.; Santabarbara, S.; Wright, J. A.; Greetham, G. M.; Towrie, M.; Parker, A. W.; Pickett, C. J.; Hunt, N. T. *The Journal of Physical Chemistry B* **2010**, *114*, 15370.

(13) Sawyer, K. R.; Cahoon, J. F.; Shanoski, J. E.; Glascoe, E. A.; Kling, M. F.; Schlegel, J. P.; Zoerb, M. C.; Hapke, M.; Hartwig, J. F.; Webster, C. E.; Harris, C. B. *Journal of the American Chemical Society* **2010**, *132*, 1848.

(14) Clark, I. P.; George, M. W.; Greetham, G. M.; Harvey, E. C.; Long, C.; Manton, J. C.; Pryce, M. T. *The Journal of Physical Chemistry A* **2011**, *115*, 2985.

(15) Kania, R.; Frederix, P. W. J. M.; Wright, J. A.; Ulijn, R. V.; Pickett, C. J.; Hunt, N. T. *The Journal of Chemical Physics* **2012**, *136*, 044521.

(16) Portius, P.; Yang, J.; Sun, X.-Z.; Grills, D. C.; Matousek, P.; Parker, A. W.; Towrie, M.; George, M. W. *Journal of the American Chemical Society* **2004**, *126*, 10713.

(17) Kania, R.; Stewart, A. I.; Clark, I. P.; Greetham, G. M.; Parker, A. W.; Towrie, M.; Hunt, N. T. *Physical Chemistry Chemical Physics: PCCP* **2010**, *12*, 1051.

(18) Cahoon, J. F.; Kling, M. F.; Schmatz, S.; Harris, C. B. *Journal of the American Chemical Society* **2005**, *127*, 12555.

(19) Stewart, A. I.; Wright, J. A.; Greetham, G. M.; Kaziannis, S.; Santabarbara, S.; Towrie, M.; Parker, A. W.; Pickett, C. J.; Hunt, N. T. *Inorganic Chemistry* **2010**, *49*, 9563.

(20) Ridley, A. R.; Stewart, A. I.; Adamczyk, K.; Ghosh, H. N.; Kerkeni, B. n.; Guo, Z. X.; Nibbering, E. T. J.; Pickett, C. J.; Hunt, N. T. *Inorganic Chemistry* **2008**, *47*, 7453.

(21) Glyn, P.; Johnson, F. P. A.; George, M. W.; Lees, A. J.; Turner, J. J. *Inorganic Chemistry* **1991**, *30*, 3543.

(22) Asbury, J. *Chemical Physics Letters* **2003**, *374*, 362.

(23) Rubtsov, I. V.; Kumar, K.; Hochstrasser, R. M. *Chemical Physics Letters* **2005**, *402*, 439.

(24) Kwak, K.; Rosenfeld, D. E.; Chung, J. K.; Fayer, M. D. *The Journal of Physical Chemistry B* **2008**, *112*, 13906.

(25) Rosenfeld, D. E.; Kwak, K.; Gengeliczki, Z.; Fayer, M. D. *The Journal of Physical Chemistry B* **2010**, *114*, 2383.

(26) Stewart, A. I.; Clark, I. P.; Towrie, M.; Ibrahim, S. K.; Parker, A. W.; Pickett, C. J.; Hunt, N. T. *The Journal of Physical Chemistry B* **2008**, *112*, 10023.

(27) Asbury, J. B.; Steinel, T.; Kwak, K.; Corcelli, S. A.; Lawrence, C. P.; Skinner, J. L.; Fayer, M. D. *The Journal of Chemical Physics* **2004**, *121*, 12431.

(28) Kim, Y. S.; Hochstrasser, R. M. *Proceedings of the National Academy of Sciences of the United States of America* **2005**, *102*, 11185.

(29) Park, S.; Kwak, K.; Fayer, M. D. *Laser Physics Letters* **2007**, *4*, 704.

(30) Zhao, W.; Moilanen, D. E.; Fenn, E. E.; Fayer, M. D. *Journal of the American Chemical Society* **2008**, *130*, 13927.

(31) Elsaesser, T. *Accounts of Chemical Research* **2009**, *42*, 1220.

(32) Moilanen, D. E.; Wong, D.; Rosenfeld, D. E.; Fenn, E. E.; Fayer, M. D. *Proceedings of the National Academy of Sciences of the United States of America* **2009**, *106*, 375.

(33) Park, S.; Odelius, M.; Gaffney, K. J. *The Journal of Physical Chemistry B* **2009**, *113*, 7825.

(34) King, J. T.; Baiz, C. R.; Kubarych, K. J. *The Journal of Physical Chemistry A* **2010**, *114*, 10590.

(35) Kolano, C.; Helbing, J.; Kozinski, M.; Sander, W.; Hamm, P. *Nature* **2006**, *444*, 469.

(36) Cervetto, V.; Hamm, P.; Helbing, J. *The Journal of Physical Chemistry B* **2008**, *112*, 8398.

(37) Backus, E. H. G.; Bloem, R.; Donaldson, P. M.; Ihalainen, J. A.; Pfister, R.; Paoli, B.; Caflisch, A.; Hamm, P. *The Journal of Physical Chemistry B* **2010**, *114*, 3735.

(38) Smith, A. W.; Lessing, J.; Ganim, Z.; Peng, C. S.; Tokmakoff, A.; Roy, S.; Jansen, T. L. C.; Knoester, J. *The Journal of Physical Chemistry B* **2010**, *114*, 10913.

(39) Baiz, C. R.; McRobbie, P. L.; Anna, J. M.; Geva, E.; Kubarych, K. J. *Accounts of Chemical Research* **2009**, *42*, 1395.

(40) Baiz, C. R.; McRobbie, P. L.; Preketes, N. K.; Kubarych, K. J.; Geva, E. *The Journal of Physical Chemistry A* **2009**, *113*, 9617.

(41) Hunt, N. T.; Kattner, L.; Shanks, R. P.; Wynne, K. *Journal of the American Chemical Society* **2007**, *129*, 3168.

(42) Mazur, K.; Heisler, I. A.; Meech, S. R. *The Journal of Physical Chemistry A* **2011**.

(43) Heisler, I. A.; Mazur, K.; Meech, S. R. *The Journal of Physical Chemistry B* **2011**, *115*, 1863.

(44) Santa, I.; Foggi, P.; Righini, R.; Williams, J. H. *The Journal of Physical Chemistry* **1994**, *98*, 7692.

(45) Turton, D. A.; Wynne, K. *The Journal of Chemical Physics* **2008**, *128*, 154516.

(46) Yamaguchi, S.; Mazur, K.; Heisler, I. A.; Shirota, H.; Tominaga, K.; Meech, S. R. *The Journal of Chemical Physics* **2011**, *135*, 134504.

(47) Ratajska-Gadomska, B.; Bialkowski, B.; Gadomski, W.; Radzewicz, C. *The Journal of Chemical Physics* **2007**, *126*, 184708.

(48) Turton, D. A.; Sonnleitner, T.; Ortner, A.; Walther, M.; Hefter, G.; Seddon, K. R.; Stana, S.; Plechkova, N. V.; Buchner, R.; Wynne, K. *Faraday Discussions* **2012**, *154*, 145.

(49) Xu, Q.; Souma, Y. *Topics in Catalysis* **1998**, *6*, 17.

(50) Castiglioni, M.; Deabate, S.; Garrone, E.; Giordano, R.; Onida, B.; Predieri, G.; Sappa, E. *Journal of Cluster Science* **1997**, *8*, 381.

(51) Xu, K.; Peng, H.; Lam, J. W. Y.; Poon, T. W. H.; Dong, Y.; Xu, H.; Sun, Q.; Cheuk, K. K. L.; Salhi, F.; Lee, P. P. S.; Tang, B. Z. *Macromolecules* **2000**, *33*, 6918.

(52) Souma, Y.; Tsumori, N.; Willner, H.; Xu, Q.; Mori, H.; Morisaki, Y. *Journal of Molecular Catalysis A: Chemical* **2002**, *189*, 67.

(53) Paul J, D. *Coordination Chemistry Reviews* **2004**, *248*, 2443.

(54) Kluwer, A. M.; Kapre, R.; Hartl, F.; Lutz, M.; Spek, A. L.; Brouwer, A. M.; van Leeuwen, P. W. N. M.; Reek, J. N. H. *Proceedings of the National Academy of Sciences of the United States of America* **2009**, DOI: 10.1073/pnas.0809666106.

(55) Song, L.-C.; Gai, B.; Wang, H.-T.; Hu, Q.-M. *Journal of Inorganic Biochemistry* **2009**, *103*, 805.

(56) Song, L.-C.; Luo, X.; Wang, Y.-Z.; Gai, B.; Hu, Q.-M. *Journal of Organometallic Chemistry* **2009**, *694*, 103.

(57) Wang, H.-Y.; Wang, W.-G.; Si, G.; Wang, F.; Tung, C.-H.; Wu, L.-Z. *Langmuir* **2011**, *26*, 9766.

(58) Zipoli, F.; Car, R.; Cohen, M. H.; Selloni, A. *Catalysis Today* **2011**, *165*, 160.

(59) Song, L.-C.; Wang, L.-X.; Yin, B.-S.; Li, Y.-L.; Zhang, X.-G.; Zhang, Y.-W.; Luo, X.; Hu, Q.-M. *European Journal of Inorganic Chemistry* **2008**, 291.

(60) Thomas, C. M.; Liu, T.; Hall, M. B.; Darensbourg, M. Y. *Inorganic Chemistry* **2008**, *47*, 7009.

(61) Tard, C.; Pickett, C. J. *Chemical Reviews* **2009**, *109*, 2245.

(62) Greco, C.; Fantucci, P.; De Gioia, L.; Suarez-Bertoa, R.; Bruschi, M.; Talarmin, J.; Schollhammer, P. *Dalton Transactions* **2010**, *39*, 7320.

(63) Streich, D.; Astuti, Y.; Orlandi, M.; Schwartz, L.; Lomoth, R.; Hammarström, L.; Ott, S. *Chemistry - A European Journal* **2010**, *16*, 60.

(64) Apfel, U.-P.; Halpin, Y.; Görls, H.; Vos, J. G.; Weigand, W. *European Journal of Inorganic Chemistry* **2011**, 581.

(65) Durgaprasad, G.; Bolligarla, R.; Das, S. K. *Journal of Organometallic Chemistry* **2011**, *696*, 3097.

(66) Erdem, Ö. F.; Schwartz, L.; Stein, M.; Silakov, A.; Kaur-Ghumaan, S.; Huang, P.; Ott, S.; Reijerse, E. J.; Lubitz, W. *Angewandte Chemie Int. Ed.* **2011**, *50*, 1439.

(67) Harb, M. K.; Apfel, U.-P.; Sakamoto, T.; El-Khateeb, M.; Weigand, W. *European Journal of Inorganic Chemistry* **2011**, 986.

(68) Cahoon, J. F.; Sawyer, K. R.; Schlegel, J. P.; Harris, C. B. *Science (New York, N.Y.)* **2008**, *319*, 1820.

(69) Hamm, P.; Zanni, M. *Concepts and Methods of 2D Infrared Spectroscopy*; Cambridge University Press: Cambridge, **2011**.

(70) Dunning Jr., T. H.; Hay, P. J. *In Modern Theoretical Chemistry*; III, H. F. S., Ed.; Plenum: New York, **1976**; Vol. 3, p 1.

(71) Hay, P. J.; Wadt, W. R. *Ab initio effective core potentials for molecular calculations. Potentials for the transition metal atoms Sc to Hg*; AIP, **1985**; Vol. 82.

(72) Hay, P. J.; Wadt, W. R. *Ab initio effective core potentials for molecular calculations. Potentials for K to Au including the outermost core orbitals*; AIP, **1985**; Vol. 82.

(73) Wadt, W. R.; Hay, P. J. *Ab initio effective core potentials for molecular calculations. Potentials for main group elements Na to Bi*; AIP, **1985**; Vol. 82.

(74) Lee, C.; Yang, W.; Parr, R. G. *Physical Review B* **1988**, *37*, 785.

(75) Miehlich, B.; Savin, A.; Stoll, H.; Preuss, H. *Chemical Physics Letters* **1989**, *157*, 200.

(76) Becke, A. *Journal of Chemical Physics* **1993**, *98*, 5648.

(77) Peng, C.; Schlegel, H. B. *Israel Journal of Chemistry* **1994**, *33*, 449.

(78) Peng, C.; Ayala, P. Y.; Schlegel, H. B.; Frisch, M. J. *Journal of Computational Chemistry* **1996**, *17*, 49.

(79) Gaussian 03 Revision B.03, M. J. F., G. W. Trucks, H. B. Schlegel, G. E. Scuseria, M. A. Robb, J. R. Cheeseman, J. A. Montgomery, Jr., T. Vreven, K. N. Kudin, J. C. Burant, J. M. Millam, S. S. Iyengar, J. Tomasi, V. Barone, B. Mennucci, M. Cossi, G. Scalmani, N. Rega, G. A. Petersson, H. Nakatsuji, M. Hada, M. Ehara, K. Toyota, R. Fukuda, J. Hasegawa, M. Ishida, T. Nakajima, Y. Honda, O. Kitao, H. Nakai, M. Klene, X. Li, J. E. Knox, H. P. Hratchian, J. B. Cross, C. Adamo, J. Jaramillo, R. Gomperts, R. E. Stratmann, O. Yazyev, A. J. Austin, R. Cammi, C. Pomelli, J. W. Ochterski, P. Y. Ayala, K. Morokuma, G. A. Voth, P. Salvador, J. J. Dannenberg, V. G. Zakrzewski, S. Dapprich, A. D. Daniels, M. C. Strain, O. Farkas, D. K. Malick, A. D. Rabuck, K. Raghavachari, J. B. Foresman, J. V. Ortiz, Q. Cui, A. G. Baboul, S. Clifford, J. Cioslowski, B. B. Stefanov, G. Liu, A. Liashenko, P. Piskorz, I. Komaromi, R. L. Martin, D. J. Fox, T. Keith, M. A. Al-Laham, C. Y. Peng, A. Nanayakkara, M. Challacombe, P. M. W. Gill, B. Johnson, W. Chen, M. W. Wong, C. Gonzalez, and J. A. Pople, **2003**.

(80) Tye, J. W.; Darensbourg, M. Y.; Hall, M. B. *Journal of Computational Chemistry* **2006**, *27*, 1454.

(81) Feng, X.; Gu, J.; Xie, Y.; King, R. B.; Schaefer, H. F. *Journal of Chemical Theory and Computation* **2007**, *3*, 1580.

(82) Persson, B. J.; Taylor, P. R. *Theoretical Chemistry Accounts: Theory, Computation, and Modeling (Theoretica Chimica Acta)* **2003**, *110*, 211.

(83) Cotton, A. F.; Troup, J. M. *Journal of the American Chemical Society* **1974**, *96*, 4155.

(84) Yu, L.; Greco, C.; Bruschi, M.; Ryde, U.; De Gioia, L.; Reiher, M. *Inorganic Chemistry* **2011**, *50*, 3888.

(85) Zheng, J.; Kwak, K.; Fayer, M. D. *Accounts of Chemical Research* **2007**, *40*, 75.

(86) Bonner, G. M.; Ridley, A. R.; Ibrahim, S. K.; Pickett, C. J.; Hunt, N. T. *Faraday Discussions* **2010**, *145*, 429.

(87) Kaziannis, S.; Wright, J. A.; Candelaresi, M.; Kania, R.; Greetham, G. M.; Parker, A. W.; Pickett, C. J.; Hunt, N. T. *Physical Chemistry Chemical Physics: PCCP* **2011**, *13*, 10295.

5. Investigating the Vibrational Dynamics of a metalcarbonyl dimer and its $17e^-$ photoproduct using Ultrafast Multidimensional Infrared Spectroscopy.

The family of ultrafast 2D-IR spectroscopy[1-4] techniques is rapidly evolving toward novel spectroscopic techniques that exploit molecular vibrations to obtain structural and dynamical information about the solution environment. There are two characteristics that set 2D-IR spectroscopy apart from earlier time-resolved infrared spectroscopic techniques: a two dimensional representation of the spectra and the ability to frequency resolve separate contributions to vibrational relaxation mechanisms. A two-dimensional spectrum allows the representation of vibrational coupling as cross-peaks that link peaks of fundamental molecular vibrations located on the diagonal of the spectrum while the 2D lineshapes can report on the strength and dynamics of solute-solvent interactions. The dynamics of 2D spectral features reveal vibrational relaxation processes which typically display two contributions. The first, faster component is from Internal Vibrational Relaxation representing rate of energy redistribution among coupled vibrational modes while the second component arises from overall population relaxation resulting from dissipation of vibrational energy to the environment.

These characteristic features of a 2D-IR spectrum carry information relating to molecular structure permitting determination of the structure and geometry of molecules in a liquid environment.[1,3-17] Owing to this capacity 2D-IR is frequently compared to the 2D-NMR spectroscopy technique that revolutionised structural research in the fields of chemistry and biology.[18] In contrast to NMR, ultrafast 2D-IR spectroscopy offers far higher temporal resolution and sensitivity to transient molecular geometry changes. The picosecond temporal resolution of 2D-IR has found applications not only in the determination of vibrational dynamics and solute interactions,[19-39] but also to the study dynamics of ultrafast chemical processes.[31,32,40-49] Crucially, the mid-infrared radiation used in these experiments carries insufficient energy to initiate chemical processes giving accesses to ultrafast chemical dynamics at equilibrium in the electronic ground state.

Still, many chemical species such as metalcarbonyls display interesting non-equilibrium chemical dynamics.[50-55] Important optical spectroscopy approach used to explore the ultrafast photochemistry of these species to date is time resolved femtosecond UV_{pump}-IR_{probe} (TR-IR) and UV_{pump}-UV_{probe} spectroscopy.[56,57] This one-dimensional technique however suffers from several limitations. The UV radiation excitation trigger molecule dissociation producing multiple chemical species with overlapping spectral features making results interpretation difficult. Additionally, the vibrational relaxation dynamics are represented on TR-IR spectra as line narrowing, further complicating interpretation and providing only a crude estimation of the process timescale. To address the limitations of TR-IR method a new spectroscopic tool was created by the incorporation of a UV pump pulse into 2D-IR spectroscopy leading to two complementary techniques: T2D-IR EXSY spectroscopy[52,58] for investigations of excited state molecules and Transient 2D-IR spectroscopy[14,52,59-65] for the study of transients and photoproducts. Transient 2D-IR is the main focus of this chapter and can be portrayed as an extension of femtosecond TR-IR spectroscopy, where the dynamic spectral changes induced by UV irradiation is monitored by 2D-IR spectroscopy rather than the more straightforward absorption methods of TRIR. Such an approach thus brings the benefits of ultrafast 2D-IR spectroscopy to bear on studies of short lived transient molecules and photochemical reactions. This approach comes with limitations that arise from using a combination of UV and three IR wave-matter interactions that produce a far weaker signal than a ground state 2D-IR spectroscopy experiment with signals displaying intensities more akin to 5^{th} order non-linear techniques, which of course T2D-IR technically is. Other problems arise for short lived transients due to the initial vibrational excitation that is introduced by the UV pulse overlapping with the pulses used for 2D-IR spectrum acquisition. However, the latter effect can be utilized for studies of spectral diffusion.[52] Despite this, Transient 2D-IR methods have already proven to be useful in gaining insights into the solvation dynamics of electronically excited states,[66,67] photo-triggered conformational changes of small peptides,[59] excited state exchange processes[68] and irradiation induced T-jump triggering of protein unfolding process.[61] Most recently, Transient 2D-IR spectroscopy has been applied to photolysis cascades of metalcarbonyls allowing IR spectroscopic signatures of photoproduct species to be

observed[69] along with studies of rotational relaxation dynamics of the parent molecule.[70] This last example represent the most recent combined application of higher dimensionality infrared techniques to the study of ultrafast chemical dynamics of a system exhibiting ground state conformational isomerism and complex photochemistry.

In this chapter, studies of equilibrium and non-equilibrium vibrational relaxation dynamics are reported. 2D-IR is used to investigate the spectroscopy and vibrational relaxation of $[(C_3H_7)CpW(CO)_3]_2$ (**3**) and $[CpW(CO)_3]_2$ (**3'**) (Cp = η^5-cyclopentadienyl ligand) dimers including studies of different conformeric forms present in solution while Transient 2D-IR methodologies are employed to investigate the 17e$^-$ radical species $(C_3H_7)CpW(CO)_3\cdot$(**4**) and $CpW(CO)_3$ (**4'**), formed via photolysis of the intermetallic bond.

Metalcarbonyls are one of the oldest known organometallics and are widely used as precursors for the synthesis of complex molecules containing Metal-Carbon bonds and as catalysts owing to their inherently low oxidation state.[71] Polymetallic metalcarbonyls have been found to be particularly useful in the catalysis of important industrial processes such as the water gas shift reaction[72] and the Fischer-Tropsch process[73] for carbon-based fuel production. Among these, particular interest has been shown in dimeric compounds that have already been proven to be useful in hydrogen gas generation.[74-76] In addition, sterically crowded metalcarbonyl dimers such as $[CpW(CO)_3]_2$ are known to form stable radicals upon UV irradiation, opening up new frontiers in the catalysts for initiation of polymerisation reactions as well as living polymerisation.[77] Several studies have been devoted to determining the structure, conformational isomerisation and photochemistry of $[CpW(CO)_3]_2$ using X-ray diffraction, NMR, and femtosecond TR-IR spectroscopy.[78-83] It has also been established that dissolution of this compound leads to slow conformational isomerisation while photolysis leads to the generation of a relatively stable 17e$^-$ intermediate species.[78-80]

5.1. Experimental

The dimers $[(C_3H_7)CpW(CO)_3]_2$ (**3**) and $[CpW(CO)_3]_2$ (**3'**) were purchased from Acros and Sigma-Aldrich respectively. Spectroscopic grade dichloromethane

(DCM) and n-heptane were obtained from Fluka AG. All chemicals were used without further purification. Both compounds and their solutions were handled entirely under a protective atmosphere and away from ambient light due to their air and light-sensitive natures. All solvents were degassed by purging with nitrogen prior to preparing solutions. For FT-IR and 2D-IR measurements, the samples were held in airtight cells (Harrick Scientific) consisting of a pair of CaF_2 windows separated by a 200μm thickness PTFE spacer while for Transient 2D-IR studies the cell content was continuously refreshed by closed-loop circulation with bulk solution in a nitrogen-purged reservoir. An in-line 0.2 μm filter was employed to remove any particulate matter resulting from compound photodegradation, which may have led to artefacts due to light scattering. Additionally, the sample cell was rastered in two dimensions to prevent window damage. The concentration of the solutions was adjusted to yield the desired main peak optical density of around 0.5 in the carbonyl ligand stretching mode (ν_{CO}) region, which corresponded to an optical density of around 0.16 at the UV_{pump} frequency. The latter was chosen to be 490 nm, which is coincident with the low-lying charge transfer transition for this compound.

Steady state FT-IR spectra were recorded on a Bruker Vertex 70 spectrometer in a standard cell while temperature dependent measurements were performed in a thermostatically controlled cell (Harrick Scientific model TFC-525-3) accurate to ±0.1 K. Spectra of the neat solvents and the solutions were collected in the temperature range from 288-363 K for **3** in heptane and 268-308 K for **3'** in DCM allowing preliminary studies of conformational equilibrium within the limits defined by the boiling points of the solvents used.

5.1.1. Transient 2D-IR spectrometer

The 2D-IR and Transient 2D-IR spectra were recorded on the ULTRA laser system at the Central Laser Facility of the Rutherford Appleton Laboratory as a part of larger collaborative project involving the development and application of 2D-IR spectroscopy. The ULTRA Multidimensional infrared spectrometer employed quasi frequency-domain double resonance 2D-IR with some modifications to the established methodologies.[4,34,84,85] The basis of the system was a 65 MHz, Ti:Sapphire oscillator seeding dual synchronised regenerative amplifiers each

operating at a repetition rate of 10 kHz (Thales). Both cavities produced pulse trains at a wavelength of 800 nm though with different pulse durations; one was used to generate amplified pulses with a broad bandwidth and pulse duration of 50 fs, while the second produced narrow bandwidth pulses of around 1 ps duration. The output of the ps pulse duration amplifier was used to pump a white-light seeded optical parametric amplifier (OPA) equipped with difference frequency mixing of the signal and idler beams to produce the narrow band infrared pump radiation leading to tuneable frequency infrared pulses with 10-12 cm^{-1} bandwidth. The UV frequency pump was generated by using a second portion of the ps regenerative amplifier output to pump a third OPA unit equipped with 4^{th} harmonic generation to reach the UV-Vis frequency range needed. The IR probe pulses originated from an OPA pumped by the 50 fs duration pulse train from the second amplifier and yielded pulses centred near 1980 cm^{-1} with a bandwidth of around 400 cm^{-1}.

All beams were focused and spatially overlapped in the sample using calcium fluoride lenses and the samples were held in a cell (Harrick Scientific) between 2mm thick CaF_2 windows separated by PTFE spacers. The transmitted probe radiation was dispersed on a grating and detected on a 256-element HgCdTe detector (Kunming Institute of Physics (China)) giving an effective spectral resolution of 2 cm^{-1}. The interpulse time delays were controlled by optical delay lines located in UV and IR pump paths. The relative polarization of the IR pump beam was set by a half wave plate and polariser to the magic angle to remove the effects of molecular rotation while UV pump radiation polarisation was left parallel to the infrared probe beam. To facilitate the acquisition of pump on/off difference spectra, a chopper was used to modulate pump pulse train. The 2D-IR measurements required a chopper operating at half the laser repetition rate (5 kHz) modulating the infrared pump pulse train. For Transient 2D-IR measurements two choppers were required, one was used to modulate the infrared pump beam at half the laser repetition rate (5 kHz) while the second was used in the UV pump beam path and operated at a quarter of the laser repetition rate (2.5 kHz). This method allowed collection of the linear infrared spectrum IR_{probe} (UV_{pump}=IR_{pump}=off), TR-IR spectrum (UV_{pump}=on, IR_{pump}=off), 2D-IR spectrum (UV_{pump}=off, IR_{pump}=on) and T2D-IR spectrum (UV_{pump}=on, IR_{pump}=on) in consecutive laser shots. The 2D-IR spectrum represents the difference

between the linear infrared spectrum with and without the IR_{pump}. Similarly, the Transient 2D-IR spectrum is the difference spectrum showing the effect of the UV_{pump} pulse on the 2D-IR spectrum.

5.1.2. Data Analysis

The spectro-temporal data matrix f(ν,t) from the time-resolved 2D-IR and T2D-IR measurements with fixed pump frequencies were represented as a sum of Voigt line shapes $V_i(\nu)$ with an associated temporal decay function $T_i(t)$ shown in Eq. 27.

$$f(\nu,t)=\sum_{i}^{n} V_i(\nu)\cdot T_i(t) \tag{27}$$

The applied Voigt line shape is a 50/50 per cent convolution of Gaussian and Lorentzian line shapes and produced a better fit to the experimental data than pure Gaussian line shape approach outlined in Eq. 25 (p. 69). The complex nature of Voigt line shape generation renders the global analysis approach computation ineffective hence, a proper set of Voigt peaks with fixed position and peak width was found experimentally and used for all time delays. To separate the spectral function $V_i(\nu)$ from the temporal part $T_i(t)$ the chosen set of Voigt peaks was fit to all available time slices with only peak amplitudes free to vary. The temporal function $T_i(t)$ was recovered by fitting the time dependence of the Voigt peak amplitude using single- or bi-exponential functions. The results of the temporal function fit were found to be comparable to those from fitting the peak amplitude against pump-probe delay time, signifying the validity of the Voigt peak fitting method.

5.1.3. Density Functional Theory calculations

All DFT calculations were carried out using the Gaussian 03 package using the functionals, basis sets and optimization algorithms previously discussed.[86-95] Identification of the transition state energy between the *anti* and *gauche* conformers and calculation of the barrier to rotation about the inter-metallic bond were carried out through structure optimisations for fixed values of the Cp-W-W-Cp dihedral angle in the range 60^o to 180^o.

5.2. Results

5.2.1. Steady state FT-IR spectroscopy

The FTIR spectra of a solution of **3** in n-heptane and **3'** in DCM at 298 K are shown in Fig 31. When dissolved, **3** displays three intense bands at 1898, 1909 and 1955 cm^{-1} alongside a fourth much weaker band at 2013 cm^{-1}. The compound **3'** dissolved in DCM displays two intense bands at 1904 and 1954 cm^{-1} alongside a third, weaker transition at 2011 cm^{-1}. The lowest frequency band displays a low frequency shoulder resulting from the overlap of two transitions, which are observed separately for **3** in heptane solution. This is due to broadening of the absorption lines of **3'** in polar DCM solutions in comparison to heptane. Indeed, the linewidth of peaks originating from the single transition located near 1955 cm^{-1} was 3 and 10 cm^{-1} in heptane for **3**, and DCM for **3'** respectively. In addition, the high frequency band is far more prominent in the **3'** solution. The similarity of the ν_{CO} region infrared spectral features are to be expected owing to the fact that the heptane soluble **3** is a Cp ring substituted derivative of **3'** with an unaltered $[M(CO)_3]_2$ moiety. The observed differences in the FT-IR spectra are largely controlled by the solvent: DCM, unlike n-heptane, exhibits a considerable dipole moment (1.6 D), which is one of the factors that determine the strength of solute-solvent interactions. Such an increased strength of solute-solvent interactions in DCM results in the broadening of spectral lines and shifting concentration ratio of the two possible structural conformers. The first effect could be associated with acceleration of coherence dephasing process due to stronger solute-solvent interactions while the second phenomenon can be explained by considering the effects of solvent change on free formation energy of each conformeric form.

The spectral data is in good agreement with previous studies of **3'**, which have been assigned the most intense line at 1954 cm^{-1} to the a_u symmetry mode of the *anti* isomer while the shouldered transition at 1904 cm^{-1} were attributed to the two b_u symmetry modes.[78] In addition, the FTIR spectrum in Fig. 31 showed a very weak *a* symmetry mode near 2011 cm^{-1}, which is attributed to the small fraction of *gauche* conformer present in solution.[78,82,83] The population of this species is somewhat greater in polar DCM and the band is more clearly observed on this spectrum. This effect is attributed to the molecular symmetry changes in rotation of

monomeric units. The **3'** compound *anti* form is centrosymmetric and hence displays no dipole moment while the *gauche* form, owing to the acute angle twist of the monomeric units [$CpW(CO)_3$] displays a large dipole moment, estimated to be about 8D by DFT calculations.

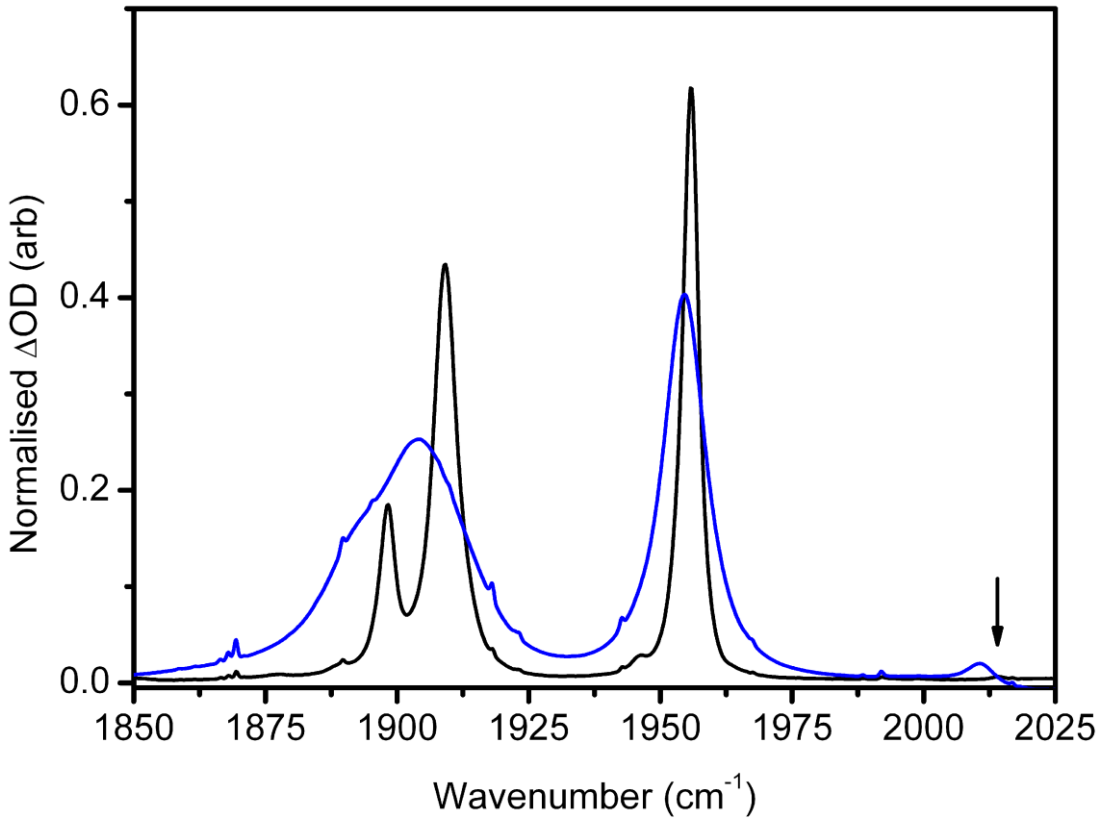

Figure 31. The ν_{CO} region of FT-IR spectrum of solutions of **3** in heptane (black) and **3'** in DCM (blue) at 298K. The arrow indicates fourth band position in **3** spectrum.

Further support for this conformeric equilibrium can be obtained from the thermal dependence of the FTIR spectra of **3** and **3'** shown in Figure 32. A series of spectra show that increasing temperature leads to an intensity decrease of the main ν_{CO} peaks and a concomitant gain in the intensity of the 2013 (2011) cm^{-1} peaks as expected for thermal redistribution of isomeric forms.

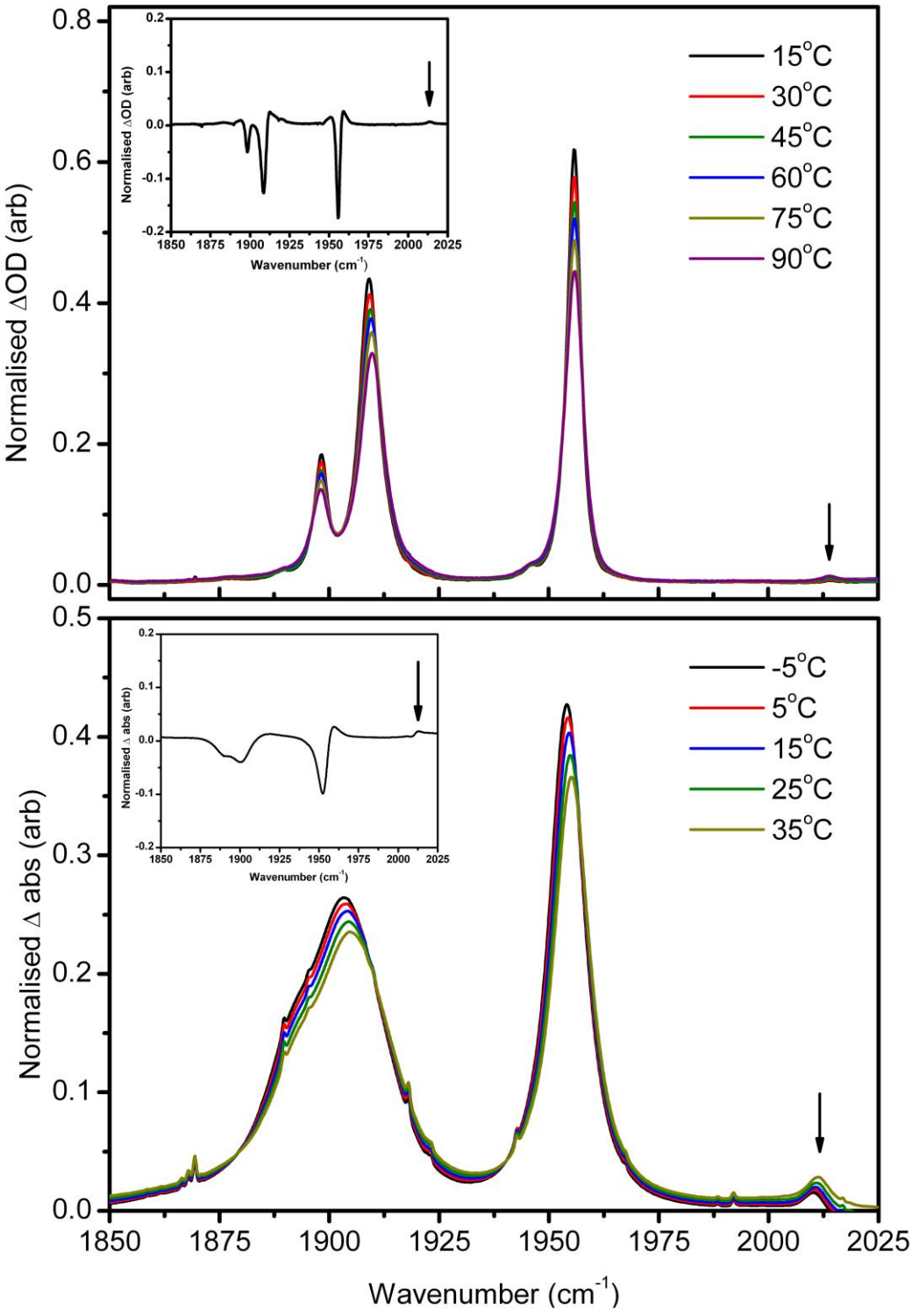

Figure 32. The temperature induced FT-IR spectrum changes for solution of **3** in n-heptane (top) for 15°C to 90°C range and **3'** in DCM (bottom) for -5°C to 35°C range. Insets show the difference spectrum for maximal and minimal temperatures with arrow indicating temperature correlated absorption rise of *gauche* isomer transition.

Analysis of the temperature dependence of the concentration ratio of the conformers based upon the intensities of the observed bands, assuming no variation of the molar extinction coefficient with temperature, suggests an isomerisation reaction enthalpy difference of ~ 11 and 12 kJ/mol for **3** and **3'**, respectively. This value is broadly in agreement with the DFT estimated formation energy difference of 21.3 kJ/mol calculated for **3'** *in vacuo*.

5.2.2. 2D IR spectroscopy

5.2.2.1. 2D-IR spectroscopy of 3 in heptane solution

The 2D-IR spectrum of **3** in heptane solution with a pump-probe delay time of 2.5 ps is shown in Fig 33. As expected, peaks are observed lying on the diagonal of the 2D-IR spectrum with (probe, pump) coordinates of (1955, 1955) and a double feature at (1910, 1910); both are marked by a circled number *1* in the figure. The peaks lying directly on the spectrum diagonal are negative features corresponding to bleaches of the ν = 0-1 transitions of the *anti* isomer observed in the FT-IR spectrum. Each diagonal bleach is also accompanied by a positive feature assignable to a transient absorption corresponding to the accompanying ν = 1-2 transition. The latter are red shifted along the probe frequency axis by 4-9 cm^{-1} due to local mode anharmonicity. The diagonal transitions of the two b_u symmetry modes of the *anti* isomer near 1898 cm^{-1} and 1909 cm^{-1} appear in the 2D-IR spectrum as a series of vertically elongated bands due to the presence of nearby off-diagonal peaks and convolution of the line shapes with the pump frequency bandwidth profile.[84] The positions of the diagonal and off-diagonal peaks in this region are more clearly seen in cross sections of the spectrum, as will be discussed subsequently. The diagonal features do not show evidence of inhomogeneous broadening, in the form of diagonal elongation of the 2D profile as has been observed for several other studies of metalcarbonyl molecules in heptane solution.[34,38]

In addition to the pairs of resonances observed on the diagonal of the spectrum, further such pairs appear in the off-diagonal region (marked with a circled *2* in the figure). Those corresponding to the *anti* isomer appear with coordinates of (1910, 1955) and (1955, 1910), linking the diagonal features due to the a_u mode with those due to the two b_u modes, indicating the presence of vibrational coupling and

population transfer between the carbonyl stretching modes of the *anti* conformer as is consistent with previous 2D-IR studies of metalcarbonyls.[19,34,38,39,46,96,97]

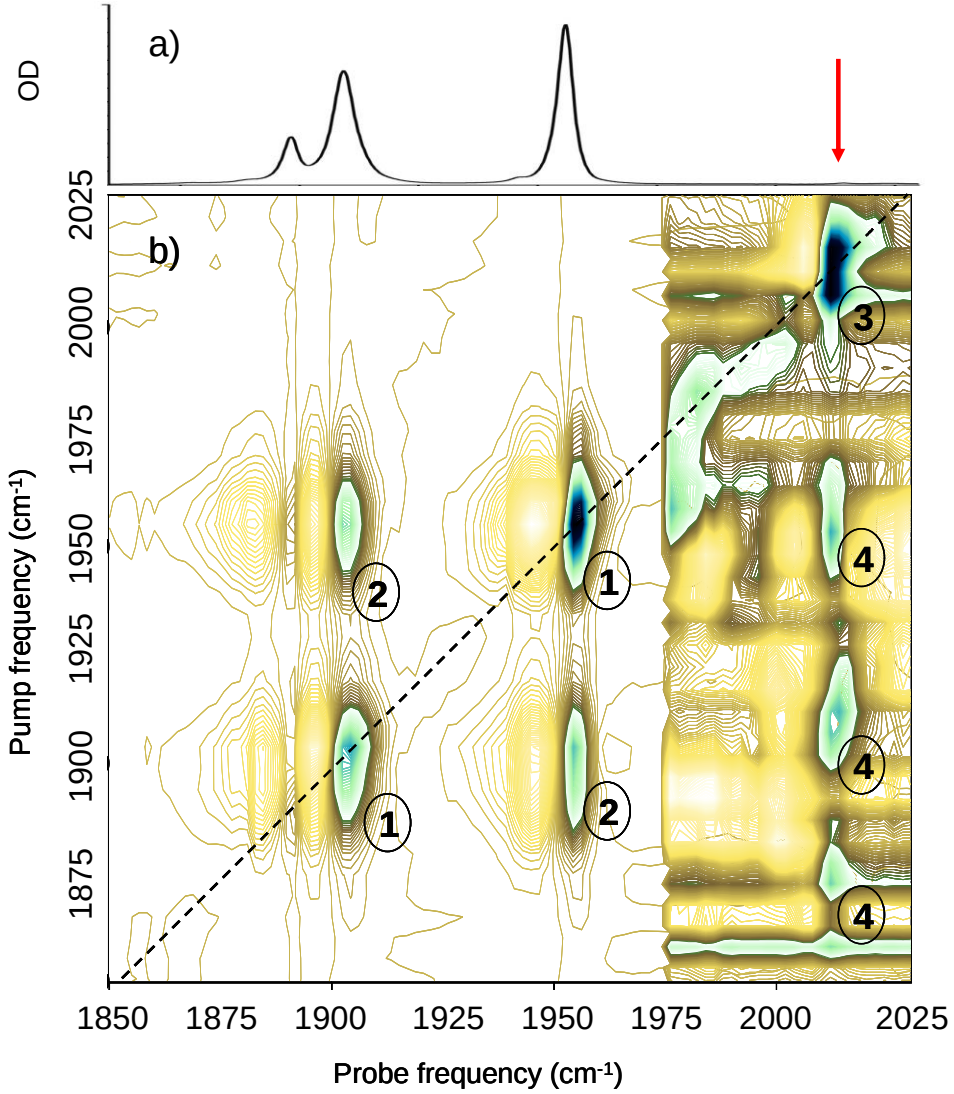

Figure 33. (a) FT-IR spectrum of a solution of **3** in heptane at 303 K (b) The 2D-IR spectrum of a similar solution obtained with a pump-probe delay time of 2.5 ps. The data at probe frequencies greater than 1980 cm^{-1} has been magnified to reveal the presence of weak bands due to the *gauche* isomer (see text). The colour spectrum runs from blue (negative) to yellow (positive)

These features are also shown in Fig. 34a, which displays a horizontal slice throughout the 2D-IR spectra at pump frequency of 1955 cm^{-1}. The slice features three clearly defined peak pairs belonging to the *anti* conformer.

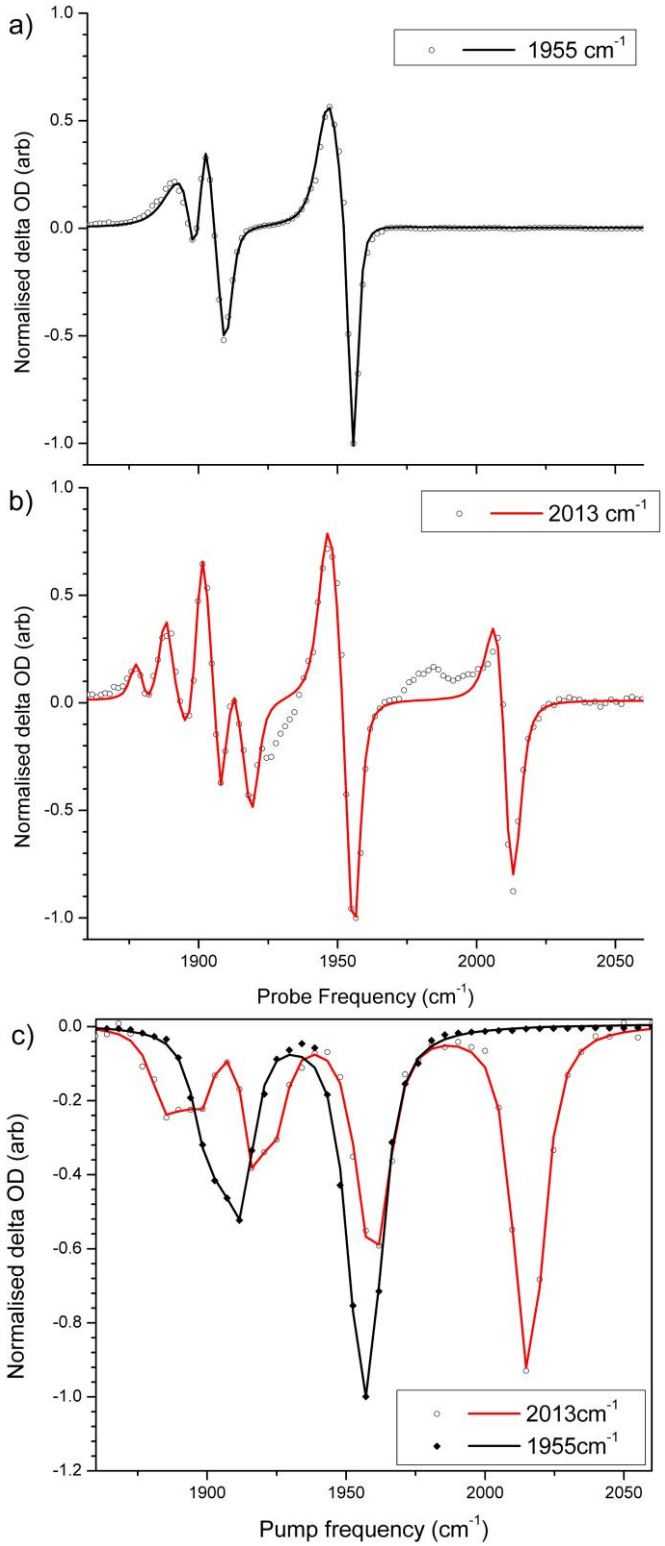

Figure 34. (a) Horizontal slice through the 2D-IR spectrum shown in Fig 33b at a pump frequency of 1955 cm^{-1} (b) similar slice taken at a pump frequency of 2013 cm^{-1} (c) vertical slices through the 2D-IR spectrum at probe frequencies of 1955 and 2013 cm^{-1}. The slices have been scaled to allow comparisons to be made.

The six Voigt lines fit to the horizontal slice shown in Fig 34a returned the positions of three negative and three positive features which are listed in Table 4. As expected, the negative features are coincidental with the *anti* conformer ν = 0-1 fundamental transitions determined from the FT-IR spectrum confirming the validity of the 2D-IR spectrum assignment.

The 2D-IR spectrum displayed in Fig 33b also shows a diagonal peak at (2013, 2013), marked with a circled *3* in the figure. This corresponds to the peak in the FT-IR spectrum assigned to the *gauche* conformeric form of **3**. Owing to the much smaller population of the *gauche* form (~1.5%), this peak is close to two orders of magnitude smaller than the diagonal peaks due to the *anti* isomer. To compensate for this, the scale has been expanded in this region of the plot and it can be seen that this feature also consists of a positive-negative pair of peaks with a similar probe-frequency separation to those of the *anti* conformer. It is interesting to note the pattern of off-diagonal resonances accompanying this *gauche* isomer diagonal peak. These are marked with a circled *4* in the figure and appear at (2013, 1962), (2013, 1916) and (2013, 1880). These are less clear in horizontal cross section at 2013 cm^{-1} pump frequency displayed in Fig 34b, due to overlap with contributions from the intense *anti* isomer transitions. The latter could arise from spectral artefacts or exchange processes and will be discussed further in more detail. Still there are features in Fig 34b that are not observed in Fig 34a when the *anti* isomer a_u mode was pumped. The slice fitting process shown in Fig 34b and in Table 4 involved the sum of twelve Voigt line profiles and confirmed the existence of additional peak pairs of which negative features were observed at 2013, 1916 and 1880 cm^{-1} coinciding with those found on the 2D-IR spectrum. It is noted that the features not fitted in Fig 34b are noise artefacts visible due to the reduced signal strength and were found not to be reproducible.

The comparison of vertical slices through the 2D-IR spectrum at a probe frequency of 2013 cm^{-1} and 1955 cm^{-1} shown in Fig 34c provides a full account of the spectral differences arising from the presence of two isomeric forms. The 1955 cm^{-1} probe frequency slice displays two lines located 1955 and 1909 cm^{-1} with a lower frequency feature showing a distinctive low frequency shoulder and a far larger line width (Table 4).

Table 4. Results of fitting slices through 2D-IR spectra shown in Figure 33(a-c) to the sum of Voigt line profiles.

		3 in n-Heptane (ps)	
Pumped transition (cm^{-1})	2D-IR spectrum Peak [freq label[a]/cm^{-1}] (v=i-j)	Peak Position [cm^{-1}]	Width [cm^{-1}]
1955 (Fig 34a) – *anti* isomer			
	Diagonal [1955] (0-1)	1955.6	3.88
	Diagonal [1955] (1-2)	1946.9	7.96
	Off-Diagonal [1909] (0-1)	1909.5	7.09
	Off-Diagonal [1909] (1-2)	1902.6	7.55
	Off-Diagonal [1898] (0-1)	1898.5	5.61
	Off-Diagonal [1898] (1-2)	1894.2	14.65
2013 (Fig 34b) – *gauche* isomer			
	Diagonal [2013] (0-1)	2012.3	7.85
	Diagonal [2013] (1-2)	2008.8	10.17
	[b]Off-Diagonal [1955] (0-1)	1955.6	5.79
	[b]Off-Diagonal [1955] (1-2)	1946.9	8.52
	Off-Diagonal [1916] (0-1)	1919.0	6.18
	Off-Diagonal [1916] (1-2)	1912.9	2.75
	[b]Off-Diagonal [1909] (0-1)	1908.0	3.68
	[b]Off-Diagonal [1909] (1-2)	1901.4	5.45
	[b]Off-Diagonal [1898] (0-1)	1895.9	6.00
	[b]Off-Diagonal [1898] (1-2)	1888.1	5.17
	Off-Diagonal [1880] (0-1)	1881.5	3.69
	Off-Diagonal [1880] (1-2)	1877.5	5.17

Probed frequency [cm^{-1}]	2D-IR Peak [pump freq/cm^{-1}]		
1955 (Fig 34c) - *anti*			
	Diagonal [1955]	1957	14
	Off-Diagonal [1909]	1908	20
2013 (Fig 34c) - *gauche*			
	Diagonal [2013]	2016	13
	Off-Diagonal [1962]	1960	14
	Off-Diagonal [1916]	1920	15
	Off-Diagonal [1880]	1890	21

a) Frequency label refers to text rather than actual fitted position.

b) Indicates contamination from lines due to *anti* isomer.

While the 2013 cm^{-1} probe frequency slice displays four lines located at 2013, 1962, 1916 and 1880 cm^{-1}. Since vertical slices through the 2D-IR spectrum display all coupled vibrations to the one selected by the probe frequency ω_3 the discussed slices contain peak patterns characteristic to the solute internal structure. Hence it is reasonable to assign those features to the *anti* and *gauche* isomers of **3**, respectively. It is to be noted that *gauche* isomer displays a characteristic vibrational frequency at 1962 cm^{-1} very close to the 1955 cm^{-1} frequency feature of the *anti* isomer used in the first vertical slice.

In order to add weight to this assignment, DFT calculations were carried out to simulate the infrared spectrum of each conformeric form. The results of the DFT calculations for the *anti* and *gauche* conformations of **3'** are shown in Fig 35.

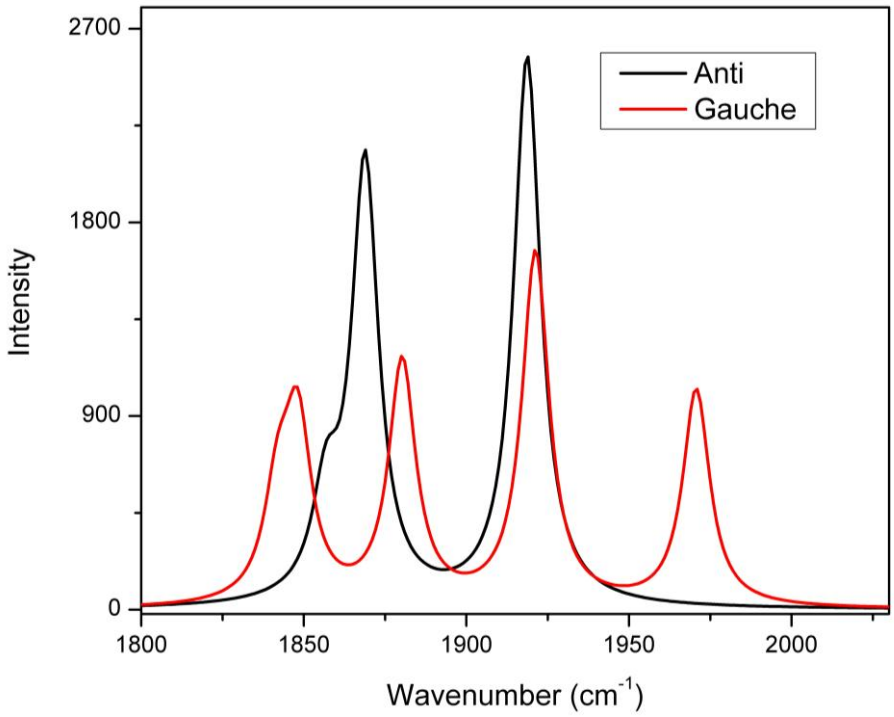

Figure 35. The results of DFT calculations of the gas phase infrared spectrum of **3'** conformers in the carbonyl stretching region of the IR.

As the only structural difference between **3** and **3'** is the presence of a propyl substituent on the Cp rings, all calculations were carried out on **3'** in order to reduce the required computational expense. Owing to the evident similarity of the structural motifs and infrared spectra of **3** and **3'** the DFT simulation results are expected to be comparable. It is clear that the overall pattern of the bands predicted is in excellent

agreement with those observed via 2D-IR spectroscopy, confirming the previous assignment. The absolute frequencies are somewhat underestimated as has been shown to be typical of the DFT calculations with the B3LYP functional and double-ζ basis set employed.[34,94,95]

The presence of apparent cross peaks between the pumped *gauche* isomer transition at 2013 cm^{-1} and the *anti* isomer features at 1955, 1909 and 1898 cm^{-1} on Fig. 34b is somewhat unexpected and could be due either to ultrafast conformational isomerisation or to collective excitation of both conformers resulting from band overlap. The latter case is particularly likely in the case of the 1955 cm^{-1} pump frequency, which according to the off-diagonal *gauche* isomer peak pattern (Fig. 33b) and DFT results (Fig. 35), appears to coincide with transitions due to both isomers. In the case of isomeric exchange, a molecule excited in the *gauche* form, but undergoing isomerisation on the timescale of the experiment prior to the arrival of the probe pulse would lead to the appearance of cross peaks at the frequency of the modes due to the *anti* form as observed for Berry pseudo-rotation in $Co_2(CO)_8$ [46] and $Fe(CO)_5$ [98] or ultrafast proton exchange reactions.[32,33,41,42,45,47-49] These cross peaks would be expected to grow in the spectrum as the pump-probe time delay approached that of the conformational exchange timescale. The presence of cross peaks due to both isomeric forms in the slice taken at a pump frequency of 2013 cm^{-1} from the very earliest pump-probe delay times would seem to indicate that exchange is an unlikely explanation for these peaks. This would suggest a very rapid rotation time for the Cp-W-W-Cp dihedral angle whereas NMR coalescence spectroscopy measurements suggest that the timescale for isomerisation of **3'** to be on the order of ms rather than a few ps.[82,83] Furthermore, analysis of changes in the optimised energy as a function of rotation about the Cp-W-W-Cp dihedral angle over the range 60^o-180^o shows a calculated energy barrier E_a of 71.4 kJ/mol for *anti* to *gauche* isomerisation of which 50.1 kJ/mol is an activation energy required by the process in both directions. This is in good agreement with the previously reported value of 63 kJ/mol,[83] leading to the conclusion that isomeric exchange is unlikely on picosecond timescales. Thus, the horizontal slices at pump frequencies coinciding with transitions of either the *anti* or *gauche* isomer contains bands due to both conformers as a result of collective excitation. In the case of the *anti* conformer

collective excitation is due to the proximity of *gauche* transitions that are small in comparison to the pump frequency bandwidth true for all modes. In the case of pumping the *gauche* transitions at 2013 cm^{-1} the intensity of 1955 cm^{-1} *anti* isomer transition at this pump frequency is sufficient to produce *anti* isomer modes with comparable intensity to *gauche* isomer.

5.2.2.2. 2D-IR spectroscopy of 3' in DCM solution

The FTIR and 2D-IR spectra of **3'** in DCM solution are displayed in Figs 36a and b, respectively the latter was obtained with a pump-probe delay time of 2.5ps. Again comparison of 2D-IR spectra underlines the similarities of these closely related derivatives. As in Fig. 33 the lines due to the a_u and b_u modes of **3'** are clearly observed in the FTIR spectrum (Fig. 36a) and on the diagonal of the 2D-IR spectrum (Fig. 36b), the latter are labelled with a circled *1* on the 2D-IR plot. The broader line widths of the carbonyl stretching bands of **3'** in polar DCM do however result in somewhat less well-resolved spectra for this combination of solute and solvent, which has led to the coalescence of the two b_u modes in both spectra. The diagonal features are linked by pairs of off-diagonal features (marked *2*) as would be expected for vibrational coupling of *anti* isomer bands as observed for **3** in heptane. Once again, no distinctive diagonal elongation was observed indicative of inhomogeneous broadening.

The main difference between the spectra obtained for this system and those obtained for **3** in heptane lies in the relative intensities of the features due to the *gauche* and *anti* isomers. In the case of the polar solvent the slightly larger population of the *gauche* form leads to stronger features attributable to this in the 2D-IR spectrum. These are once again marked with a circled *3* in the plot for the diagonal peak at (2011, 2011) and a circled *4* for the off diagonal peaks at (2011, 1954), (2011, 1904) and (2011, 1880). These positions are less definitive than those obtained for **3** in heptane however because the contributions to the horizontal and vertical slices at pump and probe frequencies of 2011 cm^{-1} respectively from peaks due to the *anti* isomer are somewhat exacerbated in this case, such that the distinct transitions due to the *gauche* isomer are not as clearly observable.

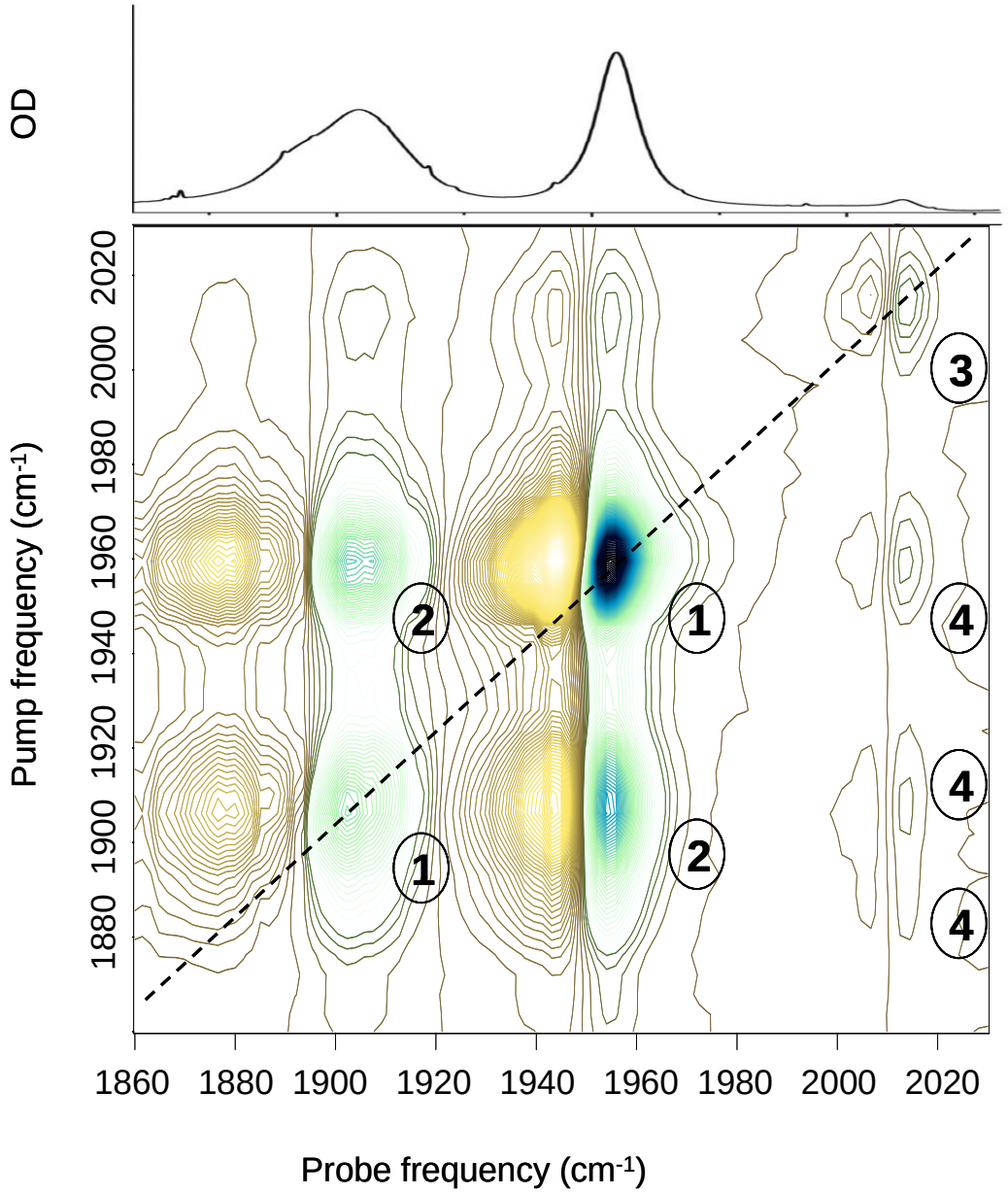

Figure 36. (a) FT-IR spectrum of **3'** in DCM at 303 K (b) The corresponding 2D-IR spectrum obtained with a pump-probe delay time of 2.5 ps. The colour spectrum runs from blue (negative) to yellow (positive)

This is due to the broadening of the transitions caused by the polar solvent, which makes it virtually impossible to avoid pumping lines due to both isomeric forms. Despite this, fitting the horizontal slice taken at a pump frequency of 1955 cm^{-1} (*anti* isomer) to Voigt line shapes and comparing these results to a similar fit of the horizontal slice taken at 2011 cm^{-1} (*gauche* isomer) indicates the presence of an additional low frequency band in the latter slice, which can be reasonably assigned to

the lowest energy transition of the *gauche* isomeric form following the arguments for **3** above. This was supported by examination of the corresponding vertical slices. All other *gauche* isomer cross-peaks were obscured by broader *anti* isomer transitions for this solvent.

5.2.3. Transient 2D-IR spectroscopy

5.2.3.1. Time-resolved infrared spectroscopy of 3 in heptane

Prior to interpreting Transient 2D-IR data, the TR-IR spectra of **3** in heptane, irradiated at 490 nm for a range of UV_{pump}-IR_{probe} delays up to 1 ns with magic angle pump-probe polarization conditions were recorded in order to ascertain the spectrum and lifetime of the monomeric $17e^-$ radical species **4** in solution. The photochemistry of **3'** in DCM solution has been well-studied, principally by the groups of Harris[78,80] and Westwell[81] and the results obtained for **3** in heptane are very similar. The TR-IR data are shown in Fig 37a in which bleaches at 1955 and 1909 cm^{-1} reveal the loss of the a_u and b_u modes of **3** respectively, while the two positive peaks at 2000 and 1890 cm^{-1} are assignable to the a_1 and e modes of **4**.[81] It was established that the population decay of **4** in heptane could be well represented by a double-exponential decay function with time constants of 100 ps and 4.5 ns. The former is attributed to geminate recombination of the monomers following photolysis while the latter is assigned to the population decay time of **4** following escape from the solvent cage. It is noted that the maximum travel of the delay stage used in this experiment was ~1 ns and as such the longest decay time recovered is not expected to be of high accuracy. The preliminary TR-IR measurements were used to establish suitability of the system for Transient 2D-IR experiments and decide on the optimal UV pump time delay. The monomer decay timescale is sufficiently long in comparison to the UV_{pump}-2D-IR delay time of the Transient 2D-IR experiments as to allow investigation of the vibrational relaxation dynamics of radical **4**. The delay time between the UV photolysis pulse and the 2D-IR probe experiment was thus set to 300 ps. At this delay time any excess vibrational energy following UV excitation had dissipated as evidenced by a cessation of the narrowing and blue-shifting of the peaks due to **4** in the TRIR data while the concentration of the monomer is sufficiently high as to produce strong transient species lines. In addition, the 300ps

delay ensures that no UV pulse induced coherence effects are seen in the 2D-IR spectrum, reducing the complexity of the Transient 2D-IR data and facilitating the study of the 2D-IR spectrum of both the parent molecule and the 'ground state' photoproduct.

5.2.3.2. Transient-2D-IR Spectroscopy of 3 in heptane

A Transient 2D-IR difference spectrum recorded for **3** in heptane solution with an UV_{pump}-IR_{pump} time delay of 300 ps and a 2D-IR pump probe delay time of 2.5 ps is shown in Fig. 37b. For this experiment, the polarizations of the 2D-IR pump and probe pulses were set to the magic angle to remove any contributions from molecular rotation to the decay of the 2D-IR signal of the radical while the UV_{pump} and IR_{pump} pulses were set to parallel polarization. The 300 ps UV_{pump}-IR_{probe} time delay ensures complete decay of UV induced coherence and anisotropy permitting the molecular rotation contribution arising from the polarised UV pump pulses to be neglected.[66]

The use of a difference T-2D-IR representation means that the spectrum displayed in Fig 37b reveals the effect of the UV pump pulse on the 2D-IR spectrum of the system. As such, the peaks due to the dimer species, **3**, occurring at (1955, 1955) and (1910, 1910) on the diagonal and at (1955, 1910) and (1910, 1955) in the off-diagonal region (highlighted by circled numerals *1* and *2* in the figure as above) are in identical positions to those observed in the ground state 2D-IR spectra discussed above but with their phases reversed. The pseudo 3rd order Transient 2D-IR spectrum can be viewed as a difference of two 2D-IR spectra, one taken with the UV pulse and one without. The parent molecule features in the Transient 2D-IR spectrum arise as a result of UV induced depletion of the parent molecule concentration and so the phases of the $\nu = 0\text{-}1$ and $\nu = 1\text{-}2$ transitions are reversed in comparison to the ground state 2D-IR spectrum. On the other hand, the UV pulse generates photoproduct, hence peaks in the Transient 2D-IR spectrum due to this species display a phase consistent with those observed in a ground state 2D-IR spectrum. In addition to these features, new peaks are observed at (2000, 2000) on the diagonal and at (1890, 2000) and (2000, 1890) in the off-diagonal region; marked with a circled number *3* in Fig 37b.

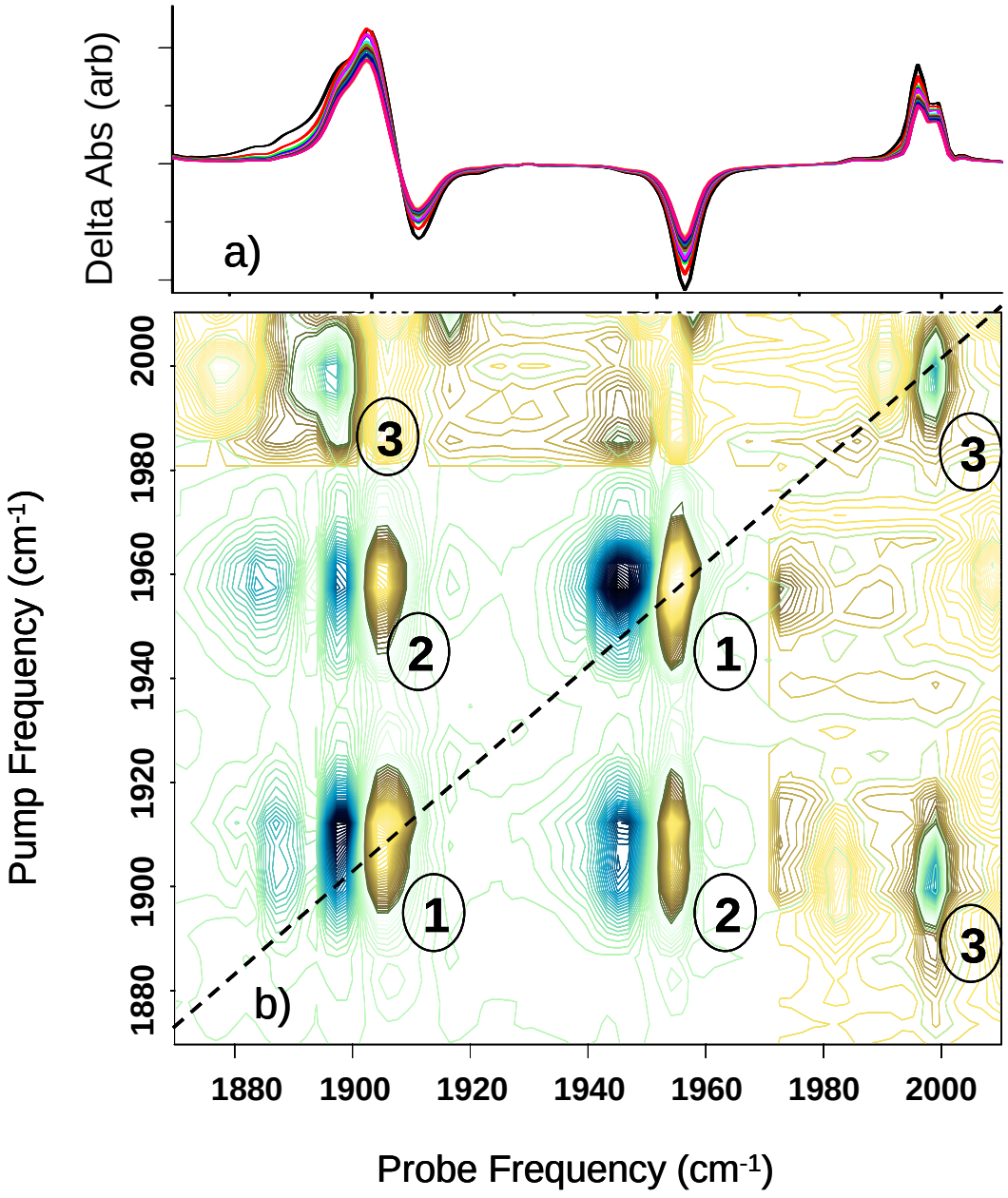

Figure 37. (a) TR-IR spectra of **3** in heptane after irradiation at 490nm for a range of pump-probe delay times up to 1 ns (b) The corresponding Transient 2D-IR spectrum obtained with an UV_{pump}-IR_{probe} delay time of 300 ps and IR_{pump}-IR_{probe} delay time of 2.5 ps. The spectral range beyond 1980 cm^{-1} for both axes has been magnified 10 times to reveal the presence of weak bands due to the monomer formation while colour scale range is retained.

These are present as pairs of peaks with similar anharmonic separations of the $\nu = 0\text{-}1$ and 1-2 contributions but with the opposite phase to those due to the dimer. The position of the (2000, 2000) diagonal peak is consistent with the position of the a_1 mode of the $17e^-$ monomer **4**, while the accompanying diagonal peak due to the *e* mode is obscured by peaks due to **3**, the off-diagonal peaks indicate the presence of a diagonal feature at the expected position. It is thus reasonable to conclude that the new peaks belong to the monomeric species **4**, the positive phase indicating the creation of this species by the UV_{pump} pulse. Almost identical results were obtained for TR-IR and T-2D-IR spectroscopy of **3'** though once again the line shapes were somewhat broadened by the presence of a polar solvent and this combined with the larger fraction of gauche isomer present meant that the off-diagonal peaks due to **4'** were somewhat less well-resolved.

5.2.4. Ultrafast vibrational dynamics of 3, 3' and 4, 4' in solution

In order to obtain information on the vibrational dynamics of both conformers of **3** and **3'** a series of 2D-IR spectra were recorded using the magic angle pump-probe polarization geometry at a range of pump-probe delay times for two pump frequencies. The first corresponded to pumping the most intense mode of the *anti* isomer at 1955 cm^{-1} (1954 cm^{-1} for **3'** in DCM) and the second to the only mode of the *gauche* isomer visible on the spectrum diagonal near 2013 cm^{-1} (2011 cm^{-1} for **3'** in DCM). These were chosen to give the clearest possible access to peaks due to the two isomers without the complication of overlapping resonances. In the case of the 1955 cm^{-1} mode, it was impossible to avoid pumping modes due to both isomers, however, the cross-peaks due to the *anti* form are sufficiently large as to remain unperturbed by the presence of small cross-peaks due to the *gauche* form while pumping this mode also give more information on the latter isomer via the isolated cross peak at 2013 cm^{-1}.

In order to extract the peaks due to the *gauche* isomer in the slices recorded with a pump frequency of 2013 cm^{-1}, those due to overlap with *anti* isomer transitions were first fitted using frequency and width parameters obtained from the slice recorded with a pump frequency of 1955 cm^{-1}.

Selected decay profiles for **3** and **3'** are displayed in Figs 38 and 39, respectively. To quantify the signal decays, the obtained profiles were fit to single or bi-exponential functions over pump-probe time delays ranging from 0 to 120 ps. The decay fitting results are collated in Table 5. In order to obtain vibrational dynamics for **4** and **4'**, Transient 2D-IR slices were recorded with an IR pump frequency of 2000 cm^{-1} in the presence of the UV_{pump} pulse again with a fixed UV_{pump}-IR_{probe} delay of 300 ps. A similar analysis process to that described above yielded vibrational relaxation data for the monomers. Example decay profiles of the diagonal and off-diagonal peaks arising in the Transient 2D-IR spectrum of **4** are shown in Fig. 40 while fitting results are collated in Table 5.

5.2.4.1. Vibrational relaxation of 3 in heptane

For solutions of **3** in heptane, with the pump frequency set to 1955 cm^{-1} the observed diagonal peak pair, consisting of the ν = 0-1 bleach and ν = 1-2 transient absorption, both display dynamics that were best represented by a bi-exponential decay function with a fast decay component of ~1.5–2 ps and a slow decay of ~23 ps (Table 5). The off-diagonal peaks belonging to the *anti* conformer at 1909 and 1898 cm^{-1} also display double-exponential dynamics with a fast rise time of between 4 and 10 ps, and subsequent slow decay with a timescale of ~27 ps. The sole exception to this appeared to be the lowest frequency ν = 1-2 off-diagonal transition, which displayed dynamics better represented by a single exponential function. It is interesting to note that the results of fitting the dynamics of the off-diagonal band attributable to the *gauche* isomer at 2013 cm^{-1} results in a single-exponential decay with a timescale of ~32 ps. However, close inspection of the data, shown in Fig. 38b, again indicates the presence of a rise time as displayed by the off-diagonal peaks due to the *anti* conformer. In this case however, the rise was somewhat faster and could not be reliably fit given the small number of data points involved and the time resolution of the spectrometer >1 ps. This data is broadly comparable with that observed for other metalcarbonyl systems.[34,39,46,96,97,99] The two timescales can be attributed to two distinct processes a faster IVR process population (T_1) relaxation. The IVR process is the result of solvent assisted vibrational energy transfer from the pumped transition to all corresponding coupled modes.

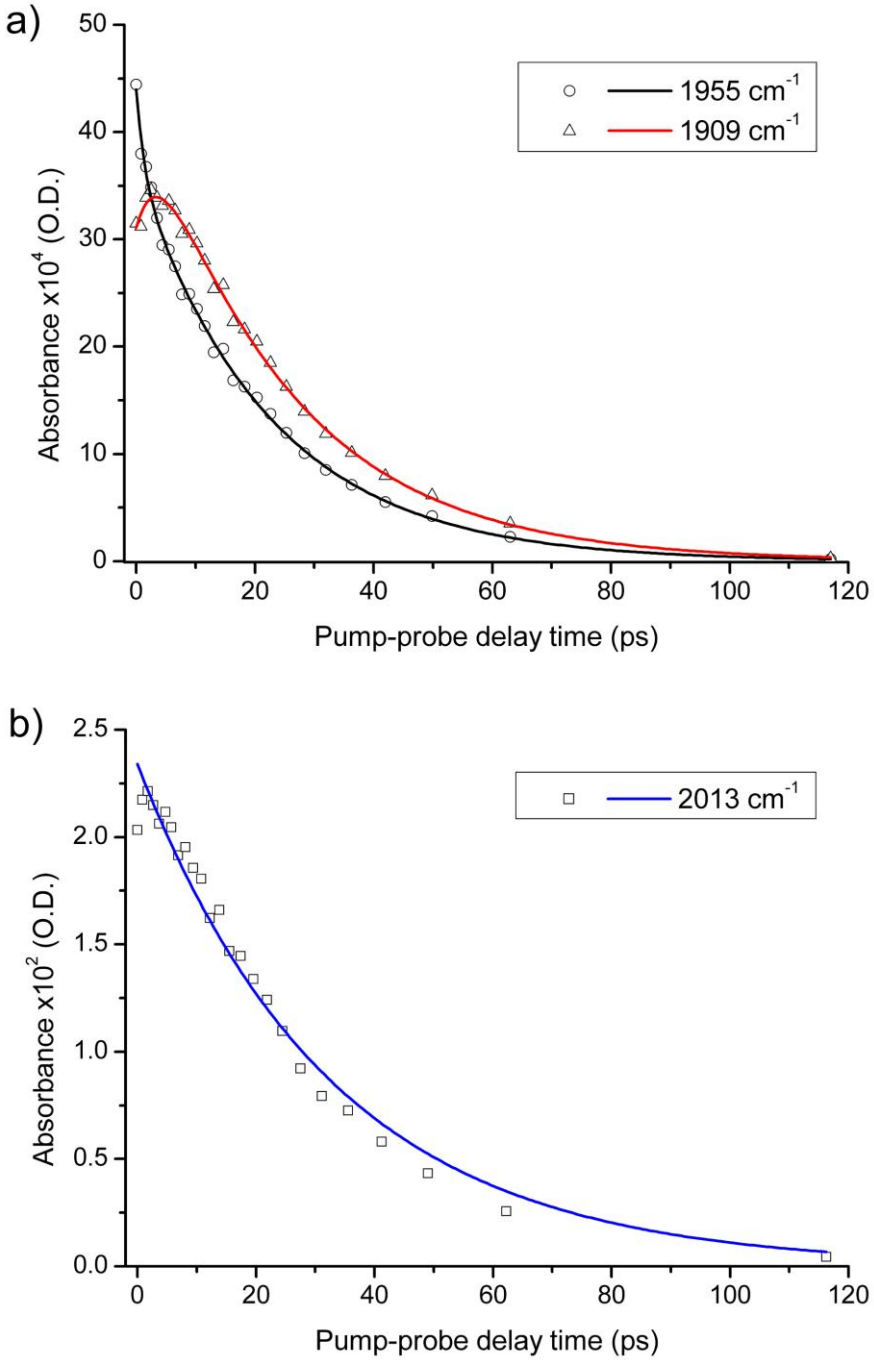

Figure 38. Vibrational relaxation dynamics of **3** in heptane for a 2D-IR spectrum horizontal slice at pump frequency of 1955 cm^{-1} (a) shows dynamics of the diagonal (black) and off-diagonal (red) ν = 0-1 features corresponding to the *anti* isomer of **3**. (b) Shows the dynamics of the cross peak arising from the ν = 0-1 transition of the *gauche* isomer arising from simultaneous pumping of both isomers at this pump frequency. The experimental data is shown as hollow shapes while the lines represent fits to bi-exponential functions. The figures legend indicates studied peak positions.

Such a process leads to a fast initial relaxation of the pumped transition and short lived rise in the intensity of coupled vibrational modes. The slower populational relaxation (T_1) leads to dissipation of excitation energy to the surrounding that terminates the vibrational relaxation process.

With a pump frequency of 2013 cm^{-1} the observed diagonal peak pair again display a bi-exponential decay function with fast decay time of ~1-2 ps followed by slow decay with a timescale of ~30 ps, though some scatter was observed in this data as a result of the smaller signal strength. As the 2013 cm^{-1} transition does not overlap with *anti* isomer bands, analysis of apparent *anti* isomer off diagonal peaks is irrelevant as these are effectively spectral artefacts. As a result of this, *gauche* isomer off-diagonal peak dynamics were extracted by first taking into account the contributions of the contamination from the *anti* isomer peaks. This approach allowed dynamics to be extracted with the off-diagonal modes showing a population relaxation time of around 24 ps, though again with some scatter due to the small signal strengths and peak overlap effects. The latter also made the IVR process harder to extract though evidence for IVR processes were clearly observed for some of the off-diagonal peaks. Once again this data is consistent with the model mentioned above and the timescales involved seem to be similar for the two isomeric forms as might be expected. There is some evidence for a slightly slower T_1 timescale for the *gauche* form though the scatter on the data arising from the small signals makes this a tentative observation.

5.2.4.2. Vibrational relaxation of 3' in DCM

In the case of **3'** in DCM solutions, the overall patterns are not dissimilar to those for **3** in heptane solutions. When pumping at 1954 cm^{-1}, the diagonal features reveal biexponential decay with a fast component of ~ 1-2 ps followed by slow decay of ~ 24-29 ps. The off-diagonal bleach belonging to the *anti* isomer $\nu = 0$-1 transition at 1904 cm^{-1} exhibits a rise time of ~1.5 ps and subsequent slow decay of ~ 26 ps, while the associated transient absorption was best represented by single exponential dynamics, once again peak overlap in this region caused by the polar solvent-induced line broadening and the presence of a rise-time close to the resolution limit of the spectrometer made separation of the individual components non-trivial.

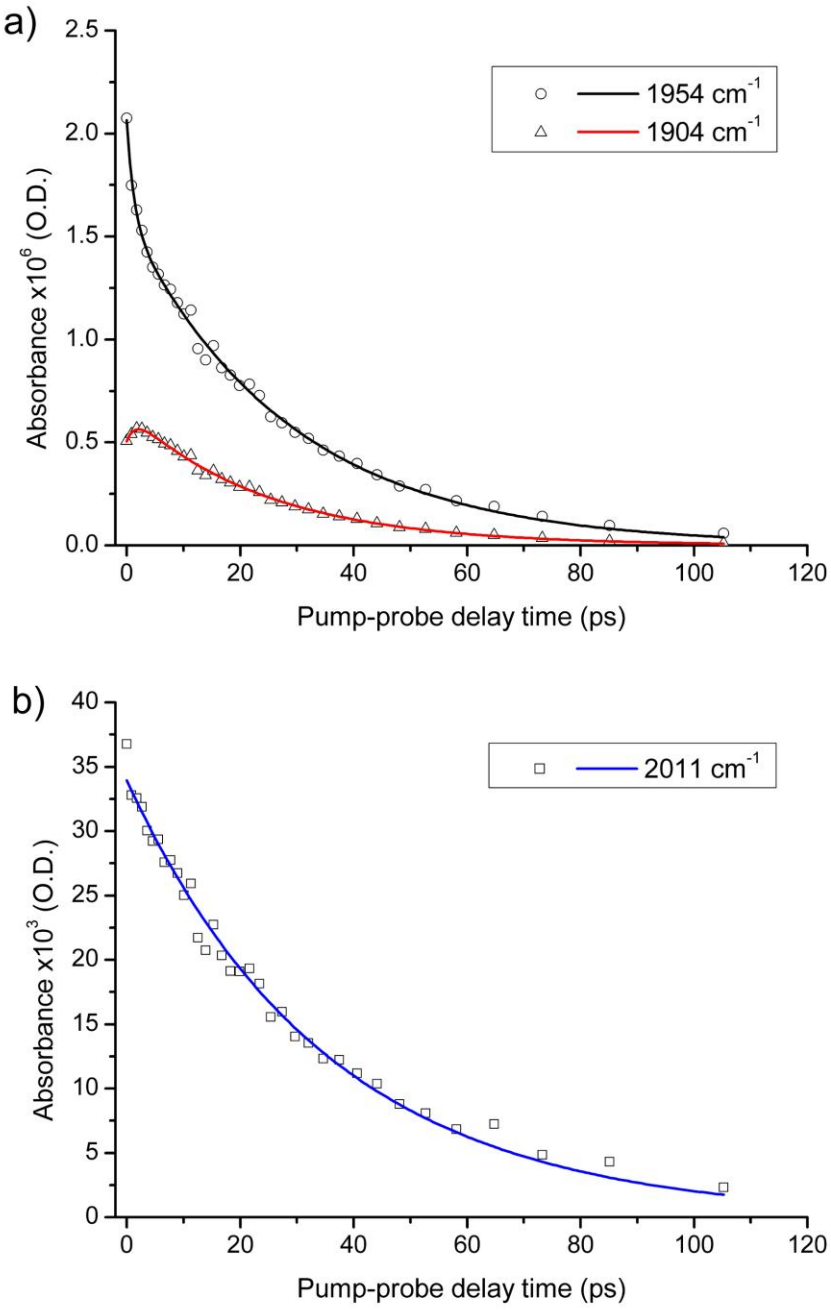

Figure 39. Vibrational relaxation dynamics of **3'** in DCM for a 2D-IR spectrum horizontal slice at pump frequency of 1954 cm^{-1} (a) shows dynamics of the diagonal (black) and off-diagonal (red) ν = 0-1 features corresponding to the *anti* isomer of **3'**. (b) Shows the dynamics of the cross peak arising from the ν = 0-1 transition of the *gauche* isomer arising from simultaneous pumping of both isomers at this pump frequency. The experimental data is shown as hollow shapes while the solid lines represent fits to bi-exponential functions. The legend figure indicates studied peak positions.

Table 5. Results of temporal dependences fitting of diagonal and off-diagonal peak amplitudes of **3, 3', 4** and **4'** from 2D-IR spectral slices recorded with pump frequencies of 2013 and 1955 cm^{-1} (**3**), 2011 and 1954 cm^{-1} (**3'**) and 2000 cm^{-1} (**4, 4'**) to exponential functions. τ_1 and τ_2 represent exponential decay timescales while τ_r indicates a rise time. Peak frequency labels relate to peak identifiers used in the text rather than actual frequencies.

2D-IR	**3** in n-Heptane (ps)				**3'** in DCM (ps)				
Pumped transition (cm^{-1})	2D-IR Peak [freq label/cm^{-1}] (v=i-j)	τ_r	τ_1	τ_2	Pumped transition (cm^{-1})	2D-IR Peak [freq label/cm^{-1}] (v=i-j)	τ_r	τ_1	τ_2
1955					**1954**				
	Diagonal [1955] (0-1)		1.4	24		Diagonal [1954] (0-1)		1.2	29
	Diagonal [1955] (1-2)		1.7	22		Diagonal [1954] (1-2)		1.1	28
	Off-Diagonal [1909] (0-1)	4		24		Off-Diagonal [1904] (0-1)	1.5		24
	Off-Diagonal [1909] (1-2)	(8)		27		Off-Diagonal [1904] (1-2)			26
	Off-Diagonal [1898] (0-1)	(10)		23					
	Off-Diagonal [1898] (1-2)			27					
	Off diagonal [2013] (0-1)			32		Off diagonal [2011] (0-1)			35.5
2013					**2011**				
	Diagonal [2013] (0-1)		1.5	26		Diagonal [2011] (0-1)		3	40
	Diagonal [2013] (1-2)		2.2	34		Diagonal [2011] (1-2)		3	38
	Off-Diagonal [1916] (0-1)			24.5					
	Off-Diagonal [1916] (1-2)	(18)		20					
	Off-Diagonal [1880] (0-1)	(15)		18					
	Off-Diagonal [1880] (1-2)			28		Off-Diagonal [1880] (1-2)	3		29
T-2D-IR	**4** in heptane (ps)				**4'** in DCM (ps)				
2000					**2000**				
	Diagonal [2000] (0-1)			23		Diagonal [2000] (0-1)			22
	Diagonal [2000] (1-2)			15		Diagonal [2000] (1-2)			24
	Off-Diagonal [1890] (0-1)			31					
	Off-Diagonal [1890] (1-2)			24					

Fitting errors within 10% unless stated. Figures in brackets indicate parameters where S/N or band overlap issues lead to uncertain fitting results.

The *gauche* isomer off-diagonal peak near 2011 cm^{-1} show a single-exponential decay of ~36 ps, in contrast to **3**, there is no evidence of a fast rise time.

When pumping the *gauche* isomer diagonal peak at 2011 cm^{-1}, the diagonal

features once again were well-represented by a bi-exponential function with timescales of 3 and 39 ps, the latter maintaining the trend from the *gauche* isomer cross peak above of showing a longer relaxation time than peaks attributable to the *anti* isomer. In the case of the off-diagonal peaks, overlap with the wings of the strong transitions due to the *anti* form made extraction of *gauche* isomer cross peak dynamics very difficult, even employing the methodologies described above. The only clearly observable transition was the lowest frequency feature, attributable to the off-diagonal $\nu = 1\text{-}2$ transition of the *gauche* isomer. Fitting the temporal decay of this peak then revealed double-exponential dynamics consisting of a fast rise time of ~3 ps and subsequent slow decay of ~29 ps. Once again the data would seem to support a model in which vibrational relaxation occurs through rapid IVR and population equilibration between carbonyl stretching modes followed by relaxation to the ground state on a timescale of tens of ps.

5.2.4.3. Vibrational relaxation of 4 and 4' in heptane and DCM

In contrast to the vibrational relaxation profiles of the dimeric species, the vibrational relaxation of the $17e^-$ species displayed only single-exponential dynamics. The values recovered for the vibrational lifetime are remarkably similar to those obtained for **3** and **3'** above. It is however interesting to note that there appears to be a complete absence of IVR type processes in the observed decay profiles of the transient species, which is in contrast to the dimer data. In the case of **4'**, the results are similar to those of **4**. Both $\nu = 0\text{-}1$ and $1\text{-}2$ components of the diagonal peak near 2000 cm^{-1} reveal single exponential dynamics with a timescale of 22-24 ps. In the case of **4'**, the polar solvent-induced line broadening and increased peak intensities arising from the *gauche* isomer cross peaks prevent effective quantitative extraction of the dynamics of the photoproduct off-diagonal peaks. However, the similarity of the diagonal peak dynamics for **4** and **4'** suggest that the situation is unlikely to be significantly dissimilar. As **4'** plays an important role as an intermediate in several photochemical reactions of **3'** and the mechanisms for handling vibrational energy during a chemical reaction are of relevance to the pathway of the reaction, this a result worthy of consideration.

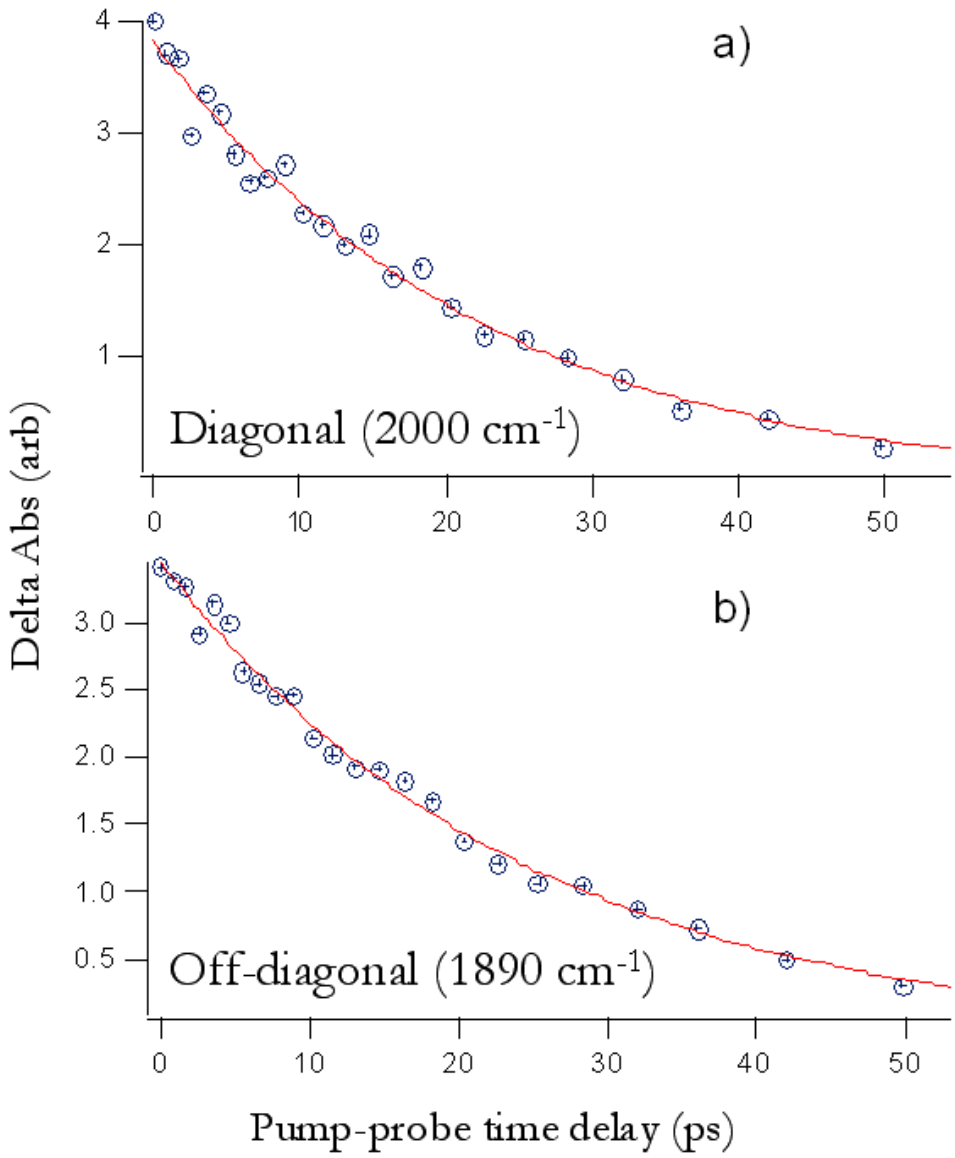

Figure 40. Vibrational relaxation dynamics of **4** in heptane for Transient 2D-IR spectrum slice at pump frequency 2000 cm^{-1}, (a) the diagonal feature 2000 cm^{-1} dynamics, (b) the off-diagonal feature dynamics 1890 cm^{-1}. The experimental data is shown as hollow shapes while the solid lines represent fits to single-exponential fits.

The observed IVR timescales for vibrational energy redistribution among the collective carbonyl stretching modes of the dimers **3** and **3'** are in the 1-3 ps timescale. The applied double resonance 2D-IR technique has limited temporal resolution to about 1-2 ps on account of pump pulse duration. Thus there are two plausible conclusions relating to the vibrational dynamics of the $17e^-$ species. Either

the IVR process observed in the parent dimer is absent or the IVR process still exists in the photoproduct but is faster than that of the parent falling beyond the temporal resolution of the applied method.

Equally interesting is a comparison of the population relaxation rates of the parent and photoproduct. The data (Table 5) shows virtually no change in the rate of vibrational energy dissipation (T_1). This is a surprising result considering that the photoproduct is a $17e^-$ radical species possessing a vacant coordination site enabling solvent coordination. In this case it might be expected that more efficient dissipation of vibrational energy to the bath may be possible but this seems not to be the case. It is plausible that such relaxation dynamics result from two opposing effects. The radical nature of the photoproduct and presence of a vacant coordination site increases the rate of IVR but the significant drop in size (50%) limits number of solvent molecules in the first solvation shell. The latter effect could slow down population relaxation since excitation energy transfer to a solvent molecule becomes less probable. Another possibility is that the lack of solvent dependence of the T_1 time points to a largely intramolecular vibrational relaxation mechanism while IVR, which requires the exchange of energy with solvent bath modes, is accelerated by the vacant coordination site.

5.3. Discussion

The results of the steady-state FT-IR spectroscopy studies of the ν_{CO} region spectra of **3** in heptane and **3'** in DCM solution confirms the existence of a geometrical isomerisation equilibrium. This is supported by ground state DFT simulations and temperature difference spectra. It has been established that the presence of alkane substitution on the Cp ring has little effect on the ν_{CO} region vibrational spectrum of **3** and does not affect the conformational isomerization previously reported for **3'**.[82,83] The spectroscopic evidence concerning the similarities of the selected metalcarbonyl dimers further supports comparative spectroscopic studies of **3** and **3'** solutions as a way to benefit from the higher resolution offered by non-polar solvents maintaining applicability of conclusions to other homologues of the compound. DFT calculations of the formation energies of both conformeric forms and an estimation of the activation energy barriers reveal a moderate

difference in stability, coinciding with large activation barrier for isomerisation. The large activation energy barrier slows down the conformational isomerisation far beyond picosecond timescales[82,83] making 2D-IR spectroscopy a useful tool for spectroscopic characterisation of each conformeric form. Moreover, since both compounds exhibit similar photo reactivity leading to stable monomeric $17e^-$ radical transients **4** and **4'** that persist over the whole picosecond timescale, vibrational relaxation dynamics of the photoproducts could be extracted with the aid of Transient 2D-IR spectroscopy.

Analysis of the cross-peak pattern of the 2D-IR spectrum has revealed the previously unobserved complete set of ν_{CO} vibrations for the less abundant *gauche* conformeric form of **3**. The spectral signatures obtained are in excellent agreement with DFT simulation of the infrared spectra. The results for **3'** solutions were less conclusive due to the obscuring effects of line broadening but, still, there was clear evidence for differences between the *anti* and *gauche* conformer spectral signatures. The conclusions from the analysis of the vibrational coupling patterns of the 2D spectrum were supported by vibrational relaxation dynamics studies of selected spectral features associated with each conformeric form. Careful analysis of vibrational relaxation data reveals small but apparent differences in population relaxation (T_1) lifetimes. The average T_1 lifetime for the *anti* isomer of **3** (**3'**) derived from spectrally isolated peaks is about ~24 (28) ps while for *gauche* conformer it is close to ~30 (36) ps. Similar but less clear are differences in the IVR rates of **3** (**3'**) for diagonal features that are close to 1.5 (1.1) ps for *anti* and 1.8 (3) ps for *gauche*, respectively.

The general lack of comparative studies of vibrational relaxation for geometrical isomers makes the origin of the observed lengthening of the T_1 lifetime in the *gauche* form versus the *anti* form somewhat unclear. The rotation around the W-W bond has a huge impact on the molecular dipole moment which changes dramatically from *anti* to *gauche* conformer potentially affecting the strength of solute-solvent interactions and hence the solvent dependant IVR and population relaxation processes. Also, the addition of the propyl substituent increases the number of vibrational modes in the **3** derivative adding low frequency δ(H-C-H) modes and statistically increasing the number of bath modes available for the IVR

process. The latter factor makes a direct comparison of the dynamics of **3** and **3'** in two different solvents more difficult. This situation is best reflected in other studies of the effects of solvent polarity changes on vibrational relaxation dynamics which indicate some degree of correlation albeit masked by other unaccounted for factors specific to the measured systems.[100,101] In some cases the marked increase of solute-solvent interactions associated with the switch from non-polar to polar media has little effect on the vibrational relaxation lifetime but a marked increase in the IVR rate was observed.[34] The IVR process is widely thought to be mediated by solvent-solute interactions since it involves the exchange of low frequency photons (<100 cm^{-1}) of which the solvent is a far more plentiful source than the solute molecule itself.[102,103]

Similarly to the 2D-IR spectrum, the Transient 2D-IR spectrum proved to be a useful tool for infrared spectra resolutions and separation of spectra due to components of a mixed solution. Again, analysing the cross-peak pattern of the Transient 2D-IR spectrum has enabled assignment of the post-excitation constituents of the solution and the obtained spectral signatures are in excellent agreement with known spectra of the parent molecule conformers and radical transient.[78-81] The results for **3'** solutions clearly indicated the presence of two vibrational transitions of the monomeric radical **4**' although line broadening somewhat impaired the achievable spectral resolution. The vibrational relaxation dynamics studies of the $17e^-$ radicals **4** and **4'** exposed similar T_1 rates for different solvents that were close to the values recovered for **3** in heptane and an absence of IVR processes. Since the parent dimer and the monomeric radical are substantially different in structure and electronic properties, the similarity of the T_1 rates is somewhat surprising. There are several major differences between the parent and photoproduct such as the extra degrees of freedom arising from the greater number of vibrational modes of the parent and the smaller size, vacant coordination site and radical nature of the photoproduct which could alter the solute-solvent interactions. It has been shown through photolysis studies[50,51,53,55,81,104,105] that creation of a vacant site at a metal centre in heptane solutions leads to solvent coordination and, given the long-lived nature of this $17e^-$ species, it would be reasonable to assume a similar occurrence in this case. It must be stressed however that any such coordination is likely to be weak

and possibly dynamic given the small solvatochromic shifts of the **4** absorptions. The implications for this in terms of the vibrational relaxation of the transient arise from a pathway through which solvent interactions are enhanced relative to the parent by the presence of the coordinated solvent. Contrary to this, the smaller size (50%) of the monomer may reduce the number (but not the density) of solvent molecules in the first solvation shell and this may impede the IVR process. The latter factor may lead to a reduction in populational relaxation rates. The lack of evidence for IVR process sets the $17e^-$ radicals apart from the majority of metalcarbonyl systems that have been studied to date[34,38,39,46,97] including the parent molecules studied here. Similar behaviour has however been observed for $(\mu\text{-}S(CH_2)_3S)Fe_2(CO)_6$ upon switching to a more strongly interacting solvent.[34] As was indicated previously, the IVR process is mediated by solute-solvent interaction but there are additional factors which set apart IVR from population relaxation. As it has been established that IVR processes are mediated by the solvent bath, the low frequency modes of which act as both source and sink for population transfer between the close-lying carbonyl stretching modes,[103] it is more likely that the IVR rates of the transient species would be faster than the parent rather than slower or absent. Indeed, it would only require a relatively small increase in the rate of IVR for it to become beyond the detection capacity of the used double-resonance 2D-IR spectrometer.

5.4. Conclusions

Ultrafast 2D-IR spectroscopic methods have been used for the first time to study the vibrational dynamics of a conformational isomerisation of the propyl-cyclopentadienyl tungsten tricarbonyl dimer transient and its $17e^-$ metalcarbonyl photoproduct. A combination of transient 2D-IR and ground-state 2D-IR techniques have shown that the relaxation processes of the parent dimer and transient photoproduct are significantly different. The dimer relaxes on two timescales corresponding to a fast relaxation process attributed to IVR on timescales of 1-3 ps alongside slower vibrational population relaxation (25-30 ps). In contrast, the monomer appears to show only the slower relaxation timescale, with no IVR processes observed. It is however suggested that the presence of solvent coordination

at the vacant site of the intermediate species may lead to faster IVR than in the parent, shifting this process beyond the time resolution of used spectrometer.

Additionally, the infrared spectrum and vibrational dynamics of the lesser-populated *gauche* isomeric form of the dimeric species in the carbonyl stretching region has been determined using the presence of off-diagonal peaks in the 2D-IR spectra. The spectral assignment has been supported by DFT calculations and an absence of rotation about the intermetallic bond on the timescale of these experiments has been confirmed. The vibrational dynamics of the two isomeric forms have been shown to be broadly similar though with a slightly longer IVR and T_1 relaxation time observed for the *gauche* isomer.

5.5. Further research perspectives

It is hoped that this data will provide an impetus for further research on similar systems in an effort to better understand the structural and dynamic factors underpinning the differences in vibrational relaxation dynamics of geometrical isomers and transient species.

In terms of the applicability of these results to wider chemical reactions, it would be particularly interesting to correlate the vibrational relaxation timescales with intermediate reactivity, for example, if an intermediate can dissipate excess energy more efficiently to the solvent or internal modes, does this promote chemical reactivity? In this case, the transient species is rather long-lived, a property that is likely to be facilitated by solvent coordination, which in turn is expected to promote IVR. It would be instructive then to know whether an intermediate with less efficient IVR, maintaining vibrational energy in a single mode would be more susceptible to reaction or less, or if indeed there correlation exists. This can only be determined with further study but it is hoped that this work provides a first step.

5.6. Acknowledgements

The author would like to acknowledge the contributions of Ian A. Stewart a collaborating postgraduate responsible for processing and interpretation of Transient 2D-IR data and Dr. Ian P. Clark, Dr. Gregory M. Greetham, Dr. Michael Towrie, and

Prof. Anthony W. Parker, who collaborated on the development of the Transient 2D-IR spectrometer and for overseeing the ultrafast spectroscopy experiments.

References:

(1) Hamm, P.; Lim, M.; Hochstrasser, R. M. *The Journal of Physical Chemistry B* **1998**, *102*, 6123.

(2) Hamm, P.; Zanni, M. *Concepts and Methods of 2D Infrared Spectroscopy*; Cambridge University Press: Cambridge, **2011**.

(3) Khalil, M.; Demirdoven, N.; Tokmakoff, A. *The Journal of Physical Chemistry A* **2003**, *107*, 5258.

(4) Hamm, P.; Lim, M.; De Grado, W. F.; Hochstrasser, R. M. *Proceedings of the National Academy of Sciences of the United States of America* **1999**, *96*, 2036.

(5) Cheatum, C. M.; Tokmakoff, A.; Knoester, J. *The Journal of Chemical Physics* **2004**, *120*, 8201.

(6) Chung, H. S.; Khalil, M.; Tokmakoff, A. *Biophysical Journal* **2004**, *86*, 526A.

(7) Demirdoven, N.; Cheatum, C. M.; Chung, H. S.; Khalil, M.; Knoester, J.; Tokmakoff, A. *Journal of the American Chemical Society* **2004**, *126*, 7981.

(8) Smith, A. W.; Cheatum, C. M.; Chung, H. S.; Demirdoven, N.; Khalil, M.; Knoester, J.; Tokmakoff, A. *Biophysical Journal* **2004**, *86*, 619A.

(9) Rubtsov, I. V.; Wang, J.; Hochstrasser, R. M. *The Journal of Chemical Physics* **2003**, *118*, 7733.

(10) Kim, Y. S.; Wang, J.; Hochstrasser, R. M. *The Journal of Physical Chemistry B* **2005**, *109*, 7511.

(11) Fang, C.; Senes, A.; Cristian, L.; De Grado, W. F.; Hochstrasser, R. M. *Proceedings of the National Academy of Sciences of the United States of America* **2006**, *103*, 16740.

(12) Hochstrasser, R. M.; Ge, N.-H.; Gnanakaran, S.; Zanni, M. T. *Bulletin of the Chemical Society of Japan* **2002**, *75*, 1103.

(13) Bredenbeck, J.; Hamm, P. *The Journal of Chemical Physics* **2003**, *119*, 1569.

(14) Kolano, C.; Helbing, J.; Kozinski, M.; Sander, W.; Hamm, P. *Nature* **2006**, *444*, 469.

(15) Kim, S. K.; Ha, T.; Schermann, J.-P. *Physical Chemistry Chemical Physics : PCCP* **2010**, *12*, 3334.

(16) Smith, A. W.; Lessing, J.; Ganim, Z.; Peng, C. S.; Tokmakoff, A.; Roy, S.; Jansen, T. L. C.; Knoester, J. *The Journal of Physical Chemistry B* **2010**, *114*, 10913.

(17) Woys, A. M.; Lin, Y.-S.; Reddy, A. S.; Xiong, W.; de Pablo, J. J.; Skinner, J. L.; Zanni, M. T. *Journal of the American Chemical Society* **2010**, *132*, 2832.

(18) Ernst, R. R.; Bodenhausen, G.; Wokaun, A. *Principles of Nuclear Magnetic Resonance in One and Two Dimensions.*, Clarendon, Oxford, **1987**.

(19) Khalil, M. *Chemical Physics* **2001**, *266*, 213.

(20) Khalil, M.; Demirdöven, N.; Tokmakoff, A. *Physical Review Letters* **2003**, *90*, 2.

(21) Okumura, K.; Tokmakoff, A.; Tanimura, Y. *Chemical Physics Letters* **1999**, *314*, 488.

(22) Roberts, S. T.; Loparo, J. J.; Tokmakoff, A. *The Journal of Chemical Physics* **2006**, *125*, 084502.

(23) Tokmakoff, A. *Science* **2007**, *317*, 54.

(24) Steinel, T.; Asbury, J. B.; Corcelli, S. A.; Lawrence, C. P.; Skinner, J. L.; Fayer, M. D. *Chemical Physics Letters* **2004**, *386*, 295.

(25) Fecko, C. J.; Loparo, J. J.; Roberts, S. T.; Tokmakoff, A. *The Journal of Chemical Physics* **2005**, *122*, 054506.

(26) Fayer, M. D. *Abstracts of Papers of the American Chemical Society* **2004**, *227*, 1.

(27) Asbury, J. B.; Steinel, T.; Fayer, M. D. *The Journal of Physical Chemistry B* **2004**, *108*, 6544.

(28) Asbury, J. B.; Steinel, T.; Kwak, K.; Corcelli, S. A.; Lawrence, C. P.; Skinner, J. L.; Fayer, M. D. *The Journal of Chemical Physics* **2004**, *121*, 12431.

(29) Zheng, J.; Kwak, K.; Asbury, J.; Chen, X.; Piletic, I. R.; Fayer, M. D. *Science* **2005**, *309*, 1338.

(30) Kwak, K.; Park, S.; Fayer, M. D. *Proceedings of the National Academy of Sciences of the United States of America* **2007**, *104*, 14221.

(31) Kwak, K.; Rosenfeld, D. E.; Chung, J. K.; Fayer, M. D. *The Journal of Physical Chemistry B* **2008**, *112*, 13906.

(32) Zheng, J.; Fayer, M. D. *The Journal of Physical Chemistry B* **2008**, *112*, 10221.

(33) Fayer, M. D. *The Annual Review of Physical Chemistry* **2009**, *60*, 21.

(34) Stewart, A. I.; Clark, I. P.; Towrie, M.; Ibrahim, S. K.; Parker, A. W.; Pickett, C. J.; Hunt, N. T. *The Journal of Physical Chemistry B* **2008**, *112*, 10023.

(35) Andresen, E. R.; Gremaud, R.; Borgschulte, A.; Ramirez-Cuesta, A. J.; Züttel, A.; Hamm, P. *The Journal of Physical Chemistry A* **2009**, *113*, 12838.

(36) Banno, M.; Ohta, K.; Yamaguchi, S.; Hirai, S.; Tominaga, K. *Accounts of Chemical Research* **2009**, *42*, 1259.

(37) McCanne, R.; Baiz, C. R.; Nee, M. J.; Anna, J.; Kubarych, K. J. *Journal of Physical Chemistry A* **2009**, *113*, 8907.

(38) Bonner, G. M.; Ridley, A. R.; Ibrahim, S. K.; Pickett, C. J.; Hunt, N. T. *Faraday Discussions* **2010**, *145*, 429.

(39) Kaziannis, S.; Wright, J. A.; Candelaresi, M.; Kania, R.; Greetham, G. M.; Parker, A. W.; Pickett, C. J.; Hunt, N. T. *Physical Chemistry Chemical Physics : PCCP* **2011**, *13*, 10295.

(40) Woutersen, S.; Mu, Y.; Stock, G.; Hamm, P. *Chemical Physics* **2001**, *266*, 137.

(41) Kwak, K.; Zheng, J. R.; Cang, H.; Fayer, M. D. *The Journal of Physical Chemistry B* **2006**, *110*, 19998.

(42) Zheng, J.; Kwak, K.; Chen, X.; Asbury, J. B.; Fayer, M. D. *Journal of the American Chemical Society* **2006**, *128*, 2977.

(43) Zhao, X.; Georgakaki, I. P.; Miller, M. L.; Yarbrough, J. C.; Darensbourg, M. Y. *Journal of the American Chemical Society* **2001**, *123*, 9710.

(44) Kim, Y. S.; Hochstrasser, R. M. *Proceedings of the National Academy of Sciences of the United States of America* **2005**, *102*, 11185.

(45) Kwak, K.; Zheng, J.; Cang, H.; Fayer, M. D. *The Journal of Physical Chemistry B* **2006**, *110*, 19998.

(46) Anna, J. M.; Ross, M. R.; Kubarych, K. J. *The Journal of Physical Chemistry A* **2009**, *113*, 6544.

(47) Moilanen, D. E.; Wong, D.; Rosenfeld, D. E.; Fenn, E. E.; Fayer, M. D. *Proceedings of the National Academy of Sciences of the United States of America* **2009**, *106*, 375.

(48) Park, S.; Odelius, M.; Gaffney, K. J. *The Journal of Physical Chemistry B* **2009**, *113*, 7825.

(49) Rosenfeld, D. E.; Kwak, K.; Gengeliczki, Z.; Fayer, M. D. *The Journal of Physical Chemistry B* **2010**, *114*, 2383.

(50) Glyn, P.; Johnson, F. P. A.; George, M. W.; Lees, A. J.; Turner, J. J. *Inorganic Chemistry* **1991**, *30*, 3543.

(51) Portius, P.; Yang, J.; Sun, X.-Z.; Grills, D. C.; Matousek, P.; Parker, A. W.; Towrie, M.; George, M. W. *Journal of the American Chemical Society* **2004**, *126*, 10713.

(52) Bredenbeck, J.; Helbing, J.; Kolano, C.; Hamm, P. *ChemPhysChem* **2007**, *8*, 1747.

(53) Kaziannis, S.; Santabarbara, S.; Wright, J. A.; Greetham, G. M.; Towrie, M.; Parker, A. W.; Pickett, C. J.; Hunt, N. T. *The Journal of Physical Chemistry B* **2010**, *114*, 15370.

(54) Sawyer, K. R.; Cahoon, J. F.; Shanoski, J. E.; Glascoe, E. A.; Kling, M. F.; Schlegel, J. P.; Zoerb, M. C.; Hapke, M.; Hartwig, J. F.; Webster, C. E.; Harris, C. B. *Journal of the American Chemical Society* **2010**, *132*, 1848.

(55) Clark, I. P.; George, M. W.; Greetham, G. M.; Harvey, E. C.; Long, C.; Manton, J. C.; Pryce, M. T. *The Journal of Physical Chemistry A* **2011**, *115*, 2985.

(56) Helbing, J.; Bonacina, L.; Pietri, R.; Bredenbeck, J.; Hamm, P.; van Mourik, F.; Chaussard, F.; Gonzalez-Gonzalez, A.; Chergui, M.; Ramos-Alvarez, C.; Ruiz, C.; López-Garriga, J. *Biophysical Journal* **2004**, *87*, 1881.

(57) Klán, P.; Wirz, J. *In Photochemistry of Organic Compounds: From Concepts to Practice*; Wiley-Blackwell: **2009**.

(58) Bredenbeck, J.; Helbing, J.; Hamm, P. *Journal of the American Chemical Society* **2004**, *126*, 990.

(59) Bredenbeck, J.; Helbing, J.; Behrendt, R.; Renner, C.; Moroder, L.; Wachtveitl, J.; Hamm, P. *The Journal of Physical Chemistry B* **2003**, *107*, 8654.

(60) Bredenbeck, J.; Helbing, J.; Hamm, P. *The Journal of Chemical Physics* **2004**, *121*, 5943.

(61) Chung, H. S.; Ganim, Z.; Jones, K. C.; Tokmakoff, A. *Proceedings of the National Academy of Sciences of the United States of America* **2007**, *104*, 14237.

(62) Cervetto, V.; Hamm, P.; Helbing, J. *The Journal of Physical Chemistry B* **2008**, *112*, 8398.

(63) Strasfeld, D. B.; Ling, Y. L.; Shim, S. H.; Zanni, M. T. *Journal of the American Chemical Society* **2008**, *130*, 6698.

(64) Baiz, C. R.; McCanne, R.; Nee, M. J.; Kubarych, K. J. *The Journal of Physical Chemistry A* **2009**, *113*, 8907.

(65) Baiz, C. R.; McCanne, R.; Kubarych, K. J. *Applied Spectroscopy* **2010**, *64*, 1037.

(66) Bredenbeck, J.; Helbing, J.; Hamm, P. *The Journal of Chemical Physics* **2004**, *121*, 5943.

(67) Bredenbeck, J. H., J.; Hamm, P. *Journal of the American Chemical Society* **2004**, *126*, 990.

(68) Bredenbeck, J.; Helbing, J.; Nienhaus, K.; Nienhaus, G. U.; Hamm, P. *Proceedings of the National Academy of Sciences of the United States of America* **2007**, *104*, 14243.

(69) Baiz, C. R.; Nee, M. J.; McCanne, R.; Kubarych, K. J. *Optics Letters* **2008**, *33*, 2533.

(70) Baiz, C. R.; McCanne, R.; Nee, M. J.; Kubarych, K. J. *The Journal of Physical Chemistry A* **2009**, *113*, 8907.

(71) Dyson, P. J. *Coordination Chemistry Reviews* **2004**, *248*, 2443.

(72) King, R. B. *Journal of Organometallic Chemistry* **1999**, *586*, 2.

(73) Zwart, J.; Snel, R. *Journal of Molecular Catalysis* **1985**, *30*, 305.

(74) Chong, D.; Georgakaki, I. P.; Mejia-Rodriguez, R.; Sanabria-Chinchilla, J.; Soriaga, M. P.; Darensbourg, M. Y. *Dalton Transactions* **2003**, 4158.

(75) Streich, D.; Astuti, Y.; Orlandi, M.; Schwartz, L.; Lomoth, R.; Hammarström, L.; Ott, S. *Chemistry - A European Journal* **2010**, *16*, 60.

(76) Brown, K. A.; Dayal, S.; Ai, X.; Rumbles, G.; King, P. W. *Journal of the American Chemical Society* **2011**, *132*, 9672.

(77) Szymanska-Buzar, T. *Coordination Chemistry Reviews* **1997**, *159*, 205.

(78) Cahoon, J. F.; Kling, M. F.; Schmatz, S.; Harris, C. B. *Journal of the American Chemical Society* **2005**, *127*, 12555.

(79) Cahoon, J. F.; Kling, M. F.; Sawyer, K. R.; Frei, H.; Harris, C. B. *Journal of the American Chemical Society* **2006**, *128*, 3152.

(80) Cahoon, J.; Kling, M.; Sawyer, K.; Andersen, L.; Harris, C. *Journal of Molecular Structure* **2008**, *890*, 328.

(81) Virrels, I. G.; George, M. W.; Johnson, F. P. A.; Turner, J. J.; Westwell, J. R. *Organometallics* **1995**, *14*, 5203.

(82) Adams, R. D. C., F. A. *Inorganica Chimica Acta* **1972**, *7*, 153.

(83) Adams, R. D. C., D. E.; Cotton, F. A. *Journal of the American Chemical Society* **1974**, *96*, 749.

(84) Cervetto, V.; Helbing, J.; Bredenbeck, J.; Hamm, P. *The Journal of Chemical Physics* **2004**, *121*, 5935.

(85) Shim, S. H.; Strasfeld, D. B.; Ling, Y. L.; Zanni, M. T. *Proceedings of the National Academy of Sciences of the United States of America* **2007**, *104*, 14197.

(86) Gaussian 03 Revision B.03, M. J. F., G. W. Trucks, H. B. Schlegel, G. E. Scuseria, M. A. Robb, J. R. Cheeseman, J. A. Montgomery, Jr., T. Vreven, K. N. Kudin, J. C. Burant, J. M. Millam, S. S. Iyengar, J. Tomasi, V. Barone, B. Mennucci, M. Cossi, G. Scalmani, N. Rega, G. A. Petersson, H. Nakatsuji, M. Hada, M. Ehara, K. Toyota, R. Fukuda, J. Hasegawa, M. Ishida, T. Nakajima, Y. Honda, O. Kitao, H. Nakai, M. Klene, X. Li, J. E. Knox, H. P. Hratchian, J. B. Cross, C. Adamo, J. Jaramillo, R. Gomperts, R. E. Stratmann, O. Yazyev, A. J. Austin, R. Cammi, C. Pomelli, J. W. Ochterski, P. Y. Ayala, K. Morokuma, G. A. Voth, P. Salvador, J. J. Dannenberg, V. G. Zakrzewski, S. Dapprich, A. D. Daniels, M. C. Strain, O. Farkas, D. K. Malick, A. D. Rabuck, K. Raghavachari, J. B. Foresman, J. V. Ortiz, Q. Cui, A. G. Baboul, S. Clifford, J. Cioslowski, B. B. Stefanov, G. Liu, A. Liashenko, P. Piskorz, I. Komaromi, R. L. Martin, D. J. Fox, T. Keith, M. A. Al-Laham, C. Y.

Peng, A. Nanayakkara, M. Challacombe, P. M. W. Gill, B. Johnson, W. Chen, M. W. Wong, C. Gonzalez, and J. A. Pople, **2003**.

(87) Dunning Jr, T. H.; Hay, P. J. *Modern Theoretical Chemistry*; Plenum: New York, **1976**; Vol. 3.

(88) Hay, P. J.; Wadt, W. R. *Ab initio effective core potentials for molecular calculations. Potentials for the transition metal atoms Sc to Hg*; AIP, **1985**; Vol. 82.

(89) Hay, P. J.; Wadt, W. R. *Ab initio effective core potentials for molecular calculations. Potentials for K to Au including the outermost core orbitals*; AIP, **1985**; Vol. 82.

(90) Wadt, W. R.; Hay, P. J. *Ab initio effective core potentials for molecular calculations. Potentials for main group elements Na to Bi*; AIP, **1985**; Vol. 82.

(91) Lee, C.; Yang, W.; Parr, R. G. *Physical Review B* **1988**, *37*, 785.

(92) Miehlich, B.; Savin, A.; Stoll, H.; Preuss, H. *Chemical Physics Letters* **1989**, *157*, 200.

(93) Becke, A. *The Journal of Chemical Physics* **1993**, *98*, 5648.

(94) Tye, J. W.; Darensbourg, M. Y.; Hall, M. B. *Journal of Computational Chemistry* **2006**, *27*, 1454.

(95) Feng, X.; Gu, J.; Xie, Y.; King, R. B.; Schaefer, H. F. *Journal of Chemical Theory and Computation* **2007**, *3*, 1580.

(96) Baiz, C. R.; McRobbie, P. L.; Anna, J. M.; Geva, E.; Kubarych, K. J. *Accounts of Chemical Research* **2009**, *42*, 1395.

(97) Baiz, C. R.; McRobbie, P. L.; Preketes, N. K.; Kubarych, K. J.; Geva, E. *The Journal of Physical Chemistry A* **2009**, *113*, 9617.

(98) Cahoon, J. F.; Sawyer, K. R.; Schlegel, J. P.; Harris, C. B. *Science* **2008**, *319*, 1820.

(99) Anna, J. M.; Kubarych, K. J. *The Journal of Chemical Physics* **2010**, *133*, 174506.

(100) Heilweil, E. J.; Cavanagh, R. R.; Stephenson, J. C. *Chemical Physics Letters* **1987**, *134*, 181.

(101) van Rentergem, M.; Claeys, E. G.; van der Kelen, G. P. *Journal of Molecular Structure* **1982**, *82*, 43.

(102) Grubbs, W. T.; Dougherty, T. P.; Heilweil, E. J. *Chemical Physics Letters* **1994**, *227*, 480.

(103) Kenkre, V. M.; Tokmakoff, A.; Fayer, M. D. *The Journal of Chemical Physics* **1994**, *101*, 10618.

(104) Ridley, A. R.; Stewart, A. I.; Adamczyk, K.; Ghosh, H. N.; Kerkeni, B. n.; Guo, Z. X.; Nibbering, E. T. J.; Pickett, C. J.; Hunt, N. T. *Inorganic Chemistry* **2008**, *47*, 7453.

(105) Stewart, A. I.; Wright, J. A.; Greetham, G. M.; Kaziannis, S.; Santabarbara, S.; Towrie, M.; Parker, A. W.; Pickett, C. J.; Hunt, N. T. *Inorganic Chemistry* **2010**, *49*, 9563.

6. Development of vibrational echo 2D-IR spectrometer

6.1. Introduction

The primary motivation for expanding the existing double-resonance 2D-IR capability of the Strathclyde spectrometer to include vibrational echo spectroscopy was the superior temporal and spatial resolution of the latter method. The time resolution limitation of the double-resonance method arises from the use of shaping techniques to obtain narrow bandwidth pump pulses. The uncertainty principle establishes a connection between spectral and temporal resolution for such pulses (the time-bandwidth product) which leads to a trade-off whereby, in order to attain the desired spectral resolution (~10 cm^{-1} close to the typical linewidth of a mid-infrared absorption of a solute), the pump pulse duration lengthens to ~1-2ps. The result of this is that the sub-picosecond temporal range, which is important for e.g. hydrogen bond dynamics becomes inaccessible. In respect of spectral resolution, the lineshape distortion caused by convolution of the pump pulse lineshape with the molecular response induces severe pump axis broadening. Such convolution can mask closely separated transitions and obscure lineshape evolution making the assessment of solute-solvent interaction dynamics more challenging. As demonstrated in previous chapters, despite these temporal and spatial resolution limitations, specific chemical problems can benefit from the robustness and relative ease of application of the double-resonance method.[1,2]

The vibrational echo spectroscopy a time-domain 2D-IR technique, utilizes a sequence of excitation pulses and interferometric detection to differentiate the vibrational interaction pathways of individual modes. The change from using an intense narrow band pump pulse (double resonance) which transfers the system directly into a population state to the use of two femtosecond pump pulses which achieves a population state in a stepwise fashion (vibrational echo) has two advantages. One is the extension of the effective temporal resolution of the spectrometer into the sub-picosecond regime, typically ~100 fs. The second advantage is that the distorting effects arising from convolution of the pump pulse lineshape with the system response lineshape has a negligible effect on the overall

spectrum. This is because the <100 fs duration pulses are far shorter than both coherence dephasing (T_2) and populational relaxation (T_1) timescales determining observed lineshape e.g. typical coherence dephasing process for metalcarbonyls in solution display lifetimes of ~1-5 ps.[1,2] A major disadvantage of vibrational echo 2D-IR spectroscopy the is increased complexity of the optical assembly that requires far more precise control over pulse timing and overlap e.g. ultrafast timescales of vibrational relaxation demand a femtosecond interferogram resolution leading to sub-micrometer stage translations (1fs ≅ 300nm) with at least a few times higher precision. This high precision pulse timing control results in a lengthening of the spectrum acquisition time, which is major factor limiting the application of this technique to a broader spectrum of scientific problems.

The very first vibrational echo 2D-IR spectrometer was designed with an optical arrangement consisting of four independently propagating laser beams. Three of these were arranged in a boxcar geometry that three pulse trains propagation vectors connect a single common point to three corners of a rectangle sending photon echo signal into the direction toward fourth corner of rectangle where is overlapped with last beam serving as a local oscillator (LO).[3-14] In this configuration the isolated 3rd order molecular response is registered entirely in the time domain, which required a time-consuming double interferometry approach involving scanning the time delays between the first and second pump pulses and LO delay time versus the third pump pulse. Moreover in order to record a purely absorptive 2D-IR spectrum it was necessary to collect a non-rephasing signal in addition to the echo response. The non-rephasing signal contains the complex conjugate components of the vibrational echo signal contributions which can be achieved by reversing the time ordering of first two pulses as shown in Section 1.6.2 (Eq. 16.1-2 (p.23)).[15] The benefit of such a system is the ability to separate and collect virtually all components of the 3rd order molecular response, including those not within the scope of the 2D-IR technique. On the other hand, such a system suffers both in the complexity of controlling four beams with very high accuracy and the very long acquisition time needed to collect a single 2D spectrum. The first step in simplifying this spectrometer assembly and shortening the spectral acquisition time was achieved by employing a frequency-resolved detection system based on an array infrared detector. This removed the need

for double interferometry, instead requiring only the scanning of the time delay between the first two pulses in the sequence.[3,14] The application of frequency-resolved detection thus speeds up the 2D spectra acquisition process in the boxcar beam geometry.

A further shortening of the acquisition time was achieved by employing a collinear input beam geometry that eliminated the need for the separate recording of the non-rephasing signal to build up an absorptive 2D-IR spectrum. In the collinear geometry the first two pulsetrains were arranged collinearly with a controllable inter-pulse timing. This collinearity of the first two pulses results in both the rephasing and the non-rephasing 3rd order molecular response signals into a phase matched direction collinear with the direction of the third beam. This gives the opportunity to exploit the interference of the transmitted third pulse with the photon echo signal and eliminate need for separate LO. The mechanism of this process was discussed in Section 2.2.3 (p. 51). Such a system is more robust, owing to the fact that collinear system directly registers the purely absorptive signal, eliminating need for the repetition of the interferogram for the reversed order of the 1st and 2nd pump pulses. Similarly, LO interferometry was replaced by the direct interference of the transmitted part of the 3rd pulse with the molecular response on a frequency-domain detection system.[7,16] The transition from boxcar-type to collinear geometry combined with frequency-resolved detection has reduced the complexity of the vibrational echo 2D-IR spectrometer's optical layout to a level comparable to that of a double-resonance spectrometer but still such spectrometer does not in general match the robustness of the latter method.

Further developments of the vibrational echo 2D-IR technique have concentrated on reducing the spectrum acquisition time, of which a major part is collecting the interferogram with femtosecond temporal resolution. This pursuit of reduced spectral acquisition time has resulted in a variety of collinear 2D-IR spectrometer designs that differ only in the method of generating the co-propagating sequences of pump pulses. One way of generating this pulse pair with a controllable delay time between them was introduced by Deflores *et al.*[16] and Helbing *et al*[17] where the splitting of a single pulse was achieved by a modified Mach–Zehnder interferometer. In these systems, a single pump pulse was split into two pulses of

equal intensity by a beam splitter and then sent into separate arms of the interferometer. One of these arms is of fixed length while the second arm incorporates an optical delay line. The two pulses are recombined in a collinear geometry by a second beam splitter to create a co-propagating pulse pair with variable time delay. A major issue in such a system is the precision of the pulse timing control. It was found that, in order to obtain a good quality of interferogram the time delay needs to be scanned with an interval of less than 4 fs. This is equivalent to around 600 nm of travel of the retroreflector.[18-21] While modern high precision translation stages are capable of the required step resolution, some suffer from a lower position determination accuracy for such small steps. Fluctuations of the interferogram introduced by such poor stage positioning can have a detrimental effect on the 2D spectra since the resulting non-equidistant scanning of the interferogram introduces an apparatus function. The latter arises from errors in the positioning which adopt a Gaussian-type distribution, assuming the absence of any systematic error related to the design of stage. This distribution is convoluted into the frequency domain spectrum leading to a broadening of the spectral features and the appearance of "ghost" peaks not due to the sample signal. In Signal Analysis such distortions can be removed by use of an apodization function but, up to now, there are no good and universal functions developed for 2D-IR spectroscopy.[22,23]

In order to tackle this problem the infrared interferometer was paired with a second interferometer operating at visible wavelengths (HeNe laser) offering far superior positional precision. This design used the HeNe interferometer as reference to correct the pathlength error via piezoelectric mirror mounts within the infrared interferometer assembly. Unfortunately, such a solution improves the quality of the recorded interferogram but does not accelerate spectral acquisition beyond the time established by the delay stage stepping motion and also adds complications to the experimental control. In order to increase the acquisition rate, another modification was proposed where the interferometer stage was allowed to continuously translate across the required range while the signal from the optical interferometer was used to register the stage position for each pulse pair.[17] Averaging of several such interferograms produced a complete 2D-IR spectrum in a fraction of the time

required by the precise scanning of the time delay albeit with the overall quality strongly dependent on the number of averaged time traces.

A completely different approach to handling interferogram acquisition was introduced by Zanni *et al*.[2,18,20,24,25] who developed an innovative time-domain pulse-shaping technique with the aid of an acousto-optic modulator (OAM). In such system a single pump pulse is dispersed on a grating and filtered through a computer-controlled OAM following by reassemble of pulse light on second grating into a sequence of two identical pulses with a controllable interpulse time delay. To split a single pulse into a pair of pulses, the OAM filter is provided with a computer-generated Fourier transform of a pair of pulses with the desired time spacing. The major benefit of such a design is robust data acquisition and pulse timing control. The use of a computer controlled OAM filter rather than the traditional optical delay stages for pulse-timing control simplifies spectrometer operation permitting a marked acceleration and automation of the spectrum collection process and provides additional control over the pulse phases. The latter feature is used in pulse phase cycling, a process in which superposition of spectra with different pump pulse phase combinations permits elimination of pump radiation scatter. These benefits are balanced by an increased loss of laser radiation in comparison to traditional interferometers, a complex process of pulse shaping module calibration, a limited accessible range of inter-pulse time delays and distortions introduced by optical element imperfections.

The M-Z interferometer based methodology with simplifications was adopted by the author in construction of a vibrational echo 2D-IR spectrometer. The modifications involved the use of a novel closed-loop feedback translation stage equipped with an internal position sensor. Tests of this stage design revealed a positional accuracy of 120 fs, comparable to 158 nm resolution for optical interferometry with a HeNe laser (λ = 632.8 nm). This high stage positioning accuracy justified the simplification of the interferometer assembly by elimination of an optical frequency reference interferometry. The proposed system represents the simplest application of collinear vibrational echo 2D-IR spectroscopy principles offering relative complexity combined with good spectral resolution but moderate

acquisition time. This was found to be a useful compromise approach for applications to vibrational relaxation dynamics of metalcarbonyls in solution.

6.2. Strathclyde 2D-IR spectrometer development

In the initial phase of spectrometer development, the Mach–Zehnder interferometer was incorporated into the existing pump path of the double-resonance optical assembly with folding mirrors switching between experiments. Such a design would allow flexible use of both the vibrational echo and double resonance acquisition techniques depending on experimental requirements. Unfortunately this early design suffered from extensive losses of infrared light intensity. The major contribution to this intensity loss was the fact that the spectrometer uses only one output of the M-Z interferometer, which further reduces the useful mid-infrared radiation intensity by 50% combined with additional losses on slight beam splitters asymmetry of 44/56 (T/R). The second factor was the small beam divergence introduced by the optical down-conversion of the Ti:Sapphire based laser system, which was aggravated by the 6 metre long optical path necessary for the existing double resonance spectrometer on account of the need to house the grating based bandwidth shaping system. In light of the apparent disadvantages presented by this previous design, the vibrational echo optical assembly was completely separated from the double resonance 2D-IR spectrometer. In the new design, each experimental setup utilized all the available laser system radiation to generate the number of beams required. This modification allowed a large reduction in the (>60 %) optical path length and cut down the number of reflective and refractive optics required for the vibrational echo optical setup. The additional benefit of a shorter overall pathlength is smaller absorption of mid-infrared radiation by gas phase absorbers such as H_2O and CO_2 which is important for measurements using a frequency window near to the characteristic lines of those molecules.

The collinear photon echo 2D-IR spectrometer utilized the same laser system as the existing double resonance set-up, which was discussed extensively in Chapter 2. The layout of the vibrational echo 2D-IR spectrometer is shown in Figure 41. Gold-coated reflective optics were used throughout and two types of refractive optics were used for beam splitting. The first beam splitter (BS 1) is a

wedged CaF_2 plate that transmits 90% of mid-IR radiation into the pump path while reflecting 10% of the radiation into the probe path. The remaining beam splitters (BS 2, 3) are made of ZnSe providing a symmetrical pump light intensity division within interferometer assembly. The probe beam was directed into an optical delay stage (ODS1) by a set of mirrors (M 1, 2). The output of ODS 1 was directed by a set of mirrors (M 3) into the sample area (Fig. 7) where it is crossed with the pump beam. The pump path consists of a modified Mach-Zehnder Interferometer based on two 50/50 beam splitters (BS 2, 3). The initial pump beam is split by the entrance beam splitter (BS 2) into the two arms of the interferometer. The adjustable interferometer arm features an optical delay stage (ODS 2), auxiliary mirror (M 4) and optical modulator (Fig. 41 OM) while the fixed length interferometer arm contains a single mirror (M 5). The radiation from both arms is recombined on an exit beam splitter (BS 3).

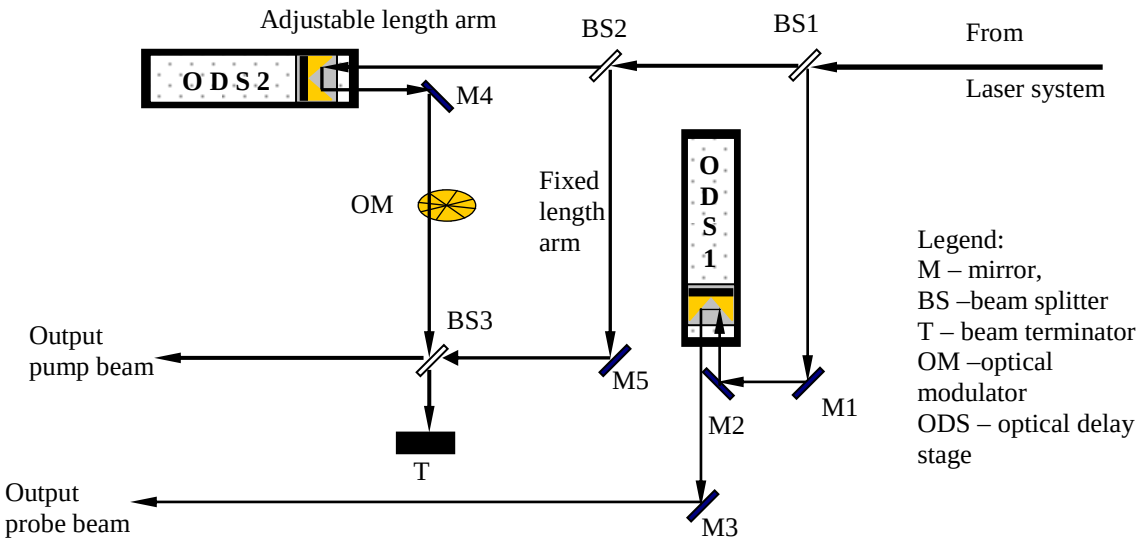

Figure 41. The layout of vibrational echo 2D-IR spectrometer optical assembly. The modified M-Z interferometer is located between BS2 and BS3 beam splitters.

From the resulting two outputs of interferometer, one is terminated (T) while the second is directed into the sample area (Fig. 7) where it is crossed with the probe beam. The transmitted pump radiation is terminated after the sample while the probe is focused onto the entrance slit of a spectrograph. The spectrographic detection unit is common to both 2D-IR acquisition methods and consists of a monochromator

combined with a 64-element MCT photoconductive array detector, as discussed previously. The chopper (OM) controlled by the detection system, facilitates the acquisition of the pump on/off spectra necessary to remove the pump-probe contribution from the recorded signal which incorporates a background due to the pump-probe signal for each of the two pump pulses leaving the MZ-interferometer as well as the desired interferogram arising from the interaction of both pump pulses.

Aligning the M-Z interferometer was performed in two stages. The different refractive index of the ZnSe beam splitter in the visible and infrared regions permitted only a rough alignment using previously described HeNe laser beam referencing approach due to the fact that refractive index of beam splitter material ZnSe is different for visible (632 nm) and mid-infrared wavelengths leading to loss of visual referencing accuracy. An initial alignment with the HeNe laser reference beam was carried out and then improved by placing a single element MCT detector behind a set of alignment irises placed according preliminary alignment with visible reference and repeating alignment procedure for the mid-infrared radiation. After this stage, overlap was sufficiently good to redirect the attenuated interferometer output into the probe path and measure the intensity of both beams simultaneously in the main detection system (MCT array). The mid-IR light intensity for each arm was maximized and equalized. Subsequently, the light from both arms was allowed to interfere on the detector producing an interference fringe pattern as shown in Figure 42. Finally, fine tuning of the alignment was performed by maximizing the contrast of the interference fringes (between peaks and troughs). After this alignment, an interferometer time delay scan was performed with 10 fs intervals for a +/-2 ps range around the estimated time zero. The recorded fringe pattern was FFT transformed into the frequency domain, showing the fringe count. Assembling all such FFT transforms for each delay time produced a two-dimensional representation of the fringe count. This formed a V shaped ridge pattern around the actual time zero as shown in Figure 43. The V shape feature corresponds to the statistical distribution of fringes for the selected range of the Interferometer adjustable arm-induced time delay.

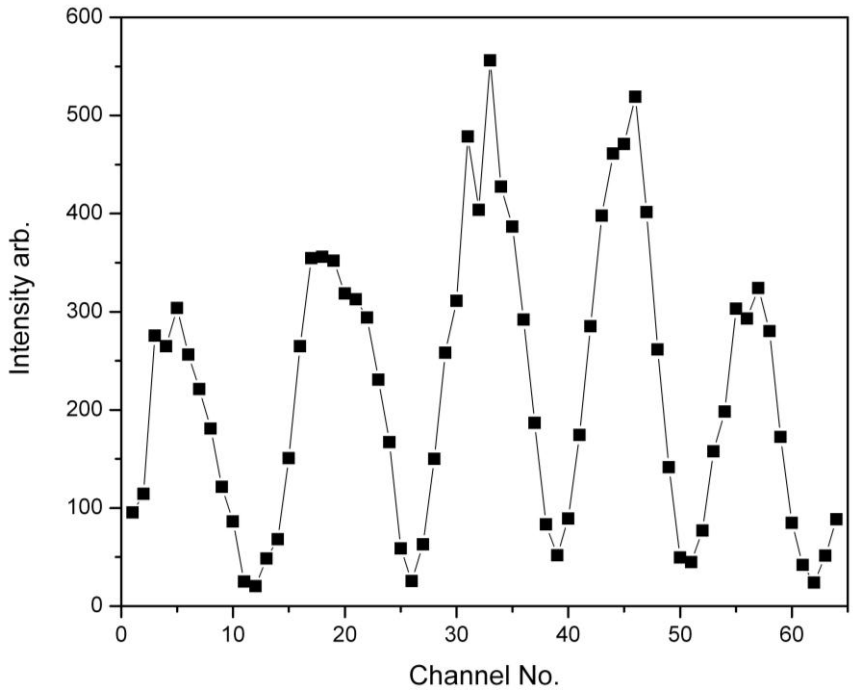

Figure 42. Fringes pattern at – 0.5 ps inter arm delay (ODS2) recorded on 64-element MCT detector.

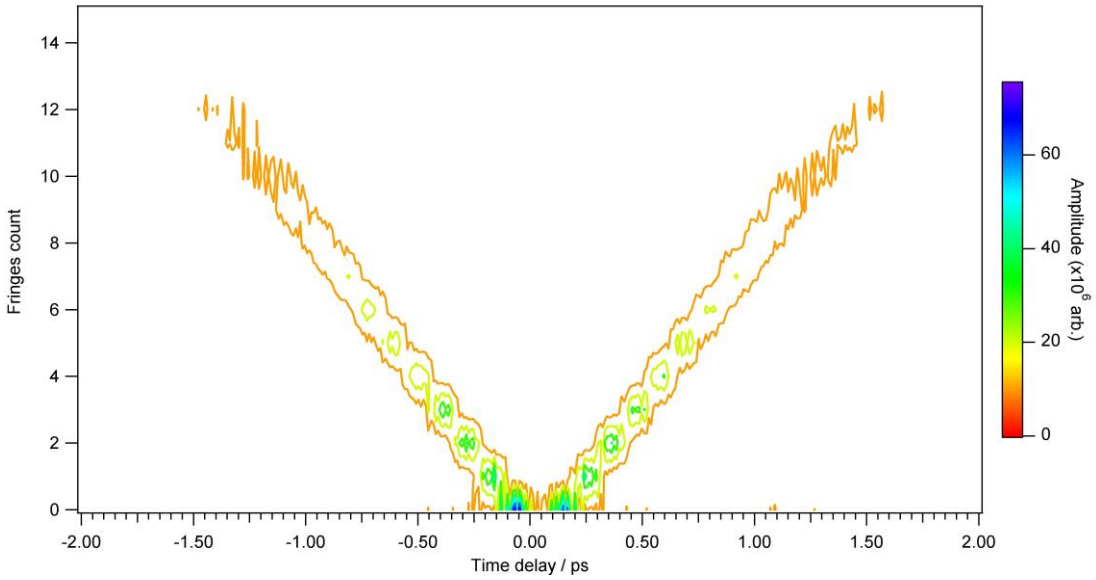

Figure 43. Plot of Fourier transformed fringes pattern against interferometer time delay. Linear regressions produced numerical value of interferometer time zero shifted +0.0036 ps from estimated zero time delay used in measurement.

The ridge of the V shape represents an average fringe count for a particular inter-pulse time delay while the observed vertical distribution is an artefact arising

from the interferogram cut-off due to the limited observation window provided by the detection system. To numerically evaluate time zero, each arm of the V shape feature was individually subjected to a linear regression. The extrapolation was used to find the location of the crossing point which provides the exact time zero of the M-Z interferometer.

6.3. Testing of vibrational echo 2D-IR spectrometer

A test spectrum recorded using the first version of the vibrational echo 2D-IR spectrometer is shown in Figure 44 along with the double resonance spectrum of the same sample.

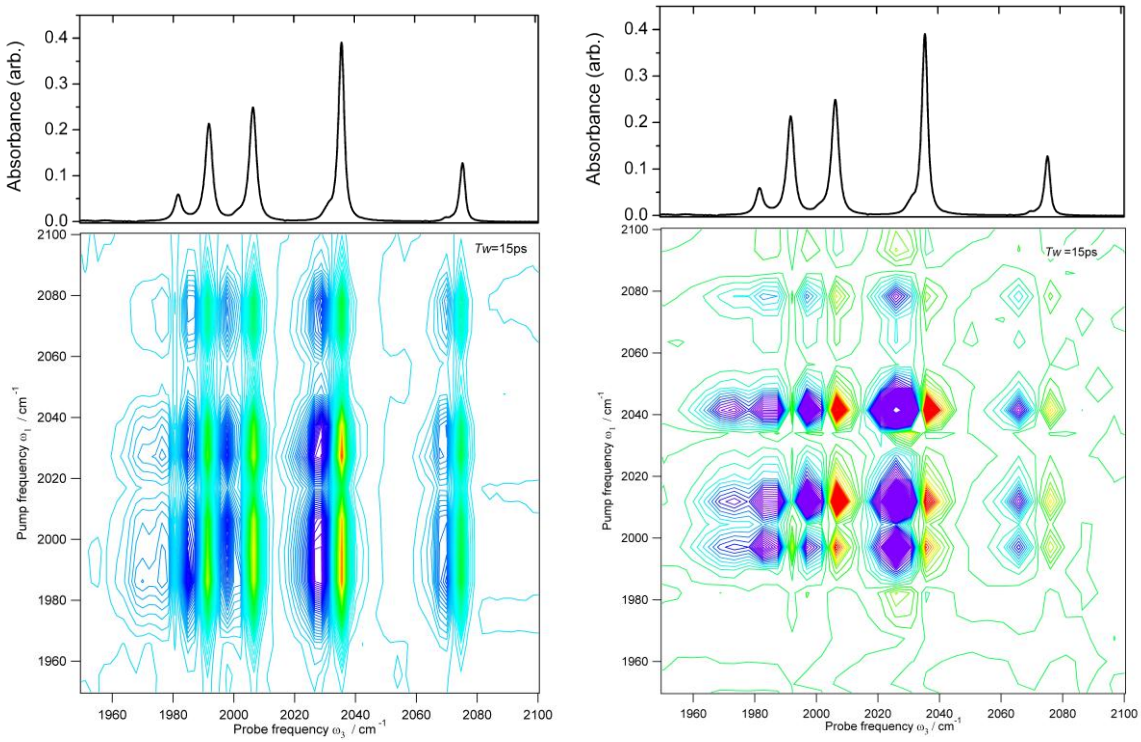

Figure 44. The FT-IR (top) and 2D-IR (bottom) spectrum of (μ-SPrS)$Fe_2(CO)_6$ solution in n-heptane for 15 ps waiting time T_w obtained using double resonance technique (left) and vibrational echo technique (right). The Echo spectrum was recorded on earlier version of M-Z interferometer set-up incorporated into double-resonance path.

Comparison of those two spectra demonstrates the major leap in 2D spectral quality but the data still suffers from several drawbacks that need to be addressed by further

development. This early version of the echo spectrometer suffered from excessive losses of mid-infrared light and a lower precision translation stage. These issues have now been addressed by the separation of the vibrational echo optical assembly from the double resonance experiment and replacement of the translation stage with a more accurate model. The improvements in signal quality and intensity exposed artefacts generated by coherent scattering of pump radiation reducing spectral quality. Pump radiation scattering creates a diagonal ridge-like artefact on the 2D spectrum obscuring diagonal features. Elimination of this effect can be achieved by incorporation of pulse phase cycling into data acquisition routine though this was not possible on the Strathclyde spectrometer.[2,5,19] Other method of coherent scatter removal is the incorporation of a wobbling Brewster window into the probe path.[5]

6.4. Software Development

6.4.1. Spectrometer control software

The existing control software for the 2D-IR spectrometer was written in Labview®. This was expanded to facilitate the vibrational echo experiments. Additions were made to the existing spectrometer main control program and the overall front panel of the new program and the module for manually controlling the interferometer stage (ODS 2) is shown in Figures 45 and 46, respectively. Setting up vibrational echo measurements requires the simultaneous use of many of the existing double resonance experimental controls (blue and black in Fig.45) along with newly added features (violet in Fig.45). The spectrometer detection system required the specification of the number of experiment repetitions, or scans, the data scanning mode, the number of laser shots per each time point. In addition, the photon echo experiment required setting of the waiting time T_w which was realised by the pump-probe time delay for the old double resonance interface, followed by parameters specific to interferogram acquisition. Interferogram acquisition required setting the range and resolution of the scan in nm (300nm ≅ 1fs). The remaining experiment-specific controls were the number of interferogram acquisitions for a particular waiting time T_w, the acquisition mode and the interferogram scanning mode. The default interferogram scanning mode (Fig. 45 half interfer.) records the interferogram from a predefined time zero position toward the negative cut-off time

(Fig. 45 Interferogram range) when the pump pulse from the adjustable arm precedes the pulse from the fixed arm. This acquisition type requires the time zero to be slightly overestimated toward positive times to ensure that the actual time zero delay is within the acquisition range.

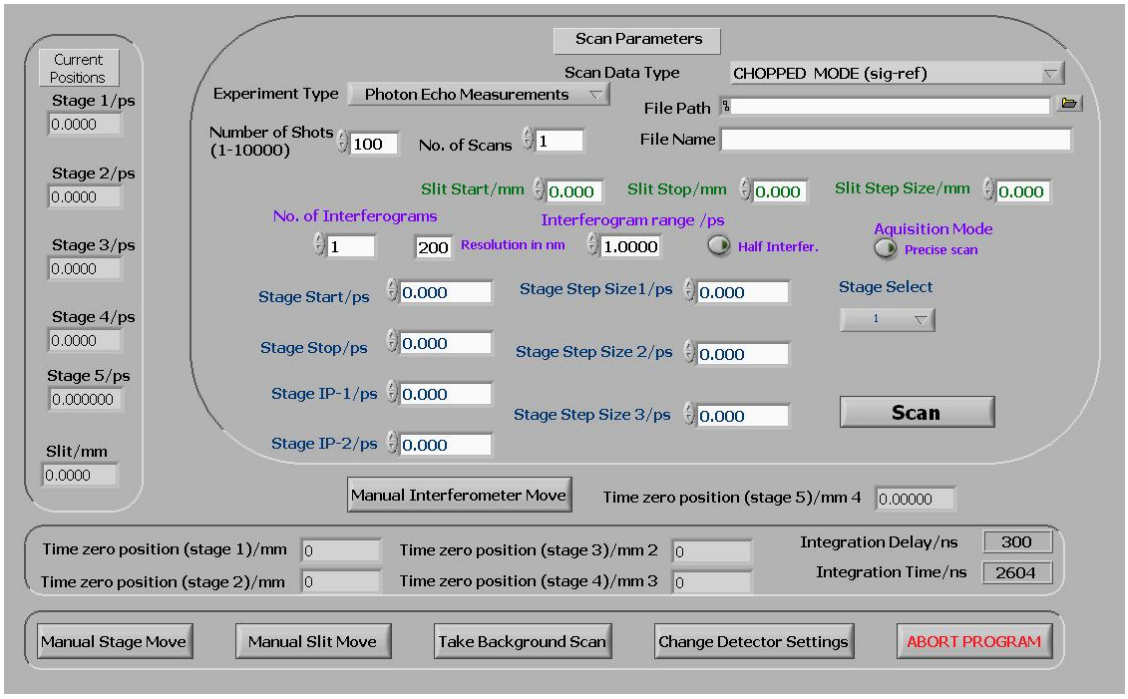

Figure 45. The expanded front panel of 2D-IR spectrometer control suite. In violet are added controls for vibrational echo acquisition management.

The full interferogram scanning mode (full interfer.) mode records a double interferogram running from the positive to negative cut-off times (Fig. 45 Interferogram range). The default acquisition mode (Fig. 45 precise scan) was designed to provide high accuracy positioning of the stage for each interferogram point by assigning an extra 300 ms of settling time for the stage servo mechanism to attain the desired position. The fast acquisition mode was designed to reduce the stage positioning time to the minimum by disabling the servo mechanism that eliminates the 300 ms settling time at the expense of slightly reduced accuracy.

The front panel of the manual interferometer stage control module is shown in Figure 46. The manual stage control panel features two graphical windows displaying the signal registered by the detector and manual stage positioning controls facilitating stage movement to a desired absolute position in mm or in time delay

(Fig. 46 bottom left panels with GO buttons) relative to a pre-set zero time position or a relative stepwise motion from the current position (Fig. 46 Fine control panel buttons).

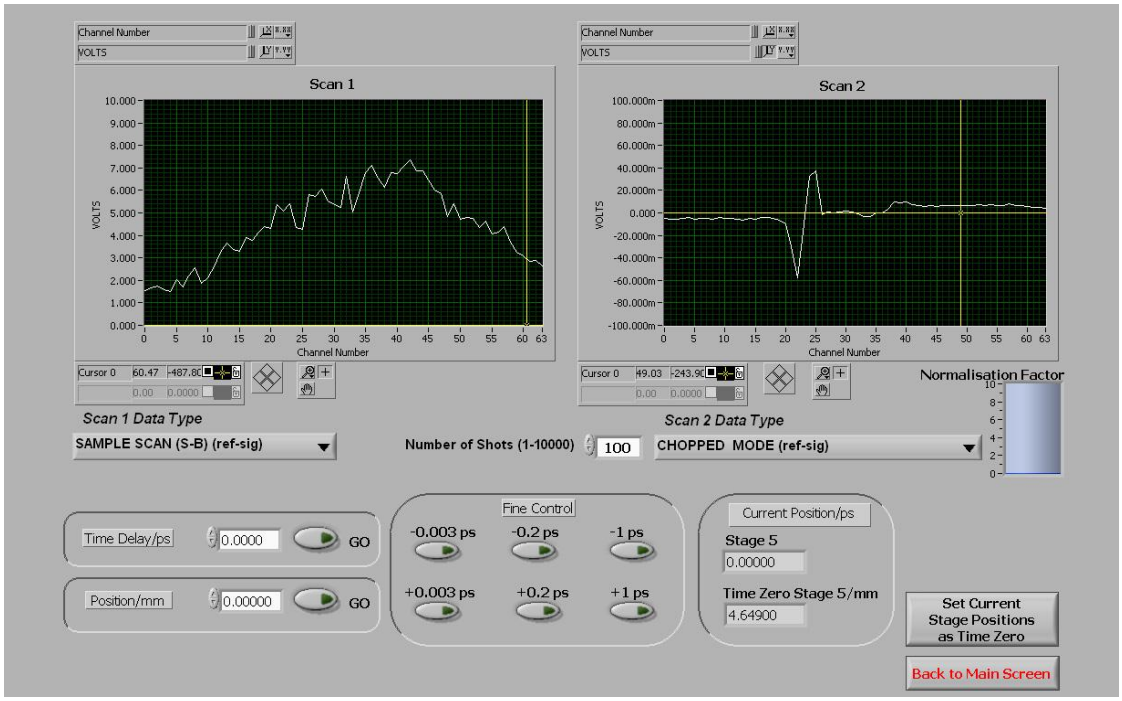

Figure 46. Front panel of the manual interferometer stage control module.

This module also permits the recording of the zero time position (Fig. 46 Set Current Stage Positions as Time Zero button) used later in the measurement. The main function of the manual interferometer stage control is in preparation for a vibrational echo experiment. To collect a vibrational echo 2D-IR spectrum, the complete interferogram needs to be acquired. The interferogram acquisition module is designed to sample the interferogram from a preset "time zero" position to a selected interferogram cut-off time (Fig. 45 Interferogram range) with a predefined step size. To ensure the completeness of the interferogram, the initial and final delay times must first be established using the manual interferometer stage control. The starting point of the interferogram acquisition must be set before the actual beginning of the interferogram owing to the fact that the Fourier Transform progress truncates initial points to finding the correct time zero and set the phase of the spectrum. Similarly, the interferogram cut-off time must be set at the point that interference oscillations have disappeared to prevent artefacts being produced in the 2D-IR spectrum.

6.4.2. Time-domain spectra processing software

The process of converting a raw interferogram into a 2D-IR spectrum begins with a pre-processing routine involving the subtraction of a background scatter spectrum and a baseline correction. Software and a numerical approach for the pre-processing of raw data have already been discussed for double-resonance 2D-IR applications in Section 2.3 (p. 57). Furthers improvements in spectrum quality can be achieved by the averaging of multiple interferograms for the same waiting time, though the outcome of such a process may be severely impaired by sample degradation and time zero/interferometer alignment drift introducing errors into the resulting spectrum. For this task, a dedicated program was designed to perform a visually aided 2D spectral averaging method and an interferogram-oriented baseline correction. The final stage of interferogram processing is the visually aided Fourier transform of the pre-processed interferogram to recover the frequency-domain 2D spectrum. Fourier transformation of the vibrational echo data into the frequency space is realised by dedicated software for setting the interferogram phase via a Fast Fourier Transformation approach. Subsequent 2D-IR spectrum analysis requires the fitting of 2D spectral features with relevant lineshape functions to recover changes of peak shapes and volumes. Igor® 6 subroutines containing fitting routines using 2D Gaussian and mixed Gaussian-Lorentzian functions were used for this along with peak volume calculating modules written to aid 2D spectral interpretation.

The main panel of the interferogram averaging program is shown in Figure 47. The program features two graphical panels displaying a selectable horizontal (Fig. 47 right) and vertical (Fig. 47 left) cross-section of the 2D data matrix, allowing data inspection and truncation point selection for the establishment of time zero. A separate module applies a polynomial background subtraction with a selectable rank. The program functions in a batch mode by performing a running average of the spectra, each divided by the total number of interferograms recognised by the number of consecutively named spectra files. The program permits the off-setting each added spectrum and selection of time zero by the truncation of a selected number data points at the front of the dataset, combined with duplication of these points at the end of the dataset to maintain a consistent dataset length.

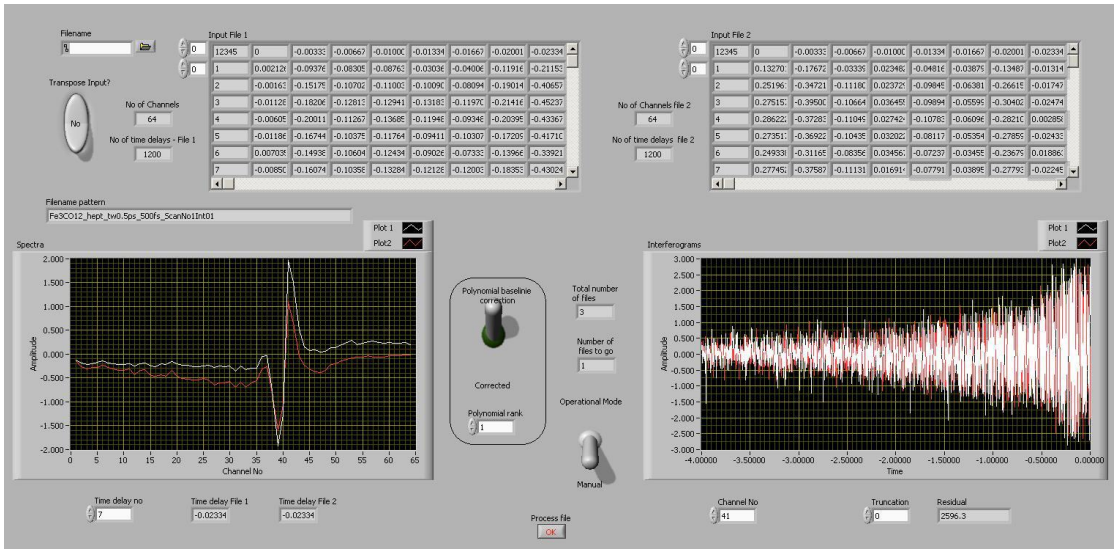

Figure 47. The main panel of 2D data matrix averaging program featuring front spectra slice truncation and polynomial baseline subtraction.

Interferogram background removal is facilitated experimentally by a chopper which allows subtraction of the pump-probe signal originating from one of the two pump pulses. This procedure is effective for longer waiting times T_w where time difference between pumps t_1 is negligible in comparison to the T_w. At shorter T_W values, the interferogram is combined with an exponentially decaying background due to the second pump-probe signal. An approximate way of correcting this interferogram baseline curvature is to fit to a low rank polynomial followed by subtraction of this from the dataset. Such treatment exploits the fact that the slowly decaying exponential background of the interferogram can be approximated by a polynomial based Taylor expansion. To avoid fitting the interferogram itself, the polynomial rank must be kept as low as possible, usually no higher than quartic. A good indication of the use of an excessive polynomial rank is the presence of an artificial interferogram ringing and an intensity increase of the near zero frequency components in the frequency domain spectra.

The main panel of the Fourier Transform program is shown in Figure 48. This program consists of three blocks: an input data decomposition featuring interferogram visualisation, a discrete Fast Fourier Transform section and FFT results visualisation and final production of the 2D spectrum. The uploaded data matrix is presented in the form of a data table and a plot (Fig. 48 top graphical panel)

of a selectable channel of the interferogram that follows the applied truncation position (time zero estimation). The remaining two graphical panels in Fig. 48 display the results of the Fast Fourier Transform for a selected data channel (right middle panel) and the whole 2D spectrum (right bottom panel) for a selected frequency range and truncation position. Additional controls allow the manipulation of the 2D spectrum by applying a linearly interpolated magnification, peak phase reversal, z-axis scaling and a switch between the Real part and Power 2D spectrum. The left hand graphical panel in Fig. 48 facilitates the visual comparison of the projection of the frequency-domain 2D spectrum onto the probe axis with a broadband pump-probe spectrum, good agreement of these signals indicate a correctly phased 2D spectrum. Once the correct time zero (truncation position) is identified, the finalized spectrum is recorded into a duplicate file where the t_1 time axis is replaced with the FFT calculated pump frequency.

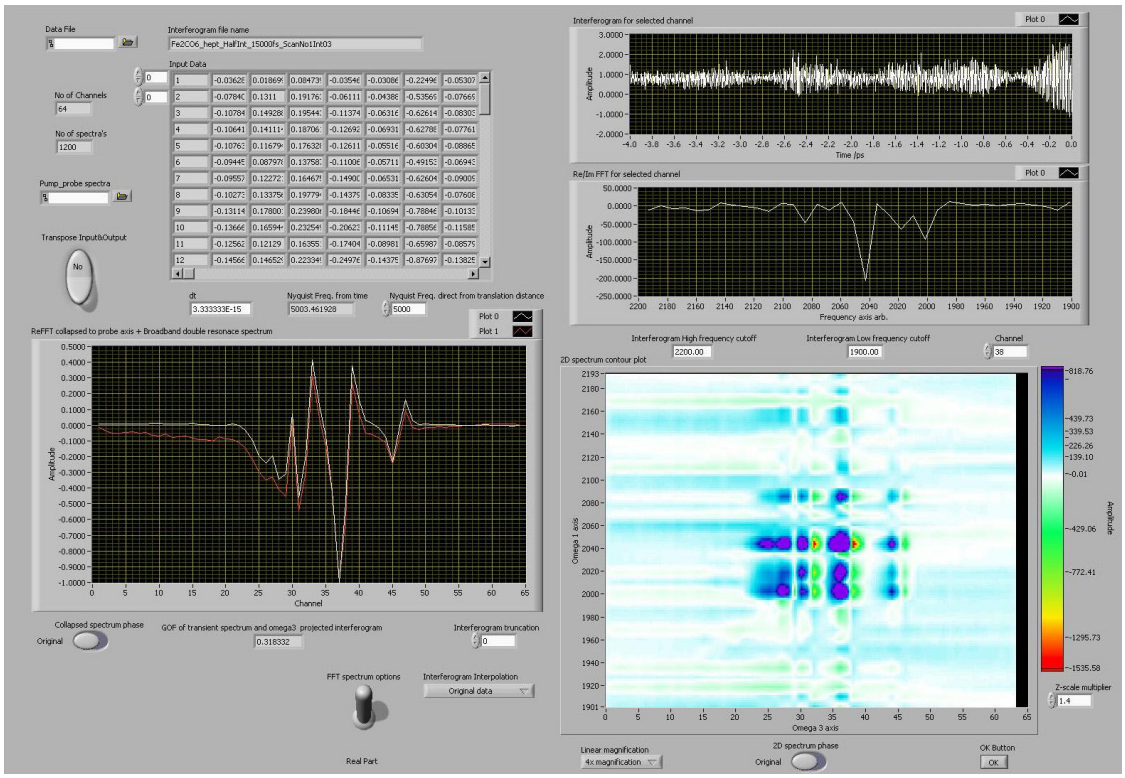

Figure 48. Main panel of visually aided Fourier Analysis program for collinear vibrational echo interferograms.

The fundamental step in the processing of a vibrational echo spectrum is the Fourier transformation of the recorded interferogram to obtain the frequency-domain

2D spectrum. The main problem of this Fourier analysis is the recovery of the correct phase of the interferogram, which originates in the selection or identification of time zero. This process is achieved by the truncation of initial points of the interferogram combined with duplication of the last data points to maintain the dataset length. Since interferogram acquisition requires long times, it is desirable to use a sampling interval (step size) that balances spectrum quality with recording time. Unfortunately, sparse sampling of the interferogram produces large phase jumps when the interferogram is truncated e.g. typically we use an interferogram sampling interval of around $1/5^{th}$ of the most prominent transition wavelength for the investigated compound, hence the phase shift per point is $\varphi = 2\pi/5 \approx 72^{o}$. To achieve finer interferogram phase tuning without increasing the acquisition time an interpolation routine was used to interpolate the interferogram with an additional ten points per original sampling interval (Fig. 48 Interferogram Interpolation button). This interpolation reduces the phase shift caused by truncation to $1/10^{th}$ of the original phase jump with the expense of slightly decreased quality of the final spectrum by errors related to the interpolation algorithm.

The recognition of the correct 2D spectrum phase is aided by two features of the program: a visual display of the 2D spectrum for a particular truncation position and a comparison of the broadband IR_{pump}-IR_{probe} spectrum with a projection of the frequency space representation of the interferogram onto the probe axis displayed in a graphical panel (Fig. 48 left bottom graphical panel). The latter feature arises from the fact that in the broadband pump-probe experiment all the characteristic frequencies of the solute are vibrationally excited, producing a cumulative spectrum which is equivalent to collapsing the frequency-space representation of the 2D interferogram involving all the characteristic system frequencies onto the probe axis.[2] The practical shortcoming of this method is that the baseline and the amplitude of the measured broadband pump-probe spectrum rarely matches those of the probe axis projected frequency-space pump axis spectrum leading to a persistent misfit of both curves and limiting the goodness of fit factor to peak values in the range 0.8 to 0.94. Much better values are achieved when using visual a representation of the 2D spectrum owed to the fact that, as discussed in the introductory chapter, the absorptive part of the 3^{rd} order molecular response is accompanied by very

characteristic dispersive part. The dispersive part is characterised by additional symmetry plane in comparison to the absorptive one producing characteristic four peak features with two positive and two negative parts lying in opposite quadrants. The correct phase factor of the 2D spectrum eliminates the dispersive part of the 3rd order molecular response and so all cross-symmetric four peak features are absent from the 2D map.

6.4.3. Time-domain spectrum analysing software

A more complete analysis of vibrational echo 2D spectra often requires the fitting of temporal changes of multiple 2D peaks, both in respect of peak volumes and shape changes. Peak volume changes occur due to population relaxation (T_1) processes while lineshape evolution represents spectral diffusion. A rigorous mathematical description of the spectral diffusion process calls upon the Frequency-Frequency Correlation Function (FFCF) that fully describes the physical processes that underpin the evolution of the lineshape.[2,22,26-28] However, from the experimental data fitting perspective it is sufficient to consider the types of functions used to represent the evolution of spectral features recorded in an experiment. In steady-state infrared spectroscopy, the spectral lines are assumed to fall into categories of fundamental lineshapes such as Lorentzian-like, in the absence of inhomogeneous broadening and Gaussian-like when inhomogeneous broadening controls the lineshape. For cases where a moderate amount of inhomogeneous broadening occurs spectral features can assume lineshapes which feature a convolution of two of the above functions that is best reproduced by a Voigt function. The 2D-IR spectral lineshapes display two non-uniform directional contributions, one parallel and a second anti-parallel to the diagonal of the spectrum. The diagonal of the 2D lineshape assumes a Gaussian-like peak function as found in the case of the steady-state infrared spectrum. In contrast, the anti-diagonal direction represents the homogeneous linewidth at short T_w values and this evolves with waiting time due to spectral diffusion of the ensemble of vibrators. The latter ensemble is a group of vibrators displaying very similar vibrational frequencies at a particular moment in time that is far narrower than the overall frequency distribution represented by the diagonal cross-section of the 2D peak. Since these vibrators are free to exchange

ensembles, the antidiagonal lineshape evolves in time in a process called spectral diffusion; the altering of vibrator frequency through solute-solvent interactions. This process causes 2D peaks to appear elongated on the diagonal while, with the progress of experimental time, the spectral features expands in the antidiagonal direction until the peaks become symmetric in both directions (round shaped).

Considering this antidiagonal lineshape evolution, the 2D spectrum features are best represented by a combination diagonal and antidiagonal Gaussian functions when the spectral diffusion contribution is pronounced. Applying fixed directional functions instead of using general FFCF functions for the 2D peak fitting process creates a difficulty in recovering spectral diffusion dynamics. There are several 2D peak functions with shape related parameters proposed to be used in place of the Frequency Fluctuation Correlation Function to recover spectral diffusion dynamics.[2,26,29,30] The author implemented two types of such functions: a cross-correlated 2D Gaussian and rotating 2D Gaussian and 2D Gaussian-Lorentzian lineshapes with constrained directional contributions. The former provides an estimation of spectral diffusion dynamics from the temporal evolution of the cross-correlation factor while the latter uses the main semi-axis tilt evolution dynamics, which according to Cho *at all.*[26] are proportional to spectral diffusion dynamics. Separate modules within the program are designed to calculate 2D peaks volumes from the fitted parameters.

The first type of fit function implementing all of the factors required for peak shape analysis is a cross-correlated 2D Gaussian function defined by the following equation 28

$$z = Baseline + A \times \exp\left[\frac{-1}{2\times(1-CrossCor^2)}\left(\left(\frac{x-x_0}{\sigma_x}\right)^2+\left(\frac{y-y_0}{\sigma_y}\right)^2-\frac{2\times CrossCor\times(x-x_0)\times(y-y_0)}{\sigma_x\times\sigma_y}\right)\right] \quad (28)$$

where *Baseline, CrossCor, x_0, y_0, A* and σ_x, σ_y define the z-axis offset, cross-correlation factor, peak position, amplitude and widths in the *x* and *y* directions, respectively. The volume of the cross-correlated 2D Gaussian is then expressed by following formula (Eq. 29)

$$V = 2\times\pi\times\sigma_x\times\sigma_y\times\sqrt{1-CrossCor^2} \quad (29)$$

The second type of fit function employs trigonometrical functions to permit the rotation of the 2D function about an axis perpendicular to spectrum plane (z-axis),

maintaining orthogonality of directional components. The 2D Gaussian fit function is defined by the following equation 30

$$z = Baseline + A \times \exp\left[\frac{-1\times\left(\cos\left(tilt\times\frac{\pi}{4}\right)\times(x-x_0)+\sin\left(tilt\times\frac{\pi}{4}\right)\times(y-y_0)\right)^2}{2\times\sigma_D^2}\right]\times\exp\left[\frac{-1\times\left(\sin\left(tilt\times\frac{\pi}{4}\right)\times(x_0-x)+\cos\left(tilt\times\frac{\pi}{4}\right)\times(y-y_0)\right)^2}{2\times\sigma_A^2}\right] \quad (30)$$

where *tilt* defines the tilt parameter. The $\pi/4$ factor allows representation of the rotation or tilting of the peak as a dimensionless quantity running from 1 for a 45^o inclination to 0 for a 90^o inclination on the *xy* plane that represents peak evolution from diagonally elongated to a round shape. The volume of such a 2D Gaussian peak is expressed by the following formula (Eq. 31)

$$V = 2\times\pi\times\sigma_D\times\sigma_A \quad (31)$$

The orthogonality of directional 2D lineshape contributions for the second type of fit functions allows a broader selection of directional components like in a mixed 2D Gaussian-Lorentzian peak as defined by the following equation 32

$$z = Baseline + A \times \exp\left[\frac{-1\times\left(\cos\left(tilt\times\frac{\pi}{4}\right)\times(x-x_0)+\sin\left(tilt\times\frac{\pi}{4}\right)\times(y-y_0)\right)^2}{2\times\sigma_D^2}\right]\times\left[\frac{1}{1+\frac{\left(\sin\left(tilt\times\frac{\pi}{4}\right)\times(x_0-x)+\cos\left(tilt\times\frac{\pi}{4}\right)\times(y-y_0)\right)^2}{\sigma_A^2}}\right] \quad (32)$$

where the Gaussian diagonal component is combined with a Lorentzian antidiagonal component. The peak volume of such a lineshape is expressed by the following formulae (Eq. 33)

$$V = \sqrt{2\times\pi}\times\pi\times\sigma_D\times\sigma_A \quad (33)$$

The above fit functions have been programmed as Igor® 6 script files to be used with a multi-peak fitting subroutine. There are separate set of scripts for fitting single peaks and peak pairs ideal for overlapping positive and negative peaks. To accelerate the fitting process scripts are self-growing determining the required number of peak functions according to the total length of the initial parameters vector.

The choice of the fit functions strongly depends on the quality of the data and the magnitude of inhomogeneous broadening. The most universal 2D Gaussian lineshape with either cross-correlation or tilt factor are functions of choice for global or long waiting times 2D spectral fitting. The mixed 2D Gaussian-Lorentzian fit function has been devised for short waiting time 2D spectra where antidiagonal peak

slopes are expected to be more accurate with Lorentzian than Gaussian lineshape. The mixed approach with application of mixed functions to early and uniform Gaussian to the long waiting times has not been tested yet but may be of merit to the 2D data analysis.

6.5. Further time-domain spectrometer development

In addition to the aforementioned improvements to the functionality of the echo spectrometer, there are other modifications which may be worth implementing. One of such modification is addressing a lack of polarisation control during measurement.[2,19,24,31-34] The fixed all parallel polarisation <zzzz> accumulates all 2D-IR spectroscopy specific Feynman pathways that are distributed over three linearly independent polarisation combinations designated as <zzxx>, <zxzx> and <zxxz>.[2,33,34] In some cases it is beneficial to select specific combinations of polarisation directions for the beams to, for example, reduce the contribution of diagonal peaks to the 2D spectrum and so maximising cross-peak visibility or to eliminate the contribution of fast solute rotation on the 2D spectrum.[2,19,32]

In order to improve the processing of the correct interferogram phase determination it would be beneficial to use the second output of the M-Z interferometer (Fig. 40) to record interference fringes while collecting the experimental data. The recorded fringe pattern would then permit automation of the Fourier analysis of the experimental data by providing a better initial estimation of the time zero position.

Another direction of possible further improvement is the reduction of the required interferogram acquisition time. Some reduction in acquisition time was achieved by reducing the position stabilisation time with an acceptable loss of accuracy. A further reduction of the acquisition time may be gained by using repetitive continuous stage motion as proposed by Hamm *at all.*[17] but using a stage position probe to record the actual time delay instead of the more complicated optical frequency interferometry reference system.

6.6. Conclusions

The development of the Strathclyde 2D-IR spectrometer to extend its functionality toward recording time-domain spectra has proven worthwhile. The proposed M-Z interferometer design without parallel visible light interferometry has proven to be a viable way of registering the vibrational echo spectrum. Early interferometer design was found to lead to unacceptable losses of signal intensity and hence the echo set-up was separated from the double-resonance experiment. This modification improved the spectral quality. Several modifications are proposed to gain more control over the experiment and shorten the spectral acquisition time.

6.7. Acknowledgements

The author would like to acknowledge contributions of Dr. Spyros Kaziannis and Dr. Katrin Adamczyk for construction and testing of the vibrational echo spectrometer optical assembly.

References:

(1) Cervetto, V.; Helbing, J.; Bredenbeck, J.; Hamm, P. *The Journal of Chemical Physics* **2004**, *121*, 5935-42.

(2) Hamm, P.; Zanni, M. *Concepts and Methods of 2D Infrared Spectroscopy*; Cambridge University Press: Cambridge, **2011**.

(3) Hochstrasser, R. M. *Proceedings of the National Academy of Sciences of the United States of America* **2007**, *104*, 14190-14196.

(4) Roberts, S. T.; Loparo, J. J.; Ramasesha, K.; Tokmakoff, A. *Optics Communications* **2011**, *284*, 1062-1066.

(5) Bloem, R.; Garrett-roe, S.; Strzalka, H.; Hamm, P.; Donaldson, P. *Optics Express* **2010**, *18*, 1747-1756.

(6) Fulmer, E. C.; Mukherjee, P.; Krummel, A. T.; Zanni, M. T. *The Journal of Chemical Physics* **2004**, *120*, 8067-78.

(7) Khalil, M.; Demirdöven, N.; Tokmakoff, A. *Physical Review Letters* **2003**, *90*, 2-5.

(8) Zheng, J.; Kwak, K.; Fayer, M. D. *Accounts of Chemical Research* **2007**, *40*, 75-83.

(9) Fayer, M. D.; Marcel Dekker, Inc.: New York, Basel, **2001**.

(10) Finkelstein, I. J.; Zheng, J.; Ishikawa, H.; Kim, S.; Kwak, K.; Fayer, M. D. *Physical Chemistry Chemical Physics : PCCP* **2007**, *9*, 1533-49.

(11) Nee, M. J.; McCanne, R.; Kubarych, K. J.; Joffre, M. *Optics Letters* **2007**, *32*, 713-5.

(12) Baiz, C. R.; Kubarych, K. J. *Optics Letters* **2011**, *36*, 187-9.

(13) Anna, J. M. B., C. R.; McCanne, R.; Nee, M. J.; Kubarych, K. J. *In Central Regional Meeting of the American Chemical Society* Cleveland, OH, United States, **2009**; Vol. CRM-493.

(14) Asplund, M. C.; Lim, M.; Hochstrasser, R. M. *Chemical Physics Letters* **2000**, *323*, 269-277.

(15) Roberts, S. T.; Loparo, J. J.; Tokmakoff, A. *Journal of Chemical Physics* **2006**, *125*, 084502.

(16) Deflores, L. P.; Nicodemus, R. a.; Tokmakoff, A. *Optics Letters* **2007**, *32*, 2966-8.

(17) Helbing, J.; Hamm, P. *Journal of the Optical Society of America* **2011**, *28*, 171.

(18) Xiong, W.; Strasfeld, D. B.; Shim, S.-H.; Zanni, M. T. *Vibrational Spectroscopy* **2009**, *50*, 136-142.

(19) Shim, S. H.; Zanni, M. T. *Physical Chemistry Chemical Physics: PCCP* **2009**, *11*, 748-761.

(20) Shim, S. H.; Strasfeld, D. B.; Ling, Y. L.; Zanni, M. T. *Proceedings of the National Academy of Sciences of the United States of America* **2007**, *104*, 14197.

(21) Xiong, W.; Zanni, M. T. *Optics Letters* **2008**, *33*, 1371-3.

(22) Kwak, K.; Park, S.; Finkelstein, I. J.; Fayer, M. D. *The Journal of Chemical Physics* **2007**, *127*, 124503.

(23) Kwak, K.; Rosenfeld, D. E.; Fayer, M. D. *The Journal of Chemical Physics* **2008**, *128*, 204505.

(24) Middleton, C. T.; Strasfeld, D. B.; Zanni, M. T. *Optics Express* **2009**, *17*, 14526-33.

(25) Strasfeld, D.; Shim, S.-H.; Zanni, M. *Physical Review Letters* **2007**, *99*, 1-4.

(26) Kwac, K.; Cho, M. *The Journal of Chemical Physics* **2003**, *119*, 2256.

(27) Hamm, P. *The Journal of Chemical Physics* **2006**, *124*, 124506.

(28) Park, S.; Kwak, K.; Fayer, M. D. *Laser Physics Letters* **2007**, *4*, 704.

(29) Zanni, M. T.; Asplund, M. C.; Hochstrasser, R. M. *The Journal of Chemical Physics* **2001**, *114*, 4579.

(30) Woutersen, S.; Pfister, R.; Hamm, P.; Mu, Y.; Kosov, D. S.; Stock, G. *The Journal of Chemical Physics* **2002**, *117*, 6833-6840.

(31) Bredenbeck, J.; Helbing, J.; Hamm, P. *The Journal of Chemical Physics* **2004**, *121*, 5943-57.

(32) Hochstrasser, R. *Chemical Physics* **2001**, *266*, 273-284.

(33) Shen, Y. R. *The principles of nonlinear optics*; Wiley, **1984**.

(34) Boyd, R. W. *Nonlinear Optics*; 2nd ed.; Academic Press: New York, **2003**.